Single-crystal titanium niobium oxide materials for fast-charging Li ion battery anodes

Fan Yu
260935568
Department of Mining and Materials Engineering,
McGill University

Submitted: April 2025

A thesis submitted to McGill University in partial fulfillment of the requirements for the degree of Doctor in Engineering in the Department of Mining and Materials Engineering

Schematic diagram of fast-charging TNO anode for LIBs

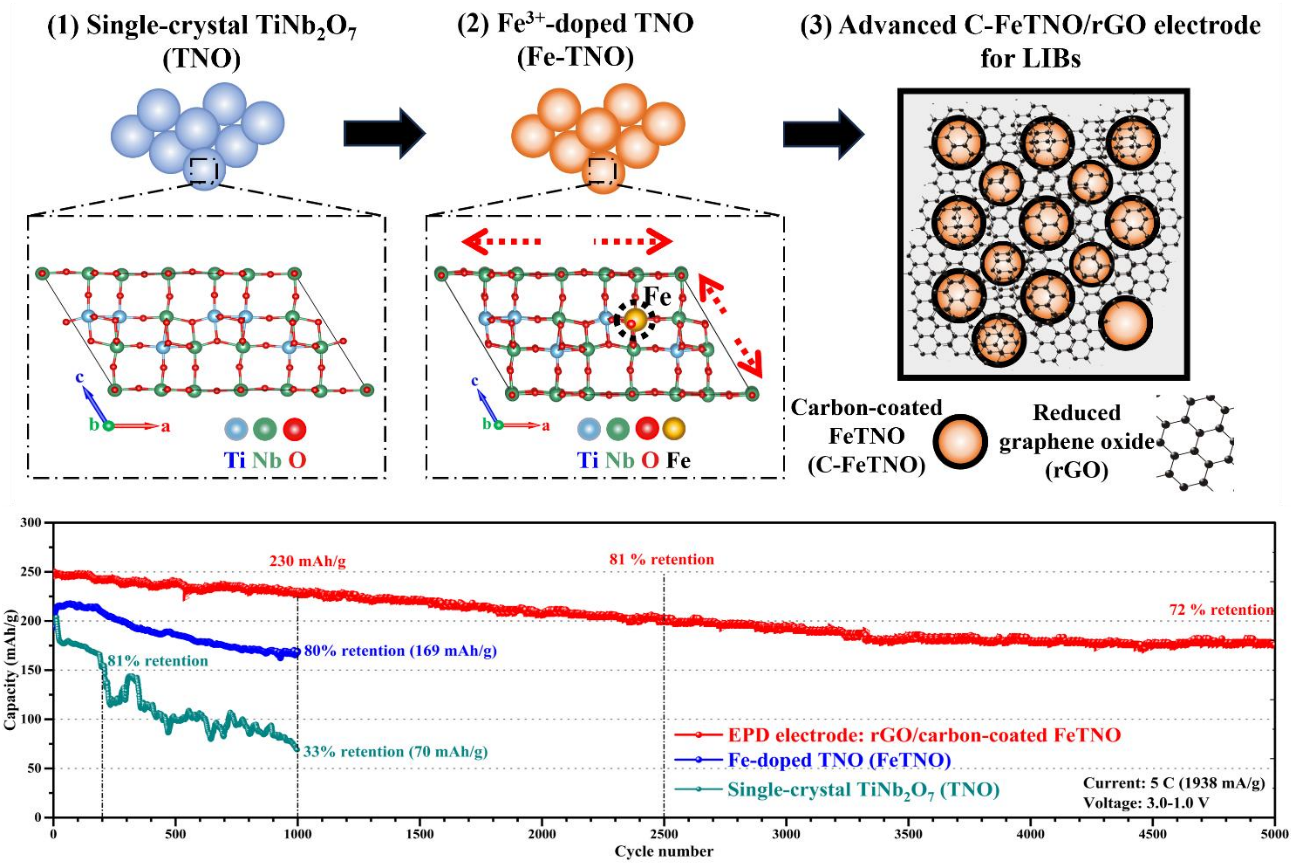

Abstract

Electric vehicles (EVs) require extreme fast charging (XFC), corresponding to a charging time of less than 15 min (> 4 C fast charging) to reach 80% state of charge, and long cycling. However, existing commercial Li-ion battery (LIB) electrode materials hardly meet these requirements. Titanium niobate ($TiNb_2O_7$, TNO) materials emerge as a promising alternative anode, offering fast ionic diffusion kinetics, high theoretical capacity, stable materials structure, and safe working potential. Nevertheless, research on TNO anode materials has been mostly restricted to synthesis of polycrystalline powders with limited associated mechanistic studies. Moreover, the cycling durability of TNO under extremely fast charging is still limited and the corresponding structural alteration mechanism remains unclear.

Firstly, a novel scalable aqueous synthesis method is reported yielding sub-micron size single-crystal TNO particles following calcination that enables fast-charging anode fabrication. The sustainable co-precipitation process yields amorphous precursor hydroxides which upon thermal conversion (calcination) transform into single crystals. The obtained TNO monocrystalline anode material at 900 °C calcination (TNO-900C) delivers a high gravimetric capacity (279 mAh/g at 1st cycle) and a high volumetric capacity (351.7 mAh/cm^3 at the initial cycle) at 0.5 C rate. Additionally, the TNO anode delivers a remarkable capacity of 223 mAh/g at 5 C and a high retention of 81.4 % after 200 cycles. In addition, TNO-900C illustrates very good fast-charging performance with a reversible capacity of 200 mAh/g at 10 C. The intercalation mechanism and diffusion behavior of the monocrystalline TNO anodes are elucidated by electrochemical kinetic analysis (GITT, CV, and EIS). The measured fast charging Li-ion storage performance can be attributed to a high Li^+ diffusion coefficient (1.37×10^{-13} cm^2/s), low polarization, and high structural stability.

Secondly, this research reports an ultra-fast charging anode with extended cycling stability enabled by Fe substitution of the TNO single-crystal nanostructured material. The underlying mechanism via which Fe substitution affects TNO's electronic properties, ionic diffusion kinetics, and structural stability is revealed through combined theoretical modeling and experimental characterization. The optimal Fe^{3+}-doped TNO monocrystalline material ($Fe_{0.05}Ti_{0.95}Nb_2O_{6.975}$) (Fe5-TNO) provides remarkable charge capacity of 238 mAh/g under 10 C (6 min charging time only) extreme fast-charging protocol (coupled with 1 C discharge), and high capacity of 200 mAh/g at 5 C and high cycling retention of 85 % after 1000 cycles. First-principles calculations

suggest that Fe^{3+} substitutional doping leads to lowering of the band gap coupled with a reduction in the Li^+ diffusion energy barrier. Overall, these factors contribute to reduced capacity decay and extreme fast charging, together promoting durable cycling performance suitable for LIB application. Reflection electron energy loss spectroscopy (REELS) reveals that Fe^{3+} doping to narrow the band gap from 3.75 eV in TNO to approximately 3.40 eV in Fe5-TNO; after initial lithiation, both TNO and Fe^{3+}-doped TNO are transformed to a higher-conductivity phase, in agreement with density functional theory (DFT) predictions. Meanwhile Fe^{3+} doping is shown to decrease the Li^+ diffusion energy barrier, boosting Li^+ diffusion coefficient by one order of magnitude, from 10^{-13} to 10^{-12} cm^2/s. This part of the research provides new insights into the design of next-generation fast-charging LIB anodes via DFT-guided substitutional doping.

Thirdly, an advanced electrode engineering method is developed further improving the performance of TNO anodes via electrophoretic deposition (EPD) of carbon-coated Fe-doped TNO (C-FeTNO) and reduced graphene oxide (rGO) upon reducing annealing. Graphene oxide is advantageously used both as binder and conductive component. This novel EPD electrode engineering method outperforms conventional approaches in constructing TNO/rGO hybrid electrodes with nanoscale homogeneous microstructure and superior percolation network, as confirmed by electron microscopic, Raman and EIS analysis. The novel electrode exhibits dramatic reduction in impedance from 183 ohm to 75 ohm and boosting of Li ion diffusion coefficient by one order of magnitude from 10^{-12} to 10^{-11} cm^2/s, compared with Fe5-TNO pristine electrode. Consequently, the EPD nanoengineered TNO/rGO hybrid anode demonstrates outstanding performance, namely capacities of 252, 246, 236, and 210 mAh/g at 0.5 C, 1 C, 2 C, and 5 C, respectively. But more remarkably, it is shown to have exceptional cycling stability of 70 % retention after 5000 cycles at 5 C.

The advances made from nanocrystal formation to DFT-guided Fe doping, and finally EPD interfacial engineering of TNO/rGO composites constitute critical contributions in the understanding and design of ultra-fast charging Li-ion electrode materials.

Resumé

Les véhicules électriques (VE) nécessitent une charge extrêmement rapide (XFC), correspondant à un temps de charge inférieur à 15 minutes (> 4 C de charge rapide) pour atteindre un état de charge de 80 %, ainsi qu'une grande stabilité en cyclage. Cependant, les matériaux d'électrodes des batteries au Li-ion (LIB) actuellement disponibles sur le marché répondent difficilement à ces exigences. Les matériaux anodiques à base de niobate de titane ($TiNb_2O_7$, TNO) apparaissent comme une alternative prometteuse, offrant une cinétique de diffusion ionique rapide, une capacité théorique élevée, une structure de matériaux stable et un potentiel de fonctionnement sécuritaire. Néanmoins, les recherches sur les matériaux d'anode TNO se sont principalement limitées à la synthèse de poudres polycristallines, avec peu d'études mécanistiques associées. En outre, la durabilité de cyclage du TNO en cas de charge extrêmement rapide est encore limitée et le mécanisme d'altération structurelle correspondant demeure à éclaircir.

De ce fait, une nouvelle méthode de synthèse aqueuse est d'abord décrite dans cette thèse, permettant d'obtenir après calcination des particules submicroniques monocristallines de TNO permettant la fabrication d'anodes à charge rapide. Le procédé de co-précipitation, développé dans l'optique d'une application industrielle à faible empreinte environnementale, produit des précurseurs composés d'hydroxydes amorphes qui, après conversion thermique (calcination), se transforment en monocristaux. Le TNO monocristallin ainsi obtenu par calcination à 900 ºC (TNO-900C) offre une capacité gravimétrique élevée (279 mAh/g au 1er cycle) et une capacité volumétrique élevée (351,7 mAh/cm^3 au cycle initial) à un taux de décharge et de décharge de 0,5 C. En outre, l'anode TNO offre une capacité remarquable de 223 mAh/g à 5 C et une excellente rétention de capacité de 81,4 % après 200 cycles. Enfin, l'anode TNO-900C présente de très bonnes performances en charge rapide avec une capacité réversible de 200 mAh/g à 10 C. Le mécanisme d'intercalation et le comportement de diffusion des anodes TNO monocristallines sont élucidés par une analyse cinétique électrochimique (GITT, CV et EIS). Ainsi, les performances d'intercalation des ions de lithium obtenues sous une charge rapide peuvent être attribuées à un coefficient de diffusion du Li^+ élevé ($1{,}37\times10^{-13}$ cm^2/s), à une faible polarisation et à une grande stabilité structurelle.

Deuxièmement, cette recherche fait état d'une anode à charge ultra-rapide avec une stabilité de cycle améliorée, rendue possible par la substitution des atomes de Ti par des atomes de Fe dans le matériau nanostructuré monocristallin TNO. La combinaison de la modélisation théorique et de

la caractérisation expérimentale permet de révéler le mécanisme sous-jacent par lequel la substitution du Fe affecte les propriétés électroniques du TNO, la cinétique de diffusion ionique et la stabilité structurelle. Le matériau monocristallin TNO dopé au Fe^{3+} ($Fe_{0.05}Ti_{0.95}Nb_2O_{6.975}$) (Fe5-TNO) offre une capacité de charge remarquable de 238 mAh/g sous un protocole de charge rapide extrême de 10 C (6 min de temps de charge seulement) couplé à une décharge de 1 C, ainsi qu'une capacité élevée de 200 mAh/g à 5 C et une rétention de capacité élevée de 85 % après 1 000 cycles. Les calculs de premiers principes suggèrent que le dopage de Fe^{3+} par substitution entraîne une diminution de la bande interdite couplée à une réduction de la barrière énergétique de diffusion du Li^+. Dans l'ensemble, ces facteurs contribuent à une diminution de la perte de capacité et permettent une charge extrêmement rapide, tout en favorisant des performances de cyclage durables adaptées à l'application des LIB. La spectroscopie de perte d'énergie par réflexion des électrons (REELS) révèle que le dopage au Fe^{3+} réduit la bande interdite, passant de 3,75 eV dans le TNO à environ 3,40 eV dans le Fe5-TNO; Après une lithiation initiale, le TNO et le TNO dopé au Fe^{3+} se transforment en une phase à conductivité plus élevée, en accord avec les prédictions de la théorie de la fonctionnelle de la densité (DFT). Par ailleurs, il est démontré que le dopage au Fe^{3+} diminue la barrière énergétique de diffusion du Li^+, augmentant le coefficient de diffusion du Li^+ d'un ordre de grandeur, de 10^{-13} à 10^{-12} cm^2/s. Cette partie de la recherche offre de nouvelles perspectives pour la conception d'anodes de LIB à charge rapide de prochaine génération grâce à un dopage substitutif guidé par la DFT.

Troisièmement, une méthode d'ingénierie des électrodes avancée a été mise au point pour améliorer les performances des anodes de TNO via la déposition électrophorétique (EPD) de TNO dopé au Fe enrobé de carbone (C-FeTNO) et d'oxyde de graphène réduit (rGO) après un recuit de réduction. L'oxyde de graphène est avantageusement utilisé à la fois comme liant et comme composant conducteur. Cette nouvelle méthode d'ingénierie d'électrode par EPD surpasse les approches conventionnelles dans la construction d'électrodes hybrides TNO/rGO avec une microstructure homogène à l'échelle nanométrique et un réseau de percolation supérieur, comme le confirment les analyses au microscope électronique, en microscopies Raman et spectroscopie d'impédance électrochimique (EIS). La nouvelle électrode présente une réduction spectaculaire de l'impédance de 183 ohms à 75 ohms et une augmentation du coefficient de diffusion de l'ion Li d'un ordre de grandeur de 10^{-12} à 10^{-11} cm^2/s, par rapport à l'électrode vierge Fe5-TNO. Par conséquent, l'anode hybride TNO/rGO nanotechnologique obtenue par EPD présente des performances exceptionnelles, à savoir des capacités de 252, 246, 236 et 210 mAh/g à 0,5 C, 1 C, 2 C et 5 C, respectivement. Plus remarquable encore, elle présente une stabilité exceptionnelle de 70 % de rétention après 5 000 cycles à 5 C.

Les progrès réalisés depuis la formation de nanocristaux jusqu'au dopage de Fe guidé par la DFT, et enfin l'ingénierie interfaciale par EPD des composites TNO/rGO constituent des contributions essentielles à la compréhension et à la conception de matériaux d'électrodes Li-ion à charge ultra-rapide.

Foreword

This thesis is based on a manuscript-based format that is offered by McGill University as an alternative to the traditional thesis format. **Chapter 3** and **Chapter 4** of this thesis have been published, whereas Chapter 6 is to be submitted shortly to a peer-reviewed journal.

Authorship contributions

Fan Yu, Senhao Wang, Rana Yekani, Andrea La Monaca, George P. Demopoulos, Single-crystal $TiNb_2O_7$ Materials via Sustainable Synthesis for Fast-charging Lithium-ion Battery Anodes, ***Journal of Energy Storage***, 95 (2024) 112482. https://doi.org/10.1016/j.est.2024.112482.

Fan Yu, Bobby Miglani, Shuaishuai Yuan, Rana Yekani, Kirk H. Bevan, George P. Demopoulos, Fe^{3+}-substitutional Doping of Nanostructured Single-crystal $TiNb_2O_7$ for Long-stable Cycling of Ultra-Fast Charging Anodes. ***Nano Energy,*** 133 (2025) 110494. https://doi.org/https://doi.org/10.1016/j.nanoen.2024.110494.

Fan Yu, Yihan Wang, Nicolas Brodusch, Bobby Miglani, Jinhyuk Lee, Raynald Gauvin, George P. Demopoulos, Ultra-fast-charging and Long-cycling Titanium Niobate/Reduced Graphene Oxide Anode via Electrophoretic Interfacial Engineering, submitted to ***Journal of Materials Chemistry A***.

All manuscripts have been prepared and submitted for publication under the supervision of Professor Demopoulos as the corresponding author. The author of this thesis has designed the experiments, carried out materials synthesis, detailed characterization, and electrochemical analysis, as well as prepared the first drafts. Rana Yekani and Andrea La Monaca assisted with the proof reading and editing of first two papers with Rana Yekani also helping with REELS characterization. Bobby Miglani, Shuaishuai Yuan, and Prof. Kirk H. Bevan assisted with theoretical computational calculation in **Chapter 4**. Nicolas Brodusch and Prof. Raynald Gauvin assisted with scanning electron microscopy characterization in **Chapter 5**. Yihan Wang assisted with the EPD tests and Prof. Jinhyuk Lee assisted with the electrochemical analysis in **Chapter 5**.

I hereby give copyright clearance for the inclusion of above papers, of which I am corresponding author, into the Ph.D. dissertation of Fan Yu.

Signature: ______________________ Date: ______________________
Prof. Dr. George P. Demopoulos
Department of Mining and Materials Engineering
McGill University
Montréal, Québec

Table of Contents

List of Figures

List of Tables

List of Symbols and Abbreviations

English Symbols

A	Contact area between the electrode and the electrolyte in GITT testing (cm^2)
a	Lattice parameter (Å)
b	Lattice parameter (Å)
B_{hkl}	Full-width at half-maximum (FWHM) (°)
c	Lattice parameter (Å)
C_{eq}	Solubility
D	Distance of separation between two interacting particles
D_{Li^+}	Chemical diffusion coefficient of Li^+ (cm^2/s)
D_{hkl}	Crystallite size in the direction perpendicular to the lattice planes (Å)
E	Energy density (Wh/kg)
e	Electronic charge (1.602×10^{-19} C)
E_{CBM}	Energy level of the conduction band minimum (eV)
E_g	Band gap (eV)
E_{VBM}	Energy level of the valence band maximum energy (eV)
F	Faraday constant = 96485 C/mol = 26.8 Ah/mol
$f(P)$	Retardation factor
I	Current (A)
I_p	Peak current (A)
$i(V)$	Total current at specific voltage (A)
J	Nucleation rate (1/s)
k_B	Boltzmann constant=1.38×10^{-23} J/K
k_g	Growth constant ($m^4/(mol\cdot s)$)
L	Diffusion length
M	Molar mass (g/mol)
m_B	Mass of active materials in GITT testing (g)
M_B	Molar mass of active materials in GITT testing (g/mol)
N	Number of nuclei
n	Number of charges
n_i	Concentration of ions (mol/L)

Q	Specific capacity (mAh/g or mAh/cm^3)
Q_g	Specific gravimetric capacity (mAh/g)
Q_v	Specific volumetric capacity (mAh/cm^3)
R	Universal gas constant
Ri	Internal resistance (ohm)
R_{ohm}	Ohmic resistance corresponding to electrolyte and current collector (ohm)
R_{CT}	Charge-transfer resistance (ohm)
r	Radius of a particle or nucleus
r_c	Critical nuclei size
S	Saturation, or Specific surface area
S_{crit}	Critical saturation ratio
t	Time (s)
T	Temperature (ºC), or Absolute temperature (K)
V	Volume (cm^3)
V_A	Van der Waals attraction potential contributions (J)
V_M	Molar volume (cm^3/mol)
V_{oc}	Open-circuit voltage
V_R	Electrostatic repulsion (J)
V_T	Total interparticle potential (J)
Z	Charge number

Greek Symbols

γ	Surface free energy per unit area (J/m^2)
ΔE_s	Steady-state voltage change stemming from the current pulse during different rest steps (V)
ΔE_t	Voltage change during the galvanostatic discharge-charge time (from τ_0 to τ_{0+t}) eliminating the iR drop (V)
ΔG	Molar Gibbs free energy (J)
ΔG_{crit}	Critical free energy (J)
ΔG_{surf}	Surface free energy change (J)
ΔG_{vol}	Volume free energy change (J)
$\Delta\mu$	Change of Gibbs free energy change per unit volume of the crystal (J/m^3)

ε	Dielectric constant of the liquid (unitless)
ε_0	Permittivity of a vacuum (C/V·m)
ζ	Zeta potential (mV)
η	Overpotential, or polarization (V)
$\eta_{act.}$	Activation overpotential, or Activation polarization (V)
$\eta_{conc.}$	Concentration overpotential, or concentration polarization (V)
θ	Angle of incidence (°)
κ	Reciprocal of the double layer thickness (1/m)
$1/\kappa$	Double layer thickness or Debye length
λ	Wavelength (Å)
μ	Chemical potential
ψ_0	Surface potential (V)
ψ_x	Electric potential (V)
ρ	Density (g/cm^3)
σ	Supersaturation
τ	Duration time of the constant current pulse in GITT testing (s)

Abbreviations

BET	Brunauer–Emmett–Teller
BJH	Barrett-Joyner-Halenda
C	Carbon
CB	Carbon black
CBM	Conduction band minimum
CE	Coulombic efficiency
CEI	Cathode electrolyte interphase
CSTR	Continuous stirred tank reactor
CV	Cyclic voltammetry
DEC	Diethyl carbonate

DETA	Diethylenetriamine
DFT	Density functional theory
DMC	Dimethyl carbonate
DOS	Density of states
DLVO	Derjaguin, Landau and Verwey and Overbeek
DLS	Dynamic light scattering
DSC	Differential scanning calorimetry
EC	Ethylene carbonate
EDS	Energy-dispersive X-ray spectroscopy
EDTA	Ethylenediaminetetraacetic acid
EDL	Electrical double layer
EIS	Electrochemical impedance spectroscopy
EVs	Electric vehicles
EPD	Electrophoretic deposition
FeTNO	Fe-doped TNO nanomaterial
FFT	Fast Fourier Transform
FTIR	Fourier transform infrared spectroscopy
GITT	Galvanostatic intermittent titration technique
GO	Graphene oxide
HAADF	High-angle annular dark-field
HOMO	Highest occupied molecular orbital
ICP	Inductively coupled plasma
ICP-OES	Inductively coupled plasma optical emission spectrometry
IEP	Isoelectric point
LCO	Lithium cobalt oxide, $LiCoO_2$
LFP	Lithium iron phosphate, $LiFePO_4$
LIBs	Lithium-ion batteries
LUMO	Lowest unoccupied molecular orbital
LTH	Lithium titanate hydrates
LTO	Lithium titanates, $Li_4Ti_5O_{12}$

NMC	Lithium nickel manganese cobalt oxides, $LiNi_xMn_yCo_{(1-x-y)}O_2$
NMP	N-Methyl-2-Pyrrolidinone
OCV	Open circuit voltage
PAW	Projector augmented wave
PBE	Functional of Perdew, Burke, and Ernzerhof
PVDF	Polyvinylidene fluoride
REELS	Reflection electron energy loss spectroscopy
rGO	Reduced graphene oxide
SAED	Selected area electron diffraction
SBR	Styrene-butadiene rubber
SEI	Solid electrolyte interphase
SEM	Scanning electron microscopy
SOC	State of charge
STEM	Scanning transmission electron microscope
TBT	Tetrabutyl titanate, $Ti(C_4H_9O)_4$
TEM	Transmission electron microscopy
HRTEM	High-resolution transmission electron microscopy
TNO	Titanium niobium oxide, titanium niobate, $TiNb_2O_7$
TGA	Thermogravimetric analysis
TTIP	Titanium isopropoxide, $Ti(OC_3H_7)_4$
TPT	Titanium isopropoxide
VASP	Vienna *ab initio* simulation package
VBM	Valence band maximum
XANES	X-ray absorption near edge structure
XFC	extreme fast charging
XPS	X-ray photoelectron spectroscopy
XRD	X-ray powder diffraction

Acknowledgements

First and foremost, I would like to express my profound gratitude to my PhD supervisor, Professor George P. Demopoulos, a full professor at McGill University, a Fellow of the Canadian Academy of Engineering (CAE), and the Gerald G. Hatch Chair in Engineering. I hold great respect for his remarkable achievements and esteemed reputation in hydrometallurgy and advanced materials. Witnessing the success of his academic family members in both academia and industry makes me proud and inspires me to strive to become an outstanding researcher. Prof Demopoulos consistently teaches me to conduct solid research and facilitates my collaboration with excellent professors, students, and associations. Based on that, I initiated many close research collaborations with Professors and their group members, enabling me to think creatively.

The years I enjoyed at the HydroMet laboratory were truly unforgettable. I'd like to thank Dr. Zhuoran Wang, Dr. Fuqiang Guo, Dr. Yan Zeng, Dr. Rana Yekani, Dr. Marianna Uceda, Han Wang, Dr. Moohyun Woo, Dr. Senhao Wang, Dr. Andrea La Monaca, Dr. François Larouche, Yihan Wang, Arian Norouzi, Joon Kyung Koong, and Philip Gamboa, and Dr Konstantina Chalastara, Dr. Majid Rasool. I deeply appreciate their support, insight, and above all, their friendship over the years. I would like to extend my heartfelt gratitude to Dr. François Larouche for his professional academic French translation of the Abstract in this thesis.

My sincere gratitude goes to Prof. Kirk Bevan, Prof. Jinhyuk Lee, Prof. Raynald Gauvin, and Prof. Sidney Omelon, Prof Philippe Ouzilleau for their professional teaching, helpful mentorship, and warm-hearted encouragement. I am grateful for Dr Shuaishuai Yuan and Bobby Miglani for their professional DFT calculation collaboration.

Finishing my PhD journey would not have been possible without my incredible family—especially, my mother, my father, my sister, and my girlfriend—who have always been rooting for my success and inspiring me to keep moving forward. I owe a debt of gratitude to my mother, a dedicated teacher, whose unwavering commitment to excellence has been a constant source of inspiration. Her dedication to her profession and family has been a beacon of strength, I extend my deepest thanks.

1. Introduction

1.1. Electric vehicles and lithium-ion batteries

Rechargeable batteries have become indispensable in modern society, powering a wide range of devices, including consumer electronics, electric vehicles, and large-scale energy storage systems.[1-5] The widespread and urgent demand for rechargeable batteries strongly raises the interest in developing advanced electrodes with high energy density, good rate performance, long cycle life, and low costs.[1,6-8]

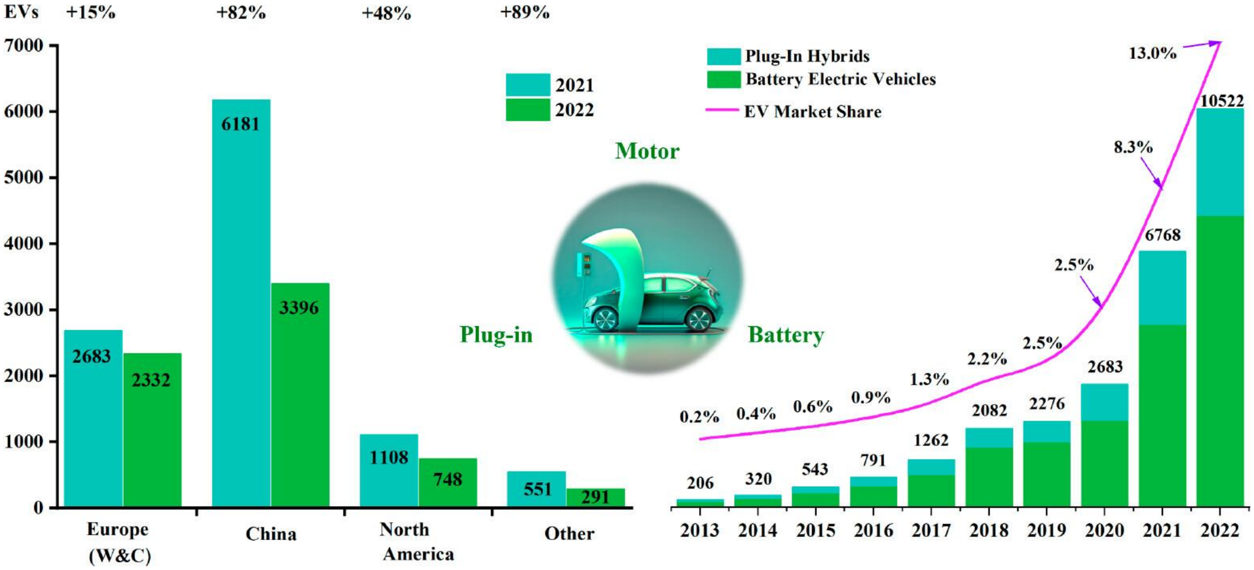

Figure 1.1. Electric vehicle development trends. Reproduced with permission.[9] Copyright 2024 American Chemical Society

To data, lithium-ion batteries (LIBs) have come to become as the most prominent type of rechargeable batteries.[5,8,9] Notably, electric vehicles and plug-in hybrids empowered by LIBs are experiencing dramatic growth trend, as shown in **Figure 1.1**.[9]

1.2. Overview of lithium-ion batteries for fast-charging applications

Electric vehicle (EV) batteries require a fast-charging function. Towards EV application, extreme fast charging (XFC) batteries have been defined, featuring less than 15 min charging time (> 4 C fast charging) to reach 80% state of charge, high specific energy (i.e., >200 Wh/kg), and long cycling.[6] However, rate capability (charging time), safety issues, and limited energy density have been the bottlenecks in meeting the increasing needs.[8] Thermal runaway of LIBs (i.e., battery fire) has been one major safety issue especially during the extremely fast charging, overcharge, over-discharge situations.[10,11] This can be attributed to the decomposition of liquid organic electrolyte and electrode material under large overpotential.[10,11] Meanwhile, the energy density of the battery is limited by the capacity of the electrodes, and proportion of inactive components, etc.[12,13]

From the perspective of LIB anode, the currently dominant and cost-effective commercial graphite anode materials with low working potential (ca., 0.1 V *vs.* Li/Li^+) suffer from Li dendrite formation safety issues due to overpotential operating under XFC situation.[14] Next-generation fast-charging anode materials with a safe operating potential, and long cycling is thus expected to address the current challenges facing XFC application in EVs. As one commercialized fast-charging anode material, spinel lithium titanate ($Li_4Ti_5O_{12}$) offers superior fast-charging capability, safe working potential (ca., 1.5 V *vs.* Li/Li^+), and excellent cycling stability, benefitting from its "zero-strain" property and high Li^+ diffusion kinetics.[15,16] But, unfortunately, $Li_4Ti_5O_{12}$ provides low theoretical capacity (175 mAh/g), only half of that of commercial graphite anode, limiting its fast-charging application in EVs. By contrast, Wadsley–Roth phase titanium niobate ($TiNb_2O_7$) provides fast-charging/high-rate properties, safe operating voltage (ca., 1.6 V *vs.* Li/Li^+), and high theoretical capacity (387 mAh/g).[17,18] Nevertheless, the $TiNb_2O_7$ anode features low electronic conductivity originating from empty 3*d*/4*d* orbitals in the *d* band of Ti/Nb and a wide band gap,[18,19] and suffers from sluggish ion diffusion kinetics.[20]

1.3. Thesis Objectives and Organization

The overall goal of this doctoral research is to advance the development of novel ultra-fast charging titanium niobium oxide ($TiNb_2O_7$, TNO) anodes by focusing on nanocrystal synthesis, substitutional doping, and electrophoretic engineering of TNO/reduced graphene oxide (rGO) highly-conducting composite structures. This thesis is structured around three well-defined objectives: (1) Sustainable synthesis of single-crystal $TiNb_2O_7$ (TNO) nanomaterials, (2) Performance improvement by substitutional Fe^{3+} doping, (3) Advanced electrophoretic electrode engineering of nanostructured $TiNb_2O_7$ (TNO) with reduced graphene oxide (rGO) acting as conducting binder. **Figure 1.2** provides a graphical description of these three research objectives.

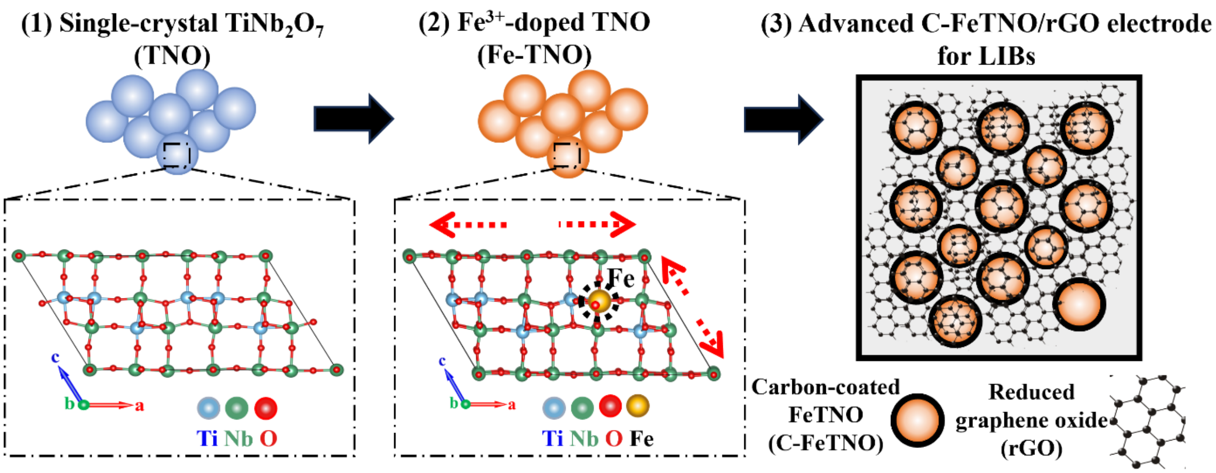

Figure 1.2. Graphical description of the three research objectives.

This thesis is organized into seven chapters, along with supporting information in Appendixes. After this introductory chapter (Chapter 1), **Chapter 2** provides a literature review on the fundamentals of LIBs, basic properties of $TiNb_2O_7$ anodes, synthesis of $TiNb_2O_7$ materials, and principles of electrophoretic deposition (EPD).

In **Chapter 3**, sustainable aqueous synthesis and property investigation of single-crystal $TiNb_2O_7$ (TNO) nanomaterials are described. The synthesis of sub-micron size single crystals was optimized through parameter adjustment in hydrolytic co-precipitation (e.g., pH, concentration) and calcination (e.g., temperature, time). The effectiveness of the synthesis and calcination processes was determined through comprehensive material characterization and correlation to electrochemical performance.

In **Chapter 4**, the substitutional Fe^{3+} doping of single-crystal TNO nanomaterials is thoroughly investigated. In-situ doping was achieved via modification of the co-precipitation process step by adding $FeCl_3$ in the reaction mixture. Extensive characterization performed to reveal the structural properties of the Fe-doped TNO and subsequently link to battery cycling stability and fast-charging capability. The underlying doping mechanism and effects have been probed through a combination of experimental results and first-principle calculations.

Chapter 5 advances a robust design of TNO/rGO all-active-material electrode, fabricated through nanoscale-controlled electrophoretic interphasial engineering. This chapter details the development of an anode based on C-coated Fe^{3+}-doped nanostructured $TiNb_2O_7$ (TNO) combined with reduced graphene oxide (rGO) to create a 3D high-conductivity network.

Chapter 6 provides a global discussion connecting the three parts of the work and **Chapter 7** includes the general conclusions, original contributions to knowledge and some ideas for future work.

1.4. References

[1] M. Armand, J.M. Tarascon, Building better batteries, Nature 451 (2008) 652-657. https://doi.org/10.1038/451652a.

[2] J.B. Goodenough, How we made the Li-ion rechargeable battery, Nat. Neurosci. 1 (2018) 204-204. https://doi.org/10.1038/s41928-018-0048-6.

[3] J.B. Goodenough, Y. Kim, Challenges for rechargeable Li batteries, Chem. Mater. 22 (2010) 587-603. https://doi.org/10.1021/cm901452z.

[4] M.S. Whittingham, Lithium batteries and cathode materials, Chem. Rev. 104 (2004) 4271-4301. https://doi.org/10.1021/cr020731c.

[5] M. Winter, B. Barnett, K. Xu, Before Li ion batteries, Chem. Rev. 118 (2018) 11433-11456. https://doi.org/10.1021/acs.chemrev.8b00422.

[6] Y. Liu, Y. Zhu, Y. Cui, Challenges and opportunities towards fast-charging battery materials, Nat. Energy 4 (2019) 540-550. https://doi.org/https://doi.org/10.1038/s41560-019-0405-3.

[7] J. Deng, C. Bae, A. Denlinger, T. Miller, Electric vehicles batteries: Requirements and challenges, Joule 4 (2020) 511-515. https://doi.org/https://doi.org/10.1016/j.joule.2020.01.013.

[8] J.W. Choi, D. Aurbach, Promise and reality of post-lithium-ion batteries with high energy densities, Nat. Rev. Mater. 1 (2016) 16013. https://doi.org/10.1038/natrevmats.2016.13.

[9] R. Wang, L. Wang, R. Liu, X. Li, Y. Wu, F. Ran, "Fast-Charging" anode materials for lithium-ion batteries from perspective of ion diffusion in crystal structure, ACS nano 18 (2024) 2611-2648. https://doi.org/10.1021/acsnano.3c08712.

[10] D.P. Finegan, E. Darcy, M. Keyser, B. Tjaden, T.M.M. Heenan, R. Jervis, J.J. Bailey, R. Malik, N.T. Vo, O.V. Magdysyuk, R. Atwood, M. Drakopoulos, M. DiMichiel, A. Rack, G. Hinds, D.J.L. Brett, P.R. Shearing, Characterising thermal runaway within lithium-ion cells by inducing and monitoring internal short circuits, Energy Environ. Sci. 10 (2017) 1377-1388. https://doi.org/10.1039/C7EE00385D.

[11] X.N. Feng, D.S. Ren, X.M. He, M.G. Ouyang, Mitigating thermal runaway of lithium-ion batteries, Joule 4 (2020) 743-770. https://doi.org/10.1016/j.joule.2020.02.010.

[12] J.B. Goodenough, K.S. Park, The Li-ion rechargeable battery: a perspective, J. Am. Chem. Soc. 135 (2013) 1167-1176. https://doi.org/10.1021/ja3091438.

[13] W. Cao, J. Zhang, H. Li, Batteries with high theoretical energy densities, Energy Storage Mater. 26 (2020) 46-55. https://doi.org/https://doi.org/10.1016/j.ensm.2019.12.024.

[14] T. Gao, Y. Han, D. Fraggedakis, S. Das, T. Zhou, C.-N. Yeh, S. Xu, W.C. Chueh, J. Li, M.Z. Bazant, Interplay of lithium intercalation and plating on a single graphite particle, Joule 5 (2021) 393-414. https://doi.org/10.1016/j.joule.2020.12.020.

[15] T. Yuan, Z. Tan, C. Ma, J. Yang, Z.-F. Ma, S. Zheng, Challenges of spinel $Li_4Ti_5O_{12}$ for lithium-ion battery industrial applications, Adv. Energy Mater. 7 (2017) 1601625. https://doi.org/https://doi.org/10.1002/aenm.201601625.

[16] T.-F. Yi, S.-Y. Yang, Y. Xie, Recent advances of $Li_4Ti_5O_{12}$ as a promising next generation anode material for high power lithium-ion batteries, J. Mater. Chem. A 3 (2015) 5750-5777. https://doi.org/10.1039/C4TA06882C.

[17] J. Han, Y. Huang, J.B. Goodenough, New anode framework for rechargeable lithium batteries, Chem. Mater. 23 (2011) 2027-2029. https://doi.org/dx.doi.org/10.1021/cm200441h.

[18] H. Park, H.B. Wu, T. Song, X.W. Lou, U. Paik, Porosity-controlled $TiNb_2O_7$ microspheres with partial nitridation as a practical negative electrode for high-power lithium-ion batteries, Adv. Energy Mater. 5 (2015) 1401945. https://doi.org/10.1002/aenm.201401945.

[19] H. Wang, R. Qian, Y. Cheng, H.-H. Wu, X. Wu, K. Pan, Q. Zhang, Micro/nanostructured $TiNb_2O_7$-related electrode materials for high-performance electrochemical energy storage: recent advances and future prospects, J. Mater. Chem. A 8 (2020) 18425-18463. https://doi.org/10.1039/D0TA04209A.

[20] K.J. Griffith, I.D. Seymour, M.A. Hope, M.M. Butala, L.K. Lamontagne, M.B. Preefer, C.P. Koçer, G. Henkelman, A.J. Morris, M.J. Cliffe, S.E. Dutton, C.P. Grey, Ionic and electronic conduction in $TiNb_2O_7$, J. Am. Chem. Soc. 141 (2019) 16706-16725. https://doi.org/10.1021/jacs.9b06669.

2. Literature Review

2.1. The Fundamentals of Lithium-ion Batteries

In 2019, the Nobel Prize in Chemistry was awarded to John B. Goodenough, M. Stanley Whittingham, and Akira Yoshino "for the development of lithium-ion batteries".[1,2] Lithium-ion batteries power a wide range of devices, from mobile phones and laptops to electric vehicles, and store large amounts of energy from solar and wind power. The Nobel Prize Committee highlighted that these lightweight, rechargeable, and powerful batteries are significant for "making possible a fossil fuel-free society".[1,2]

2.1.1. Working Principles

Goodenough defined "battery" as the energy-storage device that "stores electrical energy as chemical energy in two electrodes, a reductant (anode) and an oxidant (cathode), separated by an electrolyte that transfers the ionic component of the chemical reaction inside the cell and forces the electronic component outside the battery".[3] The chemical reactions are reversible in rechargeable batteries.[3] The lithium-ion battery (LIB), also know as "rocking chair battery"- a term coined by Michel Armand[4], is a type of rechargeable battery that involves "lithium ions" moving between the two electrodes during the charging and discharging processes. The typical LIB mainly consists of the cathode (e.g., $LiCoO_2$, $LiFePO_4$, $LiNi_xCo_yMn_zO_2$, etc.), the anode (e.g., graphite, silicon, $Li_4Ti_5O_{12}$, etc.), liquid organic electrolyte (e.g., $LiPF_6$ salt dissolved in ethylene carbonate and dimethyl carbonate (EC/DMC)), and a separator, as depicted in **Figure 2.1**.[4,5]

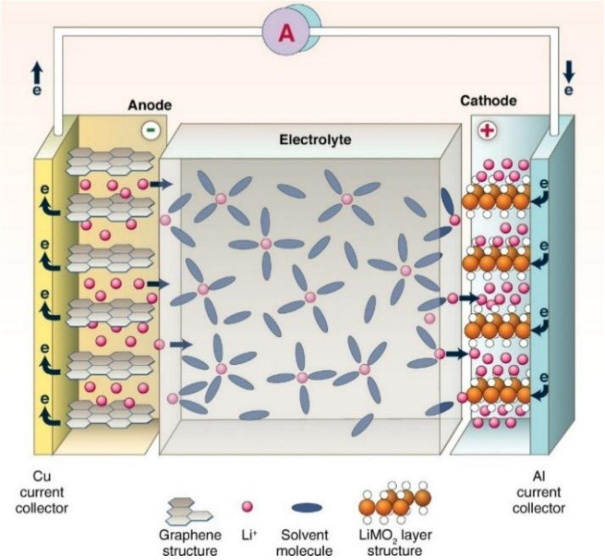

Figure 2.1 Components and working principle of LIB during discharge. Reproduced with permission.[5] Copyright 2011, American Association for the Advancement of Science.

In a typical LIB composed of graphite anode and $LiCoO_2$ cathode (**Figure 2.1**), battery discharge involves the transport of lithium ions from the graphite anode, through the electrolyte, and their insertion into the cathode (lithiation).[5] Likewise, the electrons move from the anode to the cathode through the external circuit. Li-ion intercalation within the host cathode material is enabled via the simultaneous reduction of the transition metal (charge compensation); when charging, an external power supply is used to reverse this process.[3,5,6]

The two half-reactions and the overall reaction during discharging (**Figure 2.1**) can be demonstrated as follows:[3,5-7]

$$\text{Cathode: } Li_{1-x}CoO_2 + x\,Li^+ + x\,e^- \rightarrow LiCoO_2 \qquad \textbf{(equation 2.1)}$$

$$\text{Anode: } Li_xC_6 \rightarrow C_6 + x\,Li^+ + x\,e^- \qquad \textbf{(equation 2.2)}$$

$$\text{Overall reaction: } Li_{1-x}CoO_2 + Li_xC_6 \rightarrow LiCoO_2 + C_6 \qquad \textbf{(equation 2.3)}$$

Key performance metrics of LIBs include specific (gravimetric/volumetric) capacity, voltage, energy density, rate performance, etc.[8-10] These properties are highly dependent on the chemical composition, crystal structure, and ionic/electronic properties of the electrode materials.[9]

Specific capacity (Q) includes gravimetric and volumetric capacities.[3] The specific gravimetric capacity (Q_g) is the total charge per unit weight (mAh/g), and the specific volumetric capacity (Q_v) refers to the total charge per unit volume (mAh/cm^3).[9,11] According to Faraday's first law:

$$Q_g = \frac{nF}{M} \qquad \textbf{(equation 2.4)}$$

$$Q_v = \frac{nF}{V} = Q_g \cdot \rho \qquad \textbf{(equation 2.5)}$$

where n is the number of charges (n=1 for Li^+), F is the Faraday's constant of 96,485 C/mol, M represents the molar weight (g/mol), V is the volume (cm^3), and ρ is the density (g/cm^3).[9,11] For example, theoretical gravimetric capacities of graphite (LiC_6) and $TiNb_2O_7$ ($Li_5TiNb_2O_7$) anodes can be determined as follows:

$$Q_g(C_6) = \frac{96485\left(\frac{C}{mol}\right)}{12\times 6\left(\frac{g}{mol}\right)} \times \left(\frac{1000}{3600}\right)\left(\frac{mAh}{A\cdot s}\right) = 372.24\left(\frac{mAh}{g}\right) \qquad \textbf{(equation 2.6)}$$

$$Q_g(TiNb_2O_7) = \frac{5\times 96485\left(\frac{C}{mol}\right)}{345.67\left(\frac{g}{mol}\right)} \times \left(\frac{1000}{3600}\right)\left(\frac{mAh}{A\cdot s}\right) = 387.67\left(\frac{mAh}{g}\right) \qquad \textbf{(equation 2.7)}$$

The open-circuit voltage (V_{oc}, V) is the voltage between the battery terminals when no current applied.[3] V_{oc} theoretically depends on the difference in the lithium chemical potential (μ) between the anode (μ_{Li}^{Anode}) and cathode ($\mu_{Li}^{Cathode}$):[3]

$$V_{oc} = \frac{\left(\mu_{Li}^{Cathode} - \mu_{Li}^{Anode}\right)}{nF} \qquad \textbf{(equation 2.8)}$$

The output energy density (E_{dis}) is determined by the discharge voltage (V_{dis}) and the specific discharge capacity (Q_{dis}):[3]

$$E_{dis} = \int_0^{Q_{dis}} V_{dis}\,(q)dq = \int_0^{t_{dis}} V_{dis}\,(q) I_{dis} dt \qquad \textbf{(equation 2.9)}$$

where q is the capacity, t_{dis} is the discharge time, and I_{dis} is the constant current applied in the galvanostatic mode. Practically, during the charging and discharging, V_{dis} is distinct from V_{oc} due to the development of polarization or overpotential including activation polarization ($\eta_{act.}$), Ohmic polarization (IR drop), and concentration polarization ($\eta_{conc.}$), as illustrated below:[3,8]

$$V_{dis} = V_{oc} - (IR + \eta_{conc.} + \eta_{act.}) \qquad \textbf{(equation 2.10)}$$

The C-rate describes the rate at which a battery is discharged (or charged) to its maximum capacity.[10] A 1 C rate is the current density under which the battery can be fully discharged (or charged) in 1 hour, and typically the value of the applied current (in units of mA/g) is normalized with respect to its theoretical capacity.[3,8] For example, 1 C for a graphite anode is defined as 372 mA/g, corresponding to its theoretical capacity of 372 mAh/g; 10 C for the same anode is 3720 mA/g.

Rate performance refers to the capability to retain capacity under various C-rates, particularly at high rates like 1 C, 10 C, 100 C, etc.[3,10] This metric is typically used to assess fast-charging/discharging capabilities, as well as reversibility and cycling stability.[3,10]

2.1.2. Cathode Materials

Prof. John B. Goodenough[7] was the first to identify lithium cobalt oxide ($LiCoO_2$) in 1980,[12] lithium manganese oxide ($LiMn_2O_4$) in 1983,[13] and lithium iron phosphate ($LiFePO_4$) in 1997[14,15] as cathode materials. These discoveries have paved the way for the development of numerous cathode materials.[6,7,16] Currently, there are three main types of cathode materials: layered lithium transition metal oxide materials (e.g., layered $LiMO_2$ (M= Co, Mn, Ni)),[6,12] spinel lithium transition metal oxide (e.g., spinel LiM_2O_4 (M= Co, Mn, Ni)),[13] and olivine lithium transition metal phosphates (e.g., olivine $LiMPO_4$ (M= Fe, Co, Mn, Ni))[8,17]. Each of these cathode materials is widely used for different applications according to unique characteristics and advantages.

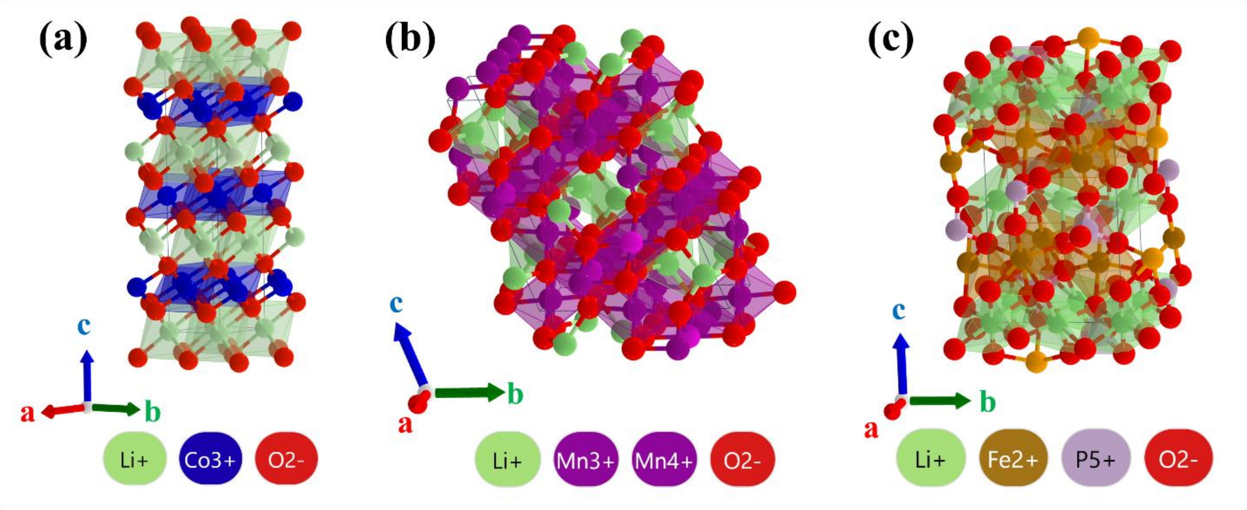

Figure 2.2. Crystal structure of (a) layered $LiCoO_2$ (trigonal system, $R\bar{3}m$ space group), (b) spinel $LiMn_2O_4$ (cubic system, $Fd\bar{3}m$ space group), and (c) olivine $LiFePO_4$ (orthorhombic system, Pnma space group). Drawn with the Material Project.[18]

Among the three, the family of layered $LiMO_2$, is known for its high energy density. These materials, where M represents Co, Mn, and/or Ni, include compounds such as $LiCoO_2$, $LiNiO_2$, $LiMnO_2$, and the mixed-metal oxide $LiNi_xCo_yMn_zO_2$.[17,19] $LiCoO_2$ (**Figure 2.2(a)**) has a trigonal structure in $R\bar{3}m$ space group.[6] Commercialized by SONY in 1991, it features a high theoretical capacity (274 mAh/g), high conductivity, high-rate properties, and good cycling stability, which has made it one of prominent choices for consumer electronics, despite the environmental issues and high cost.[12,17,20] $LiNiO_2$ offers a higher voltage and higher capacity, promising it as the highest energy density alternative for next generation, but it suffers from thermal instability and safety concerns.[21] $LiMnO_2$ provides a lower cost alternative and high safety with good thermal stability, though it has a lower capacity.[13] The $LiNi_xCo_yMn_zO_2$ benefits from the combined advantages of $LiCoO_2$, $LiNiO_2$, and $LiMnO_2$, balancing properties of capacity, voltage, stability, and cost-effectiveness according to its components.[22-24] For example, $LiNi_{0.8}Co_{0.1}Mn_{0.1}O_2$ cathode (**Table 2.1**) provides a high theoretical capacity of 276 mAh/g, a high working potential of 3.8 V (*vs*. Li/Li^+), and a high energy density of 780 Wh/kg, as well as a medium cost.[23,24]

Table 2.1 Properties of common cathode materials (derived from Ref.[25])

Structure	**Cathode**	**Theoretical Capacity** [mAh/g]	**Practical Capacity** [mAh/g]	**Avg. Voltage (*vs.* Li/Li$^+$) [V]**	**Energy density** [Wh/kg]	**Cost**
Layered	$LiCoO_2$	274	185	3.9	720	High
	$LiNi_{1/3}Co_{1/3}Mn_{1/3}O_2$	278	160	3.8	610	Medium
	$LiNi_{0.8}Co_{0.1}Mn_{0.1}O_2$	276	205	3.8	780	Medium
Spinel	$LiMn_2O_4$	148	120	4.1	490	Low
Olivine	$LiFePO_4$	170	150	3.4	510	Low

Note: Practical capacity and energy density are determined at 0.1 C and calculated based on electrode materials.

Spinel $LiMn_2O_4$ cathode (**Figure 2.2 (b)**) enhanced thermal tolerance and excellent rate performance.[17,26] These advantages of high thermal stability and fast 3D Li ion diffusion can be attributed to a 3D spinel structure.[25] It has a cubic structure in the $Fd\overline{3}m$ space group, where Mn occupies half of the octahedral sites and Li occupies one-eighth of the tetrahedral sites within the cubic close-packed oxygen framework.[26,27] In addition, $LiMn_2O_4$ is a more affordable cathode than commercial $LiCoO_2$, due to the abundant elemental distribution of Mn.[25] However, its application is limited by its lower capacity (148 mAh/g) and poor cycle life.[17,28] The severe capacity fade is caused by the dissolution of Mn due to the attack of HF acid, which is produced by side reactions of $LiPF_6$ in the electrolyte.[17,25]

The Olivine $LiFePO_4$ cathode (**Figure 2.2 (c)**) is the most popular among olivine lithium transition metal phosphates.[29] The increasing percentage in both electric vehicles and grid markets proves its excellent safety properties, remarkable cycling stability (above 10,000 cycles), and cost-effectiveness.[17,29] Its excellent structural stability stem from the strong P—O bonds that prevent the oxygen release.[30] Although pristine $LiFePO_4$ has a very low conductivity and low Li-ion diffusion coefficient, various strategies, including nanosizing and carbon coating, have been employed to address these issues.[31] However, its low working voltage (3.4 V) and low theoretical capacity (170 mAh/g) limit its energy density.[4,17]

2.1.3. Anode Materials

In the early stages, lithium metal was regarded as a promising anode for commercial batteries because of its extremely high theoretical capacity of 3860 mAh/g and its low electrochemical potential (–3.04 V versus the standard hydrogen electrode).[9,16,32,33] In the 1970s, Stanley Whittingham at Exxon used metallic lithium as an anode for Li secondary batteries.[16,32] In the late 1980s, Moli Energy first commercialized rechargeable lithium metal batteries by pairing them with a MoS_2 cathode, enabling a high energy density battery with 100 cycles.[16,32,34] However, the high chemical reactivity of metallic lithium and the uncontrollable formation of lithium dendrites during cycling resulted in short circuits, battery fires, and other serious safety hazards.[16,32] Ultimately, these safety issues caused the failure of the 1st-generation rechargeable lithium-metal battery.[32,34]

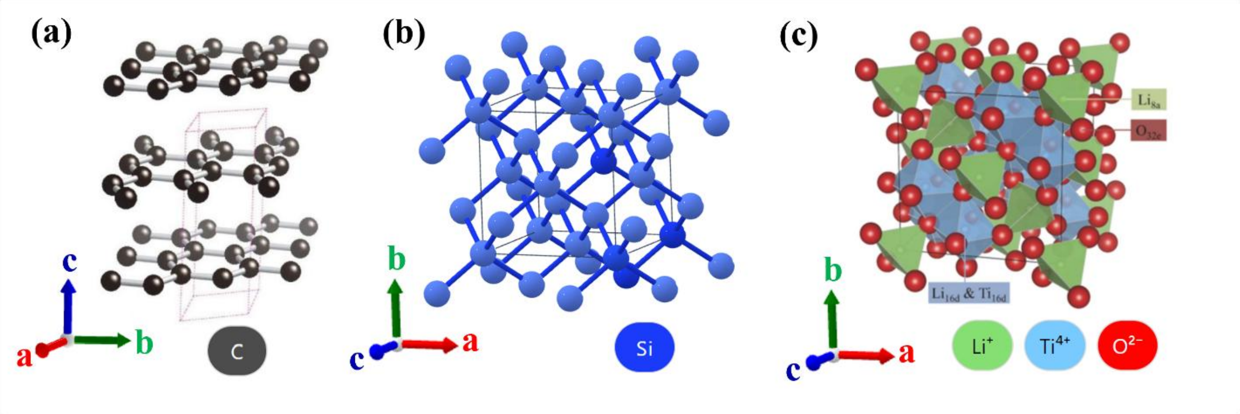

Figure 2.3. Crystal structure of (a) graphite (trigonal system, space group R$\bar{3}$m), (b) silicon (cubic system, space group Fd$\bar{3}$m). Drawn with the Materials Project.[18] and (c) $Li_4Ti_5O_{12}$ (cubic system, space group Fd $\bar{3}$ m). Reproduced with permission.[35] Copyright 2014, The Electrochemical Society

Current commercial anode materials include graphite (**Figure 2.3(a)**), silicon (**Figure 2.3(b)**), and lithium titanate ($Li_4Ti_5O_{12}$) (**Figure 2.3(c)**).[36] Graphite is the dominant anode material for LIBs.[36,37] Graphite was used in the first Li-ion battery commercialized by Sony in the 1990s for consumer electronic devices.[6,16] It provides a high theoretical gravimetric capacity of 372 mAh/g, along with a very low operating potential (ca. 0.1 V vs. Li/Li^+), enabling a high theoretical energy density of LIBs.[4,6,16] Additionally, it offers high electrical conductivity ($>10^3$ S/cm) and a high Li-ion diffusion coefficient, resulting in fast kinetics during lithium intercalation reactions.[38,39] Owing to its layered structure, it can store Li ions via an "intercalation mechanism": Li ions or atoms reside in interstitial sites within the host lattice.[38,40] This mechanism allows the lithium to be inserted and extracted with minimal strains and structural changes in the host material, which ensures good capacity retention over thousands of charge-discharge cycles.[16] Further, its excellent cost advantage due to natural abundance and simple processing contributes to its success as a commercial anode including the electric vehicle market.[16] However, from a safety perspective, its low operating potential raises the risk of lithium plating and dendrite formation, especially under large overpotential situations arising from extremely fast charging and overcharging, creating battery thermal runaways.[39,41]

Table 2.2 Comparison of common anode materials

Anode materials	Theoretical capacity [mAh/g]	Potential (vs. Li/Li$^+$) [V]	Charging time [min]	Cycle life [cycles]	Cost	Density [g/cm^3]	Ref.
Graphite	372 (LiC_6)	0.1	30-60	>1,000	Low	2.25	[42,43]
Silicon	4200 ($Li_{4.4}Si$)	0.2-0.5	60-120	>200	Low	2.33	[42,43]
$Li_4Ti_5O_{12}$	175 ($Li_7Ti_5O_{12}$)	1.55	<30	>10,000	Low	3.5	[44]

Another anode material of great commercial interest, the silicon (Si) anode (**Figure 2.3(b)**) is known for its high energy density (high capacity and low operating voltage) and low cost. It provides highest theoretical gravimetric capacity of 4200 mAh/g (based on $Li_{22}Si_5$, also known as $Li_{4.4}Si$), which is higher than that of a lithium metal anode and over ten times larger than that of a graphite anode.[40] This extremely high capacity can be attributed to its "alloying mechanism": Li forms a Li-Si alloy by breaking the bonds between host atoms.[38,40]

$$Si + x\,Li^+ + x\,e^- \rightarrow Li_xSi \qquad \textbf{(equation 2.11)}$$

However, lithiation causes dramatic structural changes: the silicon anode material suffers from significant volume change (>300 %) during lithiation, leading to structural degradation and poor cycling stability.[6,40,45] Additionally, Si has a low electronic conductivity ($<10^{-4}$ S/cm), which limits its electrochemical performance.[38,40] These limitations of pure Si as anode have led the industry to move towards its utilization in the form of composites with graphite at relatively limited proportions.[46]

Lithium titanate ($Li_4Ti_5O_{12}$) (**Figure 2.3(c)**) is the commercial anode material with the best rate performance and structural stability.[47] $Li_4Ti_5O_{12}$ features a spinel structure belonging to a cubic system and space group $Fd\bar{3}m$: lithium ions occupy the tetrahedra 8a sites and one-sixth of the 16d octahedra sites; Ti^{4+} ions occupy the remaining 16d sites.[37] This structure facilitates facile Li-ion transport involving distorted Li polyhedral in metastable intermediates along two-phase boundaries, allowing for fast Li-ion diffusion kinetics.[47] Its spinel structure and strong Ti-O bond enable a highly stable structure characterized by a small volume change (<0.3 vol%) during charging/discharging, known for its "zero strain" property.[8,48] With an electrochemical potential of 1.55 V (*vs*. Li/Li$^+$), it operates at a safe voltage, preventing electrolyte decomposition or lithium plating problems that occur below 1 V.[49] The lithiation reaction of spinel $Li_4Ti_5O_{12}$ involves three Ti^{4+} ions being reduced to Ti^{3+} ions, forming a rock salt structured $Li_7Ti_5O_{12}$, as described:

$$Li_4Ti_5O_{12} + x\ Li^+ + x\ e^- \leftrightarrow Li_{4+x}Ti_5O_{12} \qquad \textbf{(equation 2.12)}$$

This reaction provides a theoretical specific gravimetric capacity of 175 mAh/g (x=3), which is only half that of graphite (372 mAh/g). Thus, while LTO is excellent in terms of power delivery and fast-charging, it suffers from low energy density that limits its broader application in the EV market.[38,40]

2.1.4. Fast-charging Anodes

In the previous section, in describing the graphite anode, reference was made to the safety problem including battery thermal runaway (**Figure 2.4(a)**) during fast charging-discharging.[39,41,50] As graphically illustrated in **Figure 2.4**, fast charging can cause severe battery degradation and safety problems not only via lithium plating (the dendrite problem) (**Figure 2.4(b)**) but also by triggering mechanical cracking, side reactions, and eventually heat generation (**Figure 2.4(c)**).[16,39]

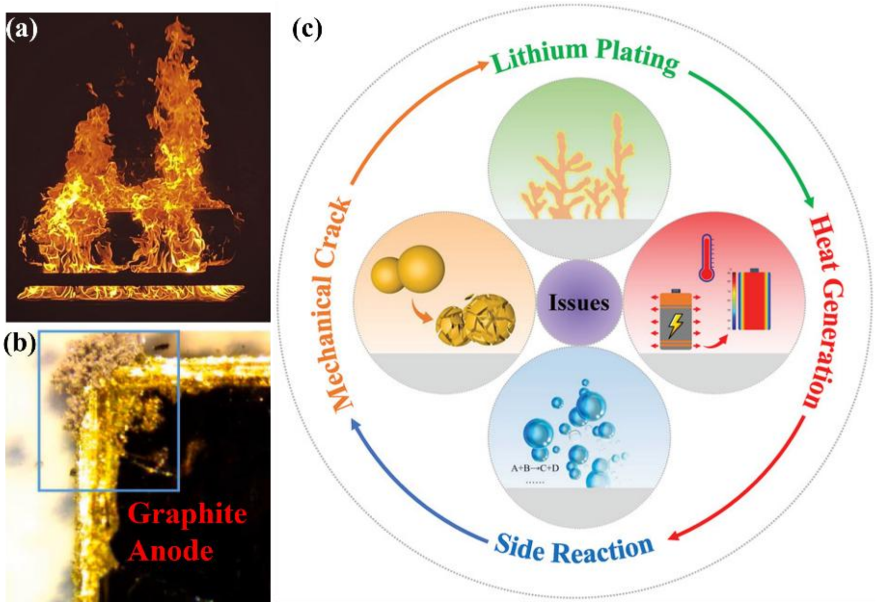

Figure 2.4 (a) Battery thermal runaway in electric vehicles. Reproduced with permission.[50] Copyright 2020 Springer Nature. (b) Lithium dendrites formed on graphite anode. Reproduced with permission.[41] Copyright 2021 Elsevier. (c) The major challenges of fast charging lithium-ion batteries. Reproduced with permission.[39] Copyright 2022 Wiley.

To be more specific, fast charging typically results in large overpotential, which directly increases the risk of nonhomogeneous lithium-ion diffusion, lithium plating, giving rise to lithium dendrite formation (**Figure 2.4(b)**).[51,52] Subsequently, this issue can further cause mechanical cracks in electrode materials and side reactions with the electrolyte.[53] These exothermic reactions can trigger chain reactions, eventually leading to heat generation and thermal runaway (**Figure 2.4(a))**.[54] This has prompted research efforts towards the development of alternative anode materials that can be safely charged-discharged at high rates.

In developing fast charging anodes, different parameters need to be considered starting first and foremost with the material itself, its reaction mechanism, and solid electrolyte interphase (SEI) formation and extending into the electrode level and finally the cell level as graphically shown in **Figure 2.5**.[38] The critical physical parameters for fast-charging anodes (**Table 2.3**) include high theoretical gravimetric and volumetric capacity, safe operating potential, high electronic conductivity, high Li ion diffusion coefficient, low volume change, etc.[38,55] At the electrode level, parameters like materials microstructure and electrode structure (**Figure 2.5**) are important.[38] The materials microstructure characteristics, including morphology, size distribution, and porosity, are directly related to the diffusion of Li ions; and electrode engineering involves factors like the electrode composition (such as binder and conductive carbon), electrode porosity, thickness, mass loading, tortuosity, etc., which practically influence the battery performance.[56] These material-level and electrode-level considerations inform the studies presented in this thesis. Finally, at the battery cell level, the actual battery cell design also needs to account for the charging protocol, the ratio of anode and cathode (N/P ratio), and heat dissipation.

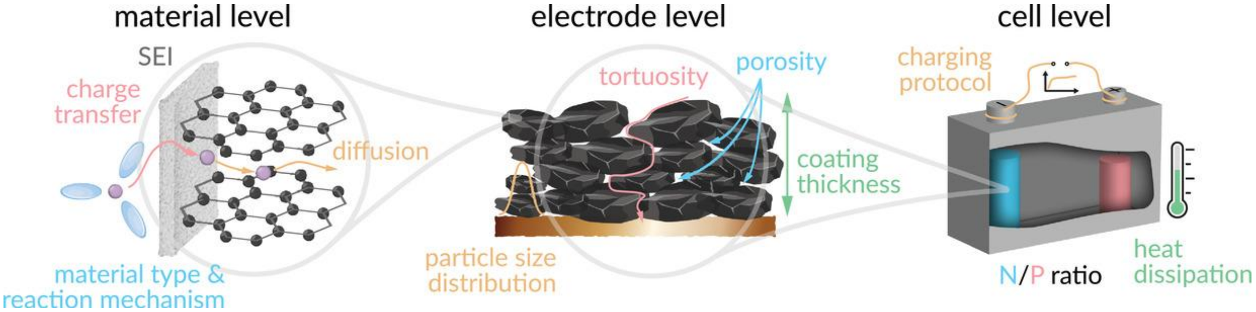

Figure 2.5 Overview of parameters relevant for fast-charging capability from material to cell level. Reproduced with permission.[38] Copyright 2021 Wiley.

Goodenough [8,57,58] introduced the concept of the “stability window” of carbonate-based electrolyte (E_g), as illustrated in **Figure 2.6(a)**, that needs to be taken into consideration in designing fast charging anodes. The “stability window” (1.0-4.1 V *vs* Li^+/Li) is delineated by the electrochemical potentials corresponding to the highest occupied molecular orbital (HOMO) and the lowest unoccupied molecular orbital (LUMO).[57] The electrolyte tends to be oxidized if the electrochemical potential of the cathode (μ_C) is below the HOMO energy level. Similarly, the electrolyte tends to be reduced if the electrochemical potential of the anode (μ_A) is above the LUMO energy level. For materials operating outside the stability window, protective passivating films, such as the solid electrolyte interphase (SEI) film and cathode-electrolyte interphase (CEI), are necessary to maintain the kinetic stability of electrode materials.[8] For example, graphite remains kinetically stable thanks to the protection of the SEI film, formed on electrode surface by the decomposition of electrolyte.[58] However, at extremely high current density conditions, large polarization (electrochemical, concentration, and ohmic) can break down this SEI film, leading to anode failure.[44] **Figure 2.6(a)** indicates that titanium oxide-based materials (e.g., $Li_4Ti_5O_{12}$ and TiO_2) and Wadsley-Roth phase materials, namely niobium oxides (e.g., Nb_2O_5) and titanium niobium oxides (e.g., $TiNb_2O_7$) are within the "stability window", stemming from the electrochemical potential of Ti^{4+}/Ti^{3+}, Nb^{5+}/Nb^{4+}, and Nb^{4+}/Nb^{3+} redox couples.[38,55] This implies that they are thermodynamically stable and promising high-safety anode alternatives under extremely fast charging.[44]

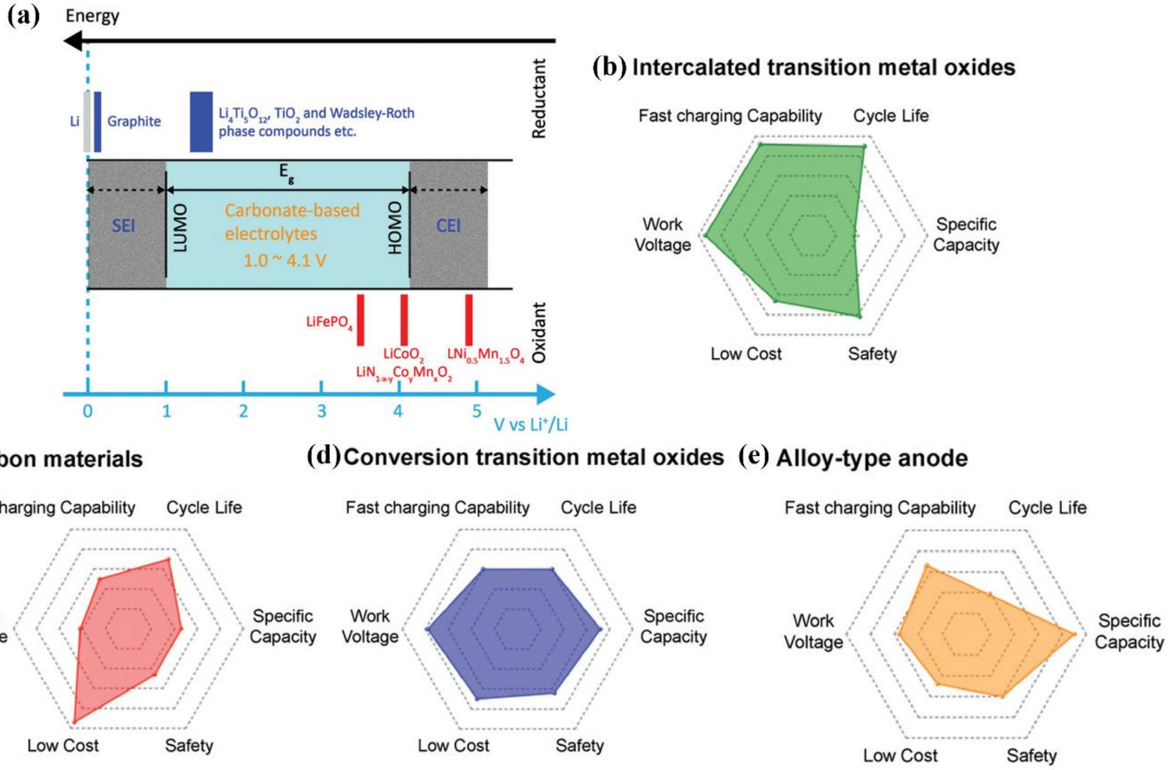

Figure 2.6 (a) Electrochemical window of a liquid-carbonate electrolyte and redox potentials of anode and cathode materials in LIBs. Reproduced with permission.[44] Copyright 2021 Wiley. Performance comparison of various fast charging anode materials, including (b) intercalated transition metal oxides, (c) carbon materials, (d) conversion transition metal oxides, and (e) alloy-type anode. Reproduced with permission.[39] Copyright 2022 Wiley.

In addition, titanium and niobium oxides together with graphite accommodate Li-ion storage via the intercalation mechanism (**Figure 2.6 (b, c)**, facilitating the insertion and extraction of Li^+ ions within the bulk electrode materials.[59] By contrast, "alloying-type" (**Figure 2.6 (e)** anode materials (e.g., Si) and "conversion-type" (**Figure 2.6 (d)** anode materials (e.g., Fe_2O_3) suffer from huge volume expansion, mechanical cracking, and subsequent battery failure during the lithium-alloying reaction, despite providing very high theoretical capacities, hence cannot be fast charged.[60]

2.1.5. Titanium and Niobium Oxide Anodes

Titanium oxide-based anode materials have been the subject of many investigations due to their intercalation mechanism and operation voltage within the "stability window" as defined above.[44] These materials are characterized by cycling durability and high safety, as well as the abundance of titanium sources.[39] Notable examples include $Li_4Ti_5O_{12}$ and TiO_2.[61,62] As the previous section discussed, $Li_4Ti_5O_{12}$ has already been commercialized for long cycling and fast-charging applications.[44] Titanium dioxide (TiO_2) provides a higher theoretical capacity compared to the $Li_4Ti_5O_{12}$ anode.[63] The reaction can be represented as:

$$TiO_2 + x\,Li^+ + x\,e^- \leftrightarrow Li_xTiO_2 \qquad \textbf{(equation 2.13)}$$

The value of x varies with different TiO_2 polymorphs: anatase (tetragonal), rutile (tetragonal), brookite (orthorhombic) can provide a theoretical capacity of 335 mAh/g (x=1), while bronze TiO_2 (b-TiO_2) (monoclinic) can offer a higher theoretical capacity of up to 420 mAh/g (x=1.25).[64-66] Bronze-phase and anatase-phase TiO_2 have exhibited interesting fast intercalation characteristics.[63,66] However, TiO_2 materials face the problem of poor electronic conductivity ($\sim 10^{-12}$ S/cm) and limited reversible capacity hindering their practical applications.[64] For example, rutile bulk materials, known as the most thermodynamically stable polymorph of TiO_2, can only provide negligible reversible Li intercalation (x<0.1) at room temperature, though this can be improved by modification strategies.[64] By contrast, anatase bulk materials can provide high reversible capacity more than 200 mAh/g.[65,66] Other than Ti oxides, Nb oxides or mixed Ti-Nb oxides offer very interesting properties as potentially fast charging anodes.

Figure 2.7 presents some Wadsley-Roth phase materials, including H-Nb_2O_5, $TiNb_{24}O_{62}$, $TiNb_6O_7$, $Ti_2Nb_{10}O_{29}$, and $TiNb_2O_7$, that have been considered for fast charging application.[67] These anode materials provide similar lithiation curves involving a single solid-solution phase region (region I), a two-phase coexistence region (region II), and another solid-solution phase region (region III), which suggest a common lithiation mechanism. The theoretical Li-ion storage properties of these oxides are provided in **Table 2.3** in reference to the properties of graphite. Among these, niobium (V) oxide-based anode materials are gaining increasing attention due to higher theoretical capacity than $Li_4Ti_5O_{12}$ originating from niobium's two redox couples of Nb^{5+}/Nb^{4+} and Nb^{4+}/Nb^{3+}.

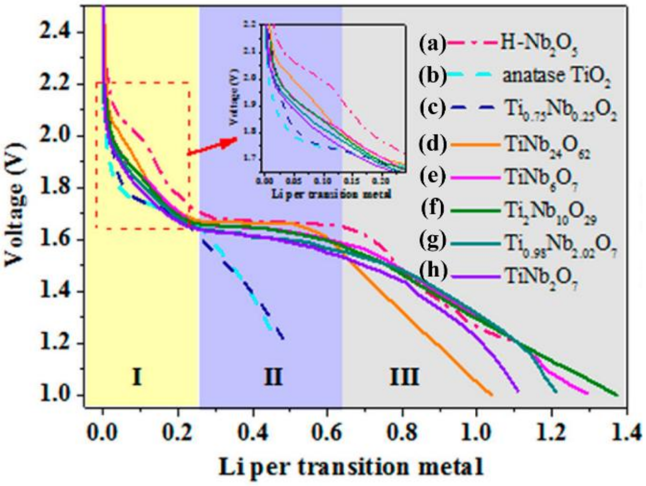

Figure 2.7 Discharge profiles of various Ti and Nb oxide pristine materials: (a) H-Nb_2O_5, (b) anatase-TiO_2,[67] (c) Nb-substituted TiO_2 ($Ti_{0.75}Nb_{0.25}O_2$),[67] (d) $TiNb_{24}O_{62}$, (e) $TiNb_6O_7$, (f) $Ti_2Nb_{10}O_{29}$, (g) $Ti_{0.98}Nb_{2.02}O_7$, and (h) $TiNb_2O_7$. Normalized by Li per transition metal (Ti and Nb). Reproduced with permission.[59] Copyright 2020 American Chemical Society.

Table 2.3 Li-ion storage characteristics of Ti and Nb oxide anode materials compared to graphite

Anode	**Theoretical Gravimetric Capacity [mAh/g]**	**Theoretical Volumetric Capacity [mAh/cm^3]**	**Potential (vs. Li/Li$^+$) [V]**	**Conductivity, σ_e [S/cm]**	**Li$^+$ diffusion coefficient, D_{Li^+} [cm^2/s]**	**Volume change [%]**	**Refs.**
Graphite	372	837	~0.1 V	$10–10^4$	$10^{-11}–10^{-17}$	10–12	[42,68,69]
$Li_4Ti_5O_{12}$	175	760	~1.55	$10^{-7}–10^{-13}$	$10^{-8}–10^{-16}$	<1	[38,42,55]
TiO_2	355	1324	~1.7	$10^{-9}–10^{-12}$	$10^{-13}–10^{-17}$	<4	[63,66,70]
Nb_2O_5	200 (x=2) 403.3 (x=4)	884.6 (x=2) 1769.2 (x=4)	~1.7	$10^{-5}–10^{-11}$	$10^{-11}–10^{-17}$	5	[44,71-73]
$TiNb_2O_7$	387.6	1680	~1.65	$10^{-4}–10^{-9}$	$10^{-8}–10^{-15}$	6–9	[56,74-77]
$Ti_2Nb_{10}O_{29}$	396	1800	~1.65	10^{-8}	$10^{-11}–10^{-13}$	1–9	[74,77-79]
$TiNb_{24}O_{62}$	401.7	1820	~1.65	$10^{-5}–10^{-8}$	$10^{-11}–10^{-13}$	1–8	[74,77,79,80]

As shown in **Figure 2.8**, Nb_2O_5 can exist in several polymorphic forms mainly including pseudohexagonal Nb_2O_5 (TT-Nb_2O_5), orthorhombic Nb_2O_5 (T-Nb_2O_5), and monoclinic Nb_2O_5 (H-Nb_2O_5).[42,43] The lithiation reaction of Nb_2O_5 can be expressed as follows:

$$Nb_2O_5 + x\,Li^+ + x\,e^- \leftrightarrow Li_xNb_2O_5 \qquad \textbf{(equation 2.14)}$$

where when x is 2, it involves the Nb^{5+}/Nb^{4+} redox couple, corresponding to a theoretical capacity of *ca.* 200 mAh/g; while when x is 4 the theoretical capacity can be up to 403 mAh/g if Nb^{5+} can be fully reduced to Nb^{3+}.[44,60,81] However, their practical electrochemical performance may vary significantly from one of polymorph to the other as it depends on crystal structure and other material characteristics.[60,81]

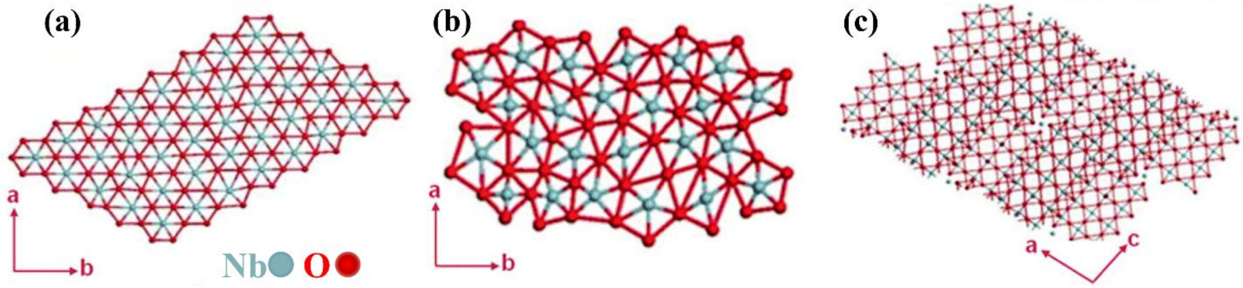

Figure 2.8 Structural schemes of (a) TT-Nb_2O_5, (b) T-Nb_2O_5, and (c) H-Nb_2O_5. Reproduced with permission.[82] Copyright 2012, Co-Action Publishing.

Among these polymorphs, it is the niobium-based oxides with Wadsley-Roth crystallographic shear (e.g., H-Nb_2O_5) that show the highest promise as high-rate anode materials for fast-charging LIBs. The "Wadsley-Roth" phase compounds system was established based on the groundbreaking research conducted by Roth and Wadsley in 1950s and 1960s.[44,83-86] R. J. Cava *et al.*[87] from Bell Laboratories further clarified the "Wadsley-Roth" phase and systematically investigated the lithium insertion behavior of Wadsley-Roth phase materials. The Wadsley-Roth crystallographic shear structure provides 3D open framework for Li ion diffusion within the bulk. The Wadsley-Roth phase is built of edge-shared and corner-shared MO_6 octahedra, which are generally found at stoichiometries between MO_3 and MO_2. **Figure 2.9**(a) illustrates the corner-shared structure of ReO_3 represented by MO_6 octahedra.[87] The Wadsley-Roth crystal structures are formed from $n \times m \times \infty$ ReO_3-type blocks, with n and m indicating the length and width of the blocks, respectively, in numbers of octahedra.[87] These blocks link to adjacent blocks either through edge sharing or a combination of edge sharing and tetrahedrally coordinated metal atoms at the block corners. The corresponding stoichiometries can be expressed as the formula $M_{nmp+1}O_{3nmp-(n+m)p+4}$, with p denoting the number of blocks at the same level connected through edge sharing.[87] Within this stoichiometry range, compounds maintain open-tunnel-like regions in their structure and are enclosed by regions of extensive edge-sharing. To date, Wadsley-Roth phase compounds with $n \times m \times \infty$ blocks (where n and m ranging from 2 to 5) or $n \times \infty \times \infty$ blocks, and various types of blocks, have been identified.[44,85,86]

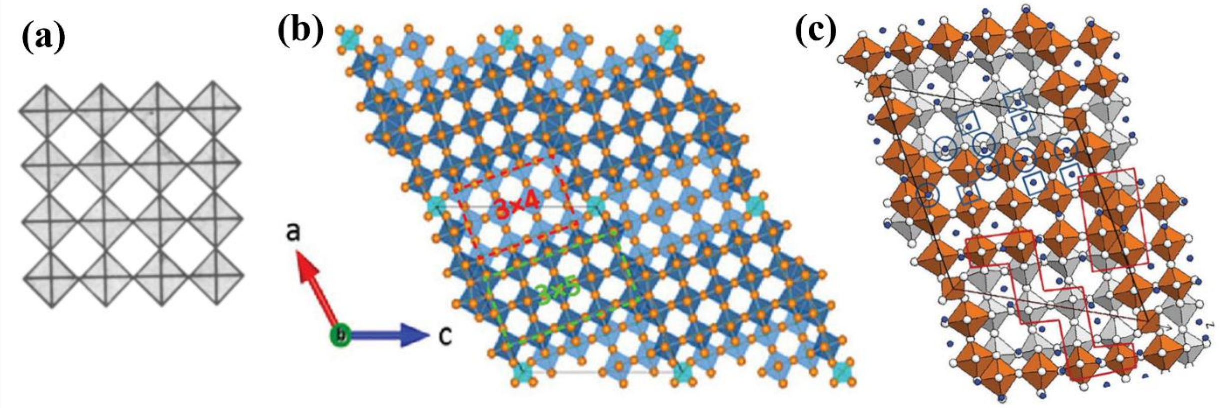

Figure 2.9. (a) Corner-shared structure of ReO_3 represented by MO_6 octahedra. Reproduced with permission.[87] Copyright 1983, ECS-The Electrochemical Society. (b) Wadsley-Roth phase structure of H-Nb_2O_5 material with $3 \times 4 \times \infty$ ReO_3-type blocks and $3 \times 5 \times \infty$ ReO_3-type blocks. Reproduced with permission.[88] Copyright 2016, American Chemical Society. (c) Crystalline structure of $Li_{1.714}Nb_2O_5$ projection onto the (010) plane, from Rietveld refinement of neutron diffraction data. Fivefold and fourfold coordinated Li atoms are shown as circles and squares, respectively. Reproduced with permission.[89] Copyright 2014, The Royal Society of Chemistry.

H-Nb_2O_5 (monoclinic Nb_2O_5), classified as a Wadsley-Roth phase material, offers a crystallographic shear structure with a space group of C2/m (**Figure 2.9(b)**).[88] It consists of $3\times5\times\infty$ ReO_3-type blocks and $3\times4\times\infty$ ReO_3-type blocks. These blocks are joined through both corner-sharing involving MO_4 tetrahedra and edge-sharing octahedra along their perimeters, extending infinitely along the b-axis direction.[87] Neutron powder diffraction measurements of the lithiated phase of H-Nb_2O_5 reveal that this structure accommodates two types of Li coordination in the asymmetric unit of $Li_{1.714}Nb_2O_5$: (1) tetracoordinated perovskite-type LiO_4 (four-coordinated) are located within the ReO_3 blocks, as denoted as blue circles (**Figure 2.9(c)**); (2) LiO_5 (five-coordinated) square-pyramidal sites exist on the block edges, depicted as blue squares (**Figure 2.9(c)**).[89] As a result, the unit cell volume expands by 5.3 %, accompanied by an increase in the *b* lattice parameter by 8.1% and a decrease in the *a* and *c* lattice parameters by -1.7 % and -1.2%, respectively.[89] This implies that Li ions accumulate in the bulk along *b* channel. Besides H-Nb_2O_5, Wadsley-Roth phase crystal structures are encountered in the mixed system of TiO_2-Nb_2O_5. In recent years, titanium niobium oxide materials ($Ti_2Nb_{2x}O_{4+5x}$, or $(TiO_2)_2(Nb_2O_5)_x$) have been found to possess very favorable structural and intercalation properties, proposed for fast charging anode applications.[59,74] This family mainly includes $TiNb_2O_7$ (x=2),

$Ti_2Nb_{10}O_{29}$ (x=5), and $TiNb_{24}O_{62}$ (x=24), which provide high theoretical gravimetric capacity of 387.6, 396, and 402 mAh/g, respectively.[56,74] These capacities surpass those of graphite, and are more than twice that of $Li_4Ti_5O_{12}$ anode. All these three compounds feature Wadsley-Roth phase monoclinic shear crystal structures with corner-shared and edge-shared ReO_3-type octahedron blocks.[74] **Figure 2.10** presents the monoclinic $TiNb_2O_7$ (space group C2/m) consisted of $3 \times 3 \times \infty$ ReO_3-type octahedron blocks, and the monoclinic $Ti_2Nb_{10}O_{29}$ (space group A2/m) and $TiNb_{24}O_{62}$ (space group C2) phases, the latter made up of $3 \times 4 \times \infty$ ReO_3-type octahedron blocks.[74] Similar to H-Nb_2O_5, Wadsley-Roth phase structures allow $Ti_2Nb_{2x}O_{4+5x}$ crystals to achieve high structural stability with minimal volume change (<8 %) during lithium intercalation. Additionally, they provide a safe working potential of above 1 V, which prevents the electrolyte decomposition (<0.8 V), and lithium dendrite formation phenomena (<0.2 V).[44] Among these, $TiNb_2O_7$ material has drawn most attention by both academia (e.g., Prof. Goodenough's pioneer research) and industry (e.g., Toshiba's commercialization project),[90] and as such it has been selected as the focus of this thesis.

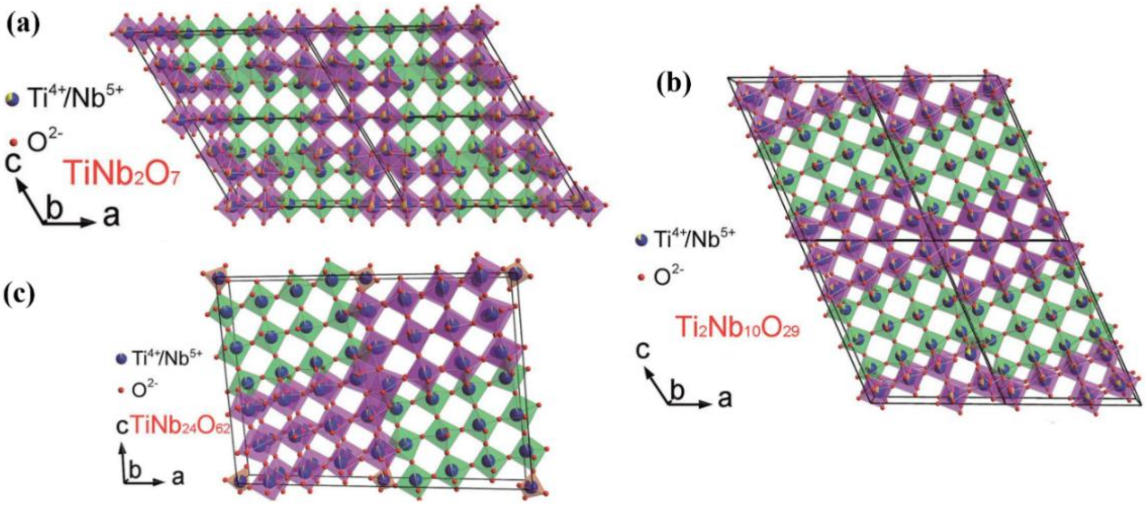

Figure 2.10. The schematic Wadsley-Roth phase crystal structures for (a) monoclinic $TiNb_2O_7$ with $3\times3\times\infty$ ReO_3-type blocks, (b) monoclinic $Ti_2Nb_{10}O_{29}$ with $3\times4\times\infty$ ReO_3-type blocks, and (c) $TiNb_{24}O_{62}$ with $3\times4\times\infty$ ReO_3-type blocks, showing green and blue blocks offset by 1/2b in the structure. Reproduced with permission.[59] Copyright 2018 The Royal Society of Chemistry.

2.2. Titanium Niobium Oxide Anodes ($TiNb_2O_7$)

Titanium niobium oxide (TNO-$TiNb_2O_7$), as briefly discussed above, is a promising candidate for fast-charging LIBs in EVs.[56] After tracking back the pioneering studies, this section provides a comprehensive review of its merits, including high-rate capability, high specific capacities, safety, and cycling stability. It also delves deeper into the fundamentals of TNO, discussing material structure, working mechanism, and electrochemical performance. Lastly, various modification methods are detailed, such as structure engineering, doping modification, and carbon modification that are applied to enhance TNO's performance as fast charging anode.

2.2.1. Pioneering Studies of $TiNb_2O_7$

In 2011, Prof. John B. Goodenough and co-workers first introduced the $TiNb_2O_7$ anode material as a new framework for LIB anodes,[91] and in 2014, they successfully obtained a US patent (US8647773B2), entitled "niobium oxide compositions and methods for using same".

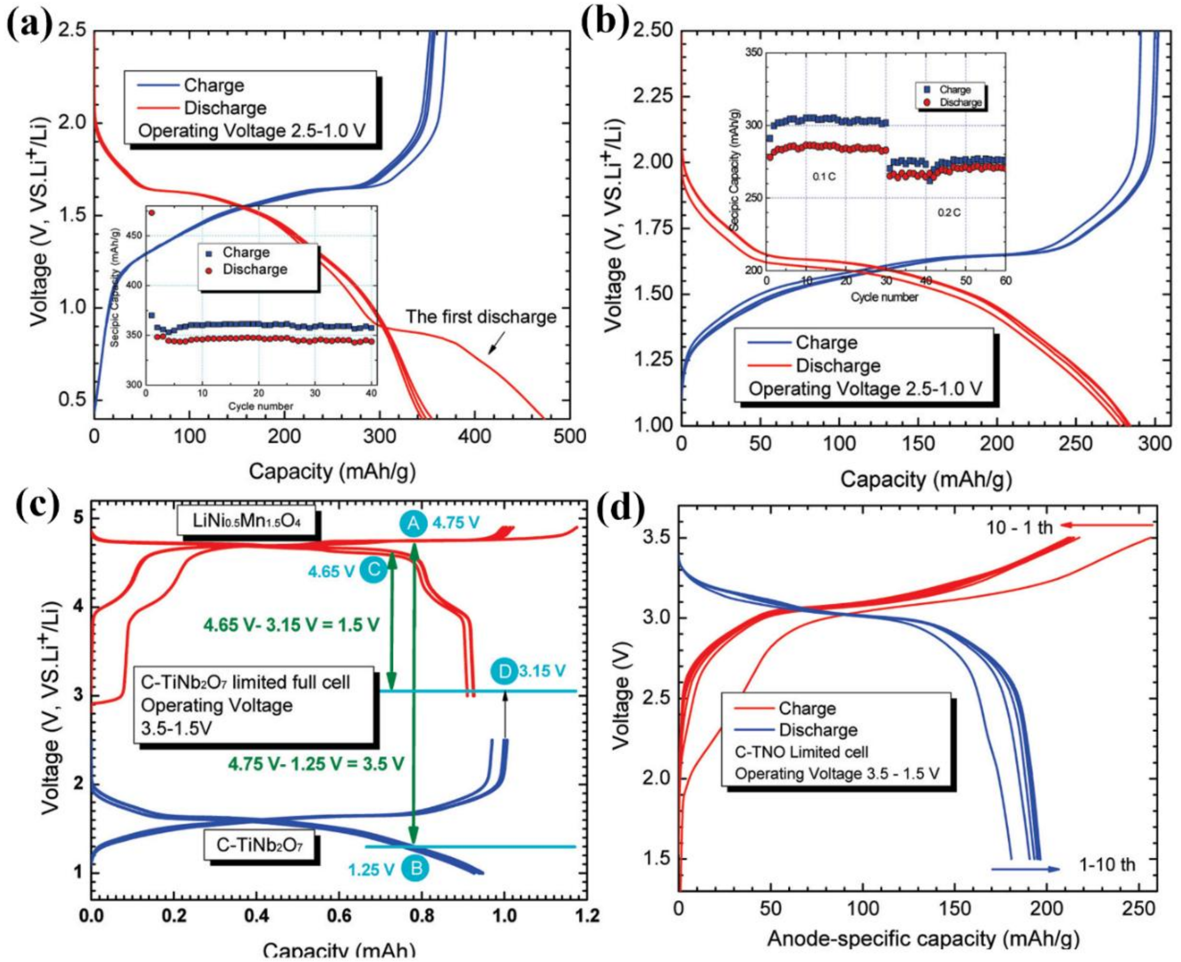

Figure 2.11. (a) Charge/discharge curves of the C-TNO anode and cycling stability over 30 cycles (inserted) cycled at 0.1 C between 1.0 and 2.5 V. (b) Charge/discharge curves of the C-TNO anode and cycling stability over 40 cycles cycled at 0.1 C between 0.4 and 2.5 V. Reproduced with permission.[91] Copyright 2011 American Chemical Society. (c) Details of capacity matchup of C-TNO anode and $LiNi_{0.5}Mn_{1.5}O_4$ cathode full cell. The cells were operated at the C/10 rate with the cutoff voltages of 1.0-2.5 V for C-TNO/Li cell and 3.0-4.9 V for $LiNi_{0.5}Mn_{1.5}O_4$/Li cell. (d) Charge/discharge curves for a C-TNO/LNMO full-cell at C/10 with capacity limited by C-TNO cycled between 1.5 and 3.5 V. Reproduced with permission.[92] Copyright 2011 American Chemical Society.

In their research, Goodenough et al.[91] synthesized micron-sized TNO particles (bare TNO sample) using a sol-gel synthesis method and applied a carbon coating modification (C-TNO). The obtained C-TNO (**Figure 2.11(a)**) provides a remarkable discharge capacity of 470 mAh/g and high charge capacity of 350 mAh/g in the first cycle at 0.1 C cycled between 2.5 V and 0.5 V, followed by a reversible capacity of 350 mAh/g over 40 cycles. The low initial Coulombic efficiency of 74% (350 mAh/g charge capacity *vs.* 470 mAh/g discharge capacity) is associated with the formation of an SEI layer. To prevent this issue, the cut-off working voltage is set to 1 V. As shown in **Figure 2.11(b)**, C-TNO delivers a high reversible discharge capacity of 280 mAh/g at 0.1 C cycled between 2.5 V and 1.0 V for 30 cycles, and a discharge capacity of 270 mAh/g at subsequent 30 cycles at 0.2 C.

Subsequently, Prof. John B. Goodenough et al.[92] reported full-cell performance of the carbon-coated $TiNb_2O_7$ (C-TNO) anode paired with a $LiNi_{0.5}Mn_{1.5}O_4$ cathode. The capacity-potential profiles (**Figure 2.11(c)**) of a C-TNO/Li half-cell (1.0-2.5 V) and $LiNi_{0.5}Mn_{1.5}O_4$/Li cell (3.0-4.9 V) detail the combination of these two half-cells into a single full cell with a 3.5 V operating voltage. Correspondingly, the C-TNO/$LiNi_{0.5}Mn_{1.5}O_4$ full-cell (**Figure 2.11(c)**), with limited C-TNO, provides a high reversible capacity of 200 mAh/g over 50 cycles and an average output voltage of 3 V, tested at C/10 between 1.5 and 3.5 V.

After that, Toshiba Company reported their research on TNO anodes in 2013, considering TNO to be a next-generation EV battery anode that promises high energy density and ultrafast recharging capability.[93-95] In 2017, Toshiba first launched the development of a commercial TNO and announced that their TNO anode achieves double the volumetric capacity compared to graphite-based anode.[90,93-97] Impressively, this company who commercially had developed the $Li_4Ti_5O_{12}$ anode since 2008 regarded TNO as a better alternative to produce a super-safe, durable, and fast-charging LIB anode.[43]

2.2.2. Electrochemical Performances and Redox Properties

Titanium niobium oxide ($TiNb_2O_7$, TNO) (**Figure 2.12**) maintains many of the safety features (operating potential window, 1.0-3.0 V) and electrochemical cycling properties associated with Ti-O based anodes, while it has a significantly higher theoretical capacity than $Li_4Ti_5O_{12}$, namely 387.6 mAh/g.[74] This high capacity results from contributions of three redox couples, including

Ti^{3+}/Ti^{4+}, Nb^{3+}/Nb^{4+}, and Nb^{4+}/Nb^{5}.[98] This high theoretical capacity can be attributed to the lithium insertion reaction of up to 5 Li-ions ($Li_5TiNb_2O_7$), given below:

$$\mathrm{TiNb_2O_7} + x\,\mathrm{Li^+} + x\,\mathrm{e^-} \rightarrow \mathrm{Li}_x\mathrm{TiNb_2O_7} \qquad \textbf{(equation 2.15)}$$

Using the true density of 4.34 g/cm^3, TNO exhibits a very high theoretical volumetric capacity of 1680 mAh/cm^3 (twice that of graphite with 837 mAh/cm^3 and almost as high as that Li metal that has 2061 mAh/cm^3).[68] Practically, available gravimetric and volumetric electrode capacity can exceed 341 mAh/g (**Figure 2.12(a)**) and 660 mAh/cm^3, respectively, as reported by Toshiba (**Figure 2.12(c)**).[94] Impressively, these performances are based on practical-level TNO electrodes featuring high composition of 91 wt.% TNO powder, an electrode density of 2.7 g/cm^3, and a high mass loading of up to 10 mg/cm^2.

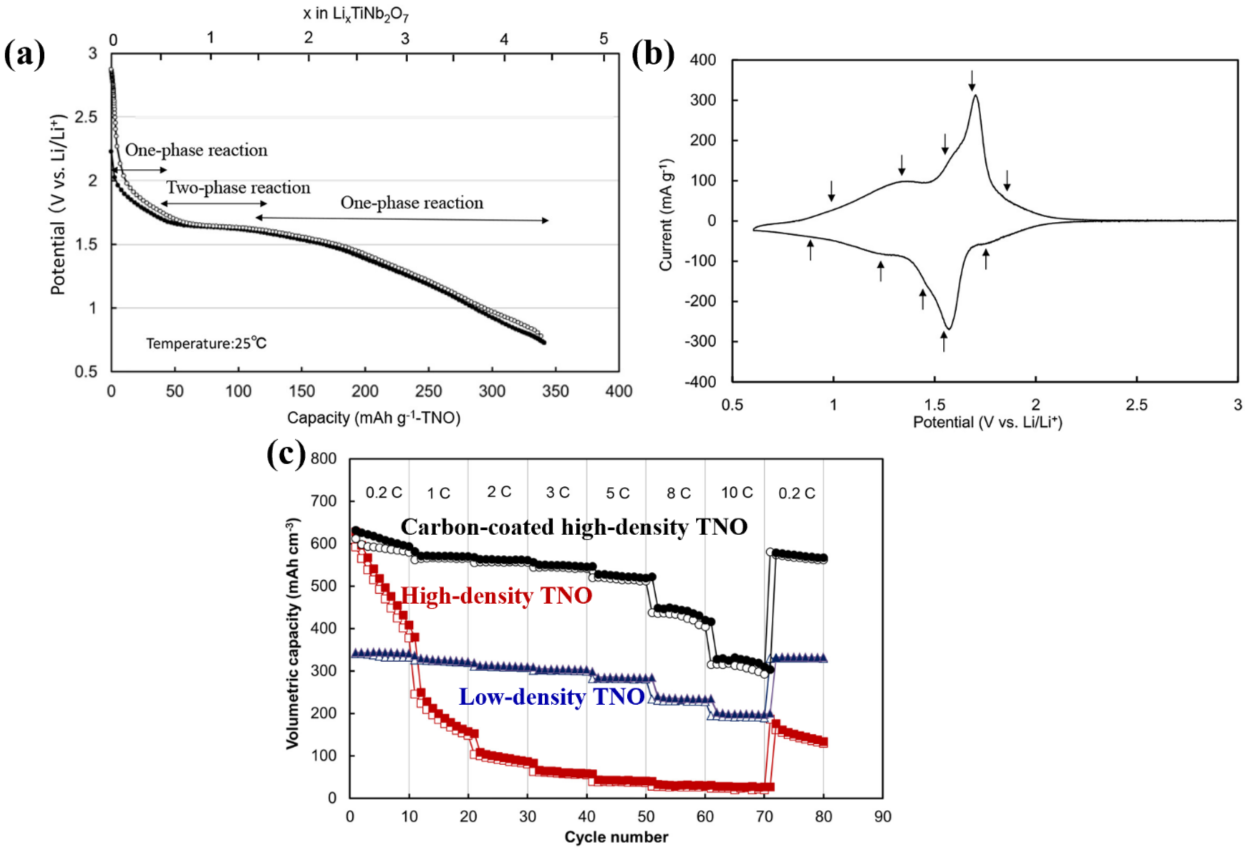

Figure 2.12 (**a**) Capacity-vs.-potential profile of TNO electrode during discharging (filled circles) and charging (open circles) at 15 mA/g. (**b**) Cyclic voltammogram of TNO electrode between 0.6 and 3.0 V vs Li$^+$/Li at a sweep rate of 0.1 mV/s. (**c**) Capacity retention of low-density TNO, high-density TNO, carbon-coated high-density TNO (●,○) cycling at various rates between 1 and 3 V. Copyright 2018, with permission from Elsevier[94].

Toshiba investigated the lithium insertion reactions of $Li_xTiNb_2O_7$ ($0 \leq x \leq 4.4$) (**Figure 2.12(a))** between 3-0.6 V at a current density of 15 mA/g.[94] The lithium insertion of pristine $TiNb_2O_7$ starts with one-phase reaction (e.g., solid-solution reaction) over the range 3-1.7 V, which corresponds to the range of x=0–0.6. With more lithium inserted into the bulk of TNO, x ranging from 0.6-1.6, a noticeable potential plateau occurs between 1.7 V and 1.6 V, which is associated to a two-phase coexistence region.[68] In the range of x=1.6-4.4, another one-phase reaction occurs over 1.6 V to 0.6 V. Overall, the $TiNb_2O_7$ anode provides a high capacity of 341 mAh/g corresponding to x=4.4. A typical cyclic voltammogram of TNO is given in **Figure 2.12(b)**. The predominant peak at 1.58/1.69 V has been assigned to the redox couple of Nb^{5+}/Nb^{4+}.[68] The peak corresponding to Nb^{4+}/Nb^{3+} can be found below 1.4 V, while the peaks of Ti^{4+}/Ti^{3+} redox reaction are broad located from ~1.8 V to ~1.0 V.[68,94] Additionally, Toshiba determined the practical volumetric capacity under various rates.[94] They compared three TNO-based electrodes including low-density TNO electrode (70 wt% TNO with 20 wt% AB conductor and 10 wt% binder) with mass loading of 1.9 g/cm^3, high-density TNO electrode (91 wt% TNO) with mass loading of 2.7 g/cm^3, and carbon-coated high-density TNO (91 wt% TNO with 2 wt% carbon coating). As shown in **Figure 2.12(c)**, the high-density TNO electrode offer a high volumetric capacity of 660 mAh/cm^3 at 0.2 C between 1 and 3 V, which is almost twice that of low-density TNO electrode (with 340 mAh/cm^3). After coating modification, the optimal carbon-coated high-density TNO electrode offer remarkable rate performance of 660, 570, 560, 550, 520, 470, and 340 mAh/cm^3 at 0.2 C, 1 C, 2 C, 3 C, 5 C, 8 C, and 10 C.

2.2.3. Crystal Structure and Lithiation Diffusion Mechanism

$TiNb_2O_7$, with the monoclinic structure, belongs to space group *C2/m* with unit cell parameters, $a \approx 20$ Å, $b \approx 3.9$ Å, $c \approx 12$ Å, and $\beta \approx 120°$.[75,99] As shown in **Figure 2.13(a)**, titanium (Ti) and niobium (Nb) atoms are each coordinated with six oxygen atoms, forming octahedral groups (NbO_6 and TiO_6) occupying the edges and corners of the structure.[74] More precisely, nine MO_6 (3×3) octahedra(M=Ti or Nb) build a crystallographic shear ReO_3-type crystal structure (**Figure 2.13(b, c)**) with linear columns along the *b*-axis.[37,84]

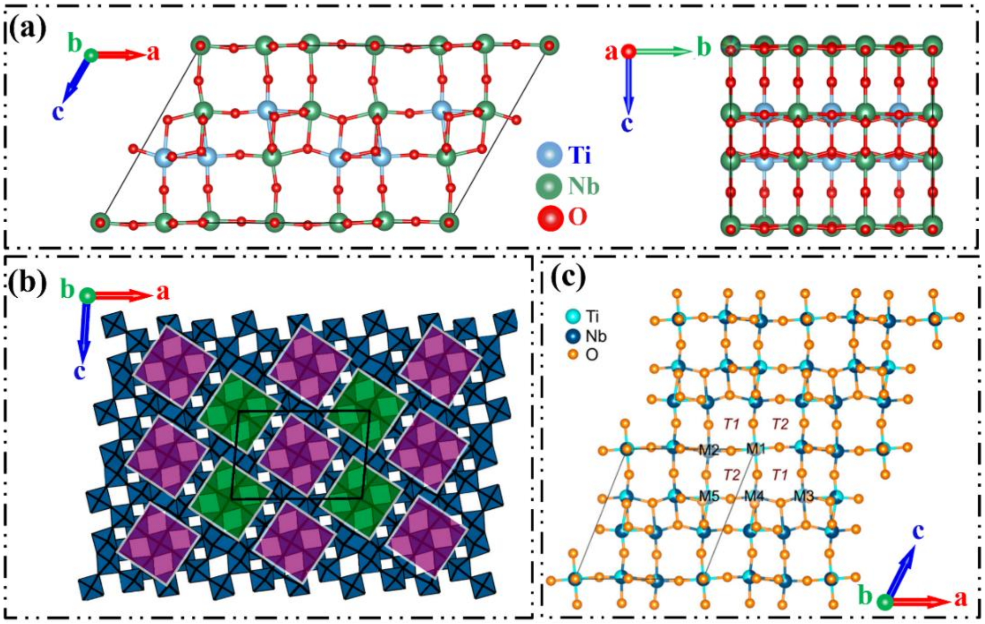

Figure 2.13 (a) Crystal unit cell of $TiNb_2O_7$ drawn using the Materials Project.[18] (b) The $3 \times 3 \times \infty$ ReO_3 shaded octahedra blocks; purple and green shaded blocks are offset by 1/2b in the structure. (c) Large crystal cell of $TiNb_2O_7$ with five symmetrically distinct transition-metal (M) sites labeled M_1−M_5 and two types of infinite tunnels along the b axis labeled T1 and T2. Reproduced with permission.[75] Copyright 2019 American Chemical Society

To reveal the crystal evolution of TNO during lithiation, Yu et al,[99] applied in-situ XRD characterization and Rietveld refinement to illustrate the lattice parameters with the results shown in **Figure 2.14(a-e)**. In the pristine TNO crystal, the lattice parameters *a* value, *b* value, *c* value, β angel, and unit-cell volume (V) are 20.353(7) Å, 3.797(8) Å, 11.881(6) Å, 120.34(1)°, and 792.4 $Å^3$, respectively. During discharge from 3 V to 1 V, the *b* value and *V* linearly increase up to 3.90 Å and 846 $Å^3$ respectively, while the *a* value and *c* value initially increase and then decrease. Overall, the volume expansion (**Figure 2.14(d)**) is determined to be 6.85% smaller than that of graphite (~9%), which suggests better crystal structure stability.[56,74] Based on these in-situ XRD refinement results, Yu et al,[99] proposed a more in-depth understanding of the phase-transformation evolution, as illustrated in **Figure 2.14(f-m)**. During the first one-phase solid-solution reaction process, as shown in **Figure 2.14(f,j)**, Li^+ ions preferentially insert into the bulk and occupy the low-energy octahedral sites namely 4i(1) and 4i(2), until the $Li_{0.88}TiNb_2O_7$ phase is formed (**Figure 2.14(g,k)**). During the two-phase transformation, internal Li ions at 4i(1) sites diffuse to the 4i(3) and 4i(4) sites, while external Li ions insert into 4i(1) sites simultaneously (**Figure 2.14(g,k)**). This process continues until 4i(1) sites are fully occupied, forming $Li_{2.67}TiNb_2O_7$ (**Figure 2.14(h,l)**). In the final solid-solution reaction (**Figure 2.14(h,l)**), the Li ions at the 4i(1) and 4i(2) sites move to the 4i(5) sites, and then, external Li^+ ions insert into the 4i(1) and 4i(2) sites. Meanwhile, the Li^+ ions at the 4i(3) sites are transferred to the 8j sites to form the final product $Li_4TiNb_2O_7$ (**Figure 2.14(i,m)**).

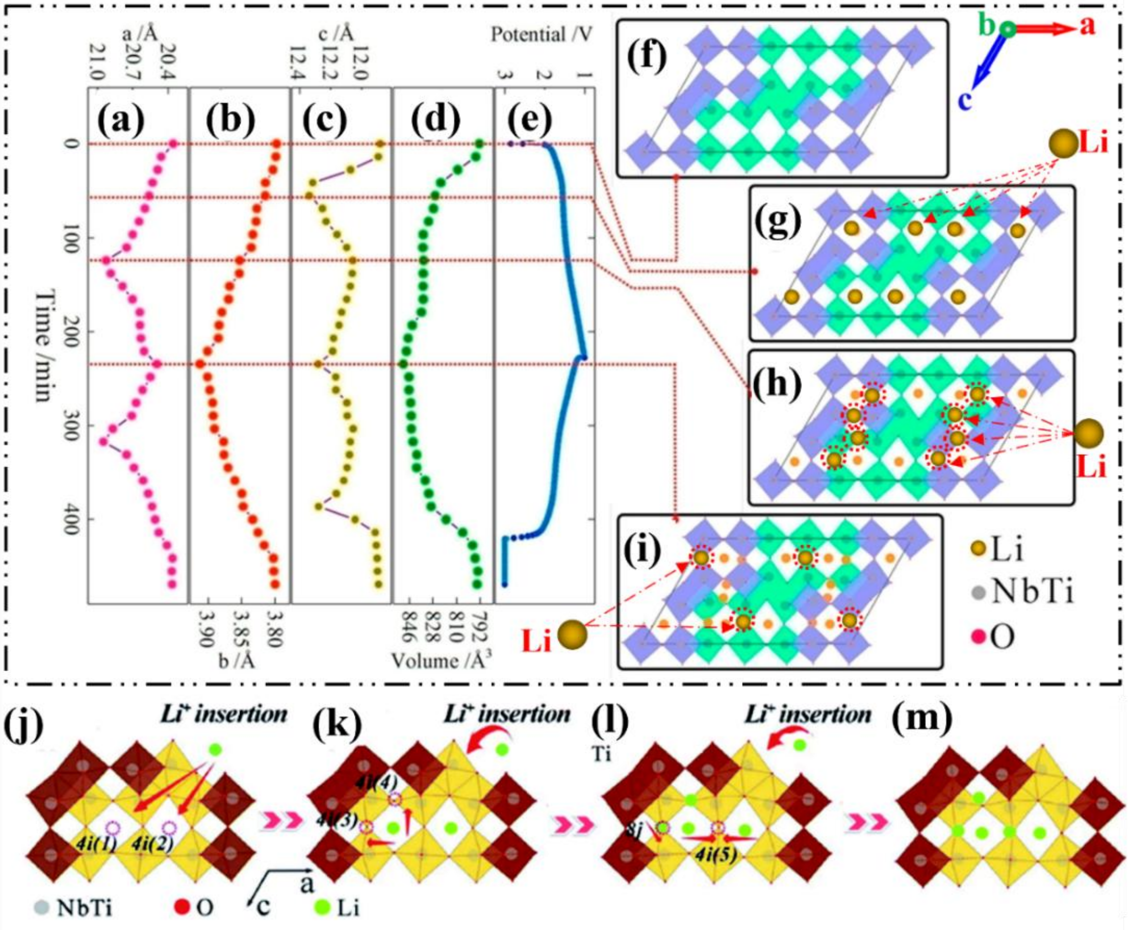

Figure 2.14 Changes in crystal lattice parameters (a) a value, (b) b value, (c) c value, and (d) unit-cell volume (V) as a function of (e) potential (state of charge) and corresponding lithiated states during discharging: (f,j) $TiNb_2O_7$, (g,k) $Li_{0.88}TiNb_2O_7$, (h,l) $Li_{2.67}TiNb_2O_7$, and (i,m) $Li_4TiNb_2O_7$. Reproduced with permission.[99] Copyright 2017 Elsevier.

This phenomenon can be attributed to the accumulation of Li^+ ions along the *b*-axis, where the *b*-axis channel is determined to be the energy-favorable channel for Li-ion diffusion within the crystal.[75] Specifically, the Grey group[75] using DFT calculations found that barriers for lithium hopping are 0.1−0.2 eV along *b*-axis tunnels but approximately 0.7−1.0 eV across the blocks (*ac* plane). Further, they found that lithium diffuses fast in the phase of $Li_xTiNb_2O_7$ ($x<3$) and lithium diffusion is hindered in the multi-redox region ($Li_xTiNb_2O_7$ ($x>3$)). Overall, the diffusion in the $TiNb_2O_7$ crystal is fast with diffusion coefficient of 10^{-11} to 10^{-12} m^2/s, as determined by galvanostatic intermittent titration technique (GITT).[75]

2.2.4. Electronic Conductivity

Despite these favourable ion diffusing merits above, the poor electronic conductivity of TNO limits attaining full capacity, high rate, and good cyclability. The absence of free electrons in the empty 3d/4d orbitals of Ti^{4+} and Nb^{5+} ions theoretically results in the insulating nature of $TiNb_2O_7$, which is consistent with the experimentally low electronic conductivity data of less than 10^{-9} S/cm (**Table 2.4**).[56,75,100]

Table 2.4 Resistivity and Conductivity of $Li_xTiNb_2O_7$ at room temperature

x in $Li_xTiNb_2O_7$	0*	0.25	0.50	1.0	1.5	2.25	3.00
Resistivity (ρ) [ohm/cm]	10^9	5×10	1×10^2	7×10^2	2×10^3	2×10^3	8×10^2
Conductivity (σ) [S/cm]	10^{-9}	2×10^{-2}	10^{-2}	1.4×10^{-3}	5×10^{-4}	5×10^{-4}	1.25×10^{-3}

Note: Resistivity of $TiNb_2O_7$ is extrapolated from 450-1100 °C data of Xing et al[100] and the resistivity of $Li_xTiNb_2O_7$ (x=0.25 to 3.00) is determined using four-point probe by Grey et al.[75]

The electronic conductivity of $TiNb_2O_7$ has been investigated by the Grey group[75] as a function of lithium composition using four-point resistivity measurements of cold-pressed pellets cycled in coin cells (**Figure 2.15(a)**). Interestingly, $TiNb_2O_7$ transforms from an insulator phase to a highly conductive phase upon lithiation ($Li_xTiNb_2O_7$), exhibiting a conductivity up to 10^{-2} S/cm in room temperature (**Table 2.4**). Theoretical calculations (**Figure 2.15(b,c)**) revealed this phenomenon to arise from n-type self-doping of $TiNb_2O_7$ with lithiation and also that electronic conduction is anisotropic.[75]

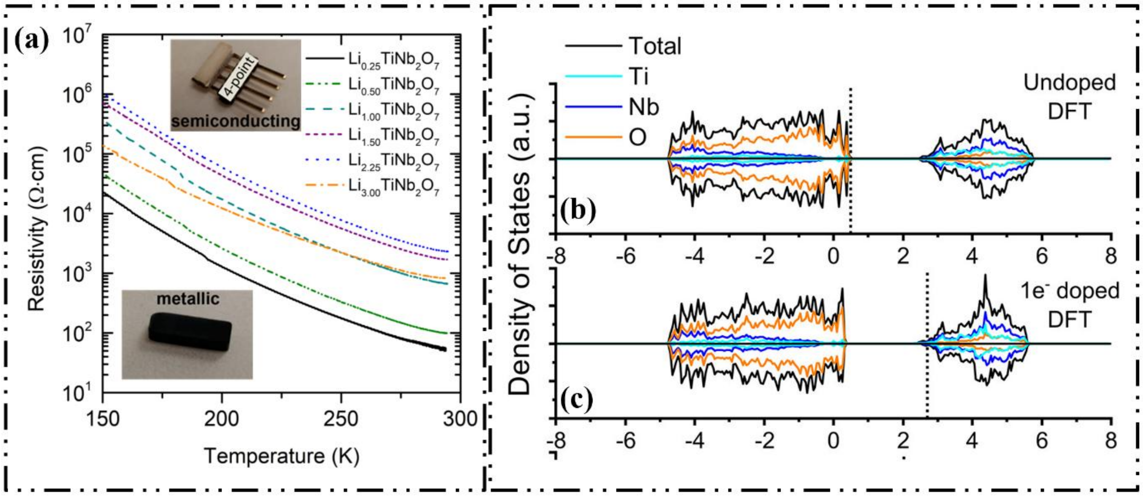

Figure 2.15 (a) Four-point probe resistivity of electrochemically lithiated pellets of $TiNb_2O_7$. Density of states (DOS) for (b) pristine and (c) lithium-doped $TiNb_2O_7$ supercell. Reproduced with permission.[75] Copyright 2019 American Chemical Society.

2.2.5. Challenges and Modification Strategies

The materials properties of TNO discussed above highlight its excellent potential as a high-rate anode. However, its drawback of inherently low electronic conductivity significantly limits its practical application.[90] Additionally, the electrochemical performance of an actual battery is hindered by the electrode architecture.[38] From the electrode-level perspective, the diffusion of Li ion involves three processes: (1) breakup of Li^+ solvation sheath (desolvation), (2) electron transfer and Li^+ diffusion through the interface, and (3) Li^+ diffusion in the material bulk.[44] Since the commonly used operating voltage is above 1 V, preventing the formation of a SEI film, modification strategies primarily focus on Process (2) and Process (3).[44,92] Accordingly, this section explores strategies including structure engineering, ion doping, and carbon modification (graphically summarized in **Figure 2.16**), which are integral parts of the research conducted in this thesis.

Structure Engineering. Crystal structure engineering can significantly improve Li^+ diffusion in material bulk (Process (3)). Structure engineering involves controlling particle size, shape, and crystal type, properties that influence electrochemical performance. First, the minimization of particle size and control of particle shape are beneficial in terms of shortening the Li-ion diffusion pathway and resisting stress from the strain induced by the lithiation/delithiation process. Second, the crystal structure (i.e., monocrystalline or polycrystalline) influences crystal orientation and grain boundaries, thereby affecting the Li ion diffusion pathway and structural stability.[90,101]

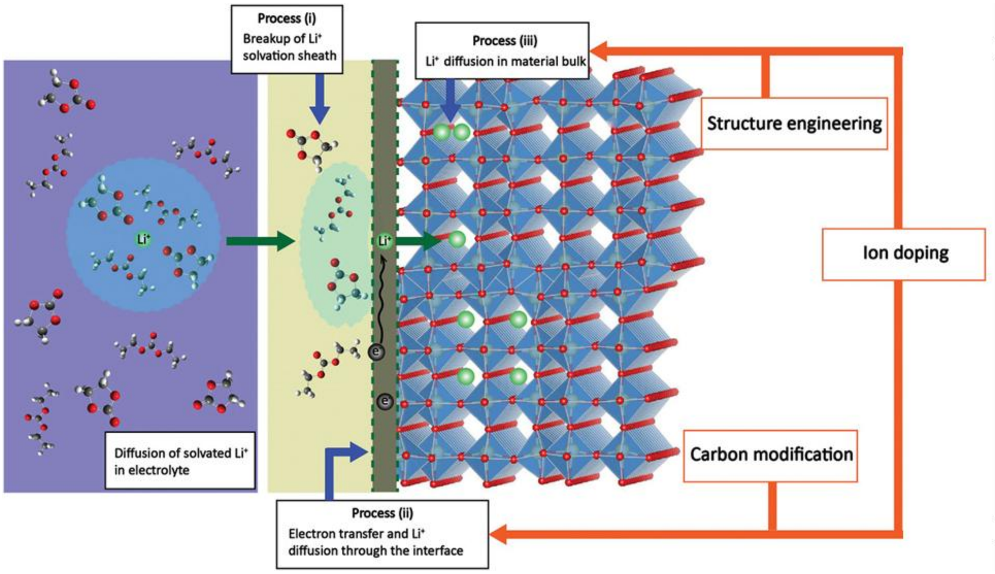

Figure 2.16 Schematic diagram of Li^+ diffusion into the anode and functions of different modification strategies. Reproduced with permission.[44] Copyright 2021 Wiley.

Ion doping. Ion doping can improve electron transfer and Li^+ diffusion through the interface (Process (2)) and Li^+ diffusion in the material bulk (Process (3)). Doping strategies are effective for increasing intrinsic electronic conductivity, mass transfer, and structural stability.[74,90,102] To increase conductivity, doping can narrow the band gap by providing mid-gap defect bands/states and by possibly also introducing more holes (p-type doping) or valence electrons (n-type doping) [56,90]. Also, doping can reduce the Li^+ hopping energy barrier, thereby increasing the lithium-ion diffusion coefficient [56,90]. Additionally, large size dopants can enlarge the diffusion channels in the $TiNb_2O_7$ crystals, such as chromium (Cr^{3+}),[103] lanthanum (La^{3+}),[104] zirconium (Zr^{4+}),[105] ruthenium (Ru^{4+}),[106] cerium (Ce^{4+}),[107] terbium (Tb^{5+}),[108] molybdenum (Mo^{5+} and Mo^{6+}),[109-111] tungsten (W^{6+}),[112,113] etc.

Carbon modification. Carbon modification can promote electron transfer and Li^+ diffusion through the interface (Process (2)). Carbon modification includes carbon coating[91,92] and mixing with graphene,[114,115] graphite,[116] carbon nanofibers,[117] carbon nanotubes,[118] and other carbon-based materials. These modifications can effectively increase the conductivity of the electrode, modify the electrode/electrolyte interface, build fast-electronic/ionic networks, and stabilize the electrode materials during cycling.[56,74]

2.3. Solution Synthesis of Titanium Niobium Oxides

2.3.1. Overview: From Solid-state Synthesis to Solution Synthesis

The investigation into $TiNb_2O_7$ crystal synthesis methods dates back 70 years. In 1955, Roth and Coughanour,[83] first successfully synthesized $TiNb_2O_7$ crystals using high-temperature calcination and systematically established the TiO_2-Nb_2O_5 phase diagram for temperatures ranging from 1450 to 1520 °C (**Figure 2.17(a)**). Their research revealed that $TiNb_2O_7$ ($TiO_2 \cdot Nb_2O_5$), $TiNb_{24}O_{62}$ ($TiO_2 \cdot 12Nb_2O_5$), $Ti_2Nb_6O_{19}$ ($2TiO_2 \cdot 3Nb_2O_5$), and other Ti-Nb-O compounds can be produced by controlling the composition ratios of TiO_2 and Nb_2O_5 under high-temperature annealing. In 1969, Jongejan and Wilkins[119] further confirmed this phase diagram (**Figure 2.17(b)**). In 2023, Liu and Gong et al.,[120] expanded the TiO_2-Nb_2O_5 phase diagram (**Figure 2.17(b)**) to cover a broader temperature range from 1100 °C to 1900 °C, combining experimental data and theoretical calculations. These works directly guide the synthesis of $TiNb_2O_7$, especially for solid-state synthesis, and establish principles for other synthesis methods. According to this phase diagram, high-temperature calcination is essential for the formation of $TiNb_2O_7$ crystals, consistent with other experimental results.[74]

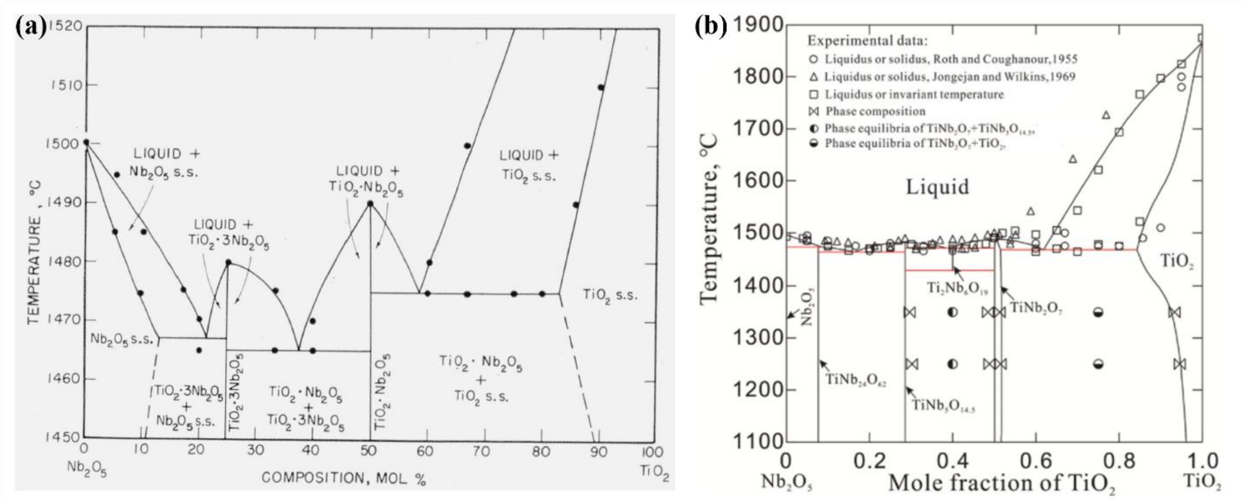

Figure 2.17 (a) Composition phase diagram of the Nb_2O_5–TiO_2 system at various calcination temperatures. Reproduced with permission.[83] (b) Calculated phase diagram of TiO_2–Nb_2O_5 system with experimental data of Roth and Coughanour,[83] Jongejan and Wilkins,[119] and Liu and Gong et al..[120] Reproduced with permission.[120] Copyright 2023 Elsevier.

Solid-state synthesis (**Figure 2.18**) involves solid phase reactions of solid particles under high-temperature calcination, forming a new phase through atomic diffusion and phase transformation.[121,122] It generally includes mixing precursors, milling, and high-temperature calcination.[17] If solid-state synthesis is using high-energy ball milling prior to calcination it is also known as mechanochemical assisted process.[17,122]

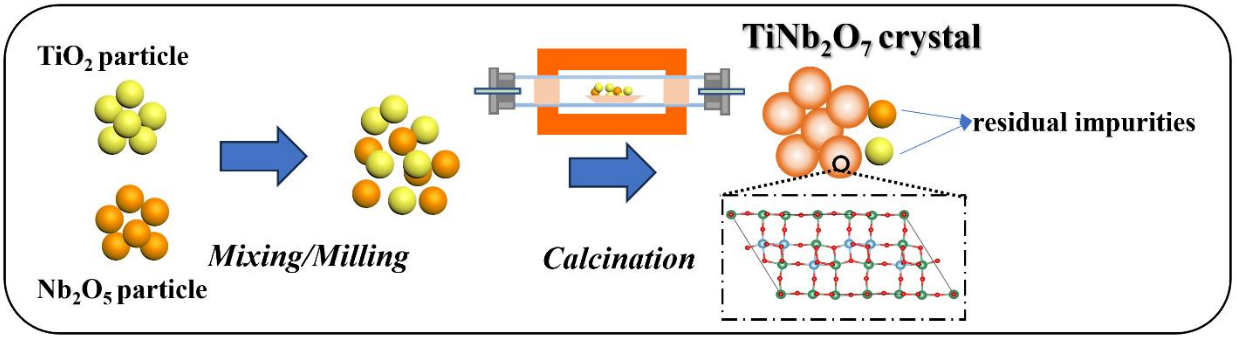

Figure 2.18. Schematic illustration of the solid-state synthesis process for $TiNb_2O_7$ crystal materials.

This method offers benefits (**Table 2.5**), including simplicity, low cost, large-scale fabrication, and good control over stoichiometry, making it highly favored for industrial production.[74,122] However, it also has disadvantages, such as high reaction temperatures, slow reaction kinetics, and non-homogeneous reactions, which cause poor control over phase purity, particle size, and morphology.[122] As evident in phase diagram (**Figure 2.17**), solid-state synthesis methods for $TiNb_2O_7$ crystal materials suffer from the drawback of formation of impurities due to incomplete conversion or side reactions ($TiNb_2O_7$+TiO_2 mixture, or $TiNb_2O_7$+Nb_2O_5 mixture), even after long-time ball milling; this issue arises due to the non-homogeneous distribution of TiO_2 and Nb_2O_5 bulk particles (**Figure 2.18**).[120,122]

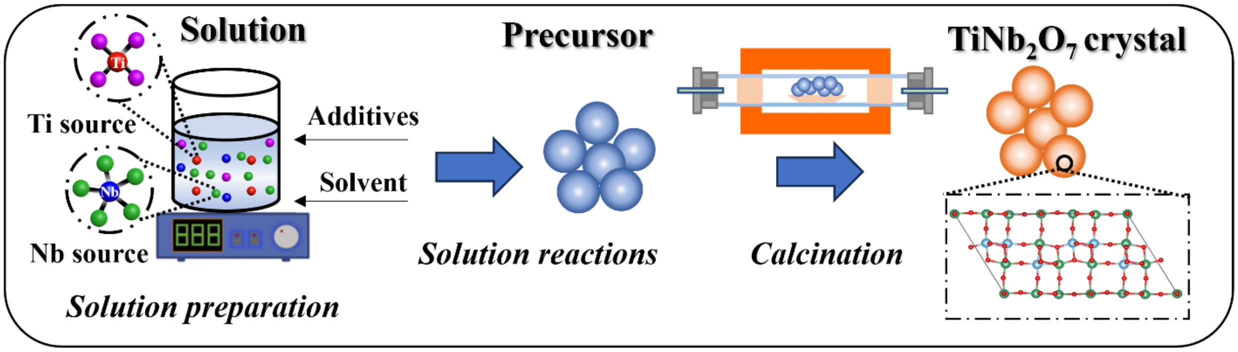

Figure 2.19. Schematic illustration of the typical fabrication process for $TiNb_2O_7$ crystal materials via solution synthesis method.

To increase the purity of components and decrease the calcination temperature, the preparation of precursor materials via solution reactions (solution synthesis methods) has been widely adopted.[120,122] Solution synthesis is defined as a synthesis technique using chemical reactions in aqueous or organic solutions to produce particulate compounds.[123,124] Solution synthesis facilitates atom/ion-level mixing of chemicals in liquid media, leading to highly homogeneous reactions.[125] Compared with the solid-state synthesis, the solution-based synthesis methods (**Figure 2.19**) apply either water or organic solvents as reaction media that allow for better dispersion of reactants and more precise control over the formation of Ti-Nb-O nanoparticle precursors (**Table 2.5**).[114,126,127] Over the past few decades, the solution-synthesis techniques have been used to produce a variety of nanomaterials with impressive morphology structures, including nanoparticles, nanofibers, nanospheres, nanorods, nanotubes, etc.[59,74] More interestingly, solution synthesis methods are more amenable to modification strategies like crystal structure control, elemental doping, and carbon modification.[56,128,129]

However, solution synthesis methods have also some disadvantages including process complexity and high cost due to the use of chemicals and solvents.[126] Depending on the types of solution media and reactions to prepare the precursor compounds, solution synthesis methods (**Figure 2.20**) can be classified into solvothermal synthesis, sol-gel synthesis, aqueous co-precipitation synthesis, and others.[74,130]

Table 2.5 Characteristics of synthesis methods for $TiNb_2O_7$ materials

Synthesis method	Advantages	Disadvantages
Solid-state synthesis	• Straightforward process • Low cost • Scalable (most favorable for industry production)	• Presence of impurity phase • High reaction temperature • Non-uniform and sluggish reaction • Poor control over size and morphology
Solution synthesis: Solvothermal & Sol-Gel	• High phase purity • Low calcination temperature • Good control over size and morphology	• Specific equipment needed (autoclave) • Safety concern (i.e., high pressure) • High cost (i.e., organic chemicals) • Low-yield reaction
Solution synthesis: Aqueous Co-precipitation	• Scalable (i.e., continuous reactions) • Low calcination temperature • Good control over size and morphology • Cost-effective • Efficient (Fast reaction kinetics)	• Challenges to control reactions • Limited control over phase purity

Among these methods, solvothermal synthesis and sol-gel synthesis have been widely used for $TiNb_2O_7$ materials.[122] By contrast, co-precipitation synthesis, though rarely applied, holds significant potential for practical application, as evidenced by its use in the production of commercial $Li_4T_5O_{12}$ anode[131] and NMC cathode materials[17,132]. Given the similarities among solution synthesis methods, solvothermal synthesis (**Figure 2.21**), has been selected to illustrate general properties of solution synthesis.

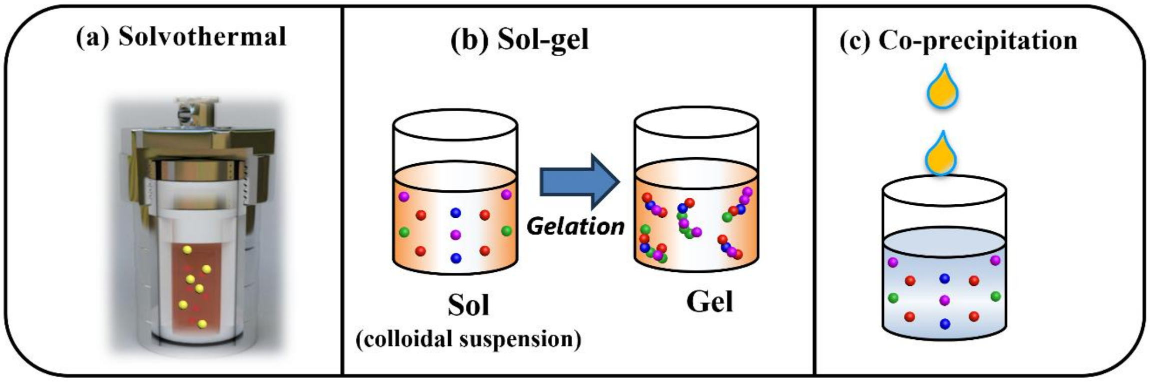

Figure 2.20. Schematic illustration of solution reactions for (a) Hydrothermal & solvothermal synthesis, (b) Sol-gel synthesis, and (c) Co-precipitation synthesis.

2.3.2. Solvothermal Synthesis

Hydrothermal synthesis involves chemical reactions in aqueous solution at temperatures above the boiling point of water in a closed system, leading to particle formation.[123,124] Solvothermal synthesis (**Figure 2.21**) is based on a similar chemical reaction but occurs in nonaqueous solutions.[125,126] These methods offer advantages over other solution synthesis by providing better control over particles size and morphology, as well as enabling synthesis of watersensitive products.[133] Currentlly, only solvothermal synthesis methods have been applied for $TiNb_2O_7$ synthesis, whereas hydrothermal synthesis has not because Ti- and Nb- salts are highly reactive with water (spontaneous hydrolysis).[105]

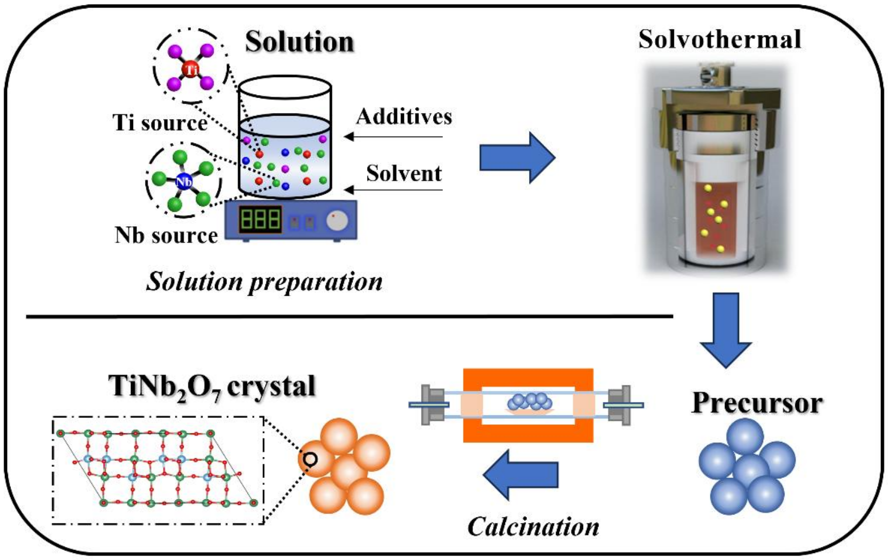

Figure 2.21 Schematic description of solvothermal synthesis of $TiNb_2O_7$.

As shown in **Figure 2.21**, the typical TNO synthesis by the solvothermal method generally consists of three-steps: (1) solution preparation, (2) solvothermal reaction in an autoclave, and (3) calcination. Thus, the TNO crystal material can be manipulated by some key parameters, including the reactants' concentrations, type of solvent, additives, temperature, etc.[134] Many studies explored the effect of various parameters and corresponding results for TNO material synthesis by this method are summarized in **Table 2.6**.

The role of the solvent in the solvothermal process is critical as its physical properties (dielectric constant, polarity, density, etc.), chemical properties (mainly the solvation and the ability or not to form complexes and solubilize salts), can affect the solid product formation and yield.[126] The solvent should provide good solubility for Nb source and Ti source salts. Alcohols have been widely applied as solvents including ethanol,[98] glycerol,[135] isopropanol(C_3H_8O),[135] etc., but also acids (e.g., acetic acid,[136]) have been used.

The selection of a metal source for Ti and Nb is a key consideration (**Table 2.6**). Both inorganic and organic metal sources have been used in recent studies. The main Ti sources are titanium isopropoxide ($Ti(OC_3H_7)_4$, TTIP),[98,136,137] tetrabutyl titanate ($Ti(OC_4H_9)_4$),[138,139] and titanium oxysulfate ($TiOSO_4$).[136,138] But another Ti source that needs to be considered is the abundant and low-cost $TiCl_4$ that has been used by our group in the synthesis of TiO_2 (Yasin et al.[140]) and $Li_4Ti_5O_{12}$ (Chiu et al.[62]). By contrast, the choices of Nb sources are fewer including the inorganic $NbCl_5$[135] and organic niobium ethoxide($Nb(OC_2H_5)_5$)[136]. Furthermore, the molar ratio of Ti and Nb generally should be about 1:2 to enable the formation of the $TiNb_2O_7$ phase rather than that of other components.

Furthermore, surfactants added in solution (e.g., Pluronic P123,[138] diethylenetriamine (DETA),[137] ethylenediamine[141] or Ethylenediaminetetraacetic acid (EDTA)[142]) may play key roles in the modification of material morphology via altering the crystallization pathway. The surfactants can be assembled in the precursor preparation step and then be removed at the high calcination step. For example, Park et al.,[137] exhibited the importance of DETA surfactants for controlling the morphology and porosity. The molar ratio of Ti/Nb metal alkoxide (C_{Me}) to DETA (C_{De}) directly influenced the formation of TNO particles. Low C_{De}/C_{Me} ratio (0.05–0.2) favored formation of microsphere structure embedded with nano TNO crystallites, whereas high C_{De}/C_{Me} ratio of 0.5 resulted in particles without regular shape.

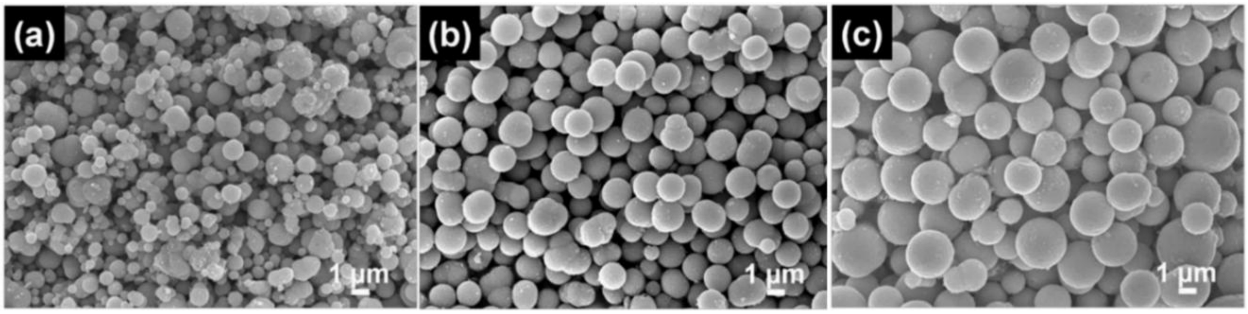

Figure 2.22 SEM images of TNO microspheres prepared at different reaction times via the solvothermal method: (a) 6 h, (b) 12 h, (c) 24 h. Reproduced with permission.[137] Copyright 2015 Wiley.

Other parameters to be controlled in a solvothermal reaction process are temperature and time the manipulation of which can lead to the formation of metastable phases and/or different particle morphologies via in situ phase transformation reactions.[137,143,144] Park et al.,[137] demonstrated the influence of reaction time during solvothermal synthesis as depicted in **Figure 2.22.** The increase in the reaction time increases the diameter of the TNO microspheres. The 6h-prepared TNO particles are with an uneven particle size distribution from tens of nanometers to microns, by contrast, the 24h-prepared TNO particles possess more uniformed particle size distribution and larger micron-level crystallite size.

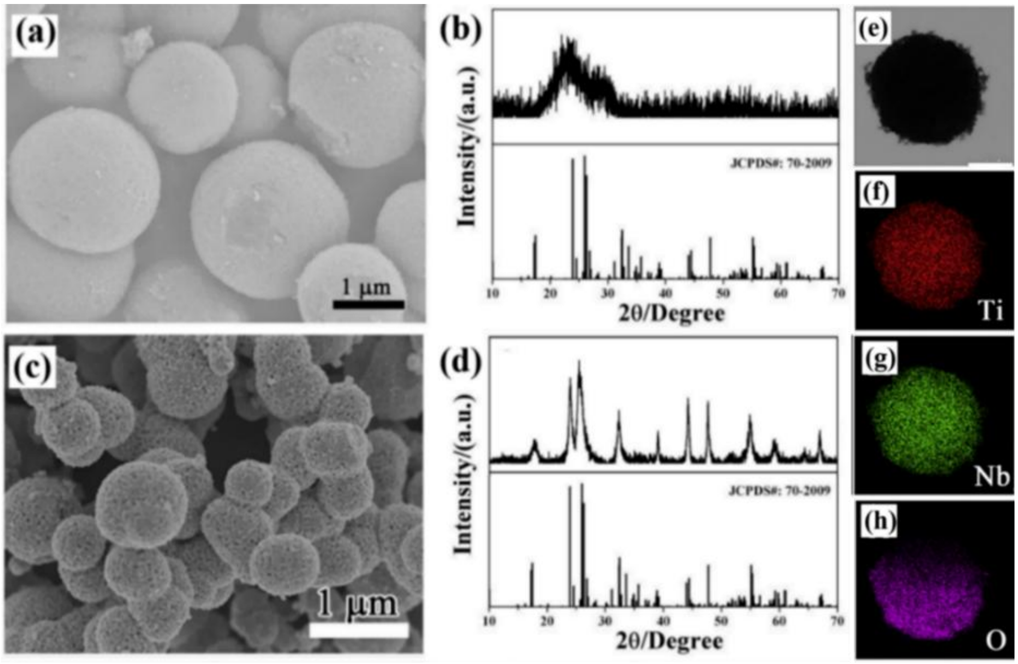

Figure 2.23 Comparison between the TNO precursor and the calcined TNO. (a) SEM image and (b) XRD pattern of TNO precursor; (c) SEM image and (d) XRD pattern of the calcined TNO; and (e-f) mapping images of mesoporous-TNO particle. Reproduced with permission.[135] Copyright 2017 Elsevier

Often, an amorphous, poorly crystalline or metastable intermediate material is obtained from the solution precipitation reaction that requires further thermal treatment to obtain the desired final crystalline phase. Therefore, an annealing/calcination processing step is indispensable in inducing crystallization of TNO as happens with other Li-ion storage materials like $Li_4Ti_5O_{12}$ (Chiu et al.[145,146]). In the annealing process, the precursor transforms into the TNO crystal structure and simultaneously particles grow or undergo other physical changes. Of interest in this context is the work of Liu et al.,[135] who applied solvothermal method and annealing/calcination to obtain TNO nanoparticles. In this study, they illustrated the importance of annealing by comparing the solvothermal-synthesized precursor before the annealing process (**Figure 2.23(a,b)**) and the calcined TNO (**Figure 2.23(c,d)**). The solvothermal-synthesized precursor had a spherical shape with the 1-1.8 μm diameter, no pores, and a rather rough surface. As **Figure 2.23(b)** illustrates, the XRD pattern reveals a poorly crystalline TNO precursor phase. By contrast, the calcined TNO material consisted of TNO nanoparticles (17nm) assembled into mesoporous microspheres (600-900 nm) with a specific surface area of 22.22 m^2/g. The calcined samples can be properly matched to the monoclinic structure of the $TiNb_2O_7$ (JCPDS: 70-2009) with homogeneous composition as disclosed by the elemental maps in **Figure 2.23(e-h)**.

Table 2.6 Summary of solvothermal synthesis studies for $TiNb_2O_7$ anode materials.

Materials	Solution preparation				Solvothermal	Calcination	Material Characterization	Electrochemical Performance	Ref.
	Ti precursor	Nb precursor	Solvent	Other Chemicals	Temp./ time/vol.	Temp./ /Time/ Gas	Diameter(nm)/ Surface area (m^2/g) / Pore volume (cm^3/g)	Cycle performance, Rate performance. (**Note**: 1 C=387 mA/g)	
Nano TNO	$Ti(OC_3H_7)_4$ TTIP (3 mmol)	Niobium ethoxide (6 mmol)	Acetic acid (43 mL)		200 ^{O}C/ 24h	900 ^{O}C for 5 h at argon	~50 nm	**Cycle**: At 0.1 C, 268 mAh/g at 1st cycle, 230 mAh/g at 50th cycle; At 1C, 75 mAh/g at 300th cycle. (1-3 V).	[136]
Nano TNO @rGO	$Ti(OC_3H_7)_4$ TTIP (3 mmol)	Niobium ethoxide (6 mmol)	Acetic acid (43 mL)	rGO	200 ^{O}C/ 24h	900 ^{O}C for 5 h at Argon	TNO with ~22-30 nm @rGO (~4 wt%)	**Cycle**: At 0.1 C, 303 mAh/g at 1st cycle, 230 mAh/g at 50th cycle; At 1 C, 200 mAh/g at 300th cycle. (1-3 V)	[136]
Nano TNO assembled in microspheres	$Ti(OC_3H_7)_4$ TTIP (0.5 mmol)	$NbCl_5$ (1 mmol)	Ethanol (22 ml)		220 ^{O}C for 3, 6, 12, 24 h in 30 mL autoclave	700 ^{O}C for 2 h (3 °C/min)	TNO microsphere with 2–3 μm, 25.26 m^2/g.	**Cycle**: At 10 C, 115 mAh/g at 500th cycle; **Rate**: 258, 175, and 138 mAh/g at 1C, 5C, 10 C.	[98]
Nano TNO embedded in porous microspheres	$Ti(OC_3H_7)_4$ TTIP (1 mmol)	$NbCl_5$ (2 mmol)	C_3H_8O (30 mL) $+C_3H_8O_3$ (10 mL)		180 ^{O}C for 24h in 50 ml autoclave	750 ^{O}C for 12 h in air	Nano TNO (17 nm) @ microspheres (600-900 nm); with 22.22 m^2/g, 0.108 m^3/g	**Cycle**:At 1C, 266 mAh/g at 1st cycle, 250 mAh/g at 100th cycle. **Rate**: 258, 206, 179, 128 and 91 mAh/g, at 1C, 5C, 10C, 20C and 30 C. (1-3 V)	[135]
TNO @carbon fiber cloth	$Ti(OC_3H_7)_4$ TTIP (0.49 mmol)	$NbCl_5$ (0.52 mmol)	Ethanol (60 ml)	EDOT, CNF	200 ^{O}C for 6h in 100 ml autoclave	700 ^{O}C for 2 h in argon	Nano TNO (30-50 nm, 4.9 wt.%) @ CF (10 μm)	**Cycle:** At 10C, 150 mAh/g at 1000th cycle. **Rate**: 240, 205, 186, 175, 162, 146 and 137 mAh/g, at 1C, 2C, 5C, 10C, 20C, 40C and 80 C. (1-2.5V)	[147]
Nano TNO	$TiOSO_4$, titanium oxysulfate	$NbCl_5$	Ethanol, +dilute sulfuric acid	Ammonia solution (to pH=8)	160 ^{O}C for 5h in 100 ml autoclave	1000 ^{O}C for 30 min	TNO with 50–300 nm, 9.4 m^2/g	**Cycle:** At 300 mA/g, 298 mAh/g at 1st cycle, 271 mAh/g at 100th cycle. **Rate**: 215 mAh/g at 4.5 A/g (11.6C). (0.5-3 V)	[95]
Porous TNO nanospheres	$Ti(OC_4H_9)_4$ (0.5 mmol)	$NbCl_5$ (0.5 mmol)	Ethanol (25 ml)	Pluronic P123 (0.6g) (surfactant)	220 ^{O}C for 16h	800 ^{O}C for 5 h in air	Nano TNO (30-50 nm) @ nanosphere (500 nm), 23.4 m^2/g, 0.155 cm^3/g.	**Cycle**: At 5 C, 212 mAh/g at 1000th cycle, 160 mAh/g at 10000th cycle. (1-2.5 V) **Rate**: 285, 260, 241, 219, 208, 185, 167 mAh/g, at 1C, 2C, 5C,10C, 20C, 30C, 50 C.	[138]
Porous $TiNb_2O_7$ nanospheres	$Ti(OC_4H_9)_4$ (0.5 mmol)	$NbCl_5$ (0.5 mmol)	Ethanol (25 ml)		220 ^{O}C for 16h	800 ^{O}C for 5 h in air	Sphere (2 μm diameter), 18.6 m^2/g (S), 0.116 cm^3/g.	**Cycle:** At 5C, 80 mAh/g at 1000th cycle. (1-2.5V) **Rate**: 220, 175, 150, 115, 90, 80,60 mAh/g, at 1C, 2C, 5C,10C, 20C, 30C, 50 C.	[138]
Nano TNO@ CNT/KB microshperes	$Ti(OC_3H_7)_4$ (10 mmol)	$NbCl_5$ (20 mmol)	Ethanol (60 ml)	CNT and ketjen black (2 g)	200 ^{O}C for 24h in 100 ml autoclave	700 ^{O}C for 2 h in N_2 (5 °C/min)	TNO nanoparticles (~40 nm, 28.20 m^2/g) on CNT/KB microsphere (2–8 μm, 217.82 m^2/g);	**Cycle**: At 5C, 220.8 mAh/g at 6th cycle, 145.4 mAh/g at 1000th cycle. **Rate**: 151.1 mAh/g at 20C. (0.8-3V)	[134]
Nano TNO @carbon fiber cloth	$Ti(OC_4H_9)_4$	$NbCl_5$ (with 2:1 molar ratio of Ti:Nb)	Ethanol (25 ml)		180 ^{O}C for 24h	900 ^{O}C for 5 h in argon (2 °C/min)	TNO nanoparticles @carbon fiber (5-6 μm); 903.70 m^2/g,0.102 cm^3/g.	**Cycle**: At 0.5C, 356 mAh/g at 1st cycle, 290 mAh/g at 500 cycle. **Rate**: 234, 212 and 183 mAh/g at to 2, 4 and 6 C. (1-3V)	[139]
N-doped porous TNO microspheres	$Ti(OC_4H_9)_4$ (1.5 mmol)	$Nb(OC_2H_5)_5$ (2.8 mmol)	Isopropyl alcohol (IPA) (40 mL)	DETA (0.025, 0.05, 0.1, 0.3 mL)	200 ^{O}C for 12h in 80 mL autoclave	700 ^{O}C for 5 h in air (5 °C/min)	Nano TNO (200nm) assembled in porous microsphere (with pore sizes of 5-35 nm)	**Cycle**: At 5C, 190 mAh/g at 1000th cycle. **Rate**: 143 mAh/g at 100 C. (1-3V)	[137]

2.3.3. Sol-gel Synthesis

Sol-gel synthesis method (**Figure 2.24(a)**) is a typical precursor preparation technique that involves condensation and gelation reactions in solutions, processed under mild conditions (e.g., room temperature).[91,122] It generally starts with metal alkoxide chemicals dissolved into organic or organic/inorganic mixed solutions to prepare a homogeneous solution.[148] The sol-gel process involves hydrolysis and condensation reactions, forming a colloidal suspension that results in a stable “sol” system.[122] This sol system can then be transformed into a three-dimensional interconnected network structure, known as a “gel” system, through further condensation and aggregation.[122] After the gel solidifies, solid TNO precursor can be obtained.[122]

Like other solution methods, sol-gel synthesis offers benefits including high phase purity, low calcination temperature, and good control over particle size, morphology, and crystallinity, outperforming solid-state synthesis.[91,122] Compared to hydrothermal/solvothermal synthesis, sol-gel synthesis features a simpler process and better accessibility, because it generally operates under atmospheric conditions and does not involve complicated facilities. However, it is more time- and energy- consuming due to the evaporation process as well as intensive in use of chemicals not to mention low yield scalable potential.[148]

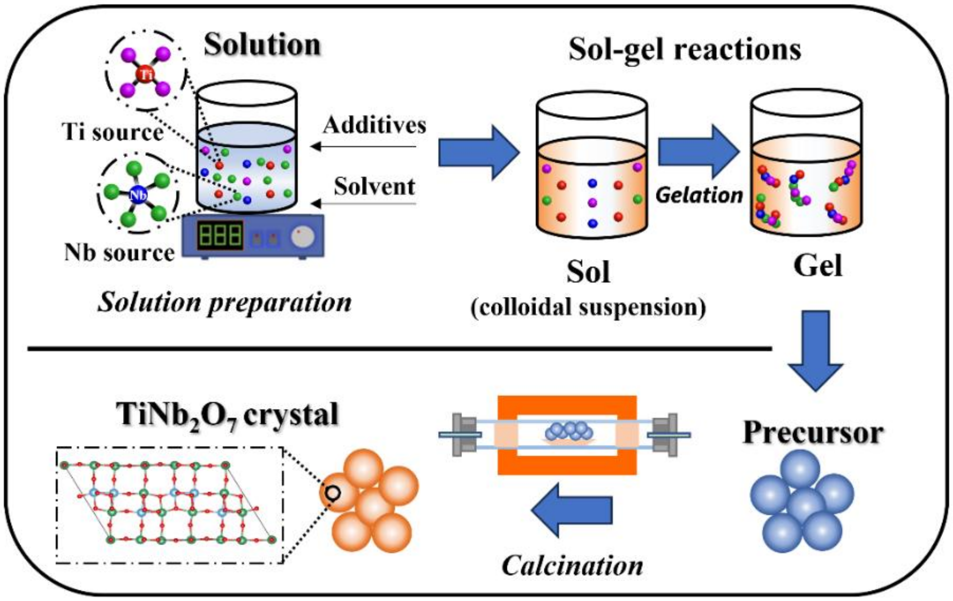

Figure 2.24 Schematic description of sol-gel synthesis method for TiNb$_2$O$_7$ crystals.

In the sol-gel synthesis, particle morphology, size and composition can be controlled by adjusting solution types, metal source chemicals, added surfactants, and procedure parameters (i.e. temperature and time).[122,148] Notably, it was through sol-gel method that Goodenough et al.

conducted their pioneering TNO research in 2011.[91] They dissolved $Ti(OC_3H_7)_4$ and Nb_2O_5 into hydrofluoric acid and citric acid solutions to prepare a stable solution containing Ti^{4+} and Nb^{5+}, and used ammonia to form a citric gel. After solidification at 140 ˚C, TNO precursor particles were obtained. Following annealing process at 900–1350 ◦C, they produced micronized $TiNb_2O_7$ crystals **Figure 2.25(a)** and carbon-coated $TiNb_2O_7$ crystals **Figure 2.25(b)**.

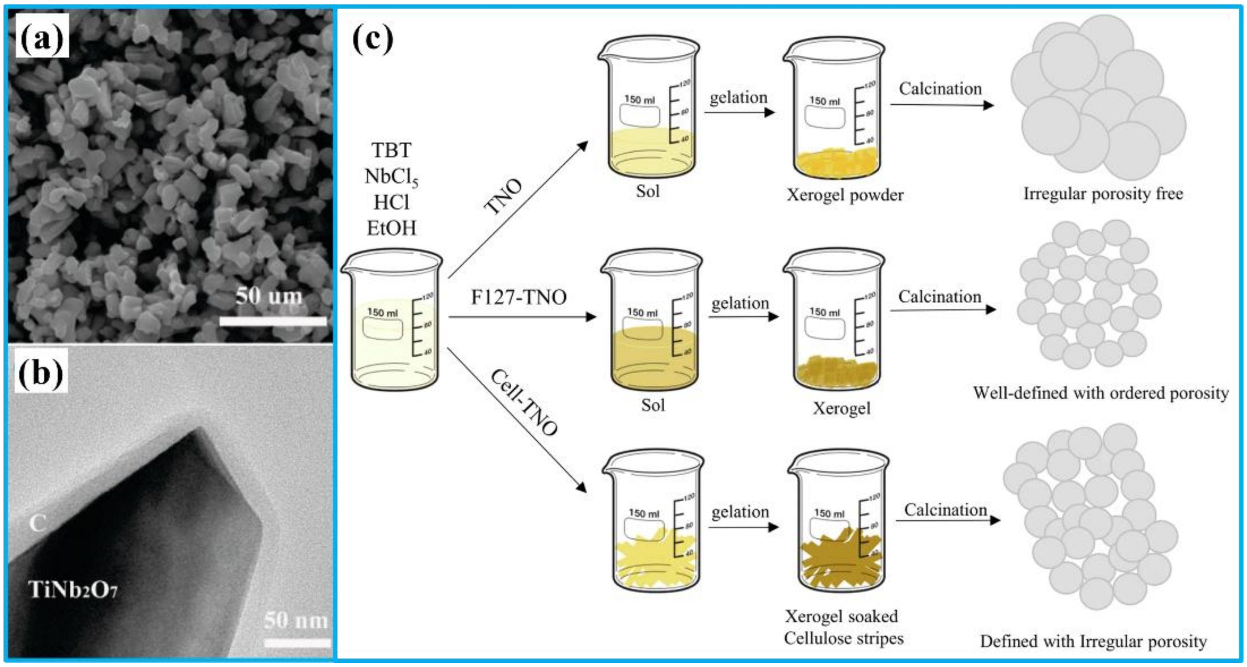

Figure 2.25 (a) SEM image of pure $TiNb_2O_7$ crystals, (b) TEM image of Carbon-coated $TiNb_2O_7$ crystal. Reproduced with permission.[91] Copyright 2011, The America Ceramic Society. (c) Sol-gel enabled soft/hard-template synthesis pathways for nanosized TNO particles. Reproduced with permission.[149] Copyright 2024 Springer Nature.

In addition, sol-gel methods can be extended to soft-template and hard-template approaches to prepare $TiNb_2O_7$ with different morphological structures and crystallinities. Recently, Rahmani et al.,[149] applied tetrabutyl titanate ($Ti(C_4H_9O)_4$, TBT), niobium pentachloride ($NbCl_5$), ethanol (EtOH), and hydrochloric acid (HCl) as starting chemicals to prepare colloidal solution, which after evaporation under ambient conditions for several days yielded a xerogel powder (**Figure 2.25 (c)**). The xerogel after calcination at 900 °C for 5 h, produced non-porous irregular bulk $TiNb_2O_7$ particles. Upon modification of this method by adding F127 co-polymer into solution as a triblock co-polymer non-ionic surfactant, nanostructured $TiNb_2O_7$ particles with well-defined porous structure were obtained. Additionally, they expanded this sol-gel method to a hard-template approach by soaking cellulose stripes into the prepared solution to create xerogel-soaked cellulose stripes, which eventually produced porous $TiNb_2O_7$ particles with different crystal characteristics.

2.3.4. Co-precipitation Synthesis

Co-precipitation synthesis involves precipitation reactions induced by neuralization using a base (**Figure 2.26**).[150] In a typical synthesis procedure, transition metal ions (Ti, Ni, Co, or Mn) can be co-precipitated into hydroxides, carbonates, or oxalates with precipitants (e.g., a base).[132,151] This method is one of the most scalable, efficient, and cost-effective solution-based synthesis methods, which can be extended for continuous reactors for industrial applications.[132,151,152] Like other solution synthesis methods, this method also enables a low calcination temperature and good control over size and morphology. However, it is challenging to precisely control the reaction procedures and the final products due to its fast reaction kinetics (e.g., hydrolysis).[105] Based on the types of solvents used, the co-precipitation method can be further classified into organic co-precipitation and aqueous co-precipitation. Currently, only organic co-precipitation synthesis methods are reported for TNO[105,153], but these methods really can be grouped together with sol-gel methods. Aqueous co-precipitation has not yet been investigated, a gap that is addressed in the present work. Like the other solution synthesis methods, co-precipitation method for $TiNb_2O_7$ comprises the steps of solution preparation, co-precipitation by neutralization, and calcination (**Figure 2.26**).

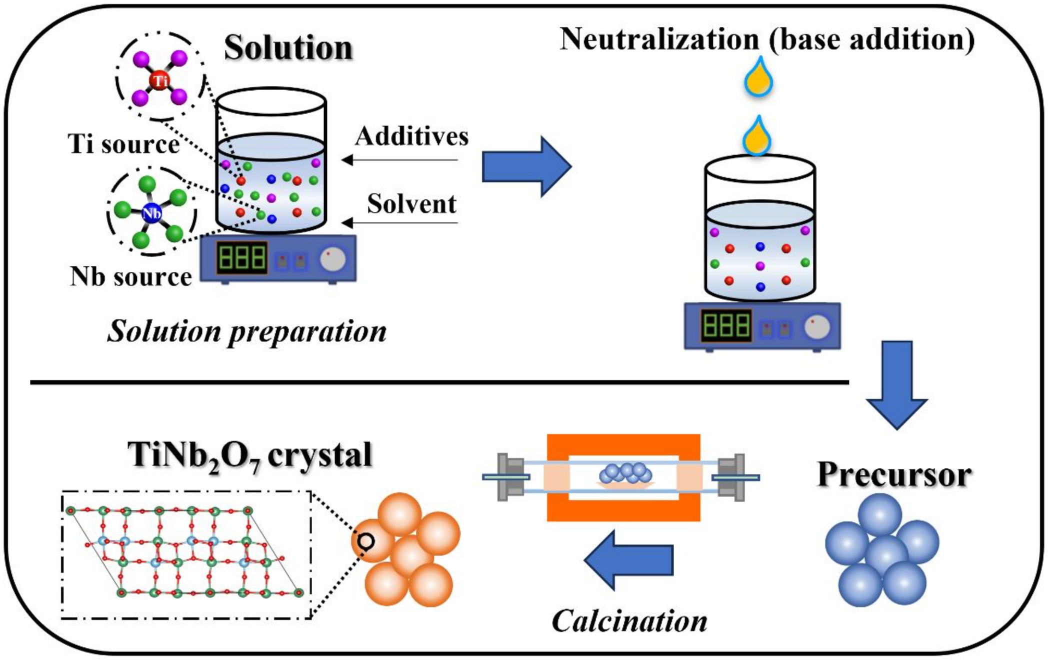

Figure 2.26 Schematic description of co-precipitation synthesis methods for $TiNb_2O_7$ crystals.

Examples of organic co-precipitation (sol-gel like) synthesis of $TiNb_2O_7$ nanoparticles are the works of Paulray et al.,[153] and Yu et al,[105]. The first group used ethanol with glacial acetic acid as solvent and $NbCl_5$ and titanium (IV) isopropoxide as metal sources to prepare a homogeneous solution. Co-precipitation was induced by adding diluted ammonia solution to adjust the pH to 9, yielding white amorphous precursor. This precursor powder was crystallized upon thermal treatment at 750 °C for 2 h. The obtained $TiNb_2O_7$ nanomaterial (50 to 100 nm) showed initial specific capacity of 186 mAh/g at 0.5 C but poor rate capability, only 64 mAh/g at 5C. Meanwhile, Yu et al,[105] demonstrated that TNO's rate capability can be significantly enhanced through substitutional zirconium doping ($Zr_{0.05}Ti_{0.95}Nb_2O_7$ and $Zr_{0.1}Ti_{0.9}Nb_2O_7$). Their optimal $Zr_{0.05}Ti_{0.95}Nb_2O_7$ ($Zr_{0.05}$-TNO) anode obtained via sol-gel/organic co-precipitation (**Table 2.7**) found to provide high-rate capabilities, namely 260.0 and 177.8 mA h/g at 0.5 and 10 C, respectively and excellent cycling durability of 170 mA h/g at 5 C after 1000 cycles.

Table 2.7 Synthesis routes and high-rate capability of $TiNb_2O_7$ anodes

Anode Materials	Synthesis Methods	Capacity at 5 C	Ref.
$TiNb_2O_7$ Micron-sized particles	**Solid-state synthesis** Chemicals: TiO_2 and Nb_2O_5 Step 1. Ball milling: 3 h Step 2. Calcination: 1100 °C for 8 h	180 mAh/g at 1st cycle, 145 mAh/g at 100th cycle, 137 mAh/g at 200th cycle	[154]
Porous $TiNb_2O_7$ microspheres	**Solvothermal synthesis** Chemicals: $Ti(OC_4H_9)_4$, $Nb(OC_2H_5)_5$, DETA Solution: isopropyl alcohol (IPA) Step 1. Solvothermal: 200 °C for 12 h. Step 2. Calcination: 700 °C for 5 h in air	215 mAh/g at 1st cycle, 200 mAh/g at 100th cycle, 200 mAh/g at 200th cycle	[137]
$TiNb_2O_7$ nanospheres	**Sol-gel synthesis (organic co-precipitation)** Chemicals: $NbCl_5$, titanium isopropoxide (TPT) Organic solvent: ethanol Additives: oxalic acid dihydrate, urea Step 1. Direct hydrolysis (adding water) Step 2. Calcination: 800 °C for 6 h in air	170 mAh/g at 1st cycle, 160 mAh/g at 100th cycle, 150 mAh/g at 200th cycle	[105]

To sum up, **Table 2.7** summarizes representative results of best performance of different $TiNb_2O_7$ anodes synthesized under optimum conditions of solid-state and solution (sol-gel/organic co-precipitation, solvothermal) synthesis methods. Briefly, solid-state method while it is low-cost and scalable is seen to yield low performance. By contrast, solution synthesis methods, including sol-gel (or organic co-precipitation) and solvothermal, offer advantages of fabricating high phase purity and nanostructured $TiNb_2O_7$ materials delivering excellent rate performance and cycling stability. But these organic-based solution methods apply flammable solvents and complex equipment (autoclaves) or chemical procedures, raising scalability challenges due to high cost and environmental concern.[95] Aqueous precipitation based synthesis promises a sustainable alternative synthesis route for $TiNb_2O_7$ electrode materials. However, this method has not yet been explored. Therefore, it is worthwhile to review aqueous synthesis and its fundamental principles, as discussed in the next section.

2.4. Nanomaterials Synthesis by Aqueous Precipitation

2.4.1. Introduction about aqueous precipitation

Aqueous-based solution synthesis, especially aqueous co-precipitation has been widely used for fabricating LIB electrode materials, including nanoscale $Li_4Ti_5O_{12}$ anode materials[131] (**Figure 2.27(a)**), $LiCoO_2$ cathode materials[155] (**Figure 2.27(b)**), and monocrystalline $LiNi_xMn_yCo_zO_2$ cathode materials[156] (**Figure 2.27(c)**).

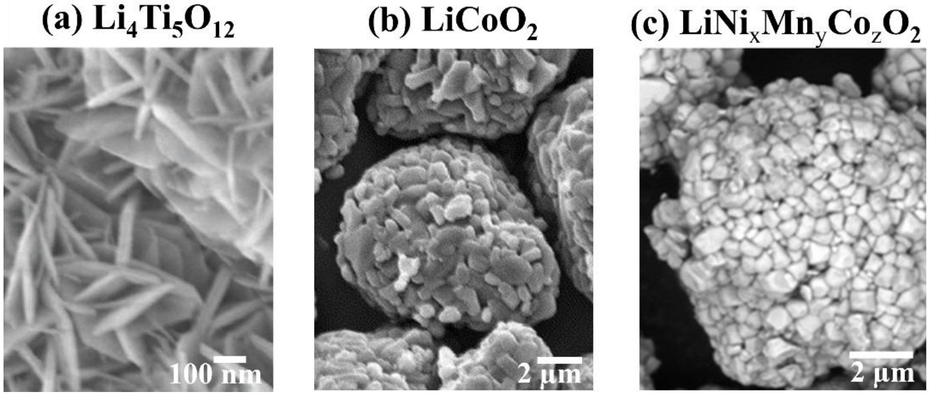

Figure 2.27 (a) $Li_4Ti_5O_{12}$ anode material. Reproduced with permission.[131] Copyright 2013 The Electrochemical Society. (b) $LiCoO_2$ cathode material. Reproduced with permission.[155] Copyright 2005 Elsevier. (c) Monocrystalline $LiNi_xMn_yCo_zO_2$ synthesized by aqueous co-precipitation approach. Reproduced with permission.[156] Copyright 2018 American Chemical Society.

Generally, aqueous precipitation synthesis (**Figure 2.28**) involves aqueous reaction to form crystalline or amorphous intermediate compounds.[124,150,157] The whole process starts with dissolving metal salts in an aqueous solution.[124,150] This solution is in an unsaturated state. As the solute concentration increases, extensive ion-association occurs, which results in the formation of electrically neutral ion-pairs (solvated with water).[157] When the solution becomes supersaturated, the solute species aggregate and polymerize, forming clusters of ion-pairs or molecules (10-1000 monomers per cluster).[124] These formed clusters convert through nucleation and growth to precipitated compounds. These precipitated compounds can be amorphous or crystalline and typically serve as precursors to final products.[158] Precursors can be further crystallized after thermal treatment (e.g., calcination) to obtain the desired crystal materials.[150]

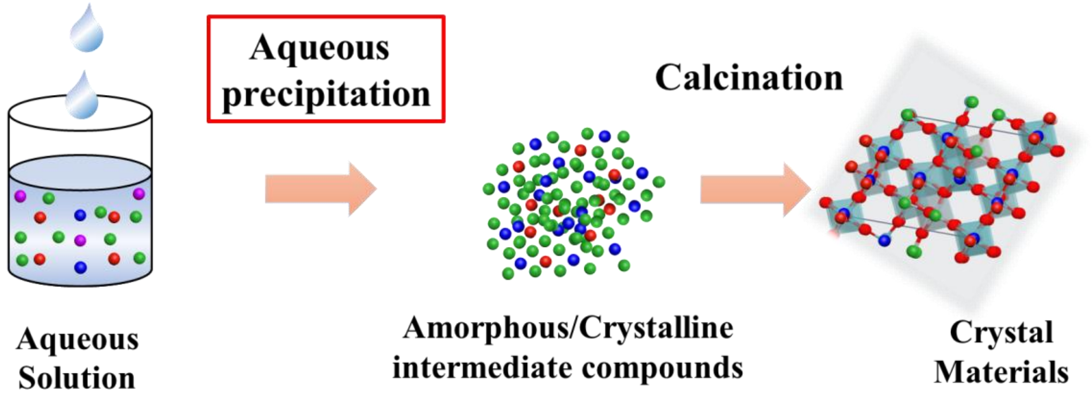

Figure 2.28 Aqueous co-precipitation approach for electrode materials synthesis.

Aqueous precipitation is defined as reactive crystallization process in aqueous solution i.e., the formation of the solid product via a chemical reaction in aqueous solution.[150,157] In case of aqueous precipitation reaction of a compound **$AB_{(s)}$**, the general chemical reaction can be expressed as:

$$\mathbf{A^{+}_{(aq)} + B^{-}_{(aq)} + X^{-}_{(aq)} + I_{(aq)}} + H_2O \rightarrow \mathbf{AB_{(s)} + (?)\ ABX\ and/or\ IB,\ ABOH} \qquad \textbf{(equation 2.16)}$$

where $A^{+}_{(aq)}$ cation, $B^{-}_{(aq)}$ anion, $X^{-}_{(aq)}$ matrix anion, other solute species $I_{(aq)}$, and H_2O can react in aqueous solution.[150] This precipitation reaction can yield the desired **$AB_{(s)}$** precipitated compound, as well as by-products (ABX and/or IB, ABOH) due to side reactions. These products or by-products can be oxides, hydroxides, carbonates, chlorides, sulfates, etc.[150,157]

2.4.2. Mechanism of Nucleation and Growth of Nanoparticles in Solution

To fabricate nanoparticles, understanding the mechanisms of nucleation and growth in solution is essential. In a solution system, a solid phase forms when the molar Gibbs free energy is negative ($\Delta G < 0$).

$$\mathbf{\Delta G = -RT\ln\left(\frac{\alpha}{\alpha_0}\right)} \qquad \textbf{(equation 2.17)}$$

The molar Gibbs free energy (ΔG (J/mol)) is dependent upon the absolute temperature (T), the activity of the solute in the initial solution (α (mol/L)), the activity of the solute in the saturated (equilibrium) solution (α_0 (mol/L)), the universal gas constant (R=8.31 J/(mol·K)).

Based on **equation 2.18**, when $^{\alpha}/_{\alpha_0}$ >1, ΔG<0. Taking activities (α) equal to concentrations (*c*) for simplification, we get:

$$\mathbf{S}=\frac{\alpha}{\alpha_0}\approx\frac{C}{C_{eq}} \qquad \textbf{(equation 2.18)}$$

where ratio $^{\alpha}/_{\alpha_0}$ is defined as saturation ratio (S) and c_{eq} is the equilibrium concentration.

Similarly, we can define the supersaturation ratio (σ):

$$\boldsymbol{\sigma}=\mathbf{S}-1=\frac{c-c_{eq}}{c_{eq}} \qquad \textbf{(equation 2.19)}$$

The supersaturation is the driving force for crystallization (e.g., nucleation and growth) of nanoparticles. When the supersaturation is equal to zero ($\sigma = 0$), ΔG is zero, and the system is at equilibrium. When the supersaturation is positive (i.e., $c > c_{eq}$), ΔG is negative meaning the reaction is favourable and thus nucleation should occur spontaneously. Actual nucleation though is controlled by kinetics factors.

The precipitation of nanoparticles involves the processes of nucleation, growth, and aggregation. Nucleation is defined as the first random formation of a thermodynamic new phase (e.g., nucleus).[123,124] There are mainly three nucleation mechanisms (**Figure 2.29**) depending on the type of nucleation sites: homogeneous nucleation, heterogeneous nucleation, and surface nucleation.[159] First, homogeneous nucleation (**Figure 2.29(a)**) constitutes a primary mode of nucleation and occurs in the absence of a surface with nuclei forming uniformly throughout the solution.[123] By contrast, heterogeneous nucleation (**Figure 2.29(b)**) is another type of primary nucleation that forms on a foreign surface (i.e., impurity or other foreign phases and container surfaces).[123,160] Thirdly, surface nucleation (**Figure 2.29(c)**) refers to the secondary production of nuclei on the surface of same precipitate solid (e.g., crystal surface) that forms in-situ or added externally as seed.[123,160]

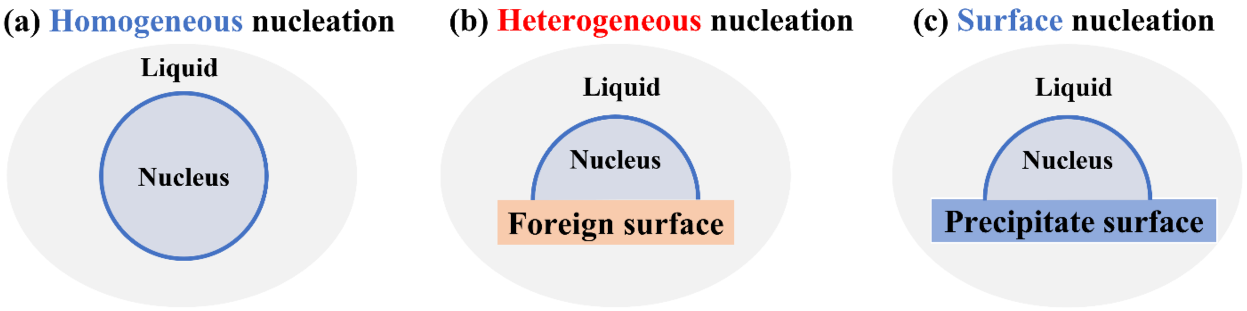

Figure 2.29 Three nucleation modes: (a) homogeneous nucleation (primary production), (b) heterogeneous nucleation (primary production), and (c) surface nucleation (secondary production).

Homogeneous nucleation (**Figure 2.29(a)**) can be illustrated by a spherical nucleus with a radius of r and surface free energy per unit area of γ (J/m^2).[150] The total free energy change (ΔG, (J)) is a sum of the surface free energy change (ΔG_{surf}) and the volume free energy change (ΔG_{vol}).[124,150]

$$\Delta G = \Delta G_{surf} + \Delta G_{vol} = 4\pi r^2\gamma + \frac{4}{3}\pi r^3 \Delta\mu \qquad \textbf{(equation 2.20)}$$

$\Delta\mu$ is change of Gibbs free energy change per unit volume of the crystal (J/m^3) and is expressed as the difference between the free energy of the monomer in the crystal and in solution, which can be defined as:

$$\Delta\mu = \frac{-k_B T ln(S)}{v} \qquad \textbf{(equation 2.21)}$$

where k_B is Boltzmann constant (1.38×10^{-23} J/K), T is the absolute temperature (K), S is the saturation ratio, v is the molar volume of the monomer in the crystal (m^3/mol).

As shown in **Figure 2.30**, total free energy change (ΔG) (y axis) increases with the radius (r) (x axis) of the nucleus peaking to maximum free energy, followed by a rapid decrease below zero. To be specific, γ is always positive and thereby ΔG_{surf} increases with the radius. By contrast, the ΔG_v always keeps negative, so ΔG_{vol} decreases with the radius.

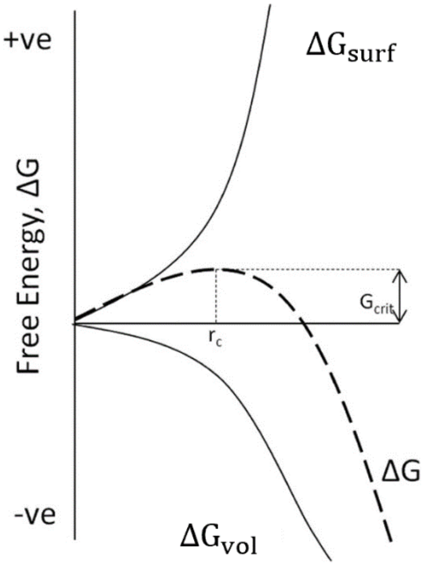

Figure 2.30 Change of Gibbs free energy as a function of the radius of nucleus. Reproduced with permission.[124] Copyright 2014 American Chemical Society

This maximum free energy, defined as critical free energy (ΔG_{crit}), is the activation energy barrier of homogeneous nucleation, which a nucleus will pass through to form a stable nucleus.[159] The corresponding radius can be defined as critical nuclei size (r_c).

By setting ${}^{d\,\Delta\,G}/_{d\,r} = 0$, r_c and ΔG_{crit} can be determined.

$$r_c = -\frac{2\gamma}{\Delta G_v} = \frac{2\gamma v}{k_B T\ ln\ S} \qquad \textbf{(equation 2.22)}$$

$$\Delta G_{crit} = \frac{16\pi\gamma^3}{3\Delta G_v{}^2} = \frac{16\pi\gamma^3 v^2}{3(k_B T\ ln\ S)^2} \qquad \textbf{(equation 2.23)}$$

The nucleation rate (J (1/s)) can be defined as the number of nuclei (N) formed per unit time and expressed as an Arrhenius equation:

$$J = \frac{dN}{dt} = A\ exp\left(-\frac{\Delta G_{crit}}{k_B T}\right) = A\ exp\left(\frac{16\pi\gamma^3 v^2}{3k_B{}^3 T^3 (ln\ S)^2}\right) \qquad \textbf{(equation 2.24)}$$

According to (**equation 2.22**), the nucleation rate is driven by saturation S, temperature T (K), and surface free energy γ. The rate equation of heterogeneous nucleation is in the same form as that of homogeneous nucleation. Among these parameters, saturation S (or supersaturation σ) provides the largest effect. Mullin et al.[150] reported J is an exponential or high power function in terms of S, ($J \propto S^{6-12}$).

Unlike homogeneous nucleation, heterogeneous nucleation and surface nucleation occur on an existing surface. Heterogeneous nucleation needs to overcome a lower activation energy barrier, which means lower critical free Gibbs energy (ΔG_{crit}), smaller critical nuclei size (r_c), and lower critical saturation ratio (S_{crit}), as shown in **Figure 2.31**.[159,161]

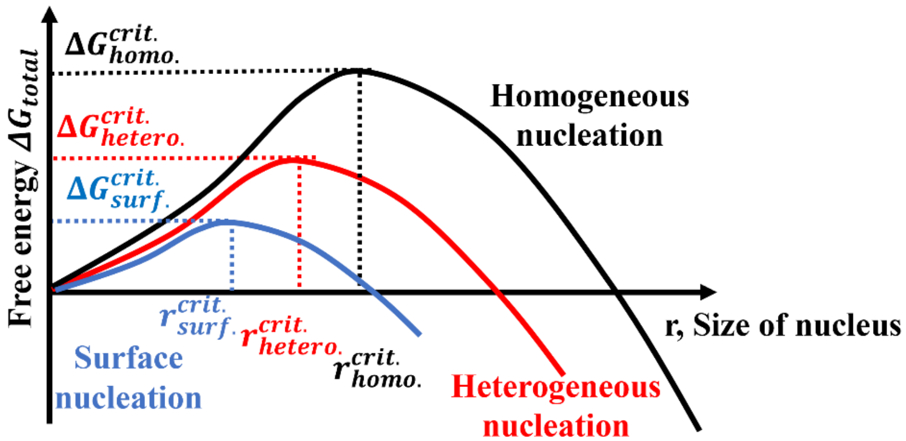

Figure 2.31 Critical free Gibbs energy (ΔG_{crit}) and critical nuclei size (r_c) of homogeneous nucleation, heterogeneous nucleation and surface nucleation.

For a spherical particle of radius $\boldsymbol{r}$, the crystal growth rate (G) can be defined by a first-order or second-order equation.

$$G = k_g\ C_{eq}(S-1) \qquad \textbf{(equation 2.25)}$$

where k_g is the growth constant (m^4/(mol·s)), C_{eq} is the solubility of the precipitating solute species (mol/m^3), S is the saturation ratio.[150]

2.4.3. Aqueous Precipitation Regimes

In a homogenous nucleation-dominated precipitation system, homogeneous nucleation occurs, when the supersaturation σ exceeds the critical supersaturation $\sigma_{homo.}^{crit.}$. This is followed by the particle growth process.[124]

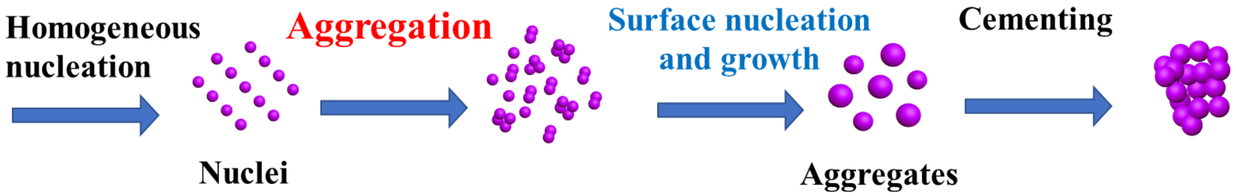

Figure 2.32 Whole process of nucleation and growth in a homogenous nucleation-dominated precipitation system. Figure adapted from Ref.[124].

Growth mode of nanoparticles in solution typically follows sequence of process including aggregation, surface nucleation and growth, and cementing, etc. (**Figure 2.32**).[159] During aggregation nuclei of 10-100 nm in size form secondary particles if colloid stability is suppressed. Surface nucleation and growth process start, after σ drops below $\sigma_{homo.}^{crit.}$. During cementing, aggregates can be cemented by continuously depositing new material on the surface of particles.

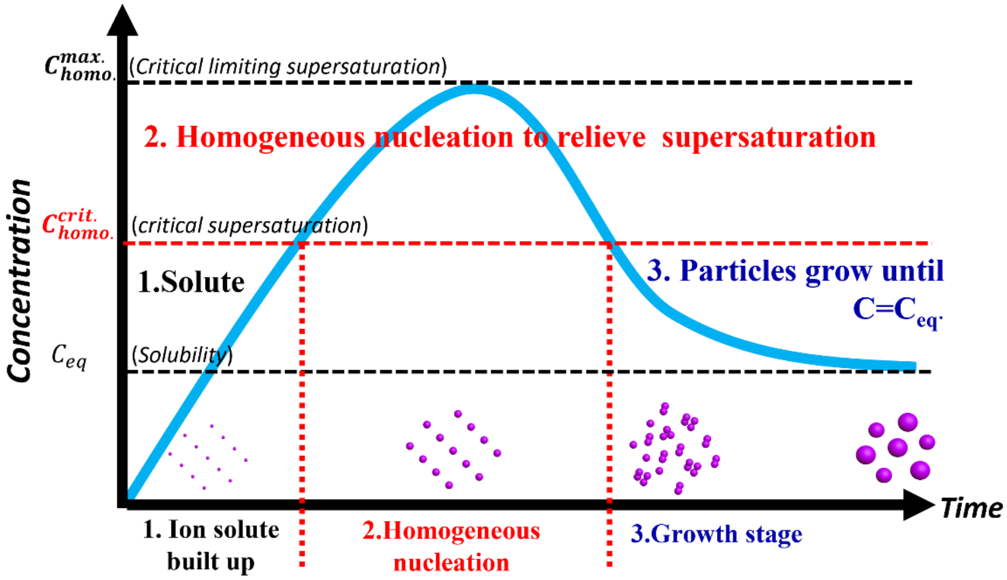

Figure 2.33 LaMer diagram schematic. Figure adapted from Ref.[124,162,163].

The whole process of nucleation and growth in solution discussed above can be quantitatively described with the aid of the LaMer diagram (**Figure 2.33**). This diagram designed by LaMer and

Dinegar[163] in 1950 demonstrates the correlations between solution concentration and process of homogeneous nucleation & growth. In the homogeneous nucleation-dominated precipitation system, atoms exist in the state of ionic solutes in the solution when concentration is below critical supersaturation $C_{homo.}^{crit.}$ After that, homogeneous nucleation occurs when concentration increases to the range between $C_{homo.}^{crit.}$ and critical limiting supersaturation ($C_{homo.}^{max}$). As homogeneous nucleation occurs, supersaturation is relieved dropping within the growth stage, between $C_{homo.}^{crit.}$ and C_{eq}, where homogeneously nucleated particles grow by aggregation, surface reaction, and cementing.

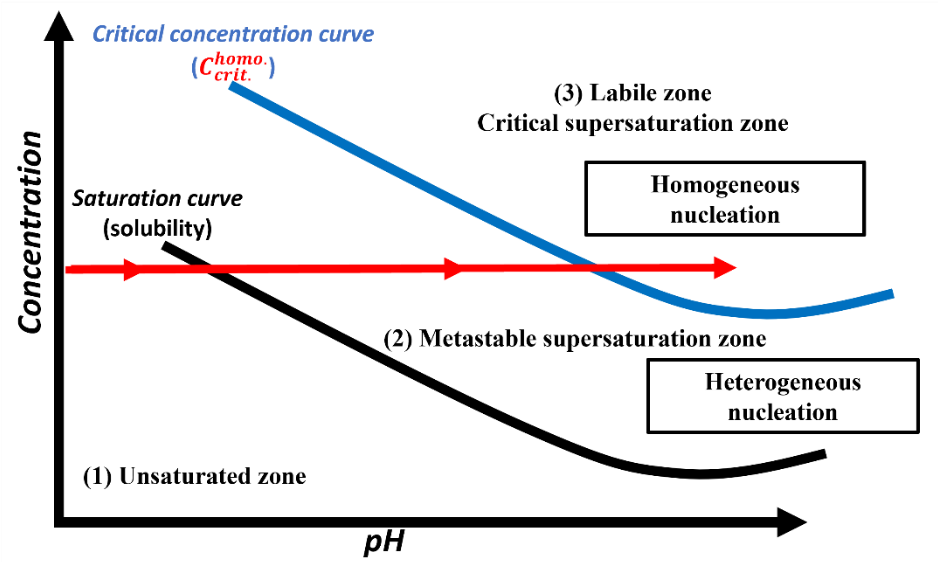

Figure 2.34 Aqueous precipitation by supersaturation control. Figure adapted from Ref.[150,163].

In the same paper in 1950, LaMer et al. presented another diagram,[150,163] which has been extended to guide supersaturation-controlled aqueous precipitation (**Figure 2.34**).[124,162,163] This diagram describes a pH-dependent aqueous precipitation reaction.[150,163] As shown in **Figure 2.34**, there are two curves, namely the saturation curve and the critical concentration curve.[150,163] The former corresponds to solubility at different pH values, and the latter represents the critical concentration for homogeneous nucleation changes with different pH values. Accordingly, diagram defines three zones, including the unsaturated zone, the metastable supersaturation zone, and the critical supersaturation zone (Labile zone). In the case of aqueous precipitation, when the pH is controlled within the unsaturated zone, a dilute solution can be prepared. As pH increases to the metastable supersaturation zone, heterogeneous nucleation, surface nucleation, and particle growth can occur. This zone can be used to produce well-grown crystals by adding seed particles. The Labile zone, in which homogeneous nucleation occurs spontaneously, can be used to obtain ultra-fine colloidal precipitates.

2.4.4. Hydrolytic Precipitation and Synthesis of Metal Oxide Materials

Hydrolysis is a typical type of aqueous precipitation and hydrolytic co-precipitation is recognized as one of most useful methods for compound precipitation.[150,164] Hydrolysis is a chemical reaction of substance with water, leading to the decomposition of both the substance (e.g., salts) and water.[150,164,165] In the hydrolysis reaction, the metallic cation (M^{z+}) reacts with water (H_2O) to produce metal hydroxide complexes ($M_x(OH)_y H_2O_{(nx-y)}^{(y-xz)-}$) and hydrogen cations ($H^+$),[158,165] as expressed as below:

$$xM^{z+} + nH_2O \rightarrow M_x(OH)_y H_2O_{(nx-y)}^{(y-xz)-} + yH^+ \qquad (\textbf{equation 2.26})$$

In most cases, hydrolysis reactions involve two pathways, namely olation and oxolation.[158,161,165,166] Olation leads to hydroxyl bridges through deprotonation of water. In one typical olation reaction, reactants are metal hydroxide complexes (M-OH) and hydrated metal ions ($M\text{-}H_2O$), while the products are metal hydroxide ($M\text{-}OH\text{-}M\text{-}OH^-$) and protons ($H^+$),[158] as illustrated in **equation 2.27** below:

$$M\text{-}OH + M\text{-}H_2O \rightarrow M\text{-}OH\text{-}M\text{-}OH^- + H^+ \qquad (\textbf{equation 2.27})$$

By contrast, oxolation (**equation 2.28**) leads to oxo bridges through dehydration.[158,165] Reactants are metal hydroxide complexes (i.e., M-OH) in the form of monomers, dimers, and polymers. The products are metal oxides (i.e., M-O-M) or metal oxy-hydroxides. This chemical reaction can be simplified as below:

$$M\text{-}OH + M\text{-}OH \rightarrow M\text{-}O\text{-}M + H_2O \qquad (\textbf{equation 2.28})$$

The hydrolytic formation of particles (**Figure 2.35**) involves complexation, reversible clustering, irreversible clustering, precipitation, and transformation steps.[158,165] The first step is the association of hydrated metallic ions to form metallic complexes monomers and dimers. These metallic complexes reversibly grow to small polymers during reversible clustering. The obtained small polymers or embryos are not stable and can be dissolved back in the solution. At certain stage irreversible clustering takes place, with the polymer embryos slowly reacting with each other to form large polymers, which convert to amorphous or poorly crystalline particles. In the final stage of phase transformation, the amorphous precipitates are converted to crystalline compounds by aging and recrystallization.

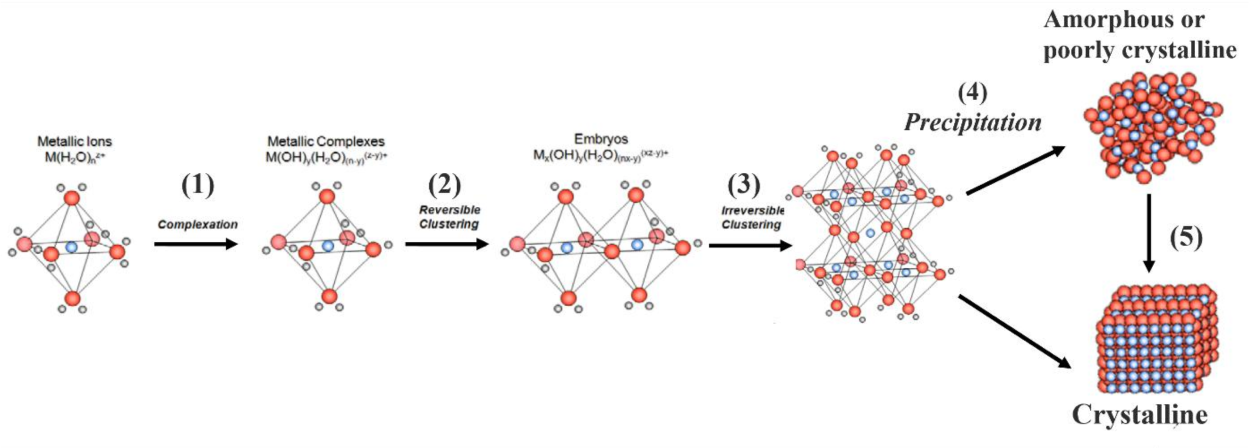

Figure 2.35 Hydrolysis: From complexes in solution to particles. Reproduced with permission.[165] Copyright 2000 CRC Press.

Hydrolytic precipitation of different oxides and oxyhydroxide has been investigated including the hydrolysis of titanium chloride ($TiCl_4$),[131,140,167-170] to produce titanium dioxide (TiO_2).[131,140,167-170] The overall hydrolytic precipitation of TiO_2 is represented by **equation 2.29**.[167] Olation pathway (**equation 2.30**) leads sequentially to hydroxy-chloro-titanium complexes ($Ti(OH)_xCl_{4-x}$), titanium hydroxide ($Ti(OH)_4$), and amorphous TiO_2(am).[168] Oxolation pathway (**equation 2.31**) forms oxy-chloro-titanium complexes ($Ti(O)Cl_2$), finally yielding TiO_2.[168]

$$TiCl_4(aq)+2H_2O \rightarrow TiO_2(s)+4HCl(aq) \qquad \textbf{(equation 2.29)}$$

$$TiCl_4(H_2O)_n \rightarrow Ti(OH)_xCl_{4-x} \rightarrow Ti(OH)_4 \rightarrow TiO_2(s) \qquad \textbf{(equation 2.30)}$$

$$TiCl_4\,(H_2O)_n \rightarrow Ti(O)Cl_2 \rightarrow TiO_2(s) \qquad \textbf{(equation 2.31)}$$

These exothermal and simultaneous reaction pathways are rather challenging to control when used for synthesizing TiO_2 nanophases.[165,168]

To address this problem, our group has studied in detail the relevant chemistry leading to identification of different synthesis routes by adjusting supersaturation. As demonstrated in **Figure 2.36**, TiO_2 nanomaterials with different properties have been synthesized which have been evaluated for energy & environmental applications including solar cells, Li-ion batteries, and photocatalytic water decontamination.[61,131,140,167-171]

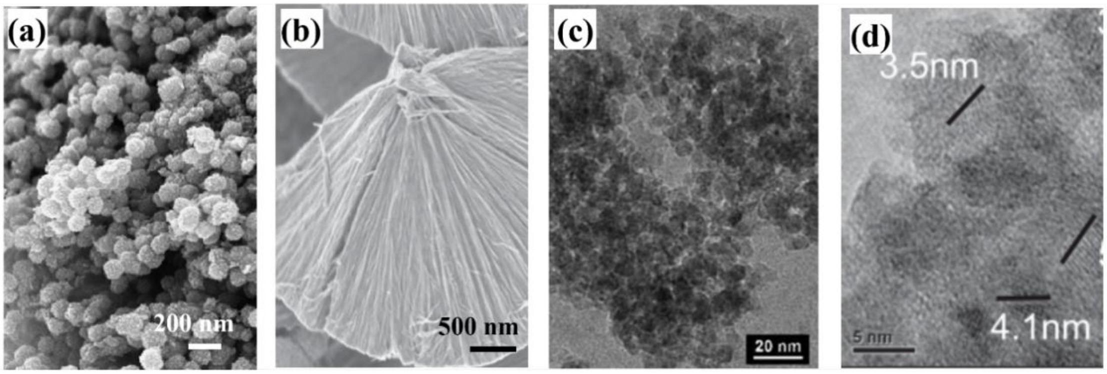

Figure 2.36 Application of hydrolytic precipitation to nano-TiO_2 synthesis at HydroMET: (a) TiO_2 nanoparticles, Reproduced with permission. Copyright 2008 Elsevier. (b) Rutile nanofibers. Reproduced with permission.[168] Copyright 2009 Elsevier. (c) Anatase nanocolloids. Reproduced with permission.[169] Copyright 2011 The Electrochemical Society. (d) Anatase nanocrystals. Reproduced with permission. Copyright 2016 Elsevier.

For example, in 2009, Li and Demopoulos[167] developed a low-temperature partial hydrolysis process induced by neutralization with MgO to prepare TiO_2 nanopoweders (**Figure 2.36(a)**). Subsequently, Charbonneau et al.[168,169] explored pH- and Temperature- controlled hydrolytic precipitation of different TiO_2 varieties from nanofiber-structured rutile particles (**Figure 2.36(b)**) to anatase nanocolloids (**Figure 2.36(c)**). These studies involved batch hydrolysis which poses challenges to scale up. It was Yasin et al. who first demonstrated the synthesis of nanoTiO_2 phases in a continuous process using continuous stirred tank reactor (CSTR) reactors.[140,170] Using this method anatase nanocrystallites and brookite nanoplatelets were synthesized which found to have interesting Li-ion storage properties. For example, the nano-anatase (**Figure 2.36(d)**). was found to store Li-ions via a dual mechanism, intercalation and pseudocapacitance, the relative contribution depending on crystallinity and surface area.[61] Meanwhile the brookite nanoplatelets were found to have the most stable cycling performance among the different TiO_2 nanophases nanophases.[171]

Recently, Chalastara, et al.,[172] modified this CSTR-based aqueous precipitation approach (**Figure 2.37(a)**) enabling the synthesis of mixed-phase (heterojunctioned) TiO_2 nanomaterials by tunable composition control: namely anatase-dominated anatase/brookite mixed-phase TiO_2 (**A/b**) (**Figure 2.37(b)**), brookite-dominated brookite/rutile mixed-phase TiO_2 (**B/r**) (**Figure 2.37(c)**), and rutile-dominated rutile/brookite mixed-phase TiO_2 (**R/b**) (**Figure 2.37(d)**). These background developments demonstrate that hydrolytic precipitation synthesis can be tunable and scalable when operated continuously in CSTRs, thus offering a sustainable and industrial route for production of nanomaterials.

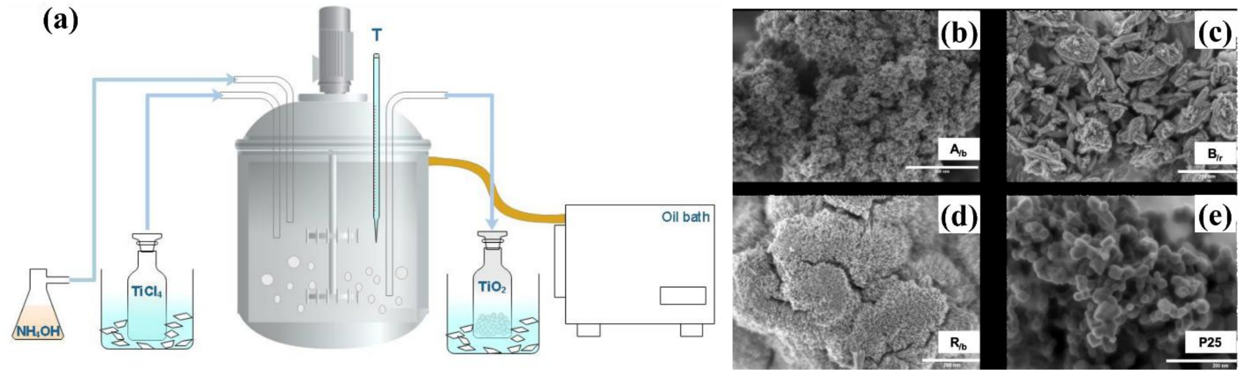

Figure 2.37 (a) Synthesis of nanocrystalline TiO_2 in a continuous stirred-tank reactor (CSTR). Mixed-phase TiO_2 nanoparticles: (b) Anatase-dominated anatase/brookite mixed-phase TiO_2 (**A/b**), (c) Brookite-dominated brookite/rutile mixed-phase TiO_2 (**B/r**), (d) Rutile-dominated rutile/brookite mixed-phase TiO_2 (**R/b**), (e) commercial TiO_2 (P25). Reproduced with permission.[172] Copyright 2020 MDPI.

Beyond TiO_2 synthesis, Chiu et al. [131,145,146,173] utilized hydrolytic precipitation reactions of $TiCl_4$ induced by neutralization with lithium hydroxide (LiOH) to obtain layered lithium titanate hydrate precursors ($(Li_{2-x}H_x)Ti_2O_5 \cdot yH_2O$),[174] which upon controlled calcination/annealing yielded $Li_4Ti_5O_{12}$ nanosheet materials as high-performance LIBs anodes.[146] The obtained $Li_4Ti_5O_{12}$ nanosheet anode (**Figure 2.38**(a)) offers an excellent reversible capacity of 163.7 mAh/g at 1 C, close to the theoretical capacity (175 mAh/g), and outstanding cycling stability with 92% retention after 300 cycles (**Figure 2.38**(b)).[173] Additionally, this anode provides (**Figure 2.38**(c)) high Li^+ ion diffusion coefficients up to 1.71×10^{-11} cm^2/s paving the way for development of fast-charging anodes.

This success with Ti-based materials forms the basis for the application of hydrolytic precipitation synthesis method to $TiNb_2O_7$ materials as described in **Chapter 4** of this thesis.

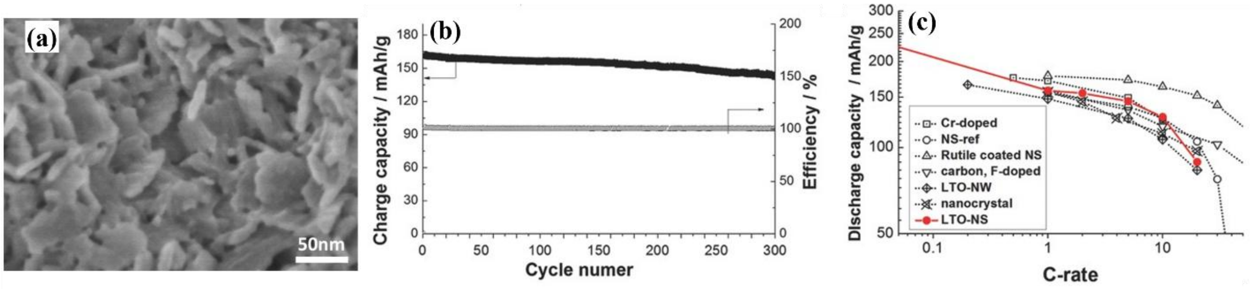

Figure 2.38 (a) The morphology and (b) Galvanostatic 1C discharge/charge cycling performance of $Li_4Ti_5O_{12}$ nanosheet anode; (c) Comparison of rate capability to other recently published LTO materials using a Ragone plot. Reproduced with permission.[173] Copyright 2016 WILEY.

2.5. Electrode Engineering via Electrophoretic Deposition

The electrode fabrication method influences the microstructural and interfacial characteristics of fast-charging LIBs including internal resistance and stability, thereby affecting cyclability and power capability.[38,39] Electrodes are typically fabricated with the tape casting process that involves mixing the active component with the conductive component (e.g., carbon black) plus a polymeric binder (e.g., Polyvinylidene Fluoride (PVDF)) dissolved in a solvent (e.g., N-Methyl-2-Pyrrolidone (NMP)).[175,176] However, non-homogeneous dispersion of active materials and conductive components in slurry accelerates the degradation of the battery electrode.[114] This effect is more serious for nanomaterials because the high surface area results in strong interactions among them and severe aggregation of the slurry.[177,178] Therefore, it is crucial for creating high-performance fast-charging TNO electrodes to equally address the engineering of the electrode as done for the $TiNb_2O_7$ crystals themselves. In this thesis, we applied the electrophoretic deposition technique to realize the nanoscale assembly of the TNO composite materials by employing graphene oxide (GO) as both binder and conductive component.

2.5.1. Mechanisms of Electrophoretic Deposition

Electrophoretic deposition (EPD) technique stems from the electrophoretic phenomenon of charged particles in a stable colloidal suspension, where the electric field drives positively (or negatively) charged particles to migrate to the oppositely charged electrode and deposit on the substrate.[179-181] Thus, the EPD setup consists of four components including the working electrode (conductive substrate), the counter electrode, colloidal suspension, and power supply.[182]

The typical EPD process has two steps: (1) preparation of a stable suspension by dispersing powder particles in the solvent (**Figure 2.39(a, b)**); (2) deposition of charged particles on a conductive substrate driven by DC power (**Figure 2.39(c, d)**).[183] As indicated in **Table 2.8**, the main suspension parameters that influence stability include (1) particle size, (2) particle concentration, (3) type of solvents, (4) suspension conductivity, (5) suspension dielectric constant, (6) suspension viscosity, (7) zeta potential, and (8) stabilizing/charging additives including inorganics and polymers.[181,183-186] There may be parameter interactions influencing the properties of obtained film products. For example, the particle migration velocity may be controlled by particle size, particle concentration, the viscosity of the solvent, and electric field (e.g., voltage and current), etc.[181,187] The stability of colloidal suspension (characterized by zeta potential) is associated with the property of surfactants and solvent, pH or other charging ions, and temperature.[182]

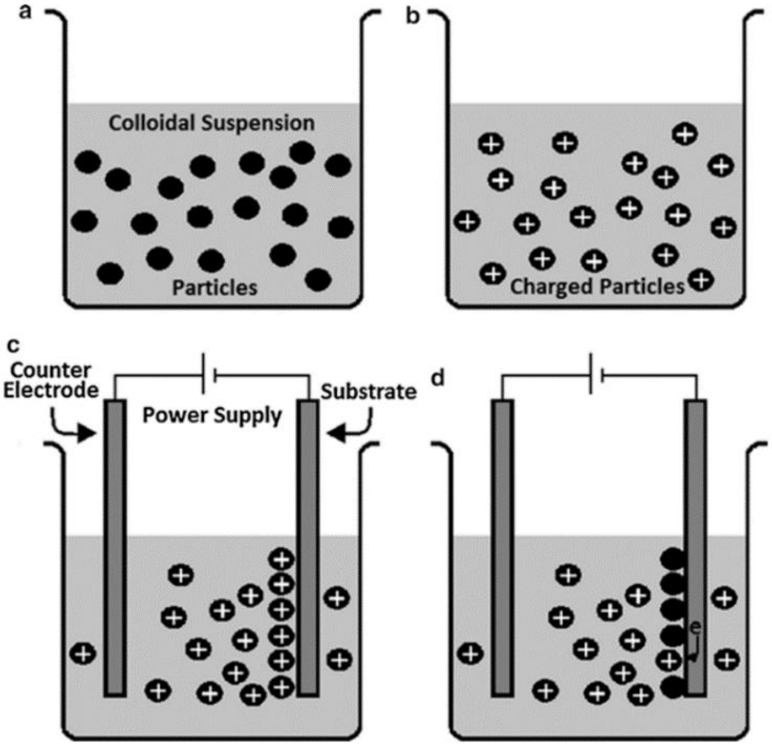

Figure 2.39 EPD processes: (a) dispersion, (b) particle charging, (c) electrophoresis and (d) deposition. Reproduced with permission.[183] Copyright 2016 Springer.

In the deposition process, the deposition time, conductivity of the substrate, and electric field selection should be considered. First, the increase in deposition time tends to result in the rise in mass and thickness of the deposition film, however, this growing coating increases resistance and results in a drop in deposition rate.[188] Second, the applied electric field strength affects the deposition rate, structure, and quality of the product.[189] High voltages enable high-rate deposition but suffer from low quality and uniformity of EPD film, while low-voltage electric fields enable slow growth of dense and even deposits. Thus, moderately applied fields (*e.g.*, 25-100 V/cm) have been regarded as a suitable power supply for EPD. Recently another means of manipulating the deposition process is to carry it out in several short duration steps as done by our HydroMET group[177,190] providing better particle packing or apply a pulse or alternating current source[184,185].

Table 2.8 Overview of key suspension parameters influencing the EPD film properties [181,183,186]

Parameters	Related effect on EPD process and product
Suspension Preparation Process	
(1) Particle size	(i) the evenness and stability of particle suspension. (ii) the uniformity of the deposition film layer.
(2) Particle concentration in suspension	(i) the deposition gradient. (ii) the uniformity of the deposition film layer.
(3) Type of solvents (*e.g.*, organic polar, nonpolar, or aqueous)	(i) the stable voltage range applied. (ii) the uniformity of the deposition film layer.
(4) The dielectric constant of the liquid	(i) forming possibilities of EPD reaction. (ii) the conductivity of liquid (especially in a pure state). (iii) the electrophoretic mobility.
(5) Conductivity of suspension	(i) the particle motion. (ii) forming possibilities of deposition.
(6) Viscosity of suspension	the dispersion state
(7) Stability of suspension	(i) flocculation of particles. (ii) forming possibilities of deposition.
(8) Zeta potential	(i) stabilization of the suspension by determining the intensity of repulsive interaction between particles. (ii) determining the direction and migration velocity of the particle. (iii) determining the density of the deposit.
Deposition Process	
(9) Deposition time	(i) deposition thickness; (ii) deposition rate.
(10) Conductivity of substrate	(i) deposition rate; (ii) deposition film quality.
(11) Applied electric field (i.e., constant, alternating, pulse voltage/current)	(i) forming possibilities of deposition. (ii) deposition rate. (iii) deposition film quality.

The theoretical basis of the electrophoretic deposition process can be understood by referring to the electrical double layer (EDL) model and DLVO theory.[191] **Figure 2.40** provides a schematic diagram of the EDL as described by Stern following integration of the earlier models of Helmholtz and Gouy-Chapman.[182,192,193]. The electric double layer includes three parts: (a) Surface charge; (b) Stern layer: the layer between the particle surface and the Stern plane, where courter-ions are closely attached to the particle surface; (c) Diffuse layer: the layer of the dispersion medium (solvent) adjacent to the particle (outside of the Stern plane).[182,193]

The interaction among potential determining ions (on the surface of the particle), hydrated counter ions (in the Stern layer), hydrated counter-ion and negative co-ion (in the diffuse layer) determine the relationship between the distance (x) and electric potential (ψ_x), as shown in **Figure**

2.40.[193] The electric potential within the electric double layer has a maximum value on the particle surface (named as the surface potential (ψ_0)).[194] Then, the potential drops with the increase in distance from the surface.[193]

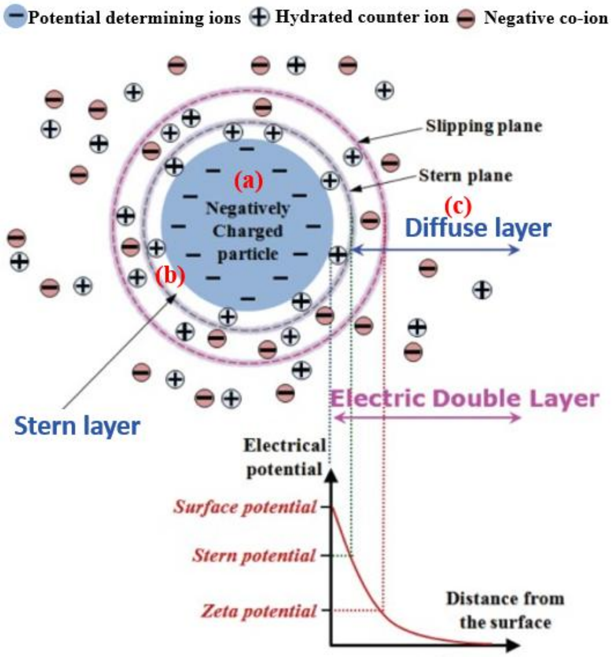

Figure 2.40 Schematic diagram of the electrical double layer model and potential drop with distance. (a) Surface charge, (b) Stern layer, and (c) Diffuse layer of counter-ions. Reproduced with permission.[193] Copyright 2011 Elsevier.

The electric potential (ψ_x) at a different distance from the surface (x) can be described by the Debye-Huckel equation[195]:

$$\psi_x = \psi_0 exp(-\kappa x) \qquad \textbf{(equation 2.32)}$$

where κ is the reciprocal of the EDL thickness otherwise called the Debye–Huckle parameter[196] with the unit of (1/length) or (1/m).

The *Double layer thickness* or *Debye length* $(1/\kappa)$ is the distance at which the potential ψ_x drops to $\frac{1}{e}$ of its value at the Stern plane. The double layer thickness controls the range of the double layer interaction. This thickness can be represented by the equation below:

$$\frac{1}{\kappa} = \left(\frac{\varepsilon\varepsilon_0 kT}{e^2 \sum_i n_i z_i^2}\right)^{\frac{1}{2}} \qquad \textbf{(equation 2.33)}$$

where e is the electronic charge (1.602×10^{-19} C), n_i (mol/L) is the concentration of ions with charge z_i, ε is the dielectric constant of the liquid, and ε_0 is the permittivity of a vacuum (C/V·m).

When a colloidal particle moves in the suspension, a layer of the surrounding liquid remains attached to the particle.[197] As shown in **Figure 2.40**, the boundary of this layer is called the slipping plane. The electric potential at the slipping plane is defined as Zeta potential (ζ).[193,197] Zeta potential gives an indication of the stability of the colloidal suspension. The higher the absolute value of the zeta potential represents the higher stability of the suspension.[194] This is because the Zeta potential is closely related to the electrostatic repulsive force. To be specific, the particles in suspension with a higher absolute value of Zeta potential tend to repel each other and prevent flocculation.[193,197]

Zeta potential is significantly influenced by pH in aqueous media.[198] Zeta potential can be controlled by manipulating a variety of charging agents such as acids, bases and specifically adsorbed ions or polyelectrolytes.[199] Taking negatively charged particle as an example, the addition of alkali results in the increase of negative charge, thereby increasing the absolute value of Zeta potential.[200] In contrast, the addition of acids tends to cause a decrease in the absolute value of Zeta potential. Thus, there is a pH of the suspension at which the net charge or zeta potential is zero, defined as isoelectric point (IEP).[201] A suspension at the IEP is not stable forming aggregates because of the absence of repulsive forces.

The state of stability of a suspension can be explained with the aid of the DLVO theory developed by Derjaguin, Landau and Verwey and Overbeek.[202-204] According to the DLVO theory, the total interparticle potential (V_T) can be determined by the addition of the electrostatic repulsion (V_R) and the van der Waals attraction potential contributions (V_A).[182]

$$V_T = V_R + V_A \qquad \textbf{(equation 2.34)}$$

$$V_R = \frac{\varepsilon a \zeta}{2} ln\{1 + exp(-\kappa D)\} \qquad \textbf{(equation 2.35)}$$

where ε is the dielectric constant of the liquid, a is the radius of the particle, ζ is zeta potential of a particle, κ is the reciprocal of the double layer thickness, and D is the distance of separation between two interacting particles.[182,186]

$$V_A = -\frac{aA_{131}}{2D} f(P) \qquad \textbf{(equation 2.36)}$$

where A_{131} is the Hamaker constant for particles of kind "1", which are separated in a liquid medium "3". The term $f(P)$ is the retardation factor determined by

$$f(P) = \frac{1}{1+1.77P} \text{ for P} \leqslant 0.5 \qquad \textbf{(equation 2.37)}$$

$$f(P) = \frac{2.45}{5P} - \frac{2.17}{15P^2} + \frac{0.59}{P^3} \text{ for P} > 0.5 \qquad \textbf{(equation 2.38)}$$

Figure 2.41 provides a graphical representation of the above interparticle potential distribution for the case of two particles, where the net attraction or repulsion depends on the relative strength of the different types of forces (electrostatic that is repulsive V_R or Van der Waals that is attractive, V_A) that varies with the distance of separation.[182,205,206] At the primary minimum-very short distance, $V_A >> V_R$ favors strong attraction leading to particle aggregation; at a large distance of separation a shallow minimum indicates weak reversible particle attraction; it is at $V_{max,}$ where $V_R >> V_A$ that repulsion forces dominate, and colloidal suspension stability is achieved.[182] Proper regulation of zeta potential or diffuse layer thickness by adjusting the ionic strength or using polymeric additives can promote suspension stability for optimum EPD performance.[205,206]

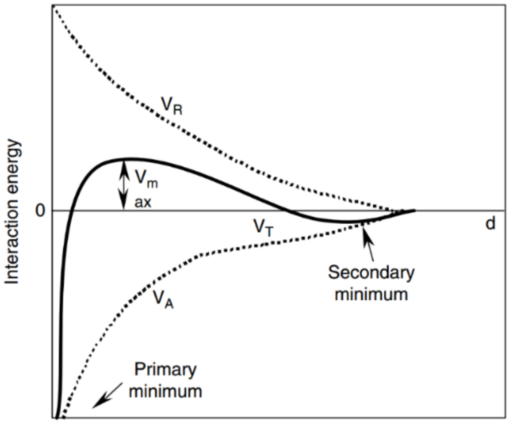

Figure 2.41 The potential energy of inter-particle interaction as a function of the separation distance between particles according to the DLVO theory. Reproduced with permission.[182,205,206] Copyright 2012 Springer.

2.5.2. Application of EPD in Fabricating LIB Electrodes

EPD due to its inherent advantages in building thin films with good characteristics has drawn attention from many researchers over the years in both industry and academic fields.[183,207,208] It has been demonstrated as a key deposition technique for ceramic films, metal coatings, interface modification etc.[183,208]

Among its advantages are deposition uniformity, morphology controllability, and scalability due to it being a simple and, depending on the type of suspension used, economically competitive process.[181,182] Firstly, the good deposition uniformity of EPD films is of importance to modify the interface within composite materials (improving point to area contact).[181,209,210] Secondly, EPD can be used to deposit an ultrathin film on 2D/3D-structure materials according to the requirement of material function or morphology.[181,210] Thirdly, multifunctional components can be assembled via EPD by depositing conductive particles or specific-property particles in various solvents.[210] For instance, graphene, carbon nanotube, carbon nanofiber, and quantum-dots can be deposited on the surface of bulk materials.[175,176] Furthermore, the EPD technique is very versatile and can be applied to the deposition of different types of materials such as Si[211,212], metal oxides (e.g., TiO_2[209] and Fe_3O_4[213]), metal sulphides (e.g., PbS[214]), and metal selenides (e.g., CdSe[215]) for a wide variety of applications from solar cells to catalysts or LIBs.

Recent developments in the EPD technique have demonstrated that high-performing electrodes for LIBs can be designed and to provide superior structural and interfacial properties.[177,181] EPD provides versatility in co-depositing active and conductive components with or without polymeric binders that are characterized by homogeneous composition, mesoporous structure, superior percolation network and good adhesion to the substrate.[176,181]

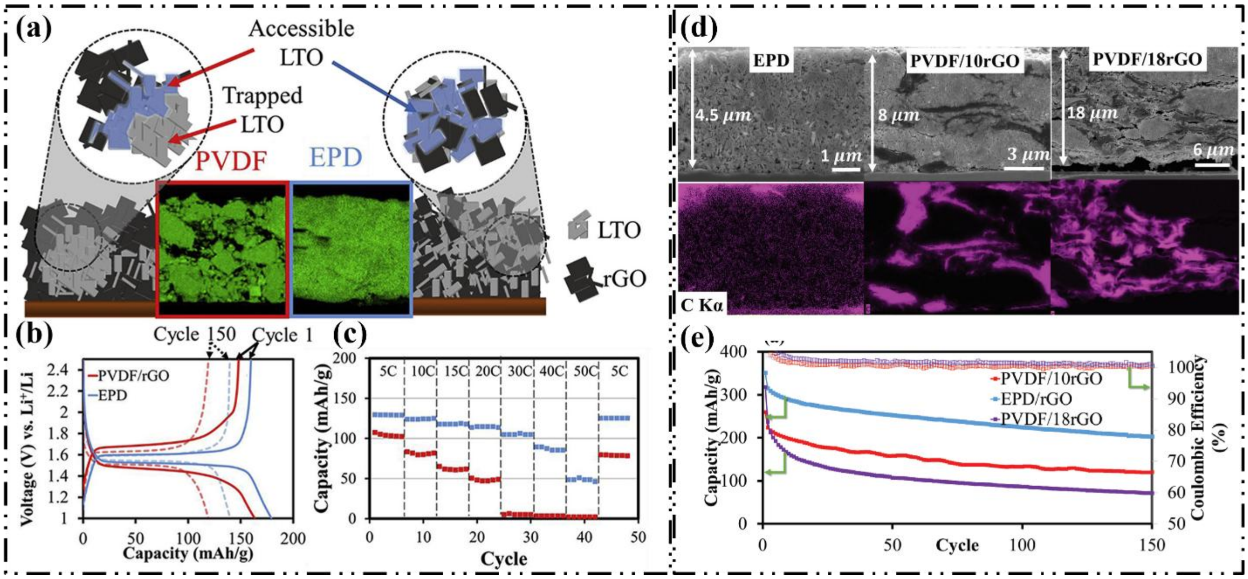

Figure 2.42 Comparison of LTO/rGO PVDF electrode and LTO/rGO EPD electrode: (a) morphology, (b) charge-discharge profile, (c) rate performance. Reproduced with permission.[176] Copyright 2020 Elsevier. Comparison of TNO/rGO EPD electrode, TNO/rGO (10 wt.%) PVDF electrode, TNO/rGO (18 wt.%) PVDF electrode: (d) Morphology and (e) cycling stability at 0.5 C (between 3 V and 0.6 V). Reproduced with permission.[114] Copyright 2020 Elsevier.

Research by our HydroMET group[216] introduced the EPD method to produce lithium-ion battery anodes by co-depositing nanosized TiO_2 and carbon black (Benehkohal, et al[190]), LTO nanoparticles and carbon black assisted via styrene-butadiene rubber (SBR) as an aqueous-soluble binder (Uceda, et al.[177]), and binder-free $Li_4Ti_5O_{12}$/reduced graphene oxide (LTO/rGO) 2D nanosized materials composite (Uceda, et al.[176]). The latter (**Figure 2.42(a,b,c)**) was accomplished through the co-deposition of a precursor, lithium titanate hydrate[145] and graphene oxide, followed by heat treatment in a hydrogen atmosphere, to induce the transformation of precursors to LTO and rGO. In all cases, the EPD-constructed electrodes provided comparable or even superior cycling performance and stability (particularly at high C-rates) compared to the conventionally prepared electrodes. This improved performance was attributed to the high electronic/ionic conductivity of the 3D matrix structure enabled by the synergistic action of rGO and EPD.

To extend this strategy to $TiNb_2O_7$ anode, Uceda, et al.[114] applied EPD electrode engineering to nanoscale assemblies of the $TiNb_2O_7$/reduced graphene oxide (TNO/rGO) electrode. As shown in **Figure 2.42(d, e)** this research proves that EPD can advantageously be employed to construct stable films with good performance characteristics and thus promote innovation on designing and developing TNO anodes (TNO/rGO).

2.6. References

[1] Nobel Prizes in Chemistry 2019, Angewandte Chemie International Edition 58 (2019) 16723-16723. https://doi.org/https://doi.org/10.1002/anie.201912886.

[2] E. Pomerantseva, F. Bonaccorso, X.L. Feng, Y. Cui, Y. Gogotsi, Energy storage: The future enabled by nanomaterials, Science 366 (2019) 969. https://doi.org/10.1126/science.aan8285.

[3] J.B. Goodenough, K.S. Park, The Li-ion rechargeable battery: a perspective, J. Am. Chem. Soc. 135 (2013) 1167-1176. https://doi.org/10.1021/ja3091438.

[4] H. Li, Z. Wang, L. Chen, X. Huang, Research on advanced materials for Li-ion batteries, Adv. Mater. 21 (2009) 4593-4607. https://doi.org/https://doi.org/10.1002/adma.200901710.

[5] B. Dunn, H. Kamath, J.-M. Tarascon, Electrical energy storage for the grid: a battery of choices, Science 334 (2011) 928-935.

[6] M. Li, J. Lu, Z.W. Chen, K. Amine, 30 years of lithium-ion batteries, Adv. Mater. 30 (2018) 1800561. https://doi.org/10.1002/adma.201800561.

[7] J.B. Goodenough, How we made the Li-ion rechargeable battery, Nat. Neurosci. 1 (2018) 204-204. https://doi.org/10.1038/s41928-018-0048-6.

[8] J.B. Goodenough, Y. Kim, Challenges for rechargeable batteries, J. Power Sources 196 (2011) 6688-6694. https://doi.org/https://doi.org/10.1016/j.jpowsour.2010.11.074.

[9] W. Cao, J. Zhang, H. Li, Batteries with high theoretical energy densities, Energy Storage Mater. 26 (2020) 46-55. https://doi.org/https://doi.org/10.1016/j.ensm.2019.12.024.

[10] H. Li, Practical Evaluation of Li-Ion Batteries, Joule 3 (2019) 911-914. https://doi.org/https://doi.org/10.1016/j.joule.2019.03.028.

[11] J. Liu, Z. Bao, Y. Cui, E.J. Dufek, J.B. Goodenough, P. Khalifah, Q. Li, B.Y. Liaw, P. Liu, A. Manthiram, Y.S. Meng, V.R. Subramanian, M.F. Toney, V.V. Viswanathan, M.S. Whittingham, J. Xiao, W. Xu, J. Yang, X.-Q. Yang, J.-G. Zhang, Pathways for practical high-energy long-cycling lithium metal batteries, Nat. Energy 4 (2019) 180-186. https://doi.org/10.1038/s41560-019-0338-x.

[12] K. Mizushima, P.C. Jones, P.J. Wiseman, J.B. Goodenough, $LixCoO_2$ ($0<x\leqslant1$): A new cathode material for batteries of high energy density, Mater. Res. Bull. 15 (1980) 783-789. https://doi.org/https://doi.org/10.1016/0025-5408(80)90012-4.

[13] M.M. Thackeray, W.I.F. David, P.G. Bruce, J.B. Goodenough, Lithium insertion into manganese spinels, Mater. Res. Bull. 18 (1983) 461-472. https://doi.org/https://doi.org/10.1016/0025-5408(83)90138-1.

[14] A.K. Padhi, K.S. Nanjundaswamy, C. Masquelier, J.B. Goodenough, Mapping of transition metal redox energies in phosphates with NASICON structure by lithium intercalation, J. Electrochem. Soc. 144 (1997) 2581. https://doi.org/10.1149/1.1837868.

[15] A.K. Padhi, K.S. Nanjundaswamy, C. Masquelier, S. Okada, J.B. Goodenough, Effect of structure on the Fe^{3+}/Fe^{2+} redox couple in iron phosphates, J. Electrochem. Soc. 144 (1997) 1609. https://doi.org/10.1149/1.1837649.

[16] M. Winter, B. Barnett, K. Xu, Before Li ion batteries, Chem. Rev. 118 (2018) 11433-11456. https://doi.org/10.1021/acs.chemrev.8b00422.

[17] S. Kaushik, T. Mehta, P. Chand, S. Sharma, G. Kumar, Recent advancements in cathode materials for high-performance Li-ion batteries: Progress and prospects, J. Energy Storage 97 (2024) 112818. https://doi.org/https://doi.org/10.1016/j.est.2024.112818.

[18] A. Jain, S.P. Ong, G. Hautier, W. Chen, W.D. Richards, S. Dacek, S. Cholia, D. Gunter, D. Skinner, G. Ceder, K.A. Persson, Commentary: The Materials Project: A materials genome approach to accelerating materials innovation, APL Mater. 1 (2013) 011002. https://doi.org/10.1063/1.4812323.

[19] Y. Huang, The discovery of cathode materials for lithium-ion batteries from the view of interdisciplinarity, Interdisciplinary Materials 1 (2022) 323-329. https://doi.org/https://doi.org/10.1002/idm2.12048.

[20] Z. Sun, J. Zhao, M. Zhu, J. Liu, Critical problems and modification strategies of realizing high-voltage $LiCoO_2$ cathode from electrolyte engineering, Adv. Energy Mater. 14 (2024) 2303498. https://doi.org/https://doi.org/10.1002/aenm.202303498.

[21] M. Bianchini, M. Roca-Ayats, P. Hartmann, T. Brezesinski, J. Janek, There and back again—The journey of $LiNiO_2$ as a cathode active material, Angewandte Chemie International Edition 58 (2019) 10434-10458. https://doi.org/https://doi.org/10.1002/anie.201812472.

[22] L.M. Morgan, M.M. Islam, H. Yang, K. O'Regan, A.N. Patel, A. Ghosh, E. Kendrick, M. Marinescu, G.J. Offer, B.J. Morgan, M.S. Islam, J. Edge, A. Walsh, From Atoms to Cells: Multiscale Modeling of $LiNi_xMn_yCo_zO_2$ Cathodes for Li-Ion Batteries, ACS Energy Lett. 7 (2022) 108-122. https://doi.org/10.1021/acsenergylett.1c02028.

[23] P. He, H. Wang, L. Qi, T. Osaka, Electrochemical characteristics of layered $LiNi_{1/3}Co_{1/3}Mn_{1/3}O_2$ and with different synthesis conditions, J. Power Sources 160 (2006) 627-632. https://doi.org/https://doi.org/10.1016/j.jpowsour.2006.01.053.

[24] L. Liang, G. Hu, F. Jiang, Y. Cao, Electrochemical behaviours of SiO_2-coated $LiNi_{0.8}Co_{0.1}Mn_{0.1}O_2$ cathode materials by a novel modification method, J. Alloy. Compd. 657 (2016) 570-581. https://doi.org/https://doi.org/10.1016/j.jallcom.2015.10.177.

[25] Y. Huang, Y. Dong, S. Li, J. Lee, C. Wang, Z. Zhu, W. Xue, Y. Li, J. Li, Lithium manganese spinel cathodes for lithium-ion batteries, Adv. Energy Mater. 11 (2021) 2000997. https://doi.org/https://doi.org/10.1002/aenm.202000997.

[26] G. Xu, Z. Liu, C. Zhang, G. Cui, L. Chen, Strategies for improving the cyclability and thermo-stability of $LiMn_2O_4$-based batteries at elevated temperatures, J. Mater. Chem. A 3 (2015) 4092-4123. https://doi.org/10.1039/C4TA06264G.

[27] A. Manthiram, An outlook on lithium ion battery technology, ACS Cent. Sci. 3 (2017) 1063-1069. https://doi.org/10.1021/acscentsci.7b00288.

[28] M.-J. Lee, S. Lee, P. Oh, Y. Kim, J. Cho, High performance $LiMn_2O_4$ cathode materials grown with epitaxial layered nanostructure for Li-ion batteries, Nano Lett. 14 (2014) 993-999. https://doi.org/10.1021/nl404430e.

[29] W. Hwang, J. Kim, S.-Y. Kim, E. Ko, S. Lee, M. Kim, S.-H. Yu, Y.-E. Sung, H.-S. Kim, C. Kim, J. Park, Unveiling olivine cathodes for high energy-density lithium-ion batteries: a comprehensive review from the atomic level to the electrode scale, J. Mater. Chem. A 12 (2024) 27800-27824. https://doi.org/10.1039/D4TA02338B.

[30] J. Wang, X. Sun, Understanding and recent development of carbon coating on $LiFePO_4$ cathode materials for lithium-ion batteries, Energy Environ. Sci. 5 (2012) 5163-5185. https://doi.org/10.1039/C1EE01263K.

[31] H. Liu, F.C. Strobridge, O.J. Borkiewicz, K.M. Wiaderek, K.W. Chapman, P.J. Chupas, C.P. Grey, Capturing metastable structures during high-rate cycling of $LiFePO_4$ nanoparticle electrodes, Science 344 (2014) 1252817. https://doi.org/10.1126/science.1252817.

[32] D. Lin, Y. Liu, Y. Cui, Reviving the lithium metal anode for high-energy batteries, Nat. Nanotechnol. 12 (2017) 194-206. https://doi.org/10.1038/nnano.2017.16.

[33] H. Chen, Y. Yang, D.T. Boyle, Y.K. Jeong, R. Xu, L.S. de Vasconcelos, Z. Huang, H. Wang, H. Wang, W. Huang, H. Li, J. Wang, H. Gu, R. Matsumoto, K. Motohashi, Y. Nakayama, K. Zhao, Y. Cui, Free-standing ultrathin lithium metal–graphene oxide host foils with controllable thickness for lithium batteries, Nat. Energy 6 (2021) 790-798. https://doi.org/10.1038/s41560-021-00833-6.

[34] X.-B. Cheng, R. Zhang, C.-Z. Zhao, Q. Zhang, Toward safe lithium metal anode in rechargeable batteries: A review, Chem. Rev. 117 (2017) 10403-10473. https://doi.org/10.1021/acs.chemrev.7b00115.

[35] P.-c. Tsai, W.-D. Hsu, S.-k. Lin, Atomistic structure and Ab initio electrochemical properties of $Li_4Ti_5O_{12}$ defect spinel for Li ion batteries, J. Electrochem. Soc. 161 (2014) A439. https://doi.org/10.1149/2.095403jes.

[36] R. Wang, L. Wang, R. Liu, X. Li, Y. Wu, F. Ran, "Fast-Charging" anode materials for lithium-ion batteries from perspective of ion diffusion in crystal structure, ACS nano 18 (2024) 2611-2648. https://doi.org/10.1021/acsnano.3c08712.

[37] J.Q. Ke, Y.F. Zhang, Z.P. Wen, S. Huang, M.H. Ye, Y.C. Tang, X.Q. Liu, C.C. Li, Designing strategies of advanced electrode materials for high-rate rechargeable batteries, J. Mater. Chem. A 11 (2023) 4428-4457. https://doi.org/10.1039/d2ta09502e.

[38] M. Weiss, R. Ruess, J. Kasnatscheew, Y. Levartovsky, N.R. Levy, P. Minnmann, L. Stolz, T. Waldmann, M. Wohlfahrt-Mehrens, D. Aurbach, M. Winter, Y. Ein-Eli, J. Janek, Fast charging of lithium-ion batteries: A review of materials aspects, Adanced Energy Materials 11 (2021) 2101126. https://doi.org/https://doi.org/10.1002/aenm.202101126.

[39] S. Li, K. Wang, G. Zhang, S. Li, Y. Xu, X. Zhang, X. Zhang, S. Zheng, X. Sun, Y. Ma, Fast charging anode materials for lithium-ion batteries: Current status and perspectives, Adv. Funct. Mater (2022) 2200796. https://doi.org/https://doi.org/10.1002/adfm.202200796.

[40] M.T. McDowell, S.W. Lee, W.D. Nix, Y. Cui, 25th anniversary article: understanding the lithiation of silicon and other alloying anodes for lithium-ion batteries, Adv. Mater. 25 (2013) 4966-4984. https://doi.org/10.1002/adma.201301795.

[41] T. Gao, Y. Han, D. Fraggedakis, S. Das, T. Zhou, C.-N. Yeh, S. Xu, W.C. Chueh, J. Li, M.Z. Bazant, Interplay of lithium intercalation and plating on a single graphite particle, Joule 5 (2021) 393-414. https://doi.org/10.1016/j.joule.2020.12.020.

[42] G.G. Eshetu, H. Zhang, X. Judez, H. Adenusi, M. Armand, S. Passerini, E. Figgemeier, Production of high-energy Li-ion batteries comprising silicon-containing anodes and insertion-type cathodes, Nat. Commun. 12 (2021) 5459. https://doi.org/10.1038/s41467-021-25334-8.

[43] H. Zhang, Y. Yang, H. Xu, L. Wang, X. Lu, X. He, $Li_4Ti_5O_{12}$ spinel anode: Fundamentals and advances in rechargeable batteries, InfoMat 4 (2022) e12228. https://doi.org/https://doi.org/10.1002/inf2.12228.

[44] Y. Yang, J. Zhao, Wadsley–Roth crystallographic shear structure niobium-based oxides: Promising anode materials for high-safety lithium-ion batteries, Adv. Sci. 8 (2021) 2004855. https://doi.org/https://doi.org/10.1002/advs.202004855.

[45] X.H. Liu, J.W. Wang, S. Huang, F.F. Fan, X. Huang, Y. Liu, S. Krylyuk, J. Yoo, S.A. Dayeh, A.V. Davydov, S.X. Mao, S.T. Picraux, S.L. Zhang, J. Li, T. Zhu, J.Y. Huang, In situ atomic-scale imaging of electrochemical lithiation in silicon, Nat. Nanotechnol. 7 (2012) 749-756. https://doi.org/10.1038/nnano.2012.170.

[46] C.-Y. Wang, T. Liu, X.-G. Yang, S. Ge, N.V. Stanley, E.S. Rountree, Y. Leng, B.D. McCarthy, Fast charging of energy-dense lithium-ion batteries, Nature 611 (2022) 485-490. https://doi.org/10.1038/s41586-022-05281-0.

[47] W. Zhang, D.-H. Seo, T. Chen, L. Wu, M. Topsakal, Y. Zhu, D. Lu, G. Ceder, F. Wang, Kinetic pathways of ionic transport in fast-charging lithium titanate, Science 367 (2020) 1030-1034. https://doi.org/10.1126/science.aax3520.

[48] M.M. Thackeray, K. Amine, Li4Ti5O12 spinel anodes, Nat. Energy 6 (2021) 683-683. https://doi.org/10.1038/s41560-021-00829-2.

[49] T. Yuan, Z. Tan, C. Ma, J. Yang, Z.-F. Ma, S. Zheng, Challenges of spinel $Li_4Ti_5O_{12}$ for lithium-ion battery industrial applications, Adv. Energy Mater. 7 (2017) 1601625. https://doi.org/https://doi.org/10.1002/aenm.201601625.

[50] P. Sun, R. Bisschop, H. Niu, X. Huang, A review of battery fires in electric vehicles, Fire Technology 56 (2020) 1361-1410. https://doi.org/10.1007/s10694-019-00944-3.

[51] A. Tomaszewska, Z. Chu, X. Feng, S. O'Kane, X. Liu, J. Chen, C. Ji, E. Endler, R. Li, L. Liu, Y. Li, S. Zheng, S. Vetterlein, M. Gao, J. Du, M. Parkes, M. Ouyang, M. Marinescu, G. Offer, B. Wu, Lithium-ion battery fast charging: A review, eTransportation 1 (2019) 100011. https://doi.org/https://doi.org/10.1016/j.etran.2019.100011.

[52] J. Liu, Z. Chu, H. Li, D. Ren, Y. Zheng, L. Lu, X. Han, M. Ouyang, Lithium-plating-free fast charging of large-format lithium-ion batteries with reference electrodes, International Journal of Energy Research 45 (2021) 7918-7932. https://doi.org/https://doi.org/10.1002/er.6375.

[53] D.P. Finegan, E. Darcy, M. Keyser, B. Tjaden, T.M.M. Heenan, R. Jervis, J.J. Bailey, R. Malik, N.T. Vo, O.V. Magdysyuk, R. Atwood, M. Drakopoulos, M. DiMichiel, A. Rack, G. Hinds, D.J.L. Brett, P.R. Shearing, Characterising thermal runaway within lithium-ion cells by inducing and monitoring internal short circuits, Energy Environ. Sci. 10 (2017) 1377-1388. https://doi.org/10.1039/C7EE00385D.

[54] X.N. Feng, D.S. Ren, X.M. He, M.G. Ouyang, Mitigating thermal runaway of lithium-ion batteries, Joule 4 (2020) 743-770. https://doi.org/10.1016/j.joule.2020.02.010.

[55] J.-C. Daigle, Y. Asakawa, M. Beaupré, V. Gariépy, R. Vieillette, D. Laul, M. Trudeau, K. Zaghib, Boosting ultra-fast charge battery performance: Filling porous nano $Li_4Ti_5O_{12}$

particles with 3D network of N-doped carbons, Sci. Rep. 9 (2019) 16871. https://doi.org/10.1038/s41598-019-53195-1.

[56] H. Wang, R. Qian, Y. Cheng, H.-H. Wu, X. Wu, K. Pan, Q. Zhang, Micro/nanostructured $TiNb_2O_7$-related electrode materials for high-performance electrochemical energy storage: recent advances and future prospects, J. Mater. Chem. A 8 (2020) 18425-18463. https://doi.org/10.1039/D0TA04209A.

[57] J.B. Goodenough, Y. Kim, Challenges for rechargeable Li batteries, Chem. Mater. 22 (2010) 587-603. https://doi.org/10.1021/cm901452z.

[58] A. Wang, S. Kadam, H. Li, S. Shi, Y. Qi, Review on modeling of the anode solid electrolyte interphase (SEI) for lithium-ion batteries, npj Comput. Mater. 4 (2018) 15. https://doi.org/10.1038/s41524-018-0064-0.

[59] T. Yuan, L. Soule, B. Zhao, J. Zou, J. Yang, M. Liu, S. Zheng, Recent advances in titanium niobium oxide anodes for high-power lithium-ion batteries, Energy & Fuels 34 (2020) 13321-13334. https://doi.org/10.1021/acs.energyfuels.0c02732.

[60] Q. Deng, Y. Fu, C. Zhu, Y. Yu, Niobium-based oxides toward advanced electrochemical energy storage: Recent advances and challenges, Small 15 (2019) 1804884. https://doi.org/https://doi.org/10.1002/smll.201804884.

[61] M.J. Sussman, A. Yasin, G.P. Demopoulos, On the complex interplay of crystallinity and surface area effects on Li-ion intercalation and pseudocapacitive storage properties of nanocrystalline anatase, J. Power Sources 272 (2014) 58-67. https://doi.org/https://doi.org/10.1016/j.jpowsour.2014.08.050.

[62] H.-c. Chiu, N. Brodusch, R. Gauvin, A. Guerfi, K. Zaghib, G.P. Demopoulos, Aqueous synthesized nanostructured $Li_4Ti_5O_{12}$ for high-performance lithium Ion battery anodes, J. Electrochem. Soc. 160 (2013) A3041-A3047. https://doi.org/10.1149/2.008305jes.

[63] Y. Liu, Y. Yang, Recent progress of TiO_2-based anodes for Li ion batteries, Journal of Nanomaterials 2016 (2016) 8123652. https://doi.org/https://doi.org/10.1155/2016/8123652.

[64] G.-N. Zhu, Y.-G. Wang, Y.-Y. Xia, Ti-based compounds as anode materials for Li-ion batteries, Energy Environ. Sci. 5 (2012) 6652-6667.

[65] M. Wagemaker, W.J.H. Borghols, F.M. Mulder, Large Impact of Particle Size on Insertion Reactions. A Case for Anatase LixTiO2, J. Am. Chem. Soc. 129 (2007) 4323-4327. https://doi.org/10.1021/ja067733p.

[66] H.-Y. Wang, H.-Y. Chen, Y.-Y. Hsu, U. Stimming, H.M. Chen, B. Liu, Modulation of crystal surface and lattice by doping: Achieving ultrafast metal-ion insertion in Anatase TiO_2, ACS Appl. Mater. Interfaces 8 (2016) 29186-29193. https://doi.org/10.1021/acsami.6b11185.

[67] M. Lübke, J. Shin, P. Marchand, D. Brett, P. Shearing, Z. Liu, J.A. Darr, Highly pseudocapacitive Nb-doped TiO_2 high power anodes for lithium-ion batteries, J. Mater. Chem. A 3 (2015) 22908-22914.

[68] B.K. Guo, X.Q. Yu, X.G. Sun, M.F. Chi, Z.A. Qiao, J. Liu, Y.S. Hu, X.Q. Yang, J.B. Goodenough, S. Dai, A long-life lithium-ion battery with a highly porous $TiNb_2O_7$ anode for large-scale electrical energy storage, Energy Environ. Sci. 7 (2014) 2220-2226. https://doi.org/10.1039/c4ee00508b.

[69] N. Nitta, F. Wu, J.T. Lee, G. Yushin, Li-ion battery materials: present and future, Mater. Today 18 (2015) 252-264. https://doi.org/https://doi.org/10.1016/j.mattod.2014.10.040.

[70] B. Scrosati, J. Garche, Lithium batteries: Status, prospects and future, J. Power Sources 195 (2010) 2419-2430. https://doi.org/https://doi.org/10.1016/j.jpowsour.2009.11.048.

[71] G. Zhao, L. Zhang, C. Li, H. Huang, X. Sun, K. Sun, A practical Li ion battery anode material with high gravimetric/volumetric capacities based on T-Nb_2O_5/graphite composite, Chem. Eng. J. 328 (2017) 844-852. https://doi.org/https://doi.org/10.1016/j.cej.2017.07.111.

[72] P. Barnes, Y. Zuo, K. Dixon, D. Hou, S. Lee, Z. Ma, J.G. Connell, H. Zhou, C. Deng, K. Smith, E. Gabriel, Y. Liu, O.O. Maryon, P.H. Davis, H. Zhu, Y. Du, J. Qi, Z. Zhu, C. Chen, Z. Zhu, Y. Zhou, P.J. Simmonds, A.E. Briggs, D. Schwartz, S.P. Ong, H. Xiong, Electrochemically induced amorphous-to-rock-salt phase transformation in niobium oxide electrode for Li-ion batteries, Nat. Mater. (2022) https://doi.org/10.1038/s41563-022-01242-0.

[73] M. Yang, S. Li, J. Huang, Three-dimensional cross-linked Nb_2O_5 polymorphs derived from cellulose substances: insights into the mechanisms of lithium storage, ACS Appl. Mater. Interfaces (2021) 39501-39512. https://doi.org/10.1021/acsami.1c11720.

[74] L. Hu, L.J. Luo, L.F. Tang, C.F. Lin, R.J. Li, Y.J. Chen, $Ti_2Nb_{2x}O_{4+5x}$ anode materials for lithium-ion batteries: a comprehensive review, J. Mater. Chem. A 6 (2018) 9799-9815. https://doi.org/10.1039/c8ta00895g.

[75] K.J. Griffith, I.D. Seymour, M.A. Hope, M.M. Butala, L.K. Lamontagne, M.B. Preefer, C.P. Koçer, G. Henkelman, A.J. Morris, M.J. Cliffe, S.E. Dutton, C.P. Grey, Ionic and electronic conduction in $TiNb_2O_7$, J. Am. Chem. Soc. 141 (2019) 16706-16725. https://doi.org/10.1021/jacs.9b06669.

[76] J.L. Gao, X.Q. Cheng, S.F. Lou, Y.L. Ma, P.J. Zuo, C.Y. Du, Y.Z. Gao, G.P. Yin, Self-doping $Ti_{1-x}Nb_{2-x}O_7$ anode material for lithium-ion battery and its electrochemical performance, J. Alloy. Compd. 728 (2017) 534-540. https://doi.org/10.1016/j.jallcom.2017.09.045.

[77] Q.L. Wu, Y.H. Kang, G.H. Chen, J.K. Chen, M.H. Chen, W. Li, Z.H. Lv, H.Y. Yang, P.X. Lin, Y. Qiao, J.B. Zhao, Y. Yang, Ultrafast carbothermal shock synthesis of Wadsley-Roth phase niobium-based oxides for fast-charging lithium-ion batteries, Adv. Funct. Mater (2024) 2315248. https://doi.org/10.1002/adfm.202315248.

[78] D. Pham-Cong, J. Kim, V.T. Tran, S.J. Kim, S.-Y. Jeong, J.-H. Choi, C.R. Cho, Electrochemical behavior of interconnected $Ti_2Nb_{10}O_{29}$ nanoparticles for high-power Li-ion battery anodes, Electrochim. Acta 236 (2017) 451-459. https://doi.org/https://doi.org/10.1016/j.electacta.2017.03.203.

[79] T. Jiang, S. Ma, J. Deng, T. Yuan, C. Lin, M. Liu, Partially reduced titanium niobium oxide: A high-performance lithium-storage material in a broad temperature range, Adv. Sci. 9 (2022) 2105119. https://doi.org/https://doi.org/10.1002/advs.202105119.

[80] H. Yu, X. Cheng, H. Zhu, R. Zheng, T. Liu, J. Zhang, M. Shui, Y. Xie, J. Shu, Deep insights into kinetics and structural evolution of nitrogen-doped carbon coated $TiNb_{24}O_{62}$ nanowires as high-performance lithium container, Nano Energy 54 (2018) 227-237. https://doi.org/https://doi.org/10.1016/j.nanoen.2018.10.025.

[81] V. Augustyn, J. Come, M.A. Lowe, J.W. Kim, P.-L. Taberna, S.H. Tolbert, H.D. Abruña, P. Simon, B. Dunn, High-rate electrochemical energy storage through Li^+ intercalation pseudocapacitance, Nat. Mater. 12 (2013) 518-522. https://doi.org/10.1038/nmat3601.

[82] Y. Zhao, X. Zhou, L. Ye, S. Chi Edman Tsang, Nanostructured Nb2O5 catalysts, Nano Reviews 3 (2012) 17631. https://doi.org/10.3402/nano.v3i0.17631.

[83] R.S. Roth, L.W. Coughanour, Phase equilibrium relations in the systems titania-niobia and zirconia-niobia, Journal of Research of the National Bureau of Standards 55 (1955) 209.

[84] A.D. Wadsley, Mixed oxides of titanium and niobium. II. The crystal structures of the dimorphic forms $Ti_2Nb_{10}O_{29}$, Acta Crystallographica 14 (1961) 664-670. https://doi.org/https://doi.org/10.1107/S0365110X6100200X.

[85] S. Andersson, J. Galy, Wadsley defects and crystallographic shear in hexagonally close-packed structures, J. Solid State Chem. 1 (1970) 576-582. https://doi.org/https://doi.org/10.1016/0022-4596(70)90144-1.

[86] A.t. Wadsley, S. Andersson, Crystallographic shear, and the niobium oxides and oxide fluorides in the composition region MXx, 2.4< x< 2.7, Perspectives in structural chemistry 3 (1970) 1-58.

[87] R.J. Cava, D.W. Murphy, S.M. Zahurak, Lithium insertion in Wadsley‐Roth phases based on niobium oxide, J. Electrochem. Soc. 130 (1983) 2345. https://doi.org/10.1149/1.2119583.

[88] K.J. Griffith, A.C. Forse, J.M. Griffin, C.P. Grey, High-rate intercalation without nanostructuring in metastable Nb_2O_5 bronze phases, J. Am. Chem. Soc. 138 (2016) 8888-8899.

[89] M. Catti, M.R. Ghaani, On the lithiation reaction of niobium oxide: structural and electronic properties of $Li_{1.714}Nb_2O_5$, Phys. Chem. Chem. Phys. 16 (2014) 1385-1392.

[90] K.J. Griffith, Y. Harada, S. Egusa, R.M. Ribas, R.S. Monteiro, R.B. Von Dreele, A.K. Cheetham, R.J. Cava, C.P. Grey, J.B. Goodenough, Titanium niobium oxide: from discovery to application in fast-charging lithium-ion batteries, Chem. Mater. 33 (2021) 4-18. https://doi.org/10.1021/acs.chemmater.0c02955.

[91] J. Han, Y. Huang, J.B. Goodenough, New anode framework for rechargeable lithium batteries, Chem. Mater. 23 (2011) 2027-2029. https://doi.org/dx.doi.org/10.1021/cm200441h.

[92] J.-T. Han, J.B. Goodenough, 3-V full cell performance of anode framework $TiNb_2O_7$/spinel $LiNi_{0.5}Mn_{1.5}O_4$, Chem. Mater. 23 (2011) 3404-3407. https://doi.org/10.1021/cm201515g.

[93] N. Takami, H. Inagaki, Y. Tatebayashi, H. Saruwatari, K. Honda, S. Egusa, High-power and long-life lithium-ion batteries using lithium titanium oxide anode for automotive and stationary power applications, J. Power Sources 244 (2013) 469-475. https://doi.org/https://doi.org/10.1016/j.jpowsour.2012.11.055.

[94] N. Takami, K. Ise, Y. Harada, T. Iwasaki, T. Kishi, K. Hoshina, High-energy, fast-charging, long-life lithium-ion batteries using $TiNb_2O_7$ anodes for automotive applications, J. Power Sources 396 (2018) 429-436. https://doi.org/10.1016/j.jpowsour.2018.06.059.

[95] K. Ise, S. Morimoto, Y. Harada, N. Takami, Large lithium storage in highly crystalline $TiNb_2O_7$ nanoparticles synthesized by a hydrothermal method as anodes for lithium-ion batteries, Solid State Ion. 320 (2018) 7-15. https://doi.org/10.1016/j.ssi.2018.02.027.

[96] N. Takami, H. Inagaki, T. Kishi, Y. Harada, Y. Fujita, K. Hoshina, Electrochemical kinetics and safety of 2-volt class Li-ion battery system using lithium titanium oxide anode, J. Electrochem. Soc. 156 (2009) A128. https://doi.org/10.1149/1.3043441.

[97] N. Takami, A. Satoh, M. Hara, T. Ohsaki, Structural and kinetic characterization of lithium intercalation into carbon anodes for secondary lithium batteries, J. Electrochem. Soc. 142 (1995) 371-379. https://doi.org/10.1149/1.2044017.

[98] H. Li, L. Shen, G. Pang, S. Fang, H. Luo, K. Yang, X. Zhang, $TiNb_2O_7$ nanoparticles assembled into hierarchical microspheres as high-rate capability and long-cycle-life anode materials for lithium ion batteries, Nanoscale 7 (2015) 619-624. https://doi.org/10.1039/C4NR04847D.

[99] H. Yu, H. Lan, L. Yan, S. Qian, X. Cheng, H. Zhu, N. Long, M. Shui, J. Shu, $TiNb_2O_7$ hollow nanofiber anode with superior electrochemical performance in rechargeable lithium ion

batteries, Nano Energy 38 (2017) 109-117. https://doi.org/https://doi.org/10.1016/j.nanoen.2017.05.057.

[100] W. Xing, L.-E. Kalland, Z. Li, R. Haugsrud, Defects and transport properties in $TiNb_2O_7$, Journal of the American Ceramic Society 96 (2013) 3775-3781. https://doi.org/https://doi.org/10.1111/jace.12558.

[101] W. Liu, J. Liu, M. Zhu, W. Wang, Y. Sun, Closely compacted $TiNb_2O_7$-C assembly for fast-charging battery anodes, ACS Appl. Energy Mater. 4 (2021) 12319-12325. https://doi.org/10.1021/acsaem.1c02144.

[102] C. Yang, D. Ma, J. Yang, M. Manawan, T. Zhao, Y. Feng, J. Li, Z. Liu, Y.-W. Zhang, R.B. Von Dreele, B.H. Toby, C.P.d.L. Albarrán, J.H. Pan, Crystallographic insight of reduced lattice volume expansion in mesoporous Cu^{2+}-doped $TiNb_2O_7$ microspheres during Li^+ insertion, Adv. Funct. Mater 33 (2023) 2212854. https://doi.org/https://doi.org/10.1002/adfm.202212854.

[103] S. Gong, Y. Wang, Q. Zhu, M. Li, Y. Wen, H. Wang, J. Qiu, B. Xu, High-rate lithium storage performance of $TiNb_2O_7$ anode due to single-crystal structure coupling with Cr^{3+}-doping, J. Power Sources 564 (2023) 232672. https://doi.org/https://doi.org/10.1016/j.jpowsour.2023.232672.

[104] K. Tian, Z. Wang, H. Di, H. Wang, Z. Zhang, S. Zhang, R. Wang, L. Zhang, C. Wang, L. Yin, Superimposed effect of La doping and structural engineering to achieve oxygen-deficient $TiNb_2O_7$ for ultrafast Li-ion storage, ACS Appl. Mater. Interfaces 14 (2022) 10478-10488. https://doi.org/10.1021/acsami.1c24909.

[105] M. Yu, Z.F. Cai, Q. Li, S. Wang, Y.Z. Ma, G.S. Song, W.D. Yang, C. Wen, Enhanced energy storage performance of Zr-doped $TiNb_2O_7$ nanospheres prepared by the hydrolytic method, ACS Sustain. Chem. Eng. 11 (2023) 5147-5154. https://doi.org/10.1021/acssuschemeng.2c07144.

[106] C. Lin, S. Yu, S. Wu, S. Lin, Z.-Z. Zhu, J. Li, L. Lu, $Ru_{0.01}Ti_{0.99}Nb_2O_7$ as an intercalation-type anode material with a large capacity and high rate performance for lithium-ion batteries, J. Mater. Chem. A 3 (2015) 8627-8635. https://doi.org/https://doi.org/10.1039/C5TA01073J.

[107] A. Shi, Y. Zhang, S. Geng, X. Song, G. Yin, S. Lou, L. Tan, Highly oxidized state dopant induced Nb-O bond distortion of $TiNb_2O_7$ for extremely fast-charging batteries, Nano Energy (2024) 109349. https://doi.org/https://doi.org/10.1016/j.nanoen.2024.109349.

[108] Y. Zhang, C. Kang, W. Zhao, B. Sun, X. Xiao, H. Huo, Y. Ma, P. Zuo, S. Lou, G. Yin, Crystallographic engineering to reduce diffusion barrier for enhanced intercalation pseudocapacitance of $TiNb_2O_7$ in fast-charging batteries, Energy Storage Mater. 47 (2022) 178-186. https://doi.org/https://doi.org/10.1016/j.ensm.2022.01.061.

[109] L.J. Zhao, S.T. Wang, Y.H. Dong, W. Quan, F. Han, Y.M. Huang, Y.T. Li, X.H. Liu, M. Li, Z.T. Zhang, J.Y. Zhang, Z.L. Tang, J. Li, Coarse-grained reduced $Mo_xTi_{1-x}Nb_2O_{7+y}$ anodes for high-rate lithium-ion batteries, Energy Storage Mater. 34 (2021) 574-581. https://doi.org/10.1016/j.ensm.2020.10.016.

[110] H. Song, Y.-T. Kim, A Mo-doped $TiNb_2O_7$ anode for lithium-ion batteries with high rate capability due to charge redistribution, Chem. Commun. 51 (2015) 9849-9852. https://doi.org/10.1039/C5CC02221E.

[111] C. Lei, X. Qin, S. Huang, T. Wei, Y. Zhang, Mo-doped $TiNb_2O_7$ microspheres as improved anode materials for lithium-ion batteries, ChemElectroChem 8 (2021) 3379-3383. https://doi.org/https://doi.org/10.1002/celc.202101056.

[112] Y.-S. Hsiao, C.-W. Chang-Jian, H. Chu Weng, H.-H. Chiang, C.-Z. Lu, W. Kong Pang, V.K. Peterson, X.-C. Jiang, P.-I. Wu, C.-P. Chen, J.-H. Huang, Doping with W^{6+} ions enhances the performance of $TiNb_2O_7$ as an anode material for lithium-ion batteries, Appl. Surf. Sci. 573 (2022) 151517. https://doi.org/https://doi.org/10.1016/j.apsusc.2021.151517.

[113] R.M. Tao, T.Y. Zhang, X.G. Sun, C.L. Do-Thanh, S. Dai, Ionothermally synthesized nanoporous $Ti_{0.95}W_{0.05}Nb_2O_7$: a novel anode material for high-performance lithium-ion batteries, Batteries & Supercaps 6 (2023) e202300101. https://doi.org/10.1002/batt.202300101.

[114] M. Uceda, H.-C. Chiu, J. Zhou, R. Gauvin, K. Zaghib, G.P. Demopoulos, Nanoscale assembling of graphene oxide with electrophoretic deposition leads to superior percolation network in Li-ion electrodes: $TiNb_2O_7$/rGO composite anodes, Nanoscale 12 (2020) 23092–23104. https://doi.org/https://doi.org/10.1039/D0NR06082H.

[115] M.L. Qi, D.L. Chao, W.F. Sun, J.H. Yin, M.H. Chen, Three-dimensional TiNb2O7 anchored on carbon nanofiber core-shell arrays as an anode for high-rate lithium ion storage, RSC Adv. 10 (2020) 6342-6350. https://doi.org/10.1039/c9ra10485b.

[116] Y.L. Sheng, X.Y. Yue, W. Hao, Y.T. Dong, Y.K. Liu, Z. Liang, Balancing the ion/electron transport of graphite anodes by a La-doped $TiNb_2O_7$ functional coating for fast-charging Li-ion batteries, Nano Lett. 24 (2024) 3694-3701. https://doi.org/10.1021/acs.nanolett.3c05151.

[117] J.J. Li, S.S. Pan, C.X. Xing, L.Q. Guo, Z.Y. Zhou, H.T. Zhang, Boosting the energy density of a flexible $TiNb_2O_7$@CNF-based lithium-ion supercapacitor with an ionogel separator, Ionics 26 (2020) 5715-5723. https://doi.org/10.1007/s11581-020-03717-7.

[118] L.Q. Cheng, X.Y. Xie, K. Chen, Y.J. He, H. Xu, R.P. Liu, M. Feng, Enhancing the electrochemical properties of $TiNb_2O_7$ anodes with SP-CNT binary conductive agents for both liquid and solid state lithium ion batteries, RSC Adv. 14 (2024) 15722-15729. https://doi.org/10.1039/d4ra02216e.

[119] A. Jongejan, A.L. Wilkins, A re-examination of the system Nb_2O_5-TiO_2 at liquidus temperatures, Journal of the Less Common Metals 19 (1969) 185-191. https://doi.org/https://doi.org/10.1016/0022-5088(69)90094-0.

[120] C.Q. Liu, P.D. Luo, Y. Feng, W.P. Gong, F. Zhang, Phase equilibria in the TiO_2-Nb_2O_5 system: New experiments and thermodynamic modeling, Ceram. Int. 49 (2023) 30471-30480. https://doi.org/10.1016/j.ceramint.2023.06.311.

[121] H. Aghamohammadi, R. Eslami-Farsani, Effects of calcination parameters on the purity, morphology, and electrochemical properties of the synthesized TiNb2O7 by the solvothermal method as anode materials for Li-ion batteries, J. Electroanal. Chem. 917 (2022) 116394. https://doi.org/https://doi.org/10.1016/j.jelechem.2022.116394.

[122] Z. Zhao, Z. Xue, Q. Xiong, Y. Zhang, X. Hu, H. Chi, H. Qin, Y. Yuan, H. Ni, Titanium niobium oxides ($TiNb_2O_7$): Design, fabrication and application in energy storage devices, Sustainable Materials and Technologies 30 (2021) e00357. https://doi.org/https://doi.org/10.1016/j.susmat.2021.e00357.

[123] J. Lee, J. Yang, S.G. Kwon, T. Hyeon, Nonclassical nucleation and growth of inorganic nanoparticles, Nat. Rev. Mater. 1 (2016) 16034. https://doi.org/10.1038/natrevmats.2016.34.

[124] N.T.K. Thanh, N. Maclean, S. Mahiddine, Mechanisms of nucleation and growth of nanoparticles in solution, Chem. Rev. 114 (2014) 7610-7630. https://doi.org/10.1021/cr400544s.

[125] S.H. Yu, Hydrothermal/solvothermal processing of advanced ceramic materials, Journal of the Ceramic Society of Japan 109 (2001) S65-S75. https://doi.org/10.2109/jcersj.109.1269_S65.

[126] G. Demazeau, Solvothermal and hydrothermal processes: the main physico-chemical factors involved and new trends, Research on Chemical Intermediates 37 (2011) 107-123. https://doi.org/10.1007/s11164-011-0240-z.

[127] K. Liu, J.A. Wang, J. Yang, D.Q. Zhao, P.Y. Chen, J.Z. Man, X.Y. Yu, Z.Q. Wen, J.C. Sun, Interstitial and substitutional V^{5+}-doped $TiNb_2O_7$ microspheres: A novel doping way to achieve high-performance electrodes, Chem. Eng. J. 407 (2021) 127190. https://doi.org/10.1016/j.cej.2020.127190.

[128] H. Aghamohammadi, N. Hassanzadeh, R. Eslami-Farsani, A review study on titanium niobium oxide-based composite anodes for Li-ion batteries: Synthesis, structure, and performance, Ceram. Int. 47 (2021) 26598-26619. https://doi.org/https://doi.org/10.1016/j.ceramint.2021.06.127.

[129] A.A. Voskanyan, M. Abramchuk, A. Navrotsky, Entropy stabilization of TiO_2-Nb_2O_5 Wadsley-Roth shear phases and their prospects for lithium ion battery anode materials, Chem. Mater. 32 (2020) 5301-5308. https://doi.org/https://dx.doi.org/10.1021/acs.chemmater.0c01553.

[130] L.T. Yan, X.H. Rui, G. Chen, W.C. Xu, G.F. Zou, H.M. Luo, Recent advances in nanostructured Nb-based oxides for electrochemical energy storage, Nanoscale 8 (2016) 8443-8465. https://doi.org/10.1039/c6nr01340f.

[131] H.C. Chiu, N. Brodusch, R. Gauvin, A. Guerfi, K. Zaghib, G.P. Demopoulos, Aqueous synthesized nanostructured $Li_4Ti_5O_{12}$ for high-performance lithium ion battery anodes, J. Electrochem. Soc. 160 (2013) A3041-A3047. https://doi.org/10.1149/2.008305jes.

[132] S. Ahmed, P.A. Nelson, K.G. Gallagher, N. Susarla, D.W. Dees, Cost and energy demand of producing nickel manganese cobalt cathode material for lithium ion batteries, J. Power Sources 342 (2017) 733-740. https://doi.org/https://doi.org/10.1016/j.jpowsour.2016.12.069.

[133] M.K. Devaraju, I. Honma, Hydrothermal and solvothermal process towards development of $LiMPO_4$ (M = Fe, Mn) nanomaterials for lithium-ion batteries, Adv. Energy Mater. 2 (2012) 284-297. https://doi.org/10.1002/aenm.201100642.

[134] M. Liu, H.C. Dong, S. Zhang, X. Chen, Y.P. Sun, S. Gao, J.Q. Xu, X.D. Wu, A.B. Yuan, W. Lu, Three-dimensional porous $TiNb_2O_7$/CNT-KB composite microspheres as lithium-ion battery anode material, ChemElectroChem 6 (2019) 3959-3965. https://doi.org/10.1002/celc.201901024.

[135] G. Liu, L. Zhao, R. Sun, W. Chen, M. Hu, M. Liu, X. Duan, T. Zhang, Mesoporous $TiNb_2O_7$ microspheres as high performance anode materials for lithium-ion batteries with high-rate capability and long cycle-life, Electrochim. Acta 259 (2018) 20-27. https://doi.org/https://doi.org/10.1016/j.electacta.2017.10.138.

[136] A.G. Ashish, P. Arunkumar, B. Babu, P. Manikandan, S. Sarang, M.M. Shaijumon, $TiNb_2O_7$/Graphene hybrid material as high performance anode for lithium-ion batteries, Electrochim. Acta 176 (2015) 285-292. https://doi.org/https://doi.org/10.1016/j.electacta.2015.06.122.

[137] H. Park, H.B. Wu, T. Song, X.W. Lou, U. Paik, Porosity-controlled $TiNb_2O_7$ microspheres with partial nitridation as a practical negative electrode for high-power lithium-ion batteries, Adv. Energy Mater. 5 (2015) 1401945. https://doi.org/10.1002/aenm.201401945.

[138] Q.S. Cheng, J.W. Liang, N. Lin, C. Guo, Y.C. Zhu, Y.T. Qian, Porous $TiNb_2O_7$ nanospheres as ultra long-life and high-power anodes for lithium-ion batteries, Electrochim. Acta 176 (2015) 456-462. https://doi.org/10.1016/j.electacta.2015.07.038.

[139] J. Luo, J. Peng, P. Zeng, Z.Y. Wu, J.Y. Li, W.W. Li, Y.H. Huang, B.B. Chang, X.Y. Wang, $TiNb_2O_7$ nano-particle decorated carbon cloth as flexible self-support anode material in lithium-ion batteries, Electrochim. Acta 332 (2020) 135469. https://doi.org/10.1016/j.electacta.2019.135469.

[140] A. Yasin, F. Guo, G.P. Demopoulos, Continuous-reactor, pH-controlled synthesis of multifunctional mesoporous nanocrystalline anatase aggregates, Chem. Eng. J. 287 (2016) 398-409. https://doi.org/https://doi.org/10.1016/j.cej.2015.11.045.

[141] H. Wei, X. Lu, H.-C. Chiu, B. Wei, R. Gauvin, Z. Arthur, V. Emond, D.-T. Jiang, K. Zaghib, G.P. Demopoulos, Ethylenediamine-enabled sustainable synthesis of mesoporous nanostructured $Li_2FeIISiO_4$ particles from Fe(III) aqueous solution for Li-ion battery application, ACS Sustain. Chem. Eng. 6 (2018) 7458-7467. https://doi.org/10.1021/acssuschemeng.8b00090.

[142] Y. Zeng, H.-C. Chiu, M. Rasool, N. Brodusch, R. Gauvin, D.-T. Jiang, D.H. Ryan, K. Zaghib, G.P. Demopoulos, Hydrothermal crystallization of $Pmn2_1$ Li_2FeSiO_4 hollow mesocrystals for Li-ion cathode application, Chem. Eng. J. 359 (2019) 1592-1602. https://doi.org/https://doi.org/10.1016/j.cej.2018.11.013.

[143] A.W. Bayeh, D.M. Kabtamu, Y.C. Chang, G.C. Chen, H.Y. Chen, G.Y. Lin, T.R. Liu, T.H. Wondimu, K.C. Wang, C.H. Wang, Synergistic effects of a $TiNb_2O_7$-reduced graphene oxide nanocomposite electrocatalyst for highperformance all- vanadium redox flow batteries, J. Mater. Chem. A 6 (2018) 13908-13917. https://doi.org/10.1039/c8ta03408g.

[144] K. Byrappa, M. Yoshimura, Hydrothermal technology—principles and applications, in: K. Byrappa, M. Yoshimura (Eds.), Handbook of Hydrothermal Technology, William Andrew Publishing, Norwich, NY, 2001, pp. 1-52.

[145] H.-C. Chiu, X. Lu, S. Elouatik, K. Zaghib, G.P. Demopoulos, Formation of lithium titanate hydrate nanosheets: insight into a two-dimension growth mechanism by in situ Raman, Crystal Growth & Design 16 (2016) 3898-3904. https://doi.org/10.1021/acs.cgd.6b00470.

[146] H.-C. Chiu, X. Lu, J. Zhou, L. Gu, J. Reid, R. Gauvin, K. Zaghib, G.P. Demopoulos, Annealing-regulated elimination of residual strain-induced structural relaxation for stable high-power $Li_4Ti_5O_{12}$ nanosheet anodes, Nano Energy 32 (2017) 533-541. https://doi.org/https://doi.org/10.1016/j.nanoen.2016.12.063.

[147] S.H. Shen, S.J. Deng, Y. Zhong, J.B. Wu, X.L. Wang, X.H. Xia, J.P. Tu, Binder-free carbon fiber/$TiNb_2O_7$ composite electrode as superior high-rate anode for lithium ions batteries, Chinese Chem. Lett. 28 (2017) 2219-2222. https://doi.org/10.1016/j.cclet.2017.11.031.

[148] L. Hu, C. Lin, C. Wang, C. Yang, J. Li, Y. Chen, S. Lin, $TiNb_2O_7$ nanorods as a novel anode material for secondary lithium-ion batteries, Functional Materials Letters 09 (2016) 1642004. https://doi.org/10.1142/s1793604716420042.

[149] A.R. Rahmani, M. Khodaei, Hard and soft templating approaches in evaporative sol-gel synthesis of $TiNb_2O_7$ nanostructures as active materials for Li-ion batteries, Journal of Sol-Gel Science and Technology 111 (2024) 475-485. https://doi.org/10.1007/s10971-024-06470-1.

[150] G.P. Demopoulos, Aqueous precipitation and crystallization for the production of particulate solids with desired properties, Hydrometallurgy 96 (2009) 199-214. https://doi.org/https://doi.org/10.1016/j.hydromet.2008.10.004.

[151] V. Pimenta, M. Sathiya, D. Batuk, A.M. Abakumov, D. Giaume, S. Cassaignon, D. Larcher, J.-M. Tarascon, Synthesis of Li-rich NMC: a comprehensive study, Chem. Mater. 29 (2017) 9923-9936. https://doi.org/10.1021/acs.chemmater.7b03230.

[152] W. Li, E.M. Erickson, A. Manthiram, High-nickel layered oxide cathodes for lithium-based automotive batteries, Nat. Energy 5 (2020) 26-34. https://doi.org/10.1038/s41560-019-0513-0.

[153] V. Paulraj, T. Saha, K. Vediappan, K. Kamala Bharathi, Synthesis and electrochemical properties of $TiNb_2O_7$ nanoparticles as an anode material for lithium ion batteries, Mater. Lett. 304 (2021) 130681. https://doi.org/https://doi.org/10.1016/j.matlet.2021.130681.

[154] H.W. Bian, J.J. Gu, Z.C. Song, H.X. Gong, Z.X. Zhang, W.T. Mao, K.Y. Bao, An effective strategy to achieve high-power electrode by tin doping: $Sn_xTiNb_2O_7$ as a promising anode material with a large capacity and high-rate performance for lithium-ion batteries, Journal of Materials Science-Materials In Electronics 34 (2023) 1826. https://doi.org/10.1007/s10854-023-11183-2.

[155] P. He, H. Wang, L. Qi, T. Osaka, Synthetic optimization of spherical LiCoO2 and precursor via uniform-phase precipitation, J. Power Sources 158 (2006) 529-534. https://doi.org/https://doi.org/10.1016/j.jpowsour.2005.08.044.

[156] N. Zhang, J. Li, H. Li, A. Liu, Q. Huang, L. Ma, Y. Li, J.R. Dahn, Structural, Electrochemical, and Thermal Properties of Nickel-Rich LiNixMnyCozO2 Materials, Chem. Mater. 30 (2018) 8852-8860. https://doi.org/10.1021/acs.chemmater.8b03827.

[157] D.O. Shah, Fine Particles: Synthesis, Characterization, and Mechanisms of Growth. Edited by T. Sugimoto, Surfactant Science Series, Vol. 92, J. Nanopart. Res. 4 (2002) 179-179. https://doi.org/10.1023/A:1020110320804.

[158] J.-P. Jolivet, S. Cassaignon, C. Chanéac, D. Chiche, E. Tronc, Design of oxide nanoparticles by aqueous chemistry, Journal of Sol-Gel Science and Technology 46 (2008) 299-305. https://doi.org/10.1007/s10971-007-1645-4.

[159] P. Reiss, M. Carrière, C. Lincheneau, L. Vaure, S. Tamang, Synthesis of semiconductor nanocrystals, focusing on nontoxic and earth-abundant materials, Chem. Rev. 116 (2016) 10731-10819. https://doi.org/10.1021/acs.chemrev.6b00116.

[160] V. Harish, M.M. Ansari, D. Tewari, M. Gaur, A.B. Yadav, M.-L. García-Betancourt, F.M. Abdel-Haleem, M. Bechelany, A. Barhoum, Nanoparticle and Nanostructure Synthesis and Controlled Growth Methods, Nanomaterials 12 (2022) 3226.

[161] J.A. Dirksen, T.A. Ring, Fundamentals of crystallization: Kinetic effects on particle size distributions and morphology, Chem. Eng. Sci. 46 (1991) 2389-2427. https://doi.org/https://doi.org/10.1016/0009-2509(91)80035-W.

[162] T. Sugimoto, Preparation of monodispersed colloidal particles, Adv. Colloid Interface Sci. 28 (1987) 65-108. https://doi.org/https://doi.org/10.1016/0001-8686(87)80009-X.

[163] V.K. LaMer, R.H. Dinegar, Theory, production and mechanism of formation of monodispersed hydrosols, J. Am. Chem. Soc. 72 (1950) 4847-4854. https://doi.org/10.1021/ja01167a001.

[164] A. Van Bommel, J. Dahn, Analysis of the growth mechanism of coprecipitated spherical and dense nickel, manganese, and cobalt-containing hydroxides in the presence of aqueous ammonia, Chem. Mater. 21 (2009) 1500-1503.

[165] T. Sugimoto, Fine particles: synthesis, characterization, and mechanisms of growth. CRC Press, 2000.

[166] M. Henry, J.P. Jolivet, J. Livage, Aqueous chemistry of metal cations: Hydrolysis, condensation and complexation, in: R. Reisfeld, C.K. Jjørgensen (Eds.), Chemistry, Spectroscopy and Applications of Sol-Gel Glasses, Springer Berlin Heidelberg, Berlin, Heidelberg, 1992, pp. 153-206.

[167] Y. Li, G.P. Demopoulos, Precipitation of nanosized titanium dioxide from aqueous titanium(IV) chloride solutions by neutralization with MgO, Hydrometallurgy 90 (2008) 26-33. https://doi.org/https://doi.org/10.1016/j.hydromet.2007.09.008.

[168] C. Charbonneau, R. Gauvin, G.P. Demopoulos, Nucleation and growth of self-assembled nanofibre-structured rutile (TiO_2) particles via controlled forced hydrolysis of titanium tetrachloride solution, J. Cryst. Growth 312 (2009) 86-94. https://doi.org/https://doi.org/10.1016/j.jcrysgro.2009.09.033.

[169] C. Charbonneau, R. Gauvin, G.P. Demopoulos, Aqueous solution synthesis of crystalline anatase nanocolloids for the fabrication of DSC photoanodes, J. Electrochem. Soc. 158 (2011) H224. https://doi.org/10.1149/1.3529238.

[170] A. Yasin, F. Guo, M.J. Sussman, R. Gauvin, G.P. Demopoulos, Steady-state, scalable production of mesoporous Rutile and Brookite particles and their use in energy conversion and storage cells, ChemNanoMat 2 (2016) 980-988. https://doi.org/10.1002/cnma.201600185.

[171] M.J. Sussman, M. Celikin, A. Yasin, G.P. Demopoulos, Mesoporous Brookite Nanoplatelets with Superior Lithium-ion Intercalation Stability, Electrochim. Acta 138 (2014) 215-223. https://doi.org/https://doi.org/10.1016/j.electacta.2014.05.148.

[172] K. Chalastara, F.Q. Guo, S. Elouatik, G.P. Demopoulos, Tunable composition aqueous-synthesized mixed-phase TiO_2 nanocrystals for photo-assisted water decontamination: comparison of anatase, brookite and rutile photocatalysts, Catalysts 10 (2020) 18. https://doi.org/10.3390/catal10040407.

[173] H.C. Chiu, X. Lu, J. Zhou, L. Gu, J. Reid, R. Gauvin, K. Zaghib, G.P. Demopoulos, Capacity fade mechanism of $Li_4Ti_5O_{12}$ nanosheet anode, Adv. Energy Mater. 7 (2017) 1601825. https://doi.org/10.1002/aenm.201601825.

[174] H.C. Chiu, X. Lu, S. Elouatik, K. Zaghib, G.P. Demopoulos, Formation of lithium titanate hydrate nanosheets: Insight into a two-dimension growth mechanism by in situ Raman, Crystal Growth & Design 16 (2016) 3898-3904. https://doi.org/10.1021/acs.cgd.6b00470.

[175] Y. Yang, J.Q. Li, D.Q. Chen, J.B. Zhao, A facile electrophoretic deposition route to the Fe_3O_4/CNTs/rGO composite electrode as a binder-free anode for lithium ion battery, ACS Appl. Mater. Interfaces 8 (2016) 26730-26739. https://doi.org/10.1021/acsami.6b07990.

[176] M. Uceda, H.-C. Chiu, R. Gauvin, K. Zaghib, G.P. Demopoulos, Electrophoretically co-deposited $Li_4Ti_5O_{12}$/reduced graphene oxide nanolayered composites for high-performance battery application, Energy Storage Mater. 26 (2020) 560–569. https://doi.org/https://doi.org/10.1016/j.ensm.2019.11.029.

[177] M. Uceda, J.G. Zhou, J. Wang, R. Gauvin, K. Zaghib, G.P. Demopoulos, Highly conductive NMP-free carbon-coated nano-lithium titanate/carbon composite electrodes via SBR-assisted electrophoretic deposition, Electrochim. Acta 299 (2019) 107-115. https://doi.org/10.1016/j.electacta.2018.12.166.

[178] R. Jain, A.S. Lakhnot, K. Bhimani, S. Sharma, V. Mahajani, R.A. Panchal, M. Kamble, F. Han, C. Wang, N. Koratkar, Nanostructuring versus microstructuring in battery electrodes, Nat. Rev. Mater. (2022) https://doi.org/10.1038/s41578-022-00454-9.

[179] M. Ammam, Electrophoretic deposition under modulated electric fields: a review, RSC Adv. 2 (2012) 7633-7646. https://doi.org/10.1039/c2ra01342h.

[180] I. Corni, M.P. Ryan, A.R. Boccaccini, Electrophoretic deposition: From traditional ceramics to nanotechnology, Journal of the European Ceramic Society 28 (2008) 1353-1367. https://doi.org/10.1016/j.jeurceramsoc.2007.12.011.

[181] L.H. Ye, K.C. Wen, Z.X. Zhang, F. Yang, Y.C. Liang, W.Q. Lv, Y.K. Lin, J.M. Gu, J.H. Dickerson, W.D. He, Highly efficient materials assembly via electrophoretic deposition for electrochemical energy conversion and storage devices, Adv. Energy Mater. 6 (2016) 1502018. https://doi.org/10.1002/aenm.201502018.

[182] J.H. Dickerson, A.R. Boccaccini, Electrophoretic deposition of nanomaterials. Springer, 2011.

[183] P. Amrollahi, J.S. Krasinski, R. Vaidyanathan, L. Tayebi, D. Vashaee, Electrophoretic deposition (EPD): fundamentals and applications from nano- to microscale structures, in: M. Aliofkhazraei, A.S.H. Makhlouf (Eds.), Handbook of Nanoelectrochemistry: Electrochemical Synthesis Methods, Properties, and Characterization Techniques, Springer International Publishing, Cham, 2016, pp. 561-591.

[184] L. Besra, T. Uchikoshi, T. Suzuki, Y. Sakka, Pulsed-DC electrophoretic deposition (EPD) of aqueous alumina suspension for controlling bubble incorporation and deposit microstructure, Key Engineering Materials, Trans Tech Publ, 2009, pp. 39-44.

[185] A. Chávez-Valdez, A.R. Boccaccini, Innovations in electrophoretic deposition: Alternating current and pulsed direct current methods, Electrochim. Acta 65 (2012) 70-89. https://doi.org/https://doi.org/10.1016/j.electacta.2012.01.015.

[186] L. Besra, M. Liu, A review on fundamentals and applications of electrophoretic deposition (EPD), Prog. Mater. Sci. 52 (2007) 1-61. https://doi.org/10.1016/j.pmatsci.2006.07.001.

[187] J. Hagberg, H.A. Maples, K.S.P. Alvim, J. Xu, W. Johannisson, A. Bismarck, D. Zenkert, G. Lindbergh, Lithium iron phosphate coated carbon fiber electrodes for structural lithium ion batteries, Composites Science and Technology 162 (2018) 235-243. https://doi.org/10.1016/j.compscitech.2018.04.041.

[188] A. Caballero, L. Hernan, M. Melero, J. Morales, R. Moreno, B. Ferrari, $LiNi_{0.5}Mn_{1.5}O_4$ thick-film electrodes prepared by electrophoretic deposition for use in high voltage lithium-ion batteries, J. Power Sources 158 (2006) 583-590. https://doi.org/10.1016/j.jpowsour.2005.09.018.

[189] K. Kanamura, J. Hamagami, Innovation of novel functional material processing technique by using electrophoretic deposition process, Solid State Ion. 172 (2004) 303-308. https://doi.org/10.1016/j.ssi.2004.01.039.

[190] N.P. Benehkohal, M.J. Sussman, H.-c. Chiu, M. Uceda, R. Gauvin, G.P. Demopoulos, Enabling green fabrication of Li-ion battery electrodes by electrophoretic deposition: Growth of thick binder-free mesoporous TiO_2-carbon anode films, J. Electrochem. Soc. 162 (2015) D3013-D3018. https://doi.org/10.1149/2.0111511jes.

[191] O. Stern, Zur theorie der elektrolytischen doppelschicht, Z. Elektrochem. Angew. Phys. Chem. 30 (1924) 508-516. https://doi.org/https://doi.org/10.1002/bbpc.192400182.

[192] R.J. Hunter, Zeta potential in colloid science: principles and applications. Academic press, 2013.

[193] S.-J. Park, M.-K. Seo, Chapter 1 - Intermolecular force, in: S.-J. Park, M.-K. Seo (Eds.), Interface Science and Technology, Elsevier, 2011, pp. 1-57.

[194] T.L. Doane, C.H. Chuang, R.J. Hill, C. Burda, Nanoparticle zeta-Potentials, Acc. Chem. Res. 45 (2012) 317-326. https://doi.org/10.1021/ar200113c.

[195] R. Moreno, B. Ferrari, Nanoparticles dispersion and the effect of related parameters in the EPD kinetics, in: Electrophoretic Deposition of Nanomaterials, Springer, 2012, pp. 73-128.

[196] O. Stern, The theory of the electrolytic double shift, Z. Elektrochem. Angew. Phys. Chem. 30 (1924) 508-516.

[197] Chapter 10-Microfluidic methods for measuring zeta potential, in: D. Li (Ed.), Interface Science and Technology, Elsevier, 2004, pp. 617-640.

[198] M.G. Carneiro-da-Cunha, M.A. Cerqueira, B.W.S. Souza, J.A. Teixeira, A.A. Vicente, Influence of concentration, ionic strength and pH on zeta potential and mean hydrodynamic diameter of edible polysaccharide solutions envisaged for multinanolayered films production, Carbohydrate Polymers 85 (2011) 522-528. https://doi.org/10.1016/j.carbpol.2011.03.001.

[199] M. Dittgen, B. Herbst, Zeta-Potential - Fundamentals, methods of measurement and application in pharmacy, Pharmazie 42 (1987) 641-656.

[200] S. Bhattacharjee, DLS and zeta potential - What they are and what they are not?, Journal of Controlled Release 235 (2016) 337-351. https://doi.org/10.1016/j.jconrel.2016.06.017.

[201] S. Salgin, U. Salgin, S. Bahadir, Zeta potentials and isoelectric points of biomolecules: The effects of ion types and ionic strengths, Int. J. Electrochem. Sci. 7 (2012) 12404-12414.

[202] E. Verwey, J.T.G. Overbeek, Theory of the stability of lyophobic colloids, Journal of Colloid Science 10 (1955) 224-225.

[203] E.J.W. Verwey, Theory of the Stability of Lyophobic Colloids, The Journal of Physical and Colloid Chemistry 51 (1947) 631-636. https://doi.org/10.1021/j150453a001.

[204] B. Derjaguin, L. Landau, Theory of the stability of strongly charged lyophobic sols and of the adhesion of strongly charged particles in solutions of electrolytes, Progress in Surface Science 43 (1993) 30-59. https://doi.org/https://doi.org/10.1016/0079-6816(93)90013-L.

[205] J.S. Laskowski, J. Ralston, Colloid chemistry in mineral processing. Elsevier, 2015.

[206] Computer simulations of colloids and macromolecules aggregate formation: Kolumne, CHIMIA 49 (1995) 300. https://doi.org/10.2533/chimia.1995.300.

[207] W.F. Pickard, Remarks on theory of electrophoretic deposition, J. Electrochem. Soc. 115 (1968) C105-&. https://doi.org/10.1149/1.2411169.

[208] B.K. Chakrabarti, C.T. John Low, Practical aspects of electrophoretic deposition to produce commercially viable supercapacitor energy storage electrodes, RSC Adv. 11 (2021) 20641-20650. https://doi.org/10.1039/D0RA09197A.

[209] Y.D. Wang, B.M. Smarsly, I. Djerdj, Niobium doped TiO_2 with mesoporosity and its application for lithium insertion, Chem. Mater. 22 (2010) 6624-6631. https://doi.org/10.1021/cm1020977.

[210] S. Awasthi, S.K. Pandey, C.P. Pandey, K. Balani, Progress in Electrochemical and Electrophoretic Deposition of Nickel with Carbonaceous Allotropes: A Review, Adv. Mater. Interfaces (2019) 1901096. https://doi.org/10.1002/admi.201901096.

[211] Y.Q. Zhang, X.H. Xia, X.L. Wang, Y.J. Mai, S.J. Shi, Y.Y. Tang, L. Li, J.P. Tu, Silicon/graphene-sheet hybrid film as anode for lithium ion batteries, Electrochem. Commun. 23 (2012) 17-20. https://doi.org/10.1016/j.elecom.2012.07.001.

[212] Y. Yang, D.Q. Chen, B. Liu, J.B. Zhao, Binder-free Si nanoparticle electrode with 3D porous structure prepared by electrophoretic deposition for lithium-ion batteries, ACS Appl. Mater. Interfaces 7 (2015) 7497-7504. https://doi.org/10.1021/acsami.5b00421.

[213] S.A. Hasan, D.W. Kavich, J.H. Dickerson, Sacrificial layer electrophoretic deposition of free-standing multilayered nanoparticle films, Chem. Commun. (2009) 3723-3725. https://doi.org/10.1039/B902622C.

[214] N.P. Benehkohal, V. Gonzalez-Pedro, P.P. Boix, S. Chavhan, R. Tena-Zaera, G.P. Demopoulos, I. Mora-Sero, Colloidal PbS and PbSeS quantum dot sensitized solar cells prepared by electrophoretic deposition, J. Phys. Chem. C 116 (2012) 16391-16397. https://doi.org/10.1021/jp3056009.

[215] E. Rabani, Structure and electrostatic properties of passivated CdSe nanocrystals, The Journal of Chemical Physics 115 (2001) 1493-1497. https://doi.org/10.1063/1.1380748.

[216] N.P. Benehkohal, G.P. Demopoulos, Green preparation of TiO_2-ZnO nanocomposite photoanodes by aqueous electrophoretic deposition, J. Electrochem. Soc. 159 (2012) B602-B610. https://doi.org/10.1149/2.016206jes.

3. Single-crystal $TiNb_2O_7$ Materials via Sustainable Synthesis for Fast-charging Lithium-ion Battery Anodes

This chapter addresses the 1st objective of thesis, i.e., to synthesize single-crystal $TiNb_2O_7$ materials via sustainable synthesis for fast-charging lithium-ion battery anodes. This chapter has been published in ***Journal of Energy Storage***, with the following citation:

Yu F, Wang S, Yekani R, La Monaca A, Demopoulos GP. "Single-crystal $TiNb_2O_7$ materials via sustainable synthesis for fast-charging lithium-ion battery anodes". *J Energy Storage. 2024;95:112482.*

Abstract

$TiNb_2O_7$ (TNO) has emerged as a promising fast-charging anode for lithium-ion batteries (LIBs). However, research on TNO anode materials has been mostly restricted to synthesis of polycrystalline materials with limited associated mechanistic studies. Herein, we report a novel scalable aqueous synthesis method yielding sub-micron size single-crystal TNO particles following calcination that enables fast-charging anode fabrication. The sustainable co-precipitation process yields amorphous intermediate hydroxides which upon thermal conversion induced crystallization form single crystals. The obtained TNO monocrystalline anode material under 900 °C calcination (TNO-900C) delivers a high gravimetric capacity (279 mAh/g at 1st cycle) and a high volumetric capacity (351.7 mAh/cm^3 at the initial cycle) at 0.5 C rate. Additionally, the TNO anode delivers a remarkable capacity of 223 mAh/g at 5 C and a high retention of 81.4 % after 200 cycles. In addition, TNO-900C illustrates outstanding fast-charging performance with a reversible capacity of 200 mAh/g at 10 C. The intercalation mechanism and diffusion behavior of the monocrystalline TNO anodes are elucidated by electrochemical kinetic analysis (GITT, CV, and EIS). The remarkable fast charging Li-ion storage performance can be attributed to a high Li^+ diffusion coefficient (1.37×10^{-13} cm^2/s), low polarization, and high structural stability.

3.1. Introduction

The widespread demand for electric vehicles (EVs) is putting a lot of pressure on current lithium-ion batteries (LIBs)[1-3]. Conventional LIBs cannot meet the increasing performance requirements of EVs because of limited energy density and low-rate capability[3,4]. From the perspective of anode materials for EV LIBs, dominant commercial graphite-based materials are prone to lithium dendrite formation and low Li-storage capacity under fast charging conditions[1,5]. By contrast, another commercial anode, lithium titanate ($Li_4Ti_5O_{12}$, LTO), demonstrates ultrafast Li-ion transport and is capable of a high-rate application without Li plating issue[6]. Despite the rate advantage of LTO, it suffers from a relatively low theoretical capacity (175 mAh/g)[7], which is less than half that of graphite (372 mAh/g)[8]. Consequently, there exists a pressing need for new fast-charging anode materials with high capacity and simultaneously providing high safety, for next-generation LIBs.

One such candidate is titanium niobate ($TiNb_2O_7$/TNO), which has emerged as one of the promising anode alternatives since the pioneering research performed by Goodenough[9], providing a high theoretical gravimetric capacity of 387.6 mAh/g. Also of paramount importance is the high-safety operating potential of TNO (*ca.*, 1.65 V vs. Li/Li^+) preventing the formation of Li dendrites and subsequent decomposition of the electrolyte at <1V (vs. Li/Li^+), a common problem with graphite anodes[4,5]. Theoretically, the Li intercalation reaction of TNO involves three redox couples (Ti^{4+}/Ti^{3+}, Nb^{5+}/Nb^{4+}, Nb^{4+}/Nb^{3+}) and five lithium ions to form $Li_5TiNb_2O_7$[10,11]. Additionally, TNO offers a high theoretical volumetric capacity (1682 mAh/cm^3)[4,12], which is twice that of graphite (841 mAh/cm^3)[13,14] and rather close to that of Li metal (2062 mAh/cm^3)[3,8]. Considering such advantages coupled with high rate, and long cycle life characteristics, TNO possesses commercialization potential for the fast-charging market[4,15]. However, the remarkable potential of TNO is severely hindered by several obstacles including non-scalable synthesis approaches[9], unsatisfactory gravimetric capacity under fast charging[16], low practical volumetric capacity[15], unclear materials formation mechanism[17], and correlation between materials structure and electrochemical performance[4,17].

Crystal engineering of TNO materials via a sustainable fabrication route emerges as an effective strategy for practical application. Single-crystal features can shorten Li ion diffusion pathways, thereby unlocking extremely fast charging capabilities of TNO anode[4,18]. This is so because in single $TiNb_2O_7$ crystals, Li-ion diffusion that is predominately occurring along one-dimension channels in TNO[19,20], takes shorter pathways than in polycrystalline structure, where different crystal orientations and grain boundaries, create longer complex ionic diffusion pathways[21]. Nevertheless, current synthesis techniques for single-crystal TNO materials, including solid-state[21,22], and solvothermal methods[23], face obstacles of insufficient purity, complicated procedures, or scalability challenges. The hydrolytic co-precipitation approach, as evidenced by its success in fabricating nanoscale LTO anode materials[24] and commercializing monocrystalline nickel manganese cobalt (NMC) cathode materials[25], promises a sustainable synthetic route for single-crystalline TNO electrode materials. Organic-solvent-based methods are hampered by environmental and cost issues, not conducive to large-scale production[26-28]. In addition, the TNO materials fabricated via these organic-solvent routes provide an unsatisfactory electrochemical performance[27,28]. To address these issues, an aqueous synthetic route featuring low cost (use of bulk metal chloride salts) is proposed to offer a sustainable TNO crystallization process overcoming scalability problems associated with current methods of synthesis, meanwhile achieving the formation of single crystal particles that enable fast-charging performance of TNO anodes.

In this work, we design one sustainable aqueous hydrolytic co-precipitation approach to develop submicron-sized single-crystal TNO anode materials for fast-charging LIB. The new scalable green synthesis method proposed makes use of precisely controlled hydrolysis and atomic-homogeneity co-precipitation to produce Ti-Nb hydroxides nanoscale precursor (within 10 nm), which are subsequently crystallized to $TiNb_2O_7$ submicron particles upon calcination. The monocrystalline TNO possesses several merits as a fast-charging sustainably produced anode: (1) an outstanding Li-storage capacity under 5 C high rate and 10 C extremely fast charging conditions, (2) a high practical capacity of 279 mAh/g and 351.7 mAh/cm^3 at 0.5 C meeting requirement of industry[4,15], and (3) a high Li diffusion coefficient of 1.37×10^{-13} cm^2/s. Moreover, a new understanding of the intercalation mechanism during the initial lithiation step of pristine TNO is advanced via systematic GITT, CV, and EIS measurements. In addition, via a detailed analysis of nanostructure, crystallinity (XRD refinement), and porosity the formation mechanism of TNO single crystals was elucidated and the relationship between electrochemical performance and material properties was revealed.

3.2. Experimental Section

3.2.1. Materials Synthesis

The synthesis route of TNO includes (1) intermediate precursor synthesis via pH-regulated hydrolytic co-precipitation and (2) high-temperature calcination, as shown in Scheme A.1 and Scheme A.2: First, homogeneous aqueous stock solutions are prepared at a temperature below 10 °C to avoid premature hydrolysis of the titanium tetrachloride ($TiCl_4$) and niobium pentachloride

($NbCl_5$) precursor solutions. The $TiCl_4$ aqueous solution is prepared by drop-wise (1 mL/min) addition of 0.15 mol (16.45 mL) of $TiCl_4$ (99.0%, Sigma-Aldrich, USA) into 500 mL of cold DI water kept cold in an ice bath while vigorously subjected to magnetic stirring. Similarly, stoichiometric $NbCl_5$ aqueous solution (0.3 mol (81.06 g) of $NbCl_5$ (99%, Thermo Fisher Scientific, USA) into another 500 mL of cold DI water) is prepared. The concentrations of these two solutions (verified by ICP-OES) are adjusted to 0.3 mol/L Ti(IV) and 0.6 mol/L Nb(V). It is worth mentioning that both solutions are stable without precipitate forming prematurely by storing them in the fridge (ca. 10 °C). The so-prepared stock $TiCl_4$ and $NbCl_5$ aqueous solutions are mixed with a 1:1 volume ratio in a volumetric flask to prepare a homogeneous Ti-Nb-Cl aqueous solution with 0.15 mol/L Ti(IV) and 0.3 mol/L of Nb(V) composition. Subsequently, the Ti-Nb-Cl solution kept cold in an ice bath is neutralized from pH<1 to pH=9 by slowly adding ammonium hydroxide (99.9% NH_4OH, 29% NH_3 basis, Sigma-Aldrich, USA) with a rate of 0.1 mL/min under agitation (400 rpm), thereby enabling hydrolytic co-precipitation of Ti(IV) and Nb(V). The obtained amorphous white solid co-precipitate (TNO-hydroxide precursor) is then centrifuged, washed five times with 1 L of warm water (60-80 °C), and dried in an oven at 80 °C overnight. Finally, the dried TNO-precursor is heat-treated/calcined at different temperatures (500 °C for 4h (TNO-500C), 700 °C for 4h (TNO-700C), 900 °C for 4h (TNO-900C), 1100 °C for 4h (TNO-1100C), respectively) in continuous flow oxygen gas (10 vol% O_2 and 90 vol% N_2) with a heating ramping rate of 5 °C/min in a tube furnace (OTF-1200X-S50-2F Mini CVD tube furnace, MTI Corporation, USA).

3.2.2. Materials Characterization

The crystal structures of materials were characterized by X-ray diffraction (XRD) using a Bruker D8 Discovery X-ray diffractometer (VANTEC Detector Cu-Source). LeBail Refinement was performed with TOPAS (Bruker) V5 software. TGA (thermogravimetric analysis) and DSC (differential scanning calorimetry) were conducted by using TGA/DSC 1 (Mettler Toledo) instrument. Crystal morphology structures and elemental distribution were recorded by scanning electron microscopy (SEM) using a Hitachi SU-8000 Cold Field-Emission Microscopy equipped with energy-dispersive X-ray spectroscopy (EDS) detector (XMax 80 mm^2 Oxford Instruments). Transmission electron microscopy (TEM), high-resolution transmission electron microscopy (HRTEM), scanning transmission electron microscopy (STEM), and selected area electron diffraction (SAED) were carried out on Thermo Scientific Talos F200X G2 TEM/STEM instrument operated at 200 kV. The STEM high-angle annular dark-field (HAADF) images were acquired at a beam convergence angle of 10.5 mrad and the detector collection angle of 58-200 mrad. The energy-dispersive X-ray spectroscopy (EDS) mapping was applied to reveal the elemental composition of Ti (Kα 4.5 keV), Nb (Lα 2.17 keV), and O (Kα 0.52 keV). The survey spectrum and high-resolution spectra at the edges of Ti 2*p*, Nb 3*d*, and O 1*s* were identified by X-ray photoelectron spectroscopy (XPS) using a Thermo Scientific K-alpha X-ray photoelectron spectrometer within an Al Kα micro-focused monochromator. XPS data were analyzed with Thermo Advantage software and normalized/calibrated referenced to adventitious C1s peak at 284.80 eV. The N_2 adsorption/desorption analysis was performed with a Micromeritics TriStar 3000 apparatus to identify the Brunauer-Emmett-Teller (BET) specific surface area and Barrett-Joyner-Halenda (BJH) pore distribution. Inductively coupled plasma optical emission spectrometry (ICP-OES) was applied to determine the Ti concentration and Nb concentration in $TiCl_4$ aqueous solution, Ti-Nb-Cl aqueous solution, TNO-Precursor, and TNO crystal particles. All solid samples were dissolved in an acid solution (1 wt.% HF and 1 wt.% HCl) before being analyzed on a Thermo Scientific iCAP 6000 Series ICP spectrometer. The particle size distribution of TNO samples was determined by a dynamic light scattering (DLS) particle analyzer (Zetasizer Nano ZS, Malvern Instruments Ltd) after ultrasonic blending of a suspension (3 g/L sample-in-ethanol) for one hour.

3.2.3. Electrochemical characterization

Coin cells were assembled for electrochemical testing. TNO active material (80 wt.%), acetylene black (10 wt.%), and poly(vinylidene difluoride) (PVDF) binder (10 wt.%) were manually milled with N-Methyl-2-pyrrolidone (NMP) solvent in a mortar and blade-coated on copper foil (99.99% Cu, 25 μm thick, MTI Corporation), followed by drying in an 80 °C vacuum oven overnight, punching, and calendering. The electrodes were calendered with different pressures (0 atm, 1500 atm, 3000 atm) for investigating the practical volumetric capacity. In an argon-filled MBraun glovebox, the coin cells (2032) were assembled with a TNO working electrode, lithium metal reference electrode, polypropylene-polyethylene-polypropylene (PP/PE/PP) film separator (Celgard 2300), and 200 μL 1M $LiPF_6$ electrolyte (in EC:DMC:DEC at 2:2:1).

The galvanostatic charging/discharging cycling at different rates was tested at room temperature using a standard 8-channel battery analyzer (BST8 WA, MTI Corp). The rate of 1 C corresponds to 387.6 mA/g according to the theoretical capacity of TNO. The mass loading of TNO active material was maintained at 3.2 ± 0.3 mg/cm^2. Gravimetric capacity is calculated based on the mass of TNO active material, and volumetric capacity is calculated based on the volume of the composite electrode (TNO, conductive carbon, binder). Both cyclic voltammetry (CV) and electrochemical impedance spectroscopy (EIS) testing were performed using a Bio-Logic VSP potentiostat/galvanostat system and analyzed by EC-Lab software. The voltammograms were collected at sweep rates of 0.056 mV/s, 0.111 mV/s, 0.278 mV/s, 0.556 mV/s, 1.110 mV/s, and 2.780 mV/s, respectively, operating between 3.0 V and 1.0 V (vs. Li/Li$^+$). EIS measurements were carried out under potentiostatic mode at 3 V operated in the frequency range of 1 MHz to 0.01 Hz under room temperature. The impedance values are calculated by fitting the Nyquist plot with the equivalent electric circuit by the Z-fit method using EC-Lab software. Galvanostatic intermittent titration technique (GITT) experiments were performed using an Arbin standard battery cycler (BT2043-10V-100mA-40, Arbin).

3.3. Results and Discussion

3.3.1. Hydrolytic Co-precipitation of nanoscale TNO-Precursor

The microstructure of the TNO-Precursor sample is investigated using SEM and TEM. **Figure 3.1(a)** displays a secondary particle structure composed of aggregated primary nanoparticles. Further nanostructural characterization is conducted using TEM (**Figure 3.1(b, c)**) and STEM HAADF images (**Figure 3.1(e)**) which reveal primary nanoparticles of about 5-10 nm size. Upon aggregation, the secondary particles develop pores ~4 nm in size according to BJH desorption pore volume results (**Figure 3.1(j)**). The BET results illustrate a typical Type IV isotherm hysteresis corresponding to a mesoporous structure characterized by a high specific surface area (266 m^2/g) and a BJH desorption pore volume of 0.1726 cm^3/g. The diffraction pattern in the SAED image (**Figure 3.1(d)**) shows a typical amorphous material ring, corroborating the result of XRD in **Figure 3.1(i)**, displaying no diffraction peaks from titanium niobium oxides/hydroxides. EDS elemental mapping from TNO-precursor results in a high-uniformity elemental distribution of Ti (**Figure 3.1(f)**), Nb (**Figure 3.1(g)**), and O (**Figure 3.1(h)**), indicating homogeneous mixing of Ti and Nb at atomic level during the synthesis process. This nanoscale intermediate obtained via the new method illustrate a superior homogeneity compared to conventional precursors used in solid-state methods and other synthesis techniques[22,29].

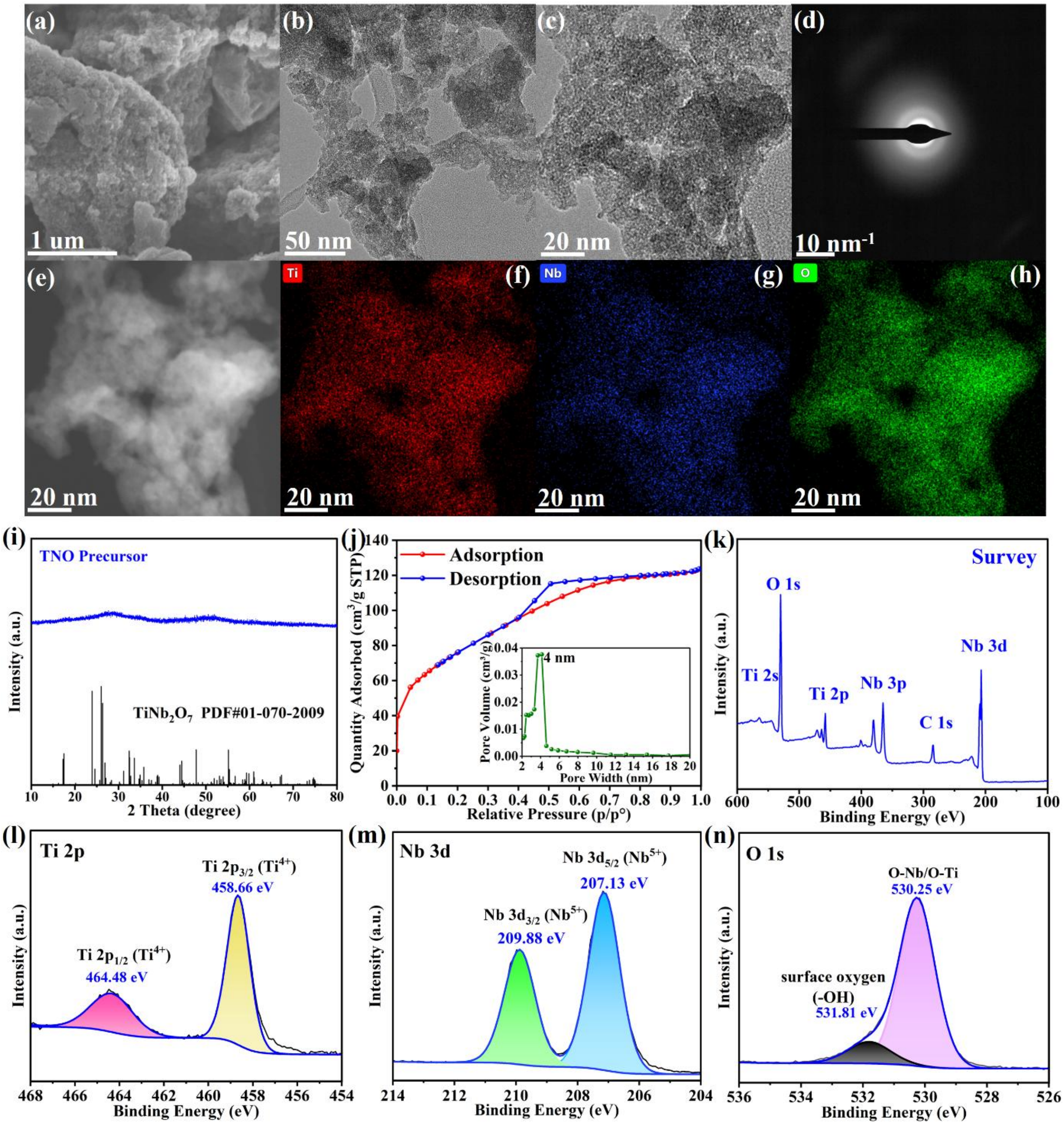

Figure 3.1 Morphology of nanoscale TNO-Precursor: (a) SEM image; (b, c) TEM images, and (d) corresponding selected area electron diffraction (SAED) image, (e) HAADF STEM image and corresponding EDS elemental mappings of (f) Ti, (g) Nb, and (h) O. Physical properties of TNO-Precursor: (i) XRD pattern; (j) N_2 adsorption/desorption isotherm and corresponding BJH desorption pore distribution curve (inset); (k) wide-scan XPS survey spectra and high-resolution XPS spectra of (l) Ti 2p, (m) Nb 3d, and (n) O 1s.

To better understand the chemical composition, bonding environment, and atomic valence state of the TNO-Precursor, XPS measurements were performed. The survey spectrum (**Figure 3.1(k)**) proves the existence of the Ti (Ti 2p), Nb (Nb 3p, Nb 3d), and O (O 1s). The C1s peak at 284.80 eV originates from carbon contaminant. Specifically, TNO-Precursor consists of 10.2 at. % Ti, 19.6 at. % Nb, and 70.2 at. % O. In the high-resolution XPS spectra of Ti (**Figure 3.1(l)**), the peaks centered at 464.48 eV and 458.66 eV are assigned to Ti $2p_{1/2}$ and Ti $2p_{3/2}$ orbitals[30], respectively, indicating the Ti^{4+}-O bonding in the TNO-Precursor[31]. In **Figure 3.1(m)**, corresponding photoelectron signals of Nb $3d_{3/2}$ and Nb $3d_{5/2}$ located at 209.88 eV and 207.13 eV, respectively, are ascribed to pentavalent Nb of the Nb-O bonding[32,33]. A prominent characteristic O 1s peak (**Figure 3.1(n)**) located at 530.25 eV corresponds to Ti^{4+}-O[32,33], and Nb^{5+}-O[34], while the other peak located at 531.81 eV stems from the hydroxyl oxygen group (-OH)[32].

3.3.2. Reactive Crystallization of $TiNb_2O_7$ by Calcination

A thorough microstructural investigation of TNO produced at three different calcination temperatures, 700 °C (TNO-700C), 900 °C (TNO-900C), and 1100 °C (TNO-1100C) was conducted by performing SEM, TEM, HAADF STEM, and SAED characterizations. **Figure 3.2(a-c)** displays SEM images of the three calcinated TNO materials. Additionally, the DLS particle size distributions (**Figure 3.3(i)**) were determined with average sizes of 230 nm (TNO-700C), 295 nm (TNO-900C), and 531 nm (TNO-1100C). These results elucidate that the submicron size of TNO can be tuned by increasing calcination temperature[35]. To be more precise, TEM images (**Figure 3.2 (d, k, r)**) demonstrate the widths of both TNO-700C and TNO-900C materials as approximately 50-300 nm, while the TNO-1100C sample measures around 200-500 nm. According to **Figure 3.2(d, e),** the TNO-700C particles are revealed to be rather secondary made from partially crystalline primary particles with 10-30 nm size (**Figure 3.2(e)**). In **Figure 3.2(e)**, the three orientations stem from the overlap of three single primary particles. The corresponding diffraction pattern from the SAED image (**Figure 3.2(f)**) shows a typical ring pattern of mixed amorphous and crystal domain materials. The TEM image in **Figure 3.2(k, l)**, along with its corresponding STEM image (**Figure 3.2(n)**), shows single crystal particles of TNO-900C with a width of 30-100 nm and length of 50-200 nm. The single-crystal property and monoclinic crystal structure of TNO-900C can be verified from **Figure 3.2(l)**, with the stripe spacing of d=1.03 nm corresponding to the (001) plane.

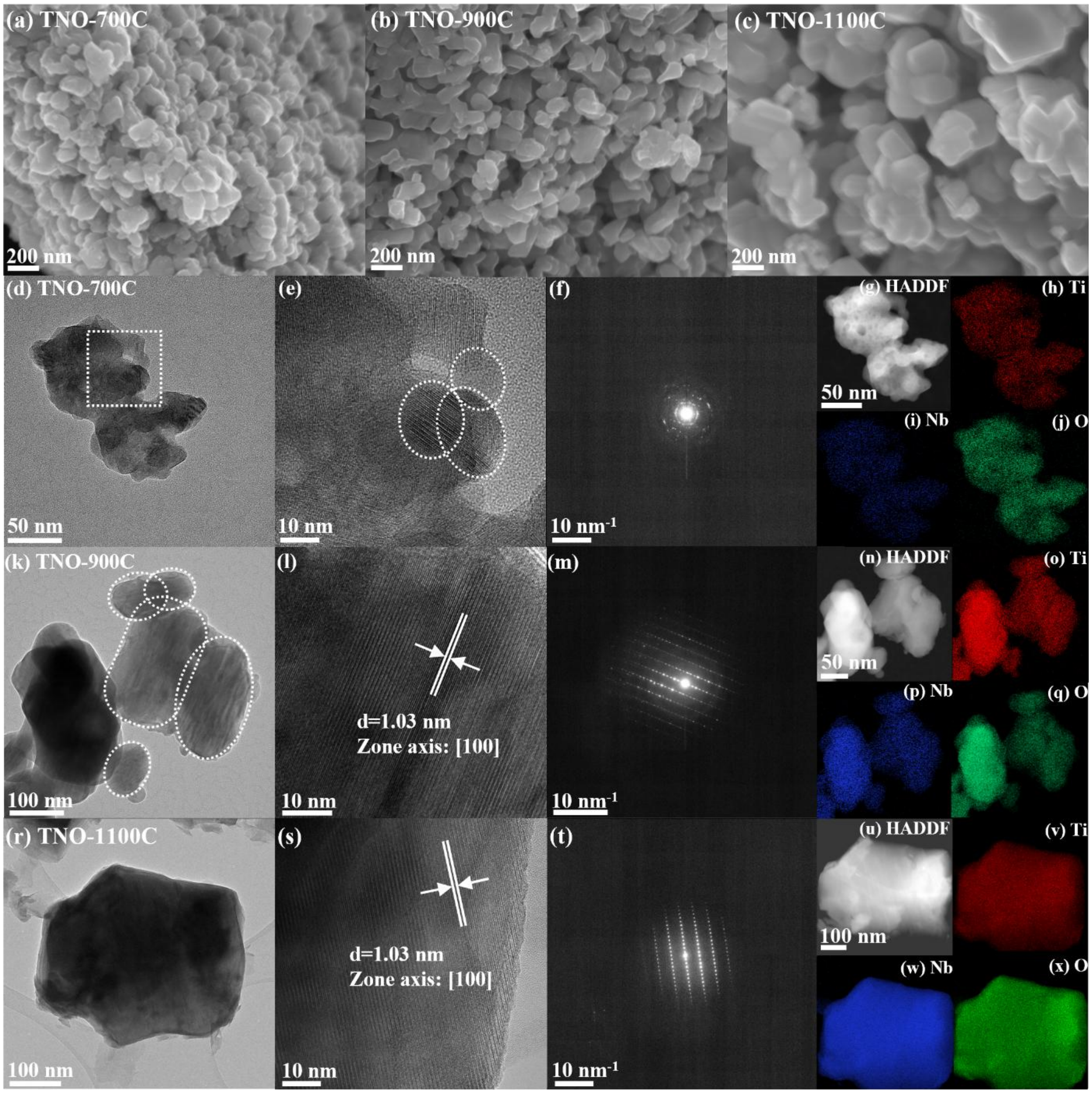

Figure 3.2 SEM images of (a) TNO-700C, (b) TNO-900C, and (c) TNO-1100C. (d) TEM, (e) HRTEM, (f) SAED, (g) HAADF STEM, and (h-j) EDS mapping (Ti, Nb, O) images of TNO-700C. (k) TEM, (l) HRTEM, (m) SAED (n) HAADF STEM, and (o-q) EDS elemental mapping images of TNO-900C. (r) TEM, (s) HRTEM, (t) SAED (u) HAADF STEM, and (v-x) EDS elemental mapping images of TNO-1100C.

The TEM elemental mapping images (**Figure 3.2(o-q)**) confirm the homogeneously distributed elements of Ti, Nb, and O in TNO-900C. **Figure 3.2(r, s)** shows the TNO-1100C material to consist of monocrystalline primary particles with a width of 400 nm and a length of 500 nm. The related SAED pattern (**Figure 3.2(t)**) confirms the single-crystalline nature of

$TiNb_2O_7$ where the stripe spacing of d=1.03 nm corresponds to the (001) plane. The EDS mappings in **Figure 3.2(v, w, x)** illustrate the highly even distribution of Ti, Nb, and O elements in TNO-1100C. This high elemental homogeneity of TNO-700C, TNO-900C, and TNO-1100C can be attributed to the novel route of the hydrolytic co-precipitation method, taking advantage of the homogeneous dispersion at the atomic level in liquid solution. By contrast, the conventional solid-state synthesis of $TiNb_2O_7$ materials can only enable particle-level dispersion thereby facing the inevitable issue of impurity (TiO_2, Nb_2O_5, or other reactants) even after long-term energy-intensive thermal treatment (>1100 ºC, >10 hours)[20,22,29].

XRD measurements are performed to investigate the effect of the calcination process on crystallinity. The XRD patterns (**Figure 3.3(a)**) show that the phase transition from amorphous to crystalline is highly temperature-dependent (the pattern for TNO precursor and $TiNb_2O_7$ are shown for comparison). TNO-500C was identified to be amorphous according to similar diffraction peak characteristics to TNO-Precursor. By contrast, TNO-700C displays some peaks corresponding to $TiNb_2O_7$ (PDF#01-070-2009), with the two most predominant diffraction peaks emerging at $2\theta=23.91^{\circ}$ and 25.99°. Therefore, TNO-700C can be regarded as the partially crystalline phase of $TiNb_2O_7$. As the calcination temperature is increased to 900 °C, the XRD pattern shows sharper peaks compared with TNO-700C. For the sample calcinated at 1100 °C (TNO-1100C), three prominent characteristic peaks appearing at 23.91°, 25.99°, 26.31° correspond to the presence of (011), (300), $(20\bar{6})$ lattice planes, respectively. These characteristic diffraction peaks are well-matched with the $TiNb_2O_7$ pattern, confirming the high purity of the TNO-1100C sample. In addition, the degree of crystallinity can be determined with the aid of **equation A.9**. Correspondingly, the crystallinity of TNO-700C, TNO-900C, and TNO-1100C is calculated to be 58.6 %, 71.5 %, and 81.7 %, respectively. Furthermore, the XRD refinement (**Figure 3.3(b, c)**) was performed via the LeBail method using TOPAS software to obtain the lattice parameter values of the TNO-900C and TNO-1100C samples. This refined XRD pattern was attributed to the monoclinic ReO3 shear structure with C2/m space group, in agreement with previous reports of $TiNb_2O_7$[12,36]. The resulting lattice parameters, volume, and theoretical density values for TNO-900C and TNO-1100C are displayed in **Figure A.1**.

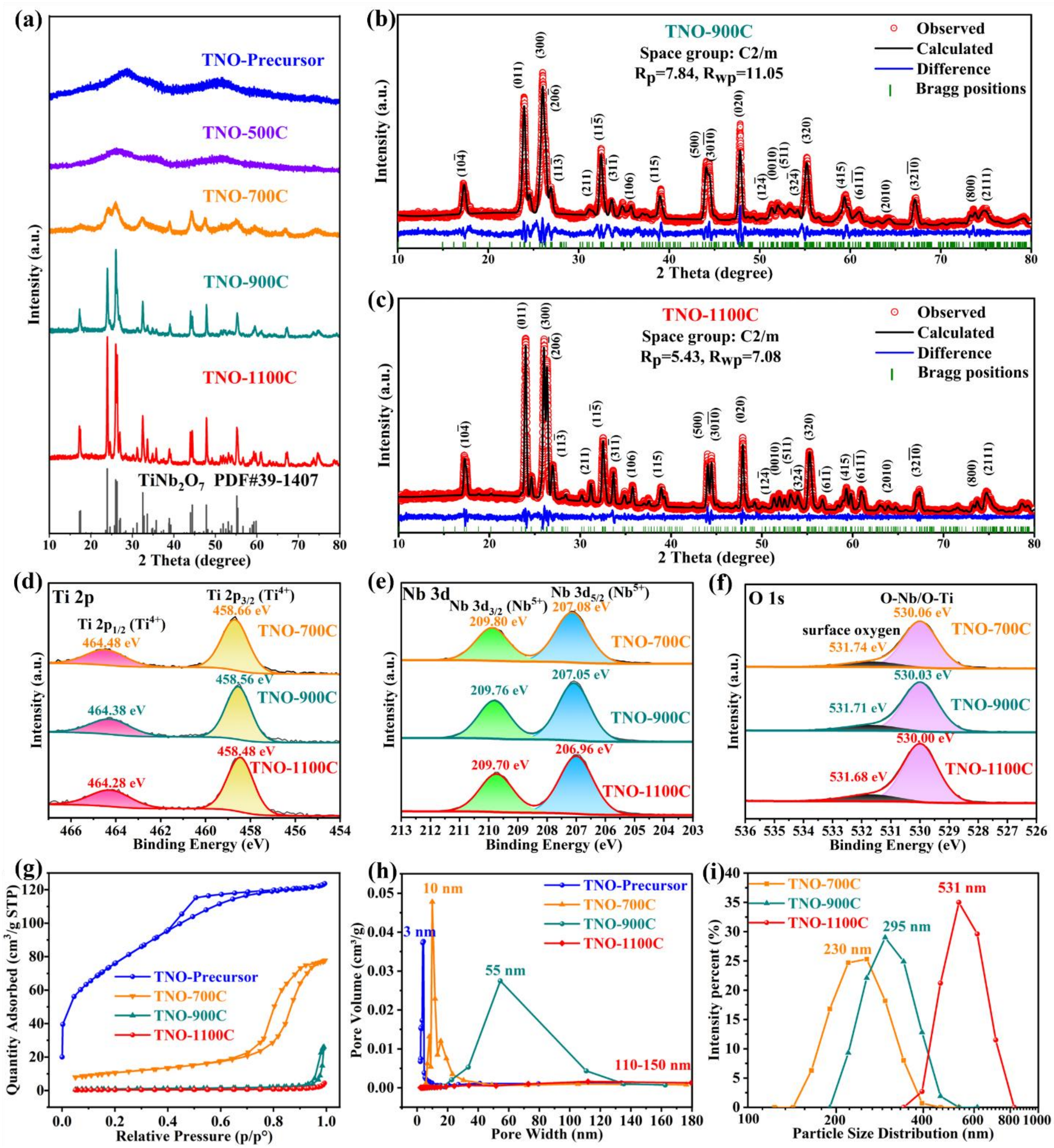

Figure 3.3 (a) XRD patterns of TNO materials calcinated at different temperatures, (b) XRD refinement of (b) TNO-900C and (c) TNO-1100C. XPS spectra: (d) Ti 2p spectra, (e) Nb 3d spectra, and (f) O 1s spectra of TNO-700C, TNO-900C and TNO-1100C samples. (g) Nitrogen adsorption-desorption isotherm, (h) BJH desorption pore distribution of TNO materials, (i) DLS particle size distribution of TNO-700C, TNO-900C, and TNO-1100C.

More insight into the transformation of TNO-Precursor during calcination was further obtained by TGA and DSC measurements (**Figure A.2**). A noticeable weight loss of 8 % observed from up to 200 ºC, can be attributed to the loss of water by evaporation from the hydrous mixed (Ti-Nb) metal hydroxides. The subsequent weight loss up to 5 % from 200 ºC to 500 ºC, coupled with two broad peaks at 285 ºC and 455 ºC in DSC curve, could be attributed to decomposition of TNO-Precursor (i.e., dehydration of metal hydroxide) to form metal oxide. In the temperature range of 500 ºC to 1100 ºC, there is no weight loss, reflecting thermal stability. Interestingly, an endothermic peak is seen at 640 ºC apparently signaling the onset of crystallization of TNO in agreement with the observed shift from amorphous (500 ºC) to crystalline (700 ºC) XRD patterns (**Figure 3.3(a)**).

To delve deeper into the chemical state of each element in different samples, XPS measurements were performed, as shown in **Figure 3.3(d-f)**. In the high-resolution XPS spectra of the Ti 2p (**Figure 3.3(d)**), characteristic peaks positioned at 464.48 eV, 464.38 eV, and 464.28 eV originate from Ti $2p_{1/2}$ photoelectrons[30,37], while those at 458.66 eV, 458.56 eV, and 458.48 eV correspond to Ti $2p_{3/2}$ photoelectrons[30,37]. These characteristic peaks of Ti $2p_{1/2}$ and Ti $2p_{3/2}$ photoelectrons indicate the oxidation state of titanium in TNO-700C, TNO-900C, and TNO-1100C to be Ti^{4+} for $TiNb_2O_7$[31]. In the Nb 3d spectra (**Figure 3.3(e)**), the single peak at 209.76 eV (TNO-700C) , 209.80 eV (TNO-900C), and 209.70 eV (TNO-1100C) is assigned to Nb $3d_{3/2}$ orbitals[32,33]; and the peak situated at 207.05 eV (TNO-700C), 207.08 eV (TNO-900C), or 206.96 eV (TNO-1100C) stem from Nb $3d_{5/2}$ orbitals[32,33], confirming the presence of Nb^{5+} state in all the samples according to previous reports[38]. In the O 1s core-level spectra **(Figure 3.3(f))**, the predominant peak at 530.06 eV, 530.03 eV, and 530.00 eV is assigned to the metal-oxygen bonds (Ti^{4+}-O and Nb^{5+}-O)[32,39], originating from lattice oxygen in the $TiNb_2O_7$ phase[39] of TNO-700C, TNO-900C, and TNO-1100C, respectively. The characteristic peaks at 531.74 eV, 531.71 eV, and 531.68 eV originate from the surface oxygen species[32]. Therefore, the obtained oxidation states of Ti, Nb, and oxygen for all TNO products obtained at different calcination temperatures correspond well to $TiNb_2O_7$.

The effect of calcination temperature on specific surface area and porosity structure was evaluated by using nitrogen adsorption-desorption isotherms (**Figure 3.3(g)**), and BJH desorption pore distribution (**Figure 3.3(h)**). TNO-700C and TNO-900C yielded Type V isotherm curves[40]. Specifically, TNO-700C processes BET specific surface area of 37.64 m^2/g, pore volume of 0.1335 cm^3/g, and average pore size of 10 nm (mesoporous structure). In comparison, TNO-900C shows a lower BET specific surface area of 4.00 m^2/g, a lower pore volume of 0.0418 cm^3/g, and an average pore size of 55 nm (macroporous structure). In contrast, TNO-1100C features a typical Type II isotherm characteristic belonging to nonporous solids with low surface area (3.51 m^2/g) and only 0.0153 cm^3/g pore volume. These calculation values of BJH desorption pore volume and BET specific surface area are summarized in **Figure A.3 and Table A.2** for comparison.

3.3.3. Li-ion Storage Analysis: Gravimetric & volumetric capacity and fast-charging performance

Figure 3.4(a) illustrates the galvanostatic charging-discharging performance of TNO materials investigated at 0.5 C between 3.0 V and 1.0 V. Among the three samples in **Figure 3.4(a)**, the TNO-900C anode offers the best performance, namely initial discharging capacity of 279 mAh/g, high initial coulombic efficiency of 93.9 %, and superior capacity retention of 219.4 mAh/g (79 %) after 100 cycles. By contrast, the TNO-700C anode delivers 230 mAh/g discharge capacity and low initial coulombic efficiency of 90 % at the first cycle and retains only 138 mAh/g of its capacity after 100 cycles. Meanwhile, the TNO-1100C sample although it registers a relatively high initial discharge capacity (235 mAh/g) and high initial coulombic efficiency (96%), its capacity faded severely dropping to <145 mAh/g before the 20th cycle. The higher initial capacities of TNO-900C and TNO-1100C than that of TNO-700C can be attributed to their higher crystallinity, while the superior cycling stability of TNO-900C vis-a-vis that of TNO-1100C can be attributed to its smaller crystal size and porous structure[35]. It appears therefore that TNO-900C, featuring sub-micron-sized single-crystal particles with porous structure, represents the best crystal microstructure for optimum electrochemical performance.

Figure 3.4(b-d) shows sloping voltage profiles of TNO-700C, TNO-900C, and TNO-1100C, which can be attributed to solid-solution storage mechanism, consistent with other literature[20,29]. The plateau region in these voltage profiles includes three zones: an initial sloping zone (3.0 V-1.7 V), a “plateau-like” solid-solution reaction zone (1.7 V-1.5 V), and a final sloping zone (1.5 V-1.0 V)[20,29]. The discharge voltage profile at the first cycle demonstrates a large overpotential due to the lithiation reaction of pristine $TiNb_2O_7$.

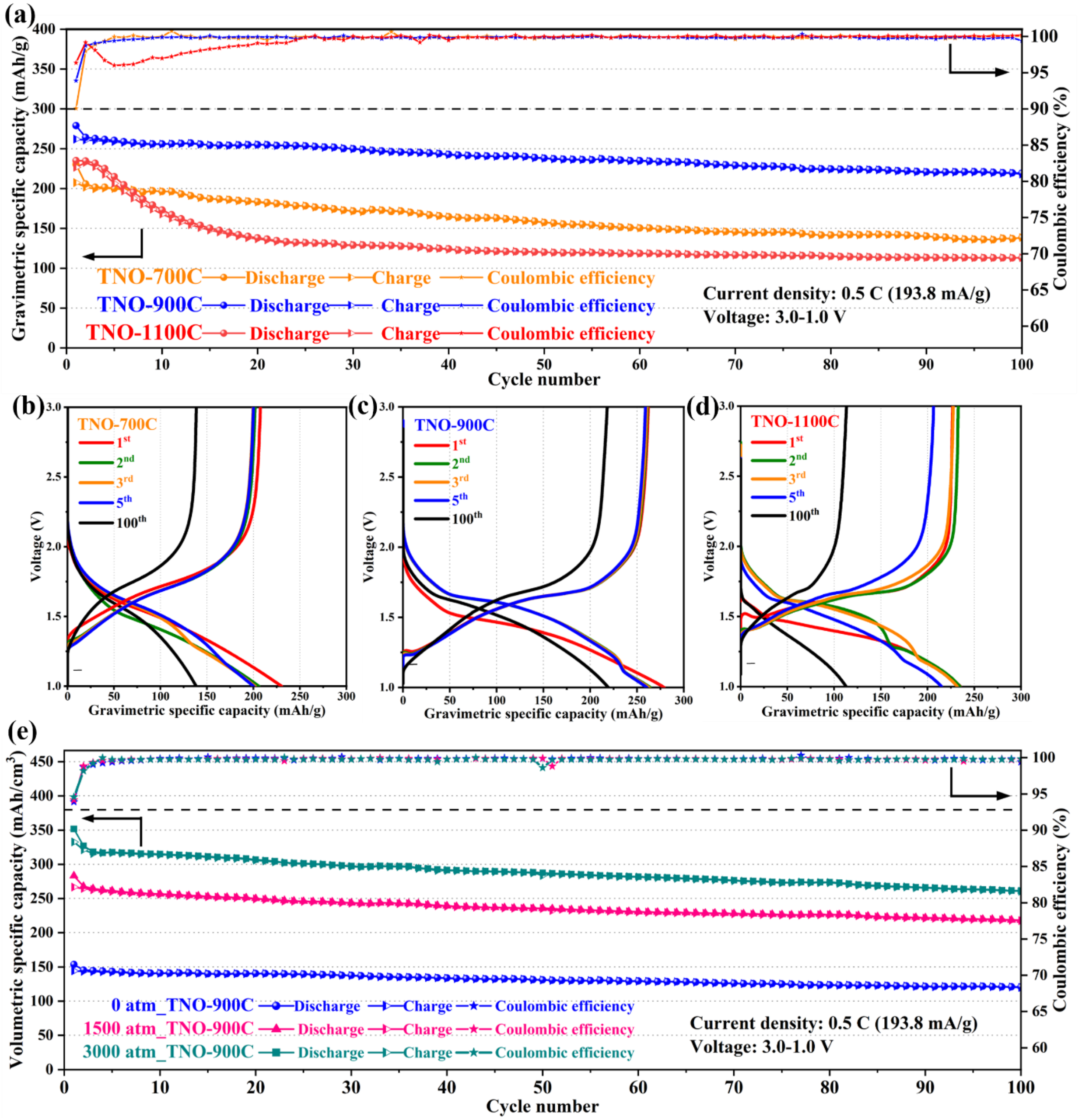

Figure 3.4 (a) Galvanostatic discharge/charge cycling at 0.5 C rate operated between 3.0 V to 1.0 V. Corresponding voltage profiles of (b)TNO-700C, (c) TNO-900C, and (d) TNO-1100C. (e) The volumetric capacity of TNO-900C composite electrodes calendered under different pressures (0 atm, 1500 atm, 3000 atm).

Besides the gravimetric-based performance, the volumetric capacity has also been determined, which has been seldom discussed in the literature[4,15]. Practical volumetric specific capacity of electrodes involves the electrode capacity (mAh), electrode mass loading (mg/cm^2), and electrode density (g/cm^3) (or electrode volume (cm^3)). The effect of calendaring pressure on gravimetric and volumetric capacities (on an electrode volume basis) is presented in **Figure 3.4(e)** and **Figure A.4:** It can be seen from **Figure A.4** and **Table A.3** that high calendering pressure reduces slightly the gravimetric specific capacity, initial coulombic efficiency, and final capacity retention. The initial discharge gravimetric capacity decreased from 279.0 mAh/g (0 atm electrode) to 243.9 mAh/g (1500 atm electrode) and 238.8 mAh/g (3000 atm electrode). All the while, high calendering pressure increases the available volumetric capacity by fabricating higher density electrodes. For example, the TNO-900C electrode pressed under 0, 1500, and 3000 atm shows densities of 0.69, 1.45, and 1.84 g/cm^3, respectively (**Table A.3**). **Figure 3.4(e)** illustrates that the 3000 atm sample provides the highest specific volumetric capacity of 351.7 mAh/cm^3, exceeding that of the 1500 atm sample (283.3 mAh/cm^3) and more dramatically that of the 0 atm electrode (153.6 mAh/cm^3). The reversible volumetric capacity of an optimal sample (3000 atm) outperforms that of pure TNO previously reported by Toshiba[15].

Rate capability is another critical requirement for EV LIBs[41]. Galvanostatic cycling of TNO-700C, TNO-900C, and TNO-1100C was conducted at different rates (0.1 C, 0.2 C, 0.5 C, 1 C, 2 C, 5 C) for six cycles and tested at 0.5 C in subsequent cycles (**Figure 3.5(a)**). TNO-900C electrode (**Figure 3.5(a, b))** provides discharge capacities of 272 mAh/g, 262 mAh/g, 256 mAh/g, 239 mAh/g, 216 mAh/g, and 133 mAh/g, at 0.1 C, 0.2 C, 0.5 C, 1 C, 2 C, and 5 C, respectively, demonstrating better rate capability compared to those of TNO-700C and TNO-1100C. Impressively, subsequent cycles of TNO-900C at 0.5 C rate demonstrate a reversible capacity of about 250-225 mAh/g, exhibiting fast-rechargeability stability. In contrast, TNO-700C delivers 55 mAh/g at 5 C, restored to 200-180 mAh/g at subsequent cycling of 0.5 C. The corresponding values for TNO-1100C are 50 mAh/g at 5 C and 135-125 mAh/g at subsequent cycling of 0.5 C. The exceptional fast-rechargeability stability of TNO-900C anode is attributed to the combined effects of single crystal and porous microstructure as opposed to TNO-700C which lacks single crystal growth and TNO-1100C which lacks porous structure[35].

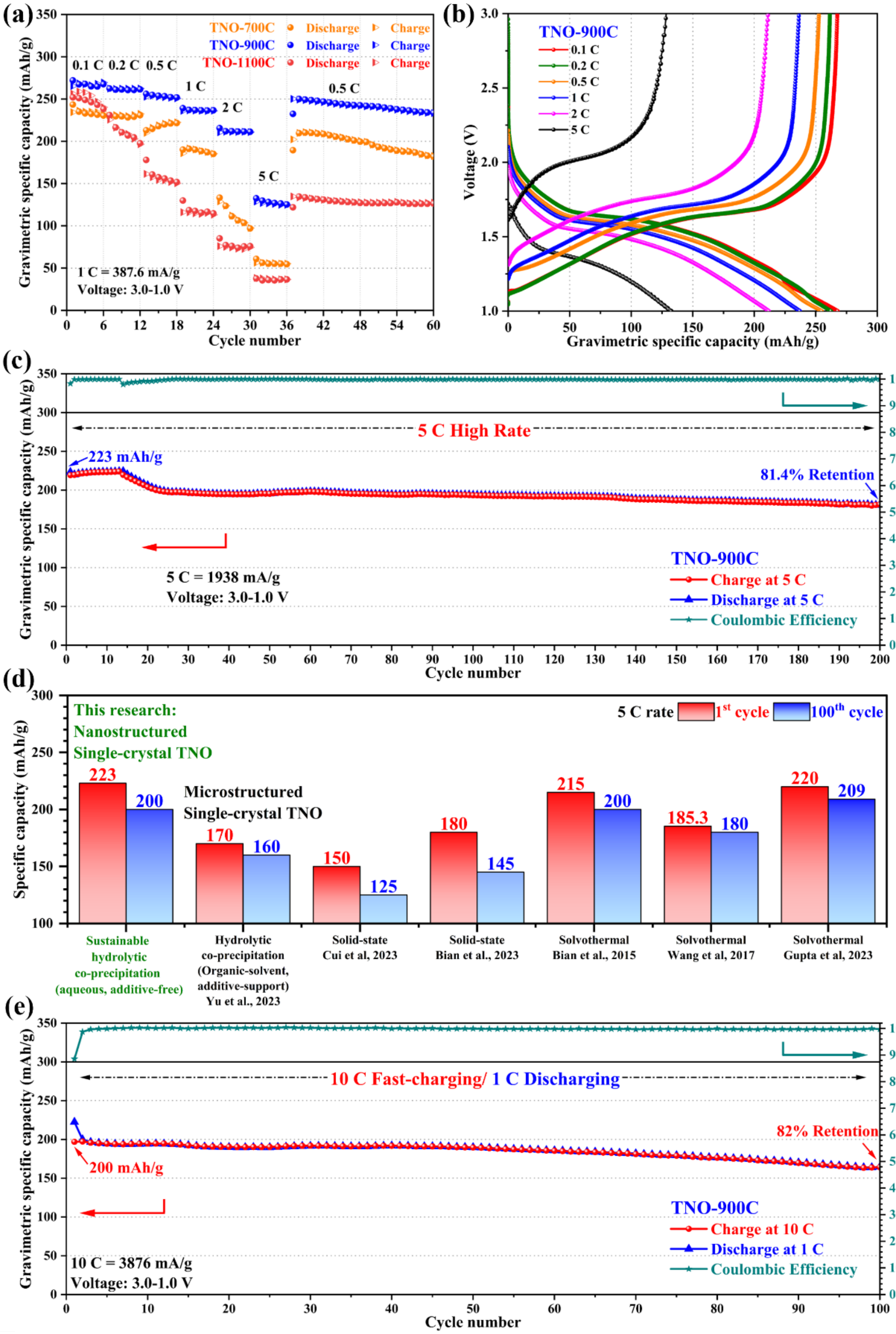

Figure 3.5 (a) Rate performance of TNO-700C, TNO-900C, and TNO-1100C. (b) Capacity voltage profile at different rates of TNO-900C. (c) Cycling performance of TNO-900C at 5 C. (d) Comparison of initial and after 100 cycles capacities at 5 C for $TiNb_2O_7$ materials synthesized via different methods. (e) Cycling performance of TNO-900C at 10 C fast charging (coupled with 1 C discharging).

The favorable rate capability of TNO-900C was further investigated by cycling it at a 5 C high rate following 10-cycle aging (electrochemical activation at 0.5 C for 10 cycles). As can be seen in **Figure 3.5(c)**, TNO-900C offers a high discharge capacity of 223 mAh/g at 1st cycle and a high capacity retention of 81.4 % (181.5 mAh/g) after 200 cycles at a high rate of 5 C. This performance outperforms several studies[26,42-46], as illustrated in **Figure 3.5(d)** and in **Table A.4**, and discussed in **Figure A.6** in terms of effect of mass loading on capacity in comparison to other works[47]. Further, the fast-charging performance of the TNO-900C anode (**Figure 3.5(e) and Figure A.5**) was tested by employing a protocol with a 10 C charging rate (full charge in 6 min) and 1 C discharging rate after 10-cycle aging. An impressive high initial charge capacity of 200 mAh/g under 10 C fast charging was obtained and a high capacity retention of 82 % (164 mAh/g) after 100 cycles. This is a remarkable fast-charging anode with high inherent cycling stability.

3.3.4. TNO Electrode Characterization: Kinetic analysis

Next, we investigated the intercalation chemistry of the three $TiNb_2O_7$ materials through electrochemical characterization. CV measurements of TNO-900C (**Figure 3.6(a)**), TNO-700C (**Figure 3.6(c)**), and TNO-1100C (**Figure 3.6(d)**) were performed at a sweep rate of 0.278 mV/s over the potential window of 3.0 V-1.0 V. Theoretically, there exist three redox couples of Ti^{4+}/Ti^{3+}, Nb^{5+}/Nb^{4+}, and Nb^{4+}/Nb^{3+} involved in the electrochemical Li intercalation reaction of TNO[48]. For the TNO-900C electrode (**Figure 3.6(a)**), the first CV curve displays a single reduction peak centered at 1.30 V, showing a significant overpotential compared with the subsequent cycles. The appearance of single reduction peaks in the CV cycle can be attributed to the overlap of the reduction reactions of Ti^{4+}/Ti^{3+}, Nb^{5+}/Nb^{4+}, and Nb^{4+}/Nb^{3+} redox couples[18,37]. After the first lithiation/delithiation cycle, the reduction peaks in the 2nd CV and 3rd CV cycles are at 1.53 V and 1.50 V, respectively, demonstrating reduced overpotential. The observed shift of reduction potential corresponds to the gradual stabilization and reversibility of electrochemical Li intercalation. Correspondingly, the dominant reduction peak at about 1.57 V and prominent oxidation peak at 1.73 V can be assigned to the redox reactions of Nb^{4+}/Nb^{5+} couple, the oxidation peaks at 1.2-1.5 V, and the reduction peak at 1.4-1.0 V can be assigned to the redox reactions of Nb^{3+}/Nb^{4+} couple[18,37]. The voltage window ranging from 1.8 to 2.2 V responds to the oxidation (anodic) peaks of Ti^{3+}/Ti^{4+} couple, and that from 1.2-1.55 V voltage window is associated with the reduction (cathodic) peaks of Ti^{4+}/Ti^{3+} couple[18,37]. In addition, EIS measurement of TNO-900C

(**Figure 3.6(b)**) was performed to evaluate the impedance of TNO material before and after CV cycling. The equivalent circuit used for fitting the EIS data is shown in **Figure A.7(c)**. The charge transfer resistance (R_{CT}) of pristine TNO illustrates a high impedance of 618.6 ohm, which is attributed to the intrinsic low electronic conductivity of $TiNb_2O_7$[20]. By contrast, the R_{CT} value dramatically reduced to 5.8 ohms after the 1st CV cycle because residual Li in the bulk of $TiNb_2O_7$ increases the electronic conductivity[20]. Meanwhile, solid electrode interphase (SEI) is formed during the initial lithiation during 1st cycle, resulting in SEI resistance (R_{SEI}) to be 11.8 ohm. **Figure A.7(a, b)** also reveals the intercalation behavior of TNO-700C and TNO-1100C, respectively, that EIS impedance significantly decreases after the first lithiation. By contrast, the TNO-700C and TNO-1100C illustrate similar electrochemical oxide reaction peaks with potential shifts within 0.5 V in **Figure 3.6(c, d)** and reduced R_{CT} after lithiation, as shown in **Figure A.7:** However, the TNO-700C **(Figure 3.6(c))** demonstrates lower current density corresponding to its low specific capacity (**Figure 3.4(b)**), while TNO-1100C (**Figure 3.6(d)**) provides irreversible CV curves evidence of poor galvanostatic cycling stability (**Figure 3.4(a)**).

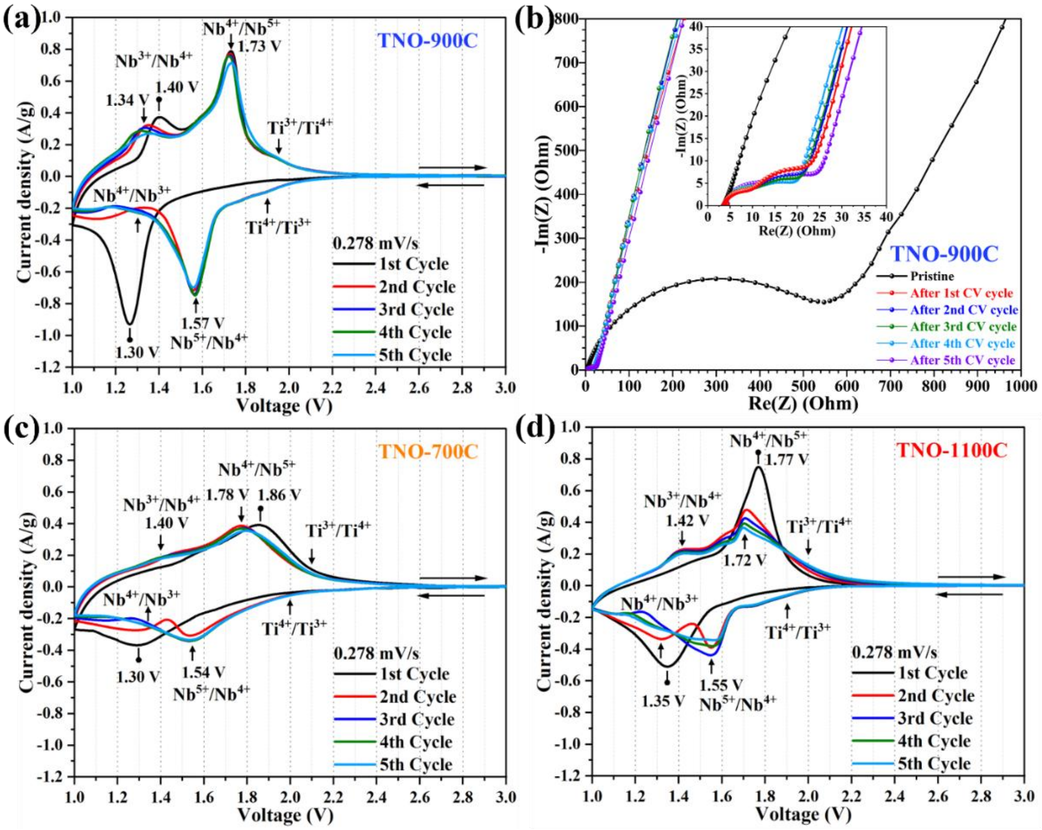

Figure 3.6 Normalized CV curves (sweep rate 0.278 mV/s) of (a) TNO-900C, (c) TNO-700C, and (d) TNO-1100C. (b) EIS results before and after each CV cycle of TNO-900C.

The Li-ion diffusion coefficient (D_{Li^+}) was comprehensively determined based on EIS, CV, and GITT measurements. Based on the EIS results in low frequency region of the Nyquist plot, the Li ion diffusion coefficient ($D_{Li^+,EIS}$) can be determined by using **equation A.12** and **equation A.13**. Accordingly, the $D_{Li^+,EIS}$ of TNO-900C is calculated to be 1.28×10^{-13} cm^2/s, which is higher than those of TNO-1100C (6.36×10^{-14} cm^2/s) and TNO-700C (5.29×10^{-16} cm^2/s). To further elucidate lithium diffusion kinetics, CV measurements at various scan rates were conducted. **Figure 3.7(a-c)** indicates that the redox peak currents and overpotentials increase with the sweep rates (v). Furthermore, the linear relation between redox peak current (I_p) and the square root of the scan rate ($v^{1/2}$) is shown in **Figure 3.7(d)**: the fitted slopes of $d(I_p)/d(v^{1/2})$ of the TNO-900C electrode are -0.16 (lithiation) and 0.21 (delithiation); that of the TNO-1100C electrode are -0.14 (lithiation) and 0.15 (delithiation); that of TNO-700C electrode are -0.11 (lithiation) and 0.13 (delithiation), respectively. By using the calculated slopes iqn **Figure 3.7(d)**, the Li^+ diffusion coefficient ($D_{Li^+,CV}$) can be determined according to Randle-Sevcik equation (**equation 3.1**)[49].

$$\mathbf{I_p=2.69\times10^5n^{3/2}SCD_{Li^+,\ CV}^{1/2}v^{1/2}} \qquad \textbf{(equation 3.1)}$$

where n is the number of electrons involved in the redox reaction (n=1 in this case), S (cm^2) is the surface area of the electrode (813.2 cm^2 for TNO-700C, 91.5 cm^2 for TNO-900C, 92.7 cm^2 for TNO-1100C), and C (mol/cm^3) is the concentration of Li ions in the $TiNb_2O_7$ anode (0.019 mol/cm^3 (lithiation) and 0.021 mol/cm^3 (delithiation) for TNO-700C; 0.019 mol/cm^3 (lithiation) and 0.026 mol/cm^3 (delithiation) for TNO-900C, 0.019 mol/cm^3 (lithiation), and 0.023 mol/cm^3 (delithiation) for TNO-1100C). The calculated results of $D_{Li^+,CV}$ are listed in **Figure 3.7(e)** and **Table A.5.** . The determined $D_{Li^+,CV}$ of TNO-900C (1.12×10^{-13} cm^2/s for lithiation, 1.08×10^{-13} cm^2/s for delithiation) is higher than those of TNO-1100C (8.33×10^{-14} cm^2/s for lithiation, 7.03×10^{-14} cm^2/s for delithiation) and TNO-700C (6.68×10^{-16} cm^2/s for lithiation, 8.20×10^{-16} cm^2/s for delithiation). The high Li^+ diffusion coefficient of TNO-900C can be attributed to the high crystallinity and nano/submicron-structure (ca. 300 nm) of $TiNb_2O_7$[35]. As shown in (**Figure 3.7(e)** and **Table A.5.**), this TNO-900C material synthesized by the new hydrolytic-coprecipitation-calcination method provides a superior Li^+ diffusion coefficient ($D_{Li^+,CV}$), compared with TNO pristine materials synthesized by solid-state synthesis[20,22,29].

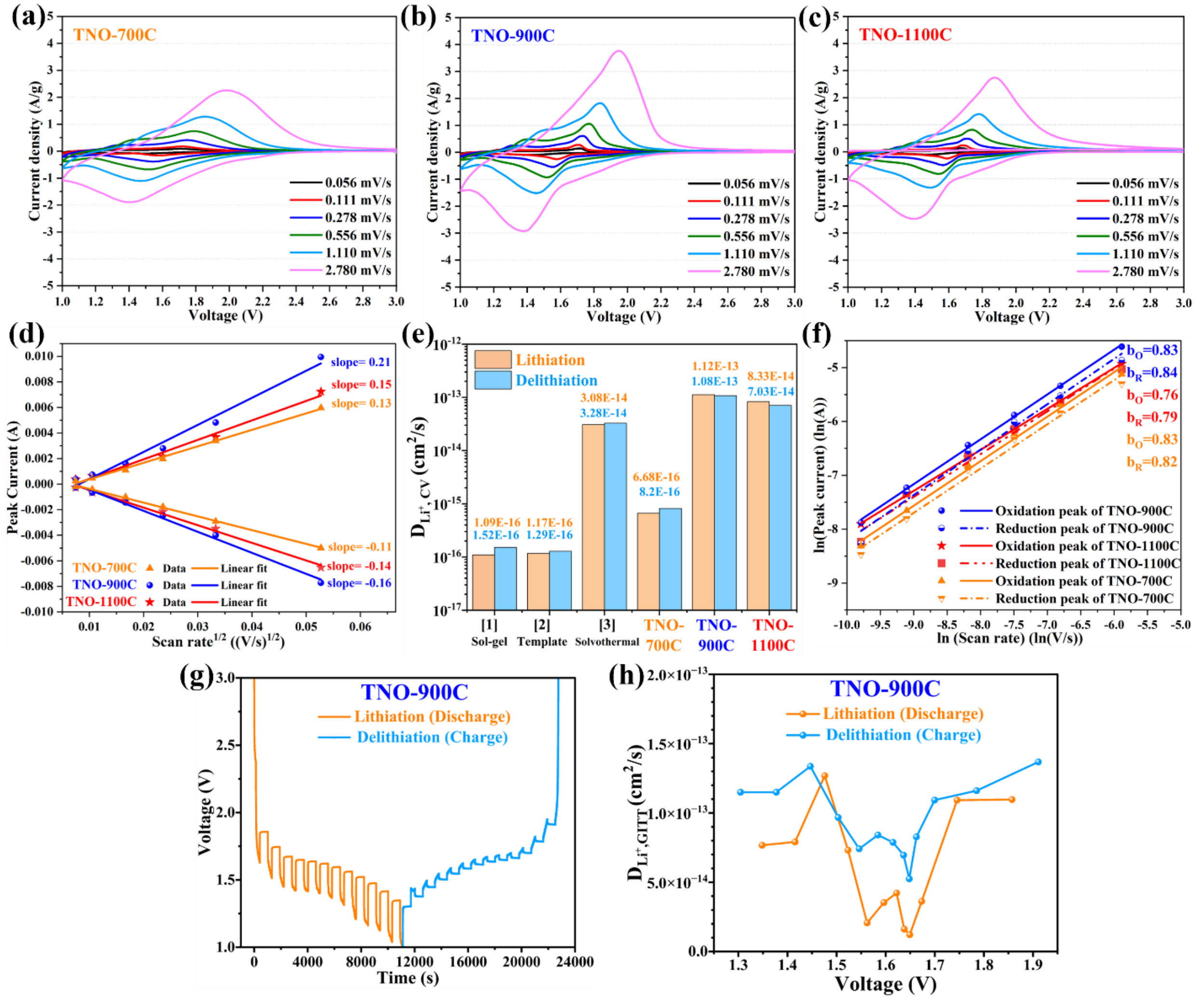

Figure 3.7 CV curves at varying sweep rates (0.056-2.78 mV/s) of (a) TNO-700C, (b) TNO-900C, and (c) TNO-1100C. (d) Comparison of peak currents (I_p) as a function of the square root of the sweep rate ($v^{1/2}$). (e) Literature comparison of $D_{Li^+,CV}$ of pristine TNO calculated according to CV data (Details shown in **Table A.5.**). (f) Linear relationship between $ln\ (I_p)$ and $ln\ (v)$ of oxidation and reduction peaks. (g) GITT curves of the 5th discharge-charge cycle at 0.5 C of TNO-900C electrode and (h) calculated $D_{Li^+,GITT}$ based on GITT data.

In addition, the Li-ion chemical diffusion coefficient can also be determined by the GITT method based on following equation (**equation 3.2**)[44,50].

$$D_{Li^+,\,GITT}=\frac{4}{\pi\tau}\left(\frac{m_B V_M}{M_B A}\right)^2\left(\frac{\Delta E_s}{\Delta E_t}\right)^2 \qquad (\tau \ll L^2/D_{Li^+}) \qquad \textbf{(equation 3.2)}$$

Where τ (s) is the duration time of the constant current pulse (300 s), m_B (g) is the mass of active materials (2.4 mg), M_B (g/mol) is the molar mass of active materials (345.68 g/mol), V_M (cm^3/mol) is the molar volume of the active materials (79.38 cm^3/mol), A (cm^2) is the contact area between the electrode and the electrolyte (96 cm^2 for TNO-900C, estimated according to BET surface area (4.0 m^2/g)); ΔE_s is the steady-state voltage change stemming from the current pulse during different rest steps, and ΔE_t is the voltage change during the galvanostatic discharge-charge time (from τ_0 to τ_{0+t}) eliminating the iR drop. As illustrated in **Figure 3.7(h)**, $D_{Li^+,GITT}$ of TNO-900C during lithiation reaction range from 1.22×10^{-14} cm^2/s to 1.27×10^{-13} cm^2/s, $D_{Li^+,GITT}$ during delithiation process vary from 5.25×10^{-14} cm^2/s to 1.37×10^{-13} cm^2/s. The lowest $D_{Li^+,GITT}$ situated at 1.55 V and 1.65 V stem from the two-phase reaction in TNb_2O_7 during lithiation/delithiation because the two-phase interface limits the diffusion of Li ions[51]. The determined values of $D_{Li^+,GITT}$ of TNO-900C (exempting the data at ~1.6 V) agree nicely with the corresponding CV-derived $D_{Li^+,CV}$ = 1.12×10^{-13} cm^2/s (**Figure 3.7(e))** and EIS-derived $D_{Li^+,EIS}$ = 1.28×10^{-13} cm^2/s values.

Lastly, the contribution of pseudocapacitance as another metric to high-rate performance is discussed. The pseudocapacitive behavior is probed first with the aid of **equation 3.3** [19,29].

$$\mathbf{i=av^b} \qquad \textbf{(equation 3.3)}$$

Where i is the peak current (A), v is the scan rate (V/s), and a, b are adjustable parameters. The value of a and b can be calculated from the plot of $\ln(i)$ versus $\ln(v)$ for both oxidation and reduction peaks. In equation 3.3, b values correlate with the Faradaic effect: the system with b=0.5 corresponds entirely to a diffusion-controlled Faradaic intercalation process; the system with b=1 originates from the surface-controlled non-Faradaic EDL effect[52]. **Figure 3.7(f)** shows that the obtained b values for the oxidation peaks/reduction peaks are 0.76/0.79 in TNO-1100C, 0.83/0.84 in TNO-900C, and 0.83/0.82 in TNO-700C, respectively. These calculated b values reveal that both lithium-ion intercalation and pseudocapacitance processes contribute to the Li-storage behavior of TNO electrodes. The higher b values of TNO-900C, compared with other samples, can be attributed to the higher crystallinity and porous nanoarchitecture, resulting in superior rate performance. Further characterization of the quantitative contribution of pseudocapacitance in the capacities of TNO-700C, TNO-900C, and TNO-1100C samples has been determined by using **equation 3.4**[53,54].

$$\mathbf{i(V)=k_1}v\mathbf{+k_2}v^{\frac{1}{2}} \qquad \textbf{(Equation 3.4)}$$

where $i(V)$ is total current at specific voltage (V), ν is voltage sweep speed, k_1 and k_2 are adjustable parameters, $k_1\nu$ denotes surface-controlled capacitive storage and $k_2\nu^{1/2}$ corresponds to diffusion-controlled intercalation storage process. **Figure A.8(a)** shows the CV behavior of TNO-900C at 0.056 mV/s with the capacitive contribution being 12.8 %. Capacitive contribution is seen to increase progressively with accelerated sweep rate reaching 50% at 2.78 mV/s for TNO-900C. The same trend is observed for all three samples (**Figure A.8(b)**), in alignment with previous reports [42,53].

3.4. Conclusion

In this study, we developed single-crystal TNO anode materials with sub-micron size for fast-charging batteries by a novel scalable hydrolytic co-precipitation method combined with optimized high-temperature calcination. The hydrolytic co-precipitation approach features advantages such as scalability, high homogeneity, and high controllability in the fabrication of nanostructured TNO-Precursor. The primary particles of the precursor were shown to exist in the range of 10 nm and enable a homogeneous crystallization reaction during the subsequent calcination process (conducted at 700, 900, and 1100 °C). The obtained TNO-900C particle characterized by a single crystal structure illustrates a high gravimetric capacity of 279 mAh/g at the initial cycle and 219.4 mAh/g after 100 cycles at 0.5 C. In addition, the TNO-900C electrode provides a practical volumetric capacity of 351.7 mAh/cm^3 after calendering at 3000 atm. In addition, TNO-900C delivers remarkable cycling stability at 5 C providing a high capacity of 223 mAh/g and a high retention of 81.4 % after 200 cycles. Most importantly, TNO-900C illustrates outstanding fast-charging performance with a reversible capacity of 200 mAh/g under 10 C fast charging (6 min full charge) and 1 C discharging. From the kinetic analysis, a high Li$^+$ diffusion coefficient was achieved for TNO-900C, ranging from 1.22×10^{-14} cm^2/s to 1.37×10^{-13} cm^2/s. This superior electrochemical performance of TNO-900C originates from its monocrystalline property and submicron size. Findings from this research, particularly on the high gravimetric/volumetric capacity and intercalation behavior of single-crystal TNO at high rates, provide new insights into developing practical TNO anode materials for fast-charging EV LIBs.

3.5. References

[1] W. Zhang, D.-H. Seo, T. Chen, L. Wu, M. Topsakal, Y. Zhu, D. Lu, G. Ceder, F. Wang, Kinetic pathways of ionic transport in fast-charging lithium titanate, Science 367 (2020) 1030-1034. https://doi.org/10.1126/science.aax3520.

[2] J.W. Choi, D. Aurbach, Promise and reality of post-lithium-ion batteries with high energy densities, Nat. Rev. Mater. 1 (2016) 16013. https://doi.org/10.1038/natrevmats.2016.13.

[3] M. Winter, B. Barnett, K. Xu, Before Li ion batteries, Chem. Rev. 118 (2018) 11433-11456. https://doi.org/10.1021/acs.chemrev.8b00422.

[4] K.J. Griffith, Y. Harada, S. Egusa, R.M. Ribas, R.S. Monteiro, R.B. Von Dreele, A.K. Cheetham, R.J. Cava, C.P. Grey, J.B. Goodenough, Titanium niobium oxide: from discovery to application in fast-charging lithium-ion batteries, Chem. Mater. 33 (2021) 4-18. https://doi.org/10.1021/acs.chemmater.0c02955.

[5] T. Gao, Y. Han, D. Fraggedakis, S. Das, T. Zhou, C.-N. Yeh, S. Xu, W.C. Chueh, J. Li, M.Z. Bazant, Interplay of lithium intercalation and plating on a single graphite particle, Joule 5 (2021) 393-414. https://doi.org/10.1016/j.joule.2020.12.020.

[6] X. Lu, L. Gu, Y.S. Hu, H.C. Chiu, H. Li, G.P. Demopoulos, L.Q. Chen, New insight into the atomic-scale bulk and surface structure evolution of $Li_4Ti_5O_{12}$ anode, J. Am. Chem. Soc. 137 (2015) 1581-1586. https://doi.org/10.1021/ja5115562.

[7] H.C. Chiu, X. Lu, J. Zhou, L. Gu, J. Reid, R. Gauvin, K. Zaghib, G.P. Demopoulos, Capacity fade mechanism of $Li_4Ti_5O_{12}$ nanosheet anode, Adv. Energy Mater. 7 (2017) 1601825. https://doi.org/10.1002/aenm.201601825.

[8] W. Cao, J. Zhang, H. Li, Batteries with high theoretical energy densities, Energy Storage Mater. 26 (2020) 46-55. https://doi.org/https://doi.org/10.1016/j.ensm.2019.12.024.

[9] J. Han, Y. Huang, J.B. Goodenough, New anode framework for rechargeable lithium batteries, Chem. Mater. 23 (2011) 2027-2029. https://doi.org/dx.doi.org/10.1021/cm200441h.

[10] Y. Wu, D. Liu, D. Qu, J. Li, Z. Xie, X. Zhang, H. Chen, H. Tang, Porous oxygen-deficient $TiNb_2O_7$ spheres wrapped by MXene as high-rate and durable anodes for liquid and all-solid-state lithium-ion batteries, Chem. Eng. J. (2022) 135328. https://doi.org/https://doi.org/10.1016/j.cej.2022.135328.

[11] K. Liu, J.A. Wang, J. Yang, D.Q. Zhao, P.Y. Chen, J.Z. Man, X.Y. Yu, Z.Q. Wen, J.C. Sun, Interstitial and substitutional V^{5+}-doped $TiNb_2O_7$ microspheres: A novel doping way to achieve high-performance electrodes, Chem. Eng. J. 407 (2021) 127190. https://doi.org/10.1016/j.cej.2020.127190.

[12] A.A. Voskanyan, M. Abramchuk, A. Navrotsky, Entropy stabilization of TiO_2-Nb_2O_5 Wadsley-Roth shear phases and their prospects for lithium ion battery anode materials, Chem. Mater. 32 (2020) 5301-5308. https://doi.org/https://dx.doi.org/10.1021/acs.chemmater.0c01553.

[13] G. Zhao, L. Zhang, C. Li, H. Huang, X. Sun, K. Sun, A practical Li ion battery anode material with high gravimetric/volumetric capacities based on T-Nb_2O_5/graphite composite, Chem. Eng. J. 328 (2017) 844-852. https://doi.org/https://doi.org/10.1016/j.cej.2017.07.111.

[14] R. Mo, X. Tan, F. Li, R. Tao, J. Xu, D. Kong, Z. Wang, B. Xu, X. Wang, C. Wang, J. Li, Y. Peng, Y. Lu, Tin-graphene tubes as anodes for lithium-ion batteries with high volumetric and gravimetric energy densities, Nat. Commun. 11 (2020) 1374. https://doi.org/10.1038/s41467-020-14859-z.

[15] N. Takami, K. Ise, Y. Harada, T. Iwasaki, T. Kishi, K. Hoshina, High-energy, fast-charging, long-life lithium-ion batteries using $TiNb_2O_7$ anodes for automotive applications, J. Power Sources 396 (2018) 429-436. https://doi.org/10.1016/j.jpowsour.2018.06.059.

[16] T. Yuan, L. Soule, B. Zhao, J. Zou, J. Yang, M. Liu, S. Zheng, Recent advances in titanium niobium oxide anodes for high-power lithium-ion batteries, Energy & Fuels 34 (2020) 13321-13334. https://doi.org/10.1021/acs.energyfuels.0c02732.

[17] Z. Zhao, Z. Xue, Q. Xiong, Y. Zhang, X. Hu, H. Chi, H. Qin, Y. Yuan, H. Ni, Titanium niobium oxides ($TiNb_2O_7$): Design, fabrication and application in energy storage devices, Sustainable

Materials and Technologies 30 (2021) e00357. https://doi.org/https://doi.org/10.1016/j.susmat.2021.e00357.

[18] W. Liu, J. Liu, M. Zhu, W. Wang, Y. Sun, Closely compacted $TiNb_2O_7$-C assembly for fast-charging battery anodes, ACS Appl. Energy Mater. 4 (2021) 12319-12325. https://doi.org/10.1021/acsaem.1c02144.

[19] C. Yang, D. Ma, J. Yang, M. Manawan, T. Zhao, Y. Feng, J. Li, Z. Liu, Y.-W. Zhang, R.B. Von Dreele, B.H. Toby, C.P.d.L. Albarrán, J.H. Pan, Crystallographic insight of reduced lattice volume expansion in mesoporous Cu^{2+}-doped $TiNb_2O_7$ microspheres during Li^+ insertion, Adv. Funct. Mater 33 (2023) 2212854. https://doi.org/https://doi.org/10.1002/adfm.202212854.

[20] K.J. Griffith, I.D. Seymour, M.A. Hope, M.M. Butala, L.K. Lamontagne, M.B. Preefer, C.P. Koçer, G. Henkelman, A.J. Morris, M.J. Cliffe, S.E. Dutton, C.P. Grey, Ionic and electronic conduction in $TiNb_2O_7$, J. Am. Chem. Soc. 141 (2019) 16706-16725. https://doi.org/10.1021/jacs.9b06669.

[21] S. Gong, Y. Wang, Q. Zhu, M. Li, Y. Wen, H. Wang, J. Qiu, B. Xu, High-rate lithium storage performance of $TiNb_2O_7$ anode due to single-crystal structure coupling with Cr^{3+}-doping, J. Power Sources 564 (2023) 232672. https://doi.org/https://doi.org/10.1016/j.jpowsour.2023.232672.

[22] X. Lu, Z.L. Jian, Z. Fang, L. Gu, Y.S. Hu, W. Chen, Z.X. Wang, L.Q. Chen, Atomic-scale investigation on lithium storage mechanism in $TiNb_2O_7$, Energy Environ. Sci. 4 (2011) 2638-2644. https://doi.org/10.1039/c0ee00808g.

[23] K. Ise, S. Morimoto, Y. Harada, N. Takami, Large lithium storage in highly crystalline $TiNb_2O_7$ nanoparticles synthesized by a hydrothermal method as anodes for lithium-ion batteries, Solid State Ion. 320 (2018) 7-15. https://doi.org/10.1016/j.ssi.2018.02.027.

[24] H.C. Chiu, N. Brodusch, R. Gauvin, A. Guerfi, K. Zaghib, G.P. Demopoulos, Aqueous synthesized nanostructured $Li_4Ti_5O_{12}$ for high-performance lithium ion battery anodes, J. Electrochem. Soc. 160 (2013) A3041-A3047. https://doi.org/10.1149/2.008305jes.

[25] Y. Han, Y. Lei, J. Ni, Y. Zhang, Z. Geng, P. Ming, C. Zhang, X. Tian, J.-L. Shi, Y.-G. Guo, Q. Xiao, Single-Crystalline Cathodes for Advanced Li-Ion Batteries: Progress and Challenges, Small 18 (2022) 2107048. https://doi.org/https://doi.org/10.1002/smll.202107048.

[26] M. Yu, Z.F. Cai, Q. Li, S. Wang, Y.Z. Ma, G.S. Song, W.D. Yang, C. Wen, Enhanced energy storage performance of Zr-doped $TiNb_2O_7$ nanospheres prepared by the hydrolytic method, ACS Sustain. Chem. Eng. 11 (2023) 5147-5154. https://doi.org/10.1021/acssuschemeng.2c07144.

[27] V. Paulraj, T. Saha, K. Vediappan, K. Kamala Bharathi, Synthesis and electrochemical properties of $TiNb_2O_7$ nanoparticles as an anode material for lithium ion batteries, Mater. Lett. 304 (2021) 130681. https://doi.org/https://doi.org/10.1016/j.matlet.2021.130681.

[28] R. Qian, C. Yang, D. Ma, K. Li, T. Feng, J. Feng, J.H. Pan, Robust lithium storage of block copolymer-templated mesoporous $TiNb_2O_7$ and $TiNb_2O_7$@C anodes evaluated in half-cell and full-battery configurations, Electrochim. Acta 379 (2021) 138179. https://doi.org/https://doi.org/10.1016/j.electacta.2021.138179.

[29] M. Uceda, H.-C. Chiu, J. Zhou, R. Gauvin, K. Zaghib, G.P. Demopoulos, Nanoscale assembling of graphene oxide with electrophoretic deposition leads to superior percolation network in Li-ion electrodes: $TiNb_2O_7$/rGO composite anodes, Nanoscale 12 (2020) 23092–23104. https://doi.org/https://doi.org/10.1039/D0NR06082H.

[30] W. Wu, W. Lin, H.J. Chen, K.Y. Wei, Z.T. Li, H.T. Yang, M.X. Liu, H.C. Xiang, L.B. Deng, L. Yao, Iron oxide encapsulated titanium niobate nanotubes as a high-performance lithium-free anode for solid-state batteries, J. Mater. Chem. A 9 (2021) 4880-4889. https://doi.org/10.1039/d0ta11030b.

[31] H. Li, L. Shen, G. Pang, S. Fang, H. Luo, K. Yang, X. Zhang, $TiNb_2O_7$ nanoparticles assembled into hierarchical microspheres as high-rate capability and long-cycle-life anode materials for lithium ion batteries, Nanoscale 7 (2015) 619-624. https://doi.org/10.1039/C4NR04847D.

[32] M. Yang, S. Li, J. Huang, Three-dimensional cross-linked Nb_2O_5 polymorphs derived from cellulose substances: insights into the mechanisms of lithium storage, ACS Appl. Mater. Interfaces (2021) 39501-39512. https://doi.org/10.1021/acsami.1c11720.

[33] Z.J. Yao, X.H. Xia, S.Z. Zhang, C.A. Zhou, G.X. Pan, Q.Q. Xiong, Y.D. Wang, X.L. Wang, J.P. Tu, Oxygen defect boosted N-doped $Ti_2Nb_{10}O_{29}$ anchored on core-branch carbon skeleton for both high-rate liquid & solid-state lithium ion batteries, Energy Storage Mater. 25 (2020) 555-562. https://doi.org/10.1016/j.ensm.2019.09.027.

[34] S.F. Lou, X.Q. Cheng, Y. Zhao, A. Lushington, J.L. Gao, Q. Li, P.J. Zuo, B.Q. Wang, Y.Z. Gao, Y.L. Ma, C.Y. Du, G.P. Yin, X.L. Sun, Superior performance of ordered macroporous $TiNb_2O_7$ anodes for lithium ion batteries: Understanding from the structural and pseudocapacitive insights on achieving high rate capability, Nano Energy 34 (2017) 15-25. https://doi.org/10.1016/j.nanoen.2017.01.058.

[35] R. Tao, G. Yang, E.C. Self, J. Liang, J.R. Dunlap, S. Men, C.-L. Do-Thanh, J. Liu, Y. Zhang, S. Zhao, H. Lyu, A.P. Sokolov, J. Nanda, X.-G. Sun, S. Dai, Ionic liquid-directed nanoporous $TiNb_2O_7$ anodes with superior performance for fast-rechargeable lithium-ion batteries, Small 16 (2020) 2001884. https://doi.org/https://doi.org/10.1002/smll.202001884.

[36] B.K. Guo, X.Q. Yu, X.G. Sun, M.F. Chi, Z.A. Qiao, J. Liu, Y.S. Hu, X.Q. Yang, J.B. Goodenough, S. Dai, A long-life lithium-ion battery with a highly porous $TiNb_2O_7$ anode for large-scale electrical energy storage, Energy Environ. Sci. 7 (2014) 2220-2226. https://doi.org/10.1039/c4ee00508b.

[37] T. Tian, L.L. Lu, Y.C. Yin, F. Li, T.W. Zhang, Y.H. Song, Y.H. Tan, H.B. Yao, Multiscale designed niobium titanium oxide anode for fast charging lithium ion batteries, Adv. Funct. Mater 31 (2021) 2007419. https://doi.org/10.1002/adfm.202007419.

[38] G. Wang, J. Chen, F. Zhang, L. Zhao, Q. Chen, G. Wang, H. Zhang, Enhanced low-temperature performance of multiscale (Nb_2O_5/$TiNb_2O_7$)@C nanoarchitectures with intensified ion diffusion kinetics, J. Energy Storage 74 (2023) 109415. https://doi.org/https://doi.org/10.1016/j.est.2023.109415.

[39] W.Q. Zhu, B.B. Zou, C.H. Zhang, D.H.L. Ng, S.A. El-Khodary, X.H. Liu, G.C. Li, J.X. Qiu, Y. Zhao, S.L. Yang, J.B. Lian, H.M. Li, Oxygen-defective $TiNb_2O_{7-x}$ nanochains with enlarged lattice spacing for high-rate lithium ion capacitor, Adv. Mater. Interfaces 7 (2020) 2000705. https://doi.org/10.1002/admi.202000705.

[40] G. Liu, L. Zhao, R. Sun, W. Chen, M. Hu, M. Liu, X. Duan, T. Zhang, Mesoporous $TiNb_2O_7$ microspheres as high performance anode materials for lithium-ion batteries with high-rate capability and long cycle-life, Electrochim. Acta 259 (2018) 20-27. https://doi.org/https://doi.org/10.1016/j.electacta.2017.10.138.

[41] S. Li, K. Wang, G. Zhang, S. Li, Y. Xu, X. Zhang, X. Zhang, S. Zheng, X. Sun, Y. Ma, Fast charging anode materials for lithium-ion batteries: Current status and perspectives, Adv. Funct. Mater (2022) 2200796. https://doi.org/https://doi.org/10.1002/adfm.202200796.

[42] P. Cui, P. Zhang, X. Chen, X. Chen, T. Wan, Y. Zhou, M. Su, Y. Liu, H. Xu, D. Chu, Oxygen defect and Cl^--doped modulated $TiNb_2O_7$ compound with high rate performance in lithium-ion batteries, ACS Appl. Mater. Interfaces 15 (2023) 43745-43755. https://doi.org/10.1021/acsami.3c08524.

[43] H.W. Bian, J.J. Gu, Z.C. Song, H.X. Gong, Z.X. Zhang, W.T. Mao, K.Y. Bao, An effective strategy to achieve high-power electrode by tin doping: $Sn_xTiNb_2O_7$ as a promising anode material with a large capacity and high-rate performance for lithium-ion batteries, Journal of Materials Science-Materials In Electronics 34 (2023) 1826. https://doi.org/10.1007/s10854-023-11183-2.

[44] H. Park, H.B. Wu, T. Song, X.W. Lou, U. Paik, Porosity-controlled $TiNb_2O_7$ microspheres with partial nitridation as a practical negative electrode for high-power lithium-ion batteries, Adv. Energy Mater. 5 (2015) 1401945. https://doi.org/10.1002/aenm.201401945.

[45] G.Q. Wang, Z.S. Wen, L.L. Du, Y.E. Yang, S. Li, J.C. Sun, S.J. Ji, Hierarchical Ti-Nb oxide microspheres with synergic multiphase structure as ultra-long-life anode materials for lithium-ion batteries, J. Power Sources 367 (2017) 106-115. https://doi.org/10.1016/j.jpowsour.2017.09.061.

[46] K.K. Gupta, K.-C. Li, S. Balaji, P.S. Kumar, C.-H. Lu, Microwave-assisted synthesis and electrochemical characterization of $TiNb_2O_7$ microspheres as anode materials for lithium-ion batteries, Journal of the American Ceramic Society 106 (2023) 4192-4201. https://doi.org/https://doi.org/10.1111/jace.19000.

[47] H. Lyu, J. Li, T. Wang, B.P. Thapaliya, S. Men, C.J. Jafta, R. Tao, X.-G. Sun, S. Dai, Carbon coated porous titanium niobium oxides as anode materials of lithium ion batteries for extreme fast charge applications, ACS Appl. Energy Mater. 3 (2020) 5657-5665.

[48] Y.-S. Hsiao, L.-Y. Weng, T.-H. Cheng, T.-Y. Huang, Y.-J. Wu, J.-H. Huang, N.-J. Wu, S.-C. Hsu, H.C. Weng, C.-P. Chen, Construction of core-shell $TiNb_2O_7/Li_4Ti_5O_{12}$ composites with improved lithium storage for lithium-ion batteries, J. Energy Storage 77 (2024) 109860. https://doi.org/https://doi.org/10.1016/j.est.2023.109860.

[49] K. Tang, X. Yu, J. Sun, H. Li, X. Huang, Kinetic analysis on $LiFePO_4$ thin films by CV, GITT, and EIS, Electrochim. Acta 56 (2011) 4869-4875. https://doi.org/https://doi.org/10.1016/j.electacta.2011.02.119.

[50] Y. Zeng, H.-C. Chiu, B. Ouyang, K. Zaghib, G.P. Demopoulos, Defect engineering of iron-rich orthosilicate cathode materials with enhanced lithium-ion intercalation capacity and kinetics, ACS Appl. Energy Mater. 3 (2020) 675-686. https://doi.org/10.1021/acsaem.9b01869.

[51] D. Li, H. Zhou, Two-phase transition of Li-intercalation compounds in Li-ion batteries, Mater. Today 17 (2014) 451-463. https://doi.org/https://doi.org/10.1016/j.mattod.2014.06.002.

[52] T. Jiang, S. Ma, J. Deng, T. Yuan, C. Lin, M. Liu, Partially reduced titanium niobium oxide: A high-performance lithium-storage material in a broad temperature range, Adv. Sci. 9 (2022) 2105119. https://doi.org/https://doi.org/10.1002/advs.202105119.

[53] Y. Zhang, C. Kang, W. Zhao, B. Sun, X. Xiao, H. Huo, Y. Ma, P. Zuo, S. Lou, G. Yin, Crystallographic engineering to reduce diffusion barrier for enhanced intercalation pseudocapacitance of $TiNb_2O_7$ in fast-charging batteries, Energy Storage Mater. 47 (2022) 178-186. https://doi.org/https://doi.org/10.1016/j.ensm.2022.01.061.

[54] C. Choi, D.S. Ashby, D.M. Butts, R.H. DeBlock, Q. Wei, J. Lau, B. Dunn, Achieving high energy density and high power density with pseudocapacitive materials, Nat. Rev. Mater. 5 (2020) 5-19. https://doi.org/10.1038/s41578-019-0142-z.

4. Fe^{3+}-substitutional Doping of Nanostructured Single-crystal $TiNb_2O_7$ for Long-stable Cycling of Ultra-Fast Charging Anodes

Bridge: In **Chapter 3**, we first report a novel scalable aqueous synthesis method yielding single-crystal TNO particles with submicron size (ca. 300 nm) for LIB anode. This monocrystalline TNO anode material illustrates outstanding fast-charging performance with a reversible capacity of 200 mAh/g under 10 C fast charging and 1 C discharging. The obtained TNO anode demonstrates a high gravimetric capacity (250 mAh/g) and an impressive volumetric capacity (360 mAh/cm^3) at 0.5 C and offers remarkable cycling stability at 2 C with a high retention of 86.8 % after 200 cycles. However, the battery degradation after hundreds of cycles under high rate impede their long-cycling application, which likely stem from the change of material structure. The work in **Chapter 4** addresses the second objective of thesis, i.e., to modify the cycling stability of single-crystal TNO by Fe^{3+} substitutional doping and investigate the underlying mechanism. Based on the universal aqueous precipitation synthesis developed in **Chapter 3**, we achieved one in-situ substitutional doping of Fe (in the form of $FeCl_3$) by leveraging the similar chemical properties and thermodynamic behavior of $TiCl_4$ and $NbCl_5$ during aqueous precipitation reactions. The novel Fe^{3+}-doped TNO monocrystalline, thanks to the increased conductivity, modulated lithium-ion diffusion channels, and enhanced material structural stability, demonstrates significant improvements in fast-charging capability and cycling durability up beyond 1000 cycles.

This chapter is a reproduction of the manuscript published in ***Nano Energy***, with the following citation:

Fan Yu, Bobby Miglani, Shuaishuai Yuan, Rana Yekani, Kirk H. Bevan, George P. Demopoulos, Fe^{3+}-substitutional Doping of Nanostructured Single-crystal $TiNb_2O_7$ for Long-stable Cycling of Ultra-Fast Charging Anodes. ***Nano Energy*** 133 (2025) 110494. https://doi.org/https://doi.org/10.1016/j.nanoen.2024.110494.

Abstract

Titanium niobate ($TiNb_2O_7$, TNO) has emerged as a promising lithium-ion battery (LIB) anode option for fast charging applications. However, the cycling durability of TNO under extremely fast charging is still limited, and the corresponding structural alteration mechanism remains unclear. This research reports an ultra-fast charging anode with long-term cycling stability

enabled by Fe substitution in single-crystal TNO nanostructures. The underlying mechanism via which Fe substitution affects TNO's electronic properties, ionic diffusion kinetics, and structural stability is revealed through combined theoretical modeling and experimental characterization. The optimal Fe^{3+}-doped TNO monocrystalline material ($Fe_{0.05}Ti_{0.95}Nb_2O_{6.975}$) (Fe5-TNO) provides a remarkable charge capacity of 238 mAh/g under a 10 C (6 min charging time only) extreme fast-charging protocol (coupled with 1 C discharge), and a high capacity of 200 mAh/g at 5 C with high cycling retention of 85 % after 1000 cycles. Our calculations suggest that Fe^{3+} substitutional doping leads to a lowering of the band gap coupled with a reduction in the Li^+ diffusion energy barrier. Overall, these factors contribute to reduced capacity decay and extreme fast charging, together promoting durable cycling performance suitable for LIB usage. Reflection electron energy loss spectroscopy (REELS) reveals that Fe^{3+} doping narrows the band gap from 3.75 eV of TNO to approximately 3.40 eV for Fe5-TNO; after initial lithiation, both TNO and Fe^{3+}-doped TNO are transformed into a higher-conductivity phase, in agreement with density functional theory (DFT) predictions. Meanwhile Fe^{3+} doping is shown exhibited to decrease the Li^+ diffusion energy barrier, boosting the Li^+ diffusion coefficient by one order of magnitude, from 10^{-13} to 10^{-12} cm^2/s. This research provides new insights into the design of next-generation fast-charging LIB anodes via DFT-guided substitutional doping.

4.1. Introduction

Electric vehicles (EVs) require extreme fast charging (XFC), corresponding to a charging time of less than 15 min (> 4 C fast charging) to reach 80% state of charge, and long cycling [1]. However, existing commercial electrode materials hardly meet these requirements. From the perspective of the LIB anode, several problems remain. For example, dominant and cost-effective commercial graphite anode materials with low working potential (ca., 0.1 V *vs.* Li/Li^+) suffer from Li dendrite formation safety issues, primarily due to overpotential operating under extreme fast charging (XFC) [2]. Next-generation fast-charging anode materials with a high rate, safe operating potential, and long cycling are thus needed to overcome these challenges. One of the most promising commercialized fast-charging anode materials, spinel lithium titanate ($Li_4Ti_5O_{12}$) offers: superior fast-charging capability, safe working potential (ca., 1.5 V *vs.* Li/Li^+), and excellent cycling stability, benefitting from its "zero-strain" property and high Li^+ diffusion kinetics. However, $Li_4Ti_5O_{12}$ possesses low theoretical capacity (175 mAh/g) that is only half of the aforementioned commercial graphite anode, limiting its further application in EVs. By contrast, titanium niobate ($TiNb_2O_7$) provides good fast-charging properties, safe operating voltage (ca. 1.6 V *vs.* Li/Li^+) at high rates, and high theoretical capacity (387 mAh/g) [3,4]. However, the stoichiometric $TiNb_2O_7$ anode is characterized by low electronic conductivity originating from a wide band gap [4,5], suffers from sluggish ion diffusion kinetics [6], and exhibits limited cyclability when subjected to fast charging.

Substitutional cation doping is a promising modification strategy for unlocking the extremely fast-charging capability of $TiNb_2O_7$ anode materials and achieving a long cycle life [7-10]. From the perspective of electronic conductivity, substitutional doping can narrow the band gap by providing mid-gap defect bands/states and by possibly also introducing more holes (p-type doping) or valence electrons (n-type doping) to increase the conductivity [5,7]. From the aspect of Li^+ diffusion, substitutional doping may also reduce the Li^+ hopping energy barrier, thereby increasing the lithium-ion diffusion coefficient [5,7]. To date, many element dopants have been investigated to efficiently enhance their electrochemical performance, such as chromium (Cr^{3+}) [11], lanthanum (La^{3+}) [12], zirconium (Zr^{4+}) [13], ruthenium (Ru^{4+}) [14], molybdenum (Mo^{5+} and Mo^{6+}) [15-17], tungsten (W^{6+}) [18,19], etc. Nevertheless, most of these dopants are costly heavy or rare elements, and in some cases, can constitute environmental hazards. Therefore, abundant, cost-efficient, and environmentally friendly elements for cation doping, including copper (Cu^{2+}) [8,20] and iron (Fe^{3+}), are worth exploring for sustainable application. For example, Yang et al. [8] have shown Cu^{2+} doping into Ti^{4+} sites enhances the electrochemical performance of TNO, proving that substitutional doping can modulate the bandgap and reduce the Li^+ diffusion energy barrier. Mechanistically, previous studies have attributed the improved Li^+ diffusion kinetics to the larger ion radius of Cu^{2+} dopant (*ca*. 0.72 Å), compared to Ti^{4+} (*ca*. 0.61 Å) and Nb^{5+} (*ca*. 0.69 Å), which results in structural changes that enlarge the Li^+ transport channels [8,20]. This mechanism is a commonly accepted explanation for cation doping with larger-radius dopants, such as Cu^{2+} [8,20], La^{3+} [12], Zr^{4+} [13], etc. However, the impact of structural distortions from quasi-equisized dopants on widening Li ion diffusion channels is not well understood. Therefore, applying Fe^{3+} with a quasi-equisized ion radius (*ca*. 0.64 Å) [21] as a dopant can provide new insights into the cation substitutional doping mechanism. Additionally, the Fe^{3+}/Fe^{2+} redox couple operated in the iron oxide anode [22] and Fe-doped niobium-based oxide [21], could also enhance Li-storage capacity. However, Fe^{3+} substitutional doping in $TiNb_2O_7$ crystals has not been investigated.

Furthermore, the nanostructure of TNO-based materials can also influence the fast-charging capability by providing shorter Li^+ diffusion pathways and suppression of crystal volume expansion. To date, however, it remains challenging to effect in-situ substitutional doping of transition metal into nanostructured TNO materials with tunable composition [1,7,9]. Current substitutional doping synthesis techniques for TNO anode materials, such as solid-state methods [14] and organic-solvent methods [4,19,23], suffer from insufficient homogeneity, complicated procedures, scalability challenges, or environmental concerns. These limitations hinder the practical application of TNO [7]. Consequently, exploring new fabrication methods that enable nanostructured TNO and compositional doping becomes crucial. Our previous research [24] developed one scalable green aqueous approach by controlled co-precipitation to engineer submicron-sized monocrystalline TNO materials, which provides upon modification a scalable in-situ substitutional doping method for single-crystal TNO nanomaterials. Given this nano-synthesis approach using $TiCl_4$ and $NbCl_5$ as precursors, Fe (in the form of $FeCl_3$) exhibits similar chemical properties and thermodynamic behavior during aqueous precipitation reactions, [25] making it a suitable choice for in-situ substitutional doping.

Herein, we investigated iron (Fe^{3+}) substitution in nanostructured TNO monocrystalline materials ($Fe_xTi_{1-x}Nb_2O_{7-x/2}$, x=0.01, 0.05, 0.10) via an aqueous homogeneous synthesis method with great promise towards industrial scalability and have further explored in-depth the mechanism of Fe^{3+} doping to enhance the ultra-fast charging response. The optimal 5% Fe^{3+}-doped TNO (Fe5-TNO) is shown to demonstrate remarkable extreme fast-charging capability (238 mAh/g under 10 C charge/1 C discharge), and outstanding cycling stability at 5 C high rate (85 % retention after 1000 cycles). This research provides new insight into the multifaceted impact of Fe doping into TNO in terms of crystal structure and redox reaction evolution during lithiation, ionic diffusion and electronic conductivity enhancement through synergetic experimental investigation and density functional theory (DFT) calculations.

4.2. Experimental Section

4.2.1. Materials Synthesis

The iron substitutional doping of nanostructured Fe-doped TNO materials is a modification of the universal homogeneous synthesis method [24] (**Scheme B.1**), which includes the following steps: (1) cold-temperature solution preparation, (2) pH-controlled hydrolytic co-precipitation, and

(3) high-temperature calcination. First, three separate individual aqueous stock solutions were prepared by slowly adding respectively, ferric chloride hexahydrate (99 % $FeCl_3 \cdot 6H_2O$, Sigma-Aldrich, USA), titanium tetrachloride (99.0% $TiCl_4$, Sigma-Aldrich, USA), and niobium pentachloride (99% $NbCl_5$, Thermo Fisher Scientific, USA) salts into cold DI water (below 10 ºC using an ice bath) under vigorous magnetic agitation. The concentrations of these three stock solutions were adjusted to 0.1 mol/L Fe(III), 1 mol/L Ti(IV), and 0.5 mol/L Nb(V), respectively. Second, the three solutions were mixed at appropriate ratios with DI water using variable amounts of Fe (x=0, 0.01, 0.05, 0.1), to yield 200 mL Fe-Ti-Nb-Cl solution containing 0.05 mol/L Nb(V). After that, the Fe-Ti-Nb-Cl aqueous solutions were neutralized from acid (pH<1) to base (pH=9) by dropwise ammonium hydroxide (99.9% NH_4OH, 29% NH_3 basis, Sigma-Aldrich, USA) at a rate of 0.1 mL/min under agitation (400 rpm) addition to produce precursor $Fe_xTi_{1-x}Nb_2O_{7-x/2}$ precipitate via hydrolytic co-precipitation reaction. The obtained amorphous co-precipitate solids (Fe-TNO precursors) were then centrifugated, washed five times with 1 L warm water (60-80 ºC), and dried in an oven at 80 ºC overnight. Finally, nanostructured $Fe_xTi_{1-x}Nb_2O_{7-x/2}$ (Fe-TNO crystal) monocrystalline materials were obtained by high-temperature calcination processing. As determined previously [24], the Fe-TNO precursor was annealed at 900 ºC for 4 h in continuous flow oxygen gas (10 vol% O_2 and 90 vol% N_2) with a heating ramping rate of 5 ºC/min in the tube furnace oven (OTF-1200X-S50-2F Mini CVD tube furnace, MTI Corporation, USA).

4.2.2. Material Characterization

The solution concentrations of Fe(III), Ti(IV), and Nb(V) and the elemental composition of solids (Fe-TNO precursors and crystals) were determined via inductively coupled plasma optical emission spectrometry (ICP-OES, Thermo scientific, iCAP 6700 Series). X-ray diffraction (XRD) analysis was performed with a Bruker D8 Discovery X-ray diffractometer (VANTEC Dector Cu-Source) and applying LeBail refinement with the aid of TOPAS (Bruker) V5 software. Crystal morphology and elemental distribution maps were characterized using a Hitachi SU-8000 Cold Field-Emission scanning electron microscope (SEM) equipped with energy-dispersive X-ray spectroscopy (EDS) detector (XMax 80 mm^2 Oxford Instruments). Transmission electron microscopy (TEM), high-resolution transmission electron microscopy (HRTEM), scanning transmission electron microscopy (STEM), selected area electron diffraction (SAED), and Fast Fourier Transform (FFT) images were obtained on Thermo Scientific Talos F200X G2 TEM/STEM instrument operated at 200 kV. The high-angle annular dark field (HAADF) imaging was performed at a beam convergence angle of 10.5 mrad and the detector collection angle of 58-200 mrad. X-ray photoelectron spectroscopy (XPS), and reflection electron energy loss spectroscopy (REELS) were performed on Thermo Scientific Nexsa G2 surface analysis system.

4.2.3. Electrochemical Characterization

Half-cells were assembled for electrochemical testing. Fe-TNO or TNO active materials (80 wt.%), acetylene black (10 wt.%), and poly(vinylidene difluoride) (PVDF) binder (10 wt.%) were manually milled with N-Methyl-2-pyrrolidone (NMP) solvent in a mortar and doctor blade-coated on copper foil (99.99% Cu, 25 μm thick, MTI Corporation), followed by drying in an 80 °C vacuum oven overnight, before punching and calendaring. The active material loading was 3 ± 0.5 mg/cm^2. The coin cells (2032) were assembled in an argon-filled MBraun glovebox comprising the TNO working electrode, lithium metal as the counter electrode, polypropylene-polyethylene-polypropylene (PP/PE/PP) film separator (Celgard 2300), and 200 μL 1M $LiPF_6$ electrolyte (in EC:DMC:DEC at 2:2:1).

The galvanostatic charging/discharging cycling at different rates (1 C=387.6 mA/g) was tested at room temperature using a standard 8 channel battery analyzer (BST8 WA, MTI Corp). Gravimetric specific capacity was calculated based on the mass of active material. Both cyclic voltammetry (CV) and electrochemical impedance spectroscopy (EIS) were performed using a Bio-Logic VSP potentiostat/galvanostat system and analyzed with EC-Lab software. CV was done at sweep rates of 0.056 mV/s, 0.111 mV/s, 0.278 mV/s, 0.556 mV/s, 1.110 mV/s, and 2.780 mV/s, respectively, operating between 3.0 V and 1.0 V (vs. Li/Li^+). Meanwhile, EIS measurement was performed before/after each CV cycle in the frequency range from 1 MHz to 0.01 Hz. Galvanostatic intermittent titration technique (GITT) experiments were performed using an Arbin standard battery cycler (BT2043-10V-100mA-40, Arbin).

4.2.4. Calculation methodology

The electronic properties of $TiNb_2O_7$, Fe-doped $TiNb_2O_7$ and their lithiated structures were studied in the framework of Density Functional Theory (DFT) within the Vienna *ab initio* Software Package (VASP) [26-28]. A set of projector augmented wave (PAW) [29,30] potentials were used for Ti, Nb, O, Fe, and Li containing 12, 13, 6, 16, and 1 valence electrons, respectively, labeled as 'Ti_sv': '3s2 3p6 4s2 3d2', 'Nb_sv': '4s2 4p6 5s1 4d4', 'O': '2s 2p4', 'Fe_sv': '3s2 3p6 3d7 4s1', and 'Li': '2s1'. A plane-wave energy cutoff of 500 eV was applied in all calculations. Moreover, all calculations were spin-polarized. Lattice relaxation was done utilizing the GGA functional of

Perdew, Burke, and Ernzerhof (PBE) [31], while a correction for electronic correlation was done using an on-site Hubbard correction term (DFT+U) [32,33] U=4.2eV on the local 3d orbitals of the Ti atoms [21].

The initial primitive cell structures were obtained from the Materials Project [34] using a fully relaxed 2×2×2 k-point grid until interatomic forces converged to 0.01eV/A. The convergence criterion for the electronic degree of freedom was set at 1×10^{-5} eV. A supercell of 1×3×1 $TiNb_2O_7$ was created and used for all further calculations. To dope TNO with 5% Fe doping, one Fe atom was substituted into a Ti site. The overall structure was fully relaxed. Both supercells, pure TNO (without doping) and Fe-doped TNO were fully relaxed with a 1×1×1 Monkhorst-Pack k-point scheme. A Gaussian smearing of 0.02 eV was used in all electronic structure calculations, but for the presentation of density of states (DOS) results, this value was increased to 0.05 eV.

The hybrid functional HSE06 with a 0.25 fraction of exact exchange [31,35] was used in all electronic structure calculations, as it yields results more closely aligned with experimental observations, especially in electronic structure calculations of transition metal oxides[31,36-38]. While, due to computational constraints, the DFT+U method was used to calculate the diffusion barrier in both pure and Fe-doped TNO [31,37,38].

Additionally, the electronic structure of lithiated TNO (adding one Li atom per supercell) and lithiated Fe-doped TNO structures was also studied. To study the effect of Fe-doping on ionic diffusion mechanisms in TNO, the two systems (pure and Fe-doped TNO) were lithiated by adding a single Li atom. All the calculation details for lithiated structures were kept the same for TNO and Fe-doped TNO.

Finally, the software package VESTA [39] was used to visualize and produce charge density difference plots.

4.3. Results and Discussions

4.3.1. Elemental Composition and Morphology of Single-crystal Nanomaterials

The nanostructured Fe^{3+}-doped TNO materials ($Fe_xTi_{1-x}Nb_2O_{7-x/2}$, x=0.01, 0.05, 0.10) have been engineered via an aqueous scalable synthesis process [24] (**Scheme B.1**). The elemental compositions of $TiNb_2O_7$ (TNO), $Fe_{0.01}Ti_{0.99}Nb_2O_{6.995}$ (Fe1-TNO), $Fe_{0.05}Ti_{0.95}Nb_2O_{6.975}$ (Fe5-TNO), and $Fe_{0.1}Ti_{0.9}Nb_2O_{6.75}$ (Fe10-TNO) materials have been confirmed by ICP-OES as shown in **Table B.1**. XPS measurements were performed to further analyze the elemental composition and chemical valence state of Fe, Ti, Nb, and O elements. The XPS survey spectrum (**Figure B.1** and **Table B.2**) proves the existence of Ti^{4+}, Nb^{5+}, O^{2-} in both TNO and Fe5-TNO plus Fe^{3+} in the latter.

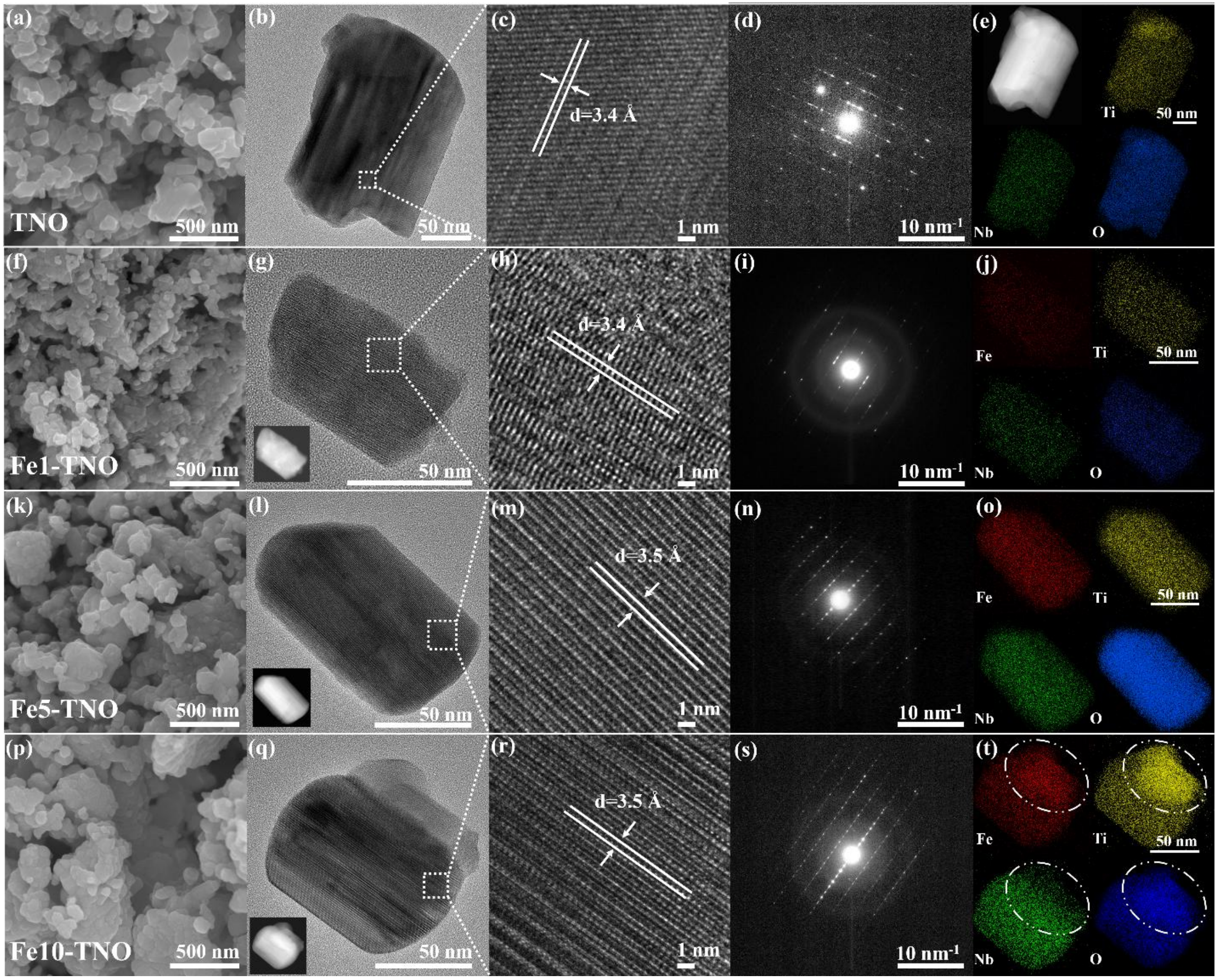

Figure 4.1 Morphology of TNO, Fe1-TNO, Fe5-TNO, and Fe10-TNO. (a) SEM, (b) TEM, (c) HRTEM, (d) SAED, (e) HAADF and EDS mapping of TNO material. (f) SEM, (g) TEM (HAADF inserted), (h) HRTEM, (i) SAED, and (j) EDS mapping of Fe1-TNO material. (k) SEM, (l) TEM (HAADF inserted), (m) HRTEM, (n) SAED, and (o) EDS mapping of Fe5-TNO material. (p) SEM, (q) TEM (HAADF inserted), (r) HRTEM, (s) SAED, and (t) EDS mapping of Fe10-TNO material.

The crystal morphologies of TNO, Fe1-TNO, Fe5-TNO, and Fe10-TNO materials are presented in **Figure 4.1**. The SEM images in **Figure 4.1(a, f, k, p)** and TEM images in **Figure 4.1(b, g, l, q)** prove all four materials to be made of nanostructured single-crystal particles. The HRTEM (**Figure 4.1(c, h, m, r)**) and corresponding SAED images (**Figure 4.1(d, i, n, s)**) confirm their monocrystalline nature and indicate the interlayer spacing of (003) plane (d_{003}) to increase from 3.4 Å in TNO and Fe1-TNO to 3.5 Å in Fe5-TNO and Fe10-TNO materials. EDS mapping in **Figure 4.1(e)** reveals the homogeneous elemental distribution of Ti, Nb, and O in undoped $TiNb_2O_7$. Similarly, EDS mapping reveals Fe, Ti, Nb, and O elements to have been homogeneously distributed in bulk of Fe1-TNO (**Figure 4.1(j)**) and Fe5-TNO (**Figure 4.1(o)**), suggesting that Fe^{3+} has been evenly substituted in Ti^{4+} sites. By contrast, **Figure 4.1(t)** displays two single particles of the Fe10-TNO material: one with high-element-homogeneity of all Fe, Ti, Nb, and O elements, while the other particle comprises only Fe, Ti, and O apparently representing an impurity phase. The impurity phase particles found in Fe10-TNO material could be correlated with the presence of a saturation limit for Fe^{3+}, above which excess iron cannot be homogeneously substituted into the $TiNb_2O_7$ lattice.

4.3.2. Structural Evolution Induced by Fe Substitution

To further investigate the effect of Fe substitution into the TNO crystal structure, atomic-level TEM images of TNO (**Figure 4.2(a-d)**) and Fe5-TNO monocrystalline particles (**Figure 4.2(e-h)**) were examined. This stoichiometry was selected for rigorous characterization, as it demonstrated the most promising electrochemical properties (as shown in **Figure 4.4**). **Figure 4.2(c)** and **Figure 4.2(g)** show the well-ordered arrangement along the [010] zone axis of TNO and Fe5-TNO crystals respectively, which match the charge density of the $TiNb_2O_7$ crystal unit cell at the [010] zone axis simulated by DFT calculation (**Figure B.6(b)**). The interlayer spacing of the (001) plane ($d_{(001)}$) in Fe5-TNO crystals is 10.40 Å (**Figure 4.2(g)**) which is larger than that in TNO with 10.30 Å (**Figure 4.2(c)**), indicating Fe substitution enlarges the interlayer distance [40]. According to **Figure 4.2(c, d)** TNO crystals are characterized by periodic arrangements similar to other reported pure $TiNb_2O_7$ materials, where prominent bright spots represent Ti and Nb atoms [23,40]. By contrast, the Fe5-TNO crystals illustrate a slight structure distortion (**Figure 4.2(g)**) with clearly different atomic arrangements in corresponding line profiles (**Figure 4.2(h)**).

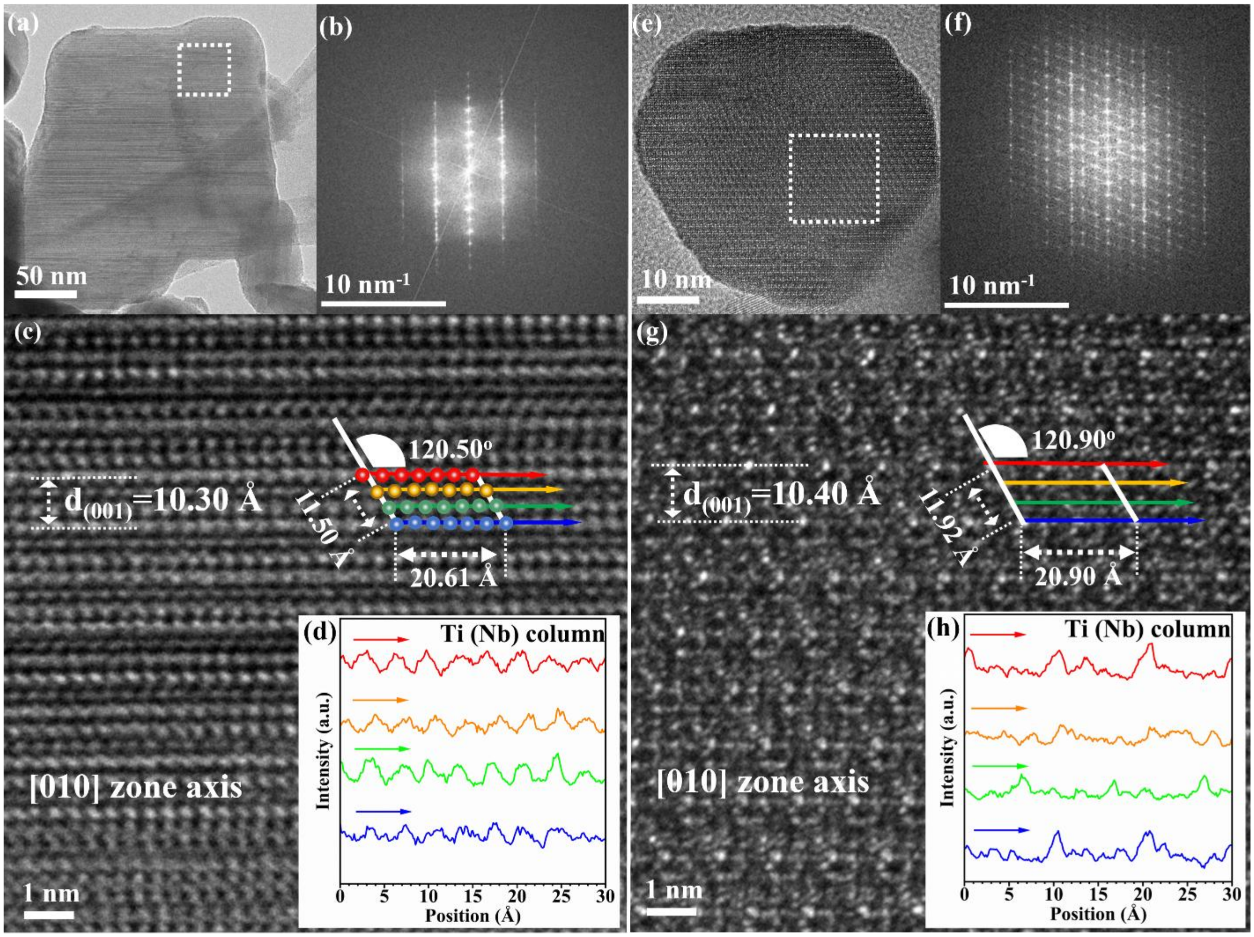

Figure 4.2 (a) TEM image, (b) FFT image, (c) atomic-resolution HRTEM image, and (d) the line profiles along the Ti(Nb) column of TNO. (e) TEM image, (f) FFT image, (g) atomic-resolution HRTEM image, and (h) the line profiles along the Ti(Nb) column of Fe5-TNO.

The effect of Fe substitution on crystallographic properties was further investigated by XRD analysis (**Figure 4.3(a-c)**). The obtained TNO and Fe-doped TNO phase patterns (**Figure 4.3(a)**) can be indexed to the $TiNb_2O_7$ phase with monoclinic C2/m space group (PDF#01-070-2009). Two predominant diffraction peaks emerge at $2\theta=23.91^{\circ}$ and 25.99° corresponding to (110) and (003) lattice planes of $TiNb_2O_7$, respectively. With the increase of Fe substitution, the peaks of (110) and (003) planes gradually shift to lower 2 *theta* values and the peak intensity ratio of (110)/(003) increases, suggesting that Fe substitution changes the crystal structure. In **Figure B.2**, the XRD pattern reveals the appearance of an impurity phase with increasing Fe content to x=0.2 and 0.5. To investigate the crystal evolution, the crystal lattice parameters of TNO and Fe5-TNO samples were determined by Le Bail refinement (**Figure 4.3(b, c)**). The detailed parameters of Fe5-TNO (in **Table B.2)** show *a*, *c* values as well as the β value to increase, consistent with the TEM results in **Figure 4.2 (c, d, g, h)**. Conversely, the *b* value and crystal volume (V) decrease.

FT-IR spectroscopy (**Figure B.3**) was conducted to compare the bonding characteristics of TNO and Fe5-TNO materials. The peaks at approximately 970 cm^{-1} and 920 cm^{-1} in both TNO and Fe5-TNO samples were assigned to the stretching vibrations of the Nb-O bonds [41]. The peaks at approximately 490 cm^{-1} in TNO and Fe5-TNO samples arise from stretching vibrations of Nb-O-Nb bridging bonds [42]. It is noteworthy that the peak corresponding to Ti-O-Ti bridging bonds illustrated a shift from 670 cm^{-1} in the TNO sample to 650 cm^{-1} in the Fe5-TNO sample [43]. The shift in the Ti-O-Ti bond peak can likely be attributed to the effect of Fe substitution into Ti within the lattice structure, in agreement with the XRD refinement results and TEM images.

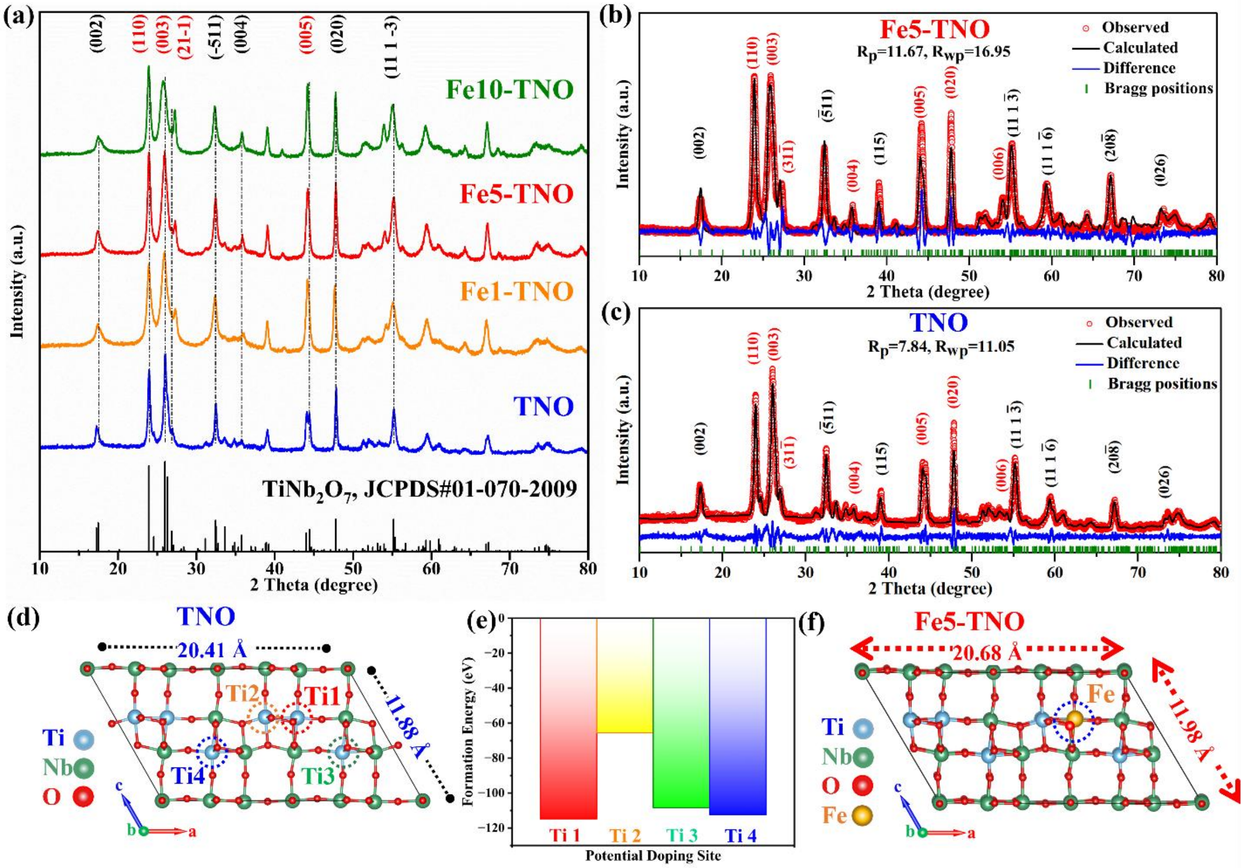

Figure 4.3 (a) XRD patterns of TNO and Fe^{3+}-doped TNO (Fe1-TNO, Fe5-TNO, Fe10-TNO); Le Bail refinement of (b) Fe5-TNO and (c) TNO. Crystal structure of (d) TNO and (f) Fe5-TNO calculated by DFT. (e) Formation energy of potential substitution doping sites calculated via DFT.

To delve deeper into the structural evolution, DFT calculations were employed to investigate potential doping sites and lattice changes. A DFT model with 5% Fe^{3+} doping was constructed to explore the lattice in TNO. The ground state total energies of four different potential Fe-doping sites (Ti1, Ti2, Ti3, and Ti4) were evaluated to determine the stable doping site of Fe in TNO as shown in **Figure 4.3(d)**. Among all the evaluated Ti doping sites with Fe (**Figure 4.3(e)**), the Ti1 site with minimum energy was determined to be the preferable Fe substitution site in the Fe5-TNO crystal unit cell. Further details on this calculation approach can be found in the Supporting Information. Based on the calculated model in **Figure 4.3(f)**, DFT studies show that the Fe^{3+} doping distorts the TNO crystal structure by increasing the *a* and *c* lattice parameters and the *β* angle with a decrease in the *b* axis, aligning qualitatively with the findings in TEM (**Figure 4.2(c, d, g, h)**) and XRD refinement (**Figure 4.3(b, c)**). This *a* and *c* value expansion implies the broadening of the *b*-tunnel diffusion channel, which is the primary diffusion channel in TNO [8,12]. Additionally, the observed decrease in the *b* value leads to a slight shortening of the diffusion channel length. Therefore, this structural evolution induced by Fe substitution is proven to both experimentally and theoretically have a favorable effect on Li ion diffusion [12,21].

4.3.3. Extreme Fast Charging Capability

The lithium storage performances of TNO, Fe1-TNO, Fe5-TNO, and Fe10-TNO electrodes were determined under galvanostatic cycling in the voltage window from 3 V to 1 V. As shown in **Figure 4.4(b, c)**, both TNO and Fe5-TNO provide 1.65 V of average working potential and feature three regions, an initial sloping profile, a “plateau-like” region, and another sloping region. Notably, Fe5-TNO shows a smaller overpotential than the TNO material at high rates (ca., 2 C and 5 C). **Figure 4.4(a)** illustrates the rate performance of TNO and Fe5-TNO corresponding to **Figure 4.4(b, c)**. The TNO material **(Figure 4.4(c))** provides 254.8, 236.8, 211.9, and 128.5 mAh/g discharge capacities at 0.5 C, 1 C, 2 C, and 5 C, respectively. By contrast, the Fe5-TNO electrode (**Figure 4.4(b))** yields superior discharge capacities of 285, 250, 225, and 195 mAh/g at 0.5 C, 1 C, 2 C, and 5 C, respectively. This different discharge curve of Fe5-TNO at about 1.2 V could be associated with the Fe^{3+}/Fe^{2+} redox couple, involving lithiation reactions that contribute to the additional discharge capacity [22,25]. The Fe1-TNO and Fe10-TNO electrodes display intermediate rate performance between that of TNO and Fe5-TNO (**Figure 4.4(a)**): discharge capacities of 260, 225, 200, and 150 mAh/g at 0.5 C, 1 C, 2 C, and 5 C, respectively.

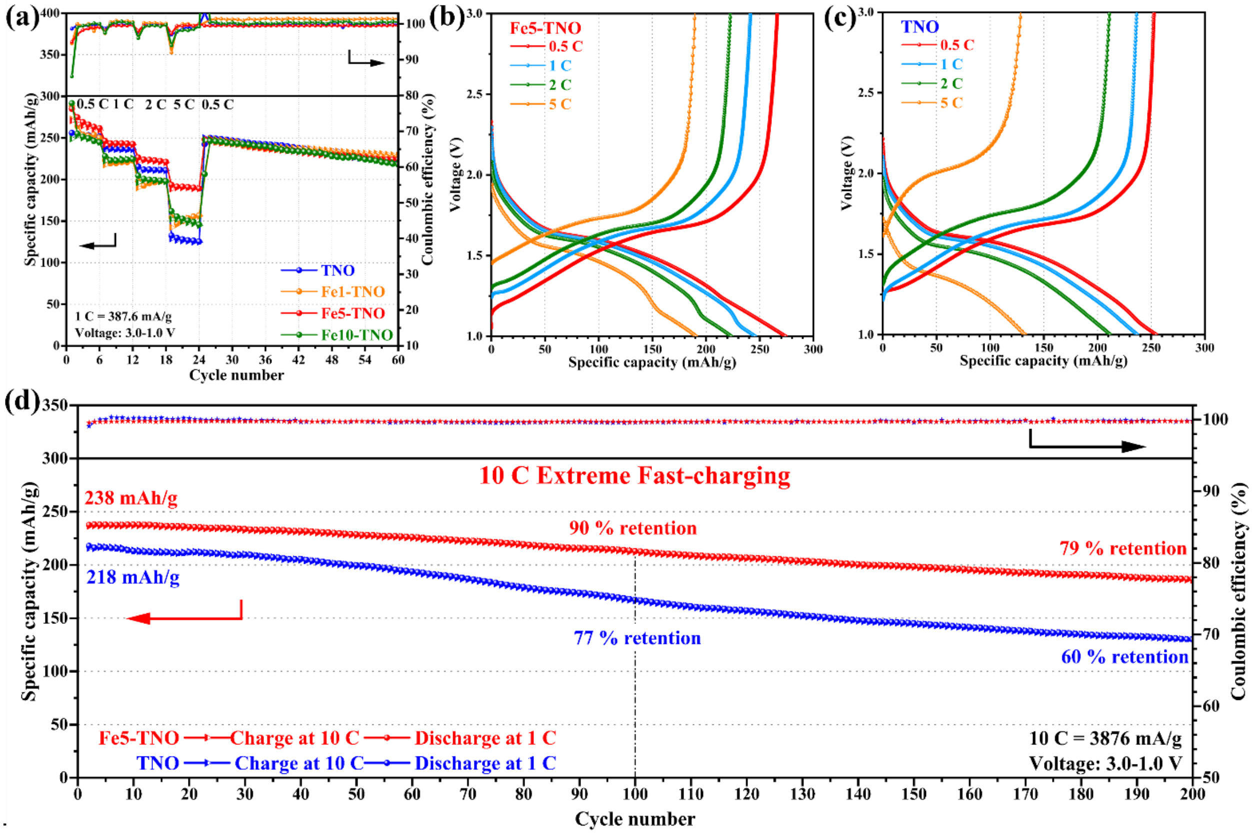

Figure 4.4 (a) Rate performance of TNO, Fe1-TNO, Fe5-TNO, and Fe10-TNO; and capacity-vs-potential profile of (b) TNO and (c) Fe5-TNO. (d) 10 C extreme fast-charging (coupled with 1 C fast-discharging) of TNO and Fe5-TNO after 0.5 C/0.5 C electrochemical activation.

More importantly, the remarkable fast-charging capability of Fe5-TNO has been proven using a new 10 C-fast-charging protocol designed to simulate actual EV battery operation, featuring 10 C charging (CC) coupled with 1 C discharging (DC) after an initial 0.5 C aging sequence (0.5 C (CC)/0.5 C (DC)). The Fe5-TNO electrode (**Figure 4.4(d)**) provides a high initial charge capacity of 238 mAh/g (at the 2nd cycle) under the 10 C-fast-charging protocol and a capacity retention of 79 % after 200 cycles, much higher than that of TNO. The superior electrochemical performance of Fe5-TNO compared to other samples can be attributed to homogeneous Fe^{3+} substitutional doping into Ti^{4+} sites and the effect of the compositional doping ratio. Specifically, improving dopant composition from 1% Fe^{3+} substitution (Fe1-TNO) to 5% Fe^{3+} substitution (Fe5-TNO) promotes the electrochemical properties of TNO materials by aiding Li^+ diffusion. However, further increasing the Fe^{3+} dopant composition to 10% Fe^{3+} substitution (Fe10-TNO) decreases battery performance, which is attributable to the formation of a Ti-Fe-O impurity phase as shown in **Figure 4.2(t)**.

4.3.4. Li ion Diffusion Kinetics

The effect of Fe substitution on Li ion diffusion kinetics was systematically evaluated through electrochemical techniques. The GITT curves (**Figure 4.5(a)**) were obtained to determine the Li-ion chemical diffusion coefficient ($D_{Li^+,\, GITT}$) based on **equation B.3** [4,44]. Accordingly, $D_{Li^+,\, GITT}$ in Fe5-TNO is calculated to be from 6.08×10^{-13} to 1.10×10^{-12} cm^2/s during discharging (**Figure 4.5(b)**) and from 3.68×10^{-13} to 1.05×10^{-12} cm^2/s during charging (**Figure 4.5(c)**), which significantly exceeds that of TNO, recorded to be from 5.25×10^{-14} to 1.37×10^{-13} cm^2/s during discharging (**Figure 4.5(b)**) and from 1.22×10^{-14} to 1.09×10^{-13} cm^2/s during charging (**Figure 4.5(c)**). The Li^+ chemical diffusion coefficient ($D_{Li^+,\ CV}$) can also be determined according to the Randle-Sevcik equation (**equation B.4**) by using CV curves [45,46]. CV curves at varying sweep rates (**Figure 4.5(d, e)**) were tested to determine the linear relation between redox peak current (I_p) and the square root of the scan rate ($v^{1/2}$). As demonstrated in **Figure 4.5(f)**, the fitted slopes of $d(I_p)/d(v^{1/2})$ for Fe5-TNO are 2.88 (charging) and -3.37 (discharging), while those of TNO electrode are 2.54 (charging) and -1.97 (discharging). According to **equation B.3**, the $D_{Li^+,\ CV}$ of Fe5-TNO is 2.68×10^{-12} cm^2/s (charging) and 1.96×10^{-12} cm^2/s (discharging) outperforming that of TNO at 1.44×10^{-13} cm^2/s (charging) and 9.8×10^{-14} cm^2/s (discharging), consistent in other words with the results by GITT.

Furthermore, DFT investigations were conducted to determine the energy barriers associated with Li^+ diffusion within both pure and Fe-doped TNO. Given that Li^+ primarily diffuses along the b-axis channel [8], the barrier was assessed along this particular axis. Since Fe doping alters the electronic orbital occupation at the conduction band edge and perturbs the crystal lattice geometry, the DFT+U method, which takes into account orbital-dependent effects, was applied as it results in self-consistent solutions [47]. These distinct high-energy solutions, representing metastable states, can differ in total energy by several electron volts per atom, making the identification of ground state minima particularly challenging [47]. Thus, due to the presence of these high-energy metastable states in the Fe-doped lattice, the conventional nudged elastic band (NEB) method might not be able to locate the actual energy minima from the interpolated images. This becomes particularly acute when an Fe-site can exchange charges with the overall lattice almost in the manner of a polaron [48-50]. Therefore, to compute the diffusion barrier and assess the impact of Fe^{3+} doping on the diffusion mechanism of Li^+ a linear interpolation technique was employed in a pure TNO lattice structure with distortions corresponding to that induced by Fe-doping in **Figure 4.3(f)**. This represents the impact of the lattice distortion itself on the diffusion process in TNO independent of any possible electronic interactions with the Fe-site.

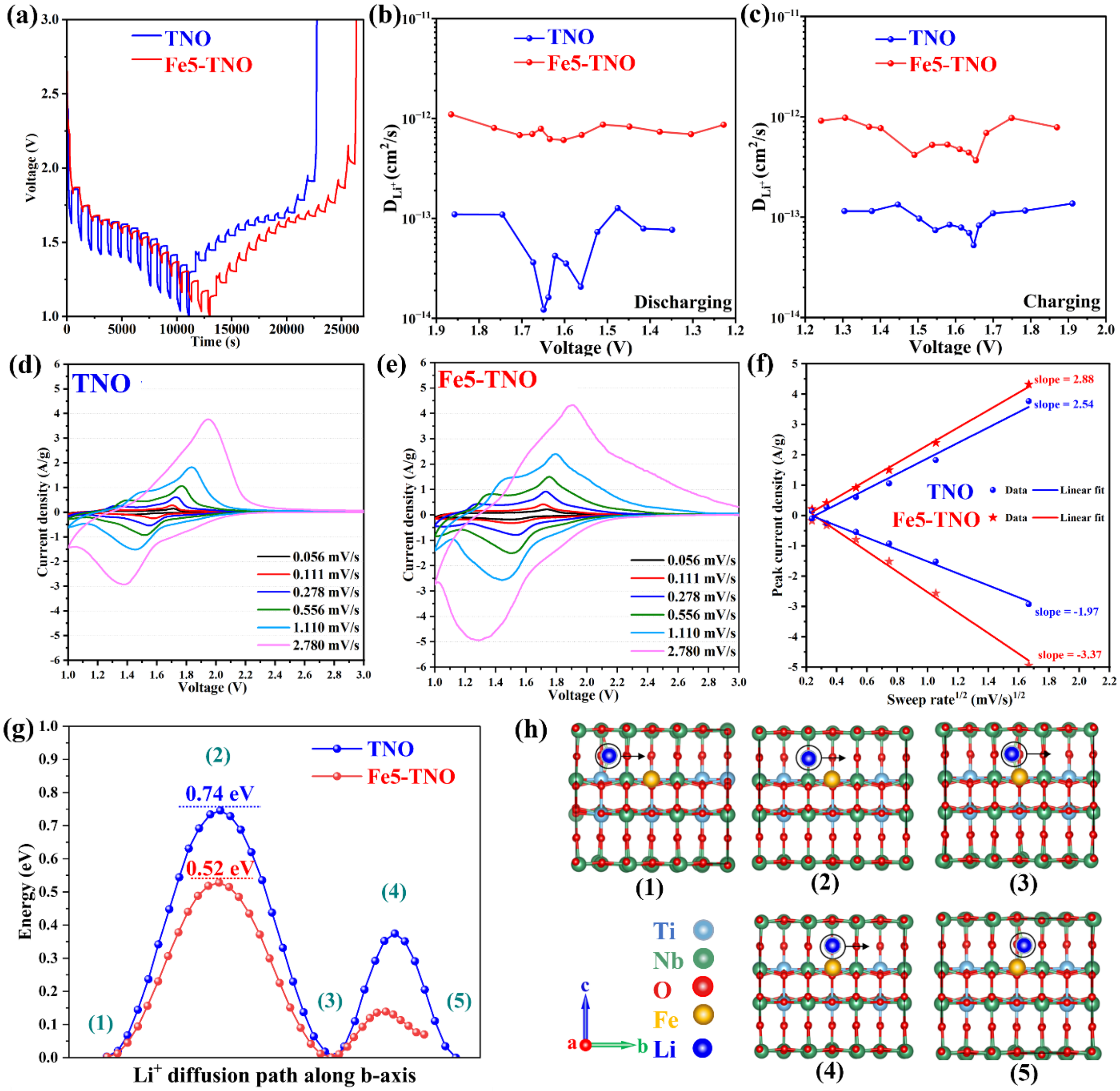

Figure 4.5 (a) GITT curves at 0.5 C. The corresponding Li$^+$ diffusion coefficients of TNO and Fe5-TNO during (b) discharging and (c) charging. CV curves at varying sweep rates (0.056-2.78 mV/s) of (d) TNO anode and (e) Fe5-TNO anode. (f) Linear relationship between ln(I$_p$) and ln(v) of oxidation and reduction peaks. (g) Li ion diffusion energy barrier along the b channel. (h) The corresponding points in the energy barrier plot represented by labels (1-5).

Figure 4.5(h) illustrates the pathway for Li^+ diffusion hopping from one site to another, revealing two sequential Li^+ hops along the *b*-axis, labeled (1)-(3) and (3)-(5) therein. As shown in **Figure 4.5(g)** the corresponding diffusion barriers for pure TNO and Fe-doped TNO were calculated and a decrease in barrier height in Fe-distorted lattice was observed. Specifically, in hop (1)-(3), Fe^{3+} doping reduced the barrier from 0.74 to 0.52 eV, thereby facilitating the diffusion and hence ionic conductivity of TNO through Fe-doping. These DFT calculations demonstrate the important role of Fe^+ doping in adjusting the diffusion barrier of Li^+ by altering the material lattice constant favorably. They are not intended to provide absolute numbers for the energy barriers but rather general trends, which agree with the experimentally measurement trends regarding improved Li diffusion coefficients with respect to Fe-doping shown in **Figure 4.5(a-f)**.

4.3.5. Redox Mechanism and Electronic Structure

The effect of Fe doping on redox reaction and impedance during lithiation was probed by CV and EIS measurements of pristine TNO and Fe5-TNO materials and lithiated materials (after CV cycle). The redox reactions of the TNO anode involve three redox couples, namely Ti^{4+}/Ti^{3+} couple, Nb^{5+}/Nb^{4+} couple, and Nb^{4+}/Nb^{3+} couple [51]. According to the magnified CV scan (inset) shown in **Figure 4.6(a)**, the cathodic reaction current corresponding to the reduction of Ti^{4+} in undoped TNO emerges at 2.55 V [21]. In contrast, the corresponding cathodic current in the Fe5-TNO CV appears at 2.72 V likely due to the reduction of Fe^{3+} to Fe^{2+}, suggesting the involvement of Fe^{3+} in the redox reactions (as was also mentioned with respect to the Fe impacted Li^+ hopping calculations discussed above). The most dominant CV peak, corresponding to the Nb^{5+}/Nb^{4+} couple with a theoretical equilibrium potential of 1.65 V, serves as a basis to evaluate the overpotential of anodic peak and cathodic peak (ΔE) [8]. Thus, according to the CV scans in **Figure 4.6(a)** Fe doping can be seen to reduce the overpotential during lithiation/delithiation, i.e. to have a depolarizing effect. The Fe5-TNO pristine electrode (**Figure 4.6(a)**) has a smaller overpotential ($\Delta E=0.31$ V) than the TNO electrode ($\Delta E=0.46$ V) during initial lithiation. A similar trend is observed with the EIS data in **Figure 4.6(b)**, where the Fe5-TNO pristine electrode demonstrates a smaller impedance of approximately 100 ohm than that of $TiNb_2O_7$ pristine at 350 ohm. After the 1st cycle as shown in **Figure 4.6(b)**, the charge transfer resistance (R_{CT}) of Fe5-TNO and $TiNb_2O_7$ decreases dramatically to ca. 26 ohm and ca. 32 ohm, respectively, due to lithium residual in the TNO structure [6].

To investigate the effect of Fe doping on the oxidation states, XPS analysis of pristine TNO, pristine Fe5-TNO, and lithiated Fe5-TNO samples (discharged to 1 V) was performed. In the high-resolution XPS spectra of Fe 2p (**Figure B.1(a)**), three predominant peaks were observed at 709.5 eV, 715.4 eV, and 722.80 eV and assigned to Fe $2p_{3/2}$ core level, satellite peak, and Fe $2p_{1/2}$ core level orbitals, respectively reveal the presence of Fe^{3+} in the Fe5-TNO sample. Notably, in the lithiated Fe5-TNO sample, the Fe 2p peaks split into five separate peaks, where besides the existing peaks for Fe^{3+}, two new peaks correspond to Fe^{2+} emerged at 711.9 eV (Fe $2p_{3/2}$ peak) and 727.9 eV (Fe $2p_{1/2}$ peak) [52]. This phenomenon could be due to the Fe^{3+} redox reaction during discharging, with Fe^{3+} likely being partially reduced to Fe^{2+} at the cut-off voltage of 1 V. In the spectrum of Ti 2p (**Figure B.1(b)**), the characteristic peaks positioned at 464.38 eV and 458.58 eV and assigned to Ti $2p_{1/2}$ and Ti $2p_{3/2}$ peaks respectively, reflect the Ti^{4+}-O bonding in the $TiNb_2O_7$ sample [53]. In contrast, in Fe5-TNO, the peak positions corresponding to Ti $2p_{1/2}$ and Ti $2p_{3/2}$ peaks slightly shift towards lower binding energies to 464.25 eV and 458.45 eV, respectively, very likely related to Fe^{3+} substitution. After discharging to 1 V, Ti^{4+} is reduced to Ti^{3+}, as confirmed in the Ti 2p spectra of the lithiated Fe5-TNO sample (**Figure B.1(b)**) where the Ti $2p_{1/2}$ and Ti $2p_{3/2}$ peaks moved to 464.00 eV and 458.10 eV, respectively. For Nb 3d spectra (**Figure B.1(c)**), no obvious peak position shift is observed in Fe5-TNO compared to TNO. The predominant Nb $3d_{3/2}$ and Nb $3d_{5/2}$ peaks (**Figure B.1(c)**) related to pentavalent Nb involved in Nb-O bonding [54,55] appear in TNO spectrum at 209.70 eV and 207.02 eV as well as in the Fe5-TNO spectrum at 209.76 eV and 207.05 eV. After lithiation, the Nb $3d_{3/2}$ and Nb $3d_{5/2}$ peaks shifted to 209.5 eV and 206.75 eV, suggesting Nb^{5+} is reduced to Nb^{4+} and Nb^{3+} [56]. In the O 1s spectra (**Figure B.1(d)**), the characteristic peak originating from metal-oxygen bonds appears at 530.01 eV in the case of Ti^{4+}-O [54,55] and Nb^{5+}-O [41] in TNO and at 530.15 eV in the case of Fe5-TNO respectively.

REELS was performed to experimentally determine the band gap (E_g) of TNO and Fe5-TNO (**Figure 4.6(c)** and **Figure B.3**). **Figure B.3** exhibits the original REELS spectra of TNO and Fe5-TNO based on applied kinetic energy and response count intensity. The main peaks originate from elastically scattered electrons and correspond to excitation energy and are equivalent to the energy level of the valence band maximum energy (E_{VBM}) [57]. The corresponding peaks for TNO and Fe5-TNO are positioned at 1002.10 eV (±0.05 eV) and 1002.20 eV (±0.05 eV), respectively, which are applied to normalize the energy loss of the REELS spectrum. As shown in **Figure B.4**, this onset of energy loss is used for calculating the energy level of the conduction band minimum

(E_{CBM}) [58]. For the $TiNb_2O_7$ sample, the onset of energy loss of $TiNb_2O_7$ is situated at 998.35 eV (±0.05 eV), while that of Fe5-TNO displays a visible shift to 998.80 eV (±0.05 eV). Then, E_g can be measured as the intercept of the linear extrapolation of the leading edge to the background level (**Figure 4.4(c)**) [57]. Accordingly, the E_g values for TNO and Fe5-TNO from REELS are determined to be 3.75 eV and 3.40 eV, respectively. The reduction of E_g in Fe5-TNO can be attributed to Fe^{3+} substitutional doping.

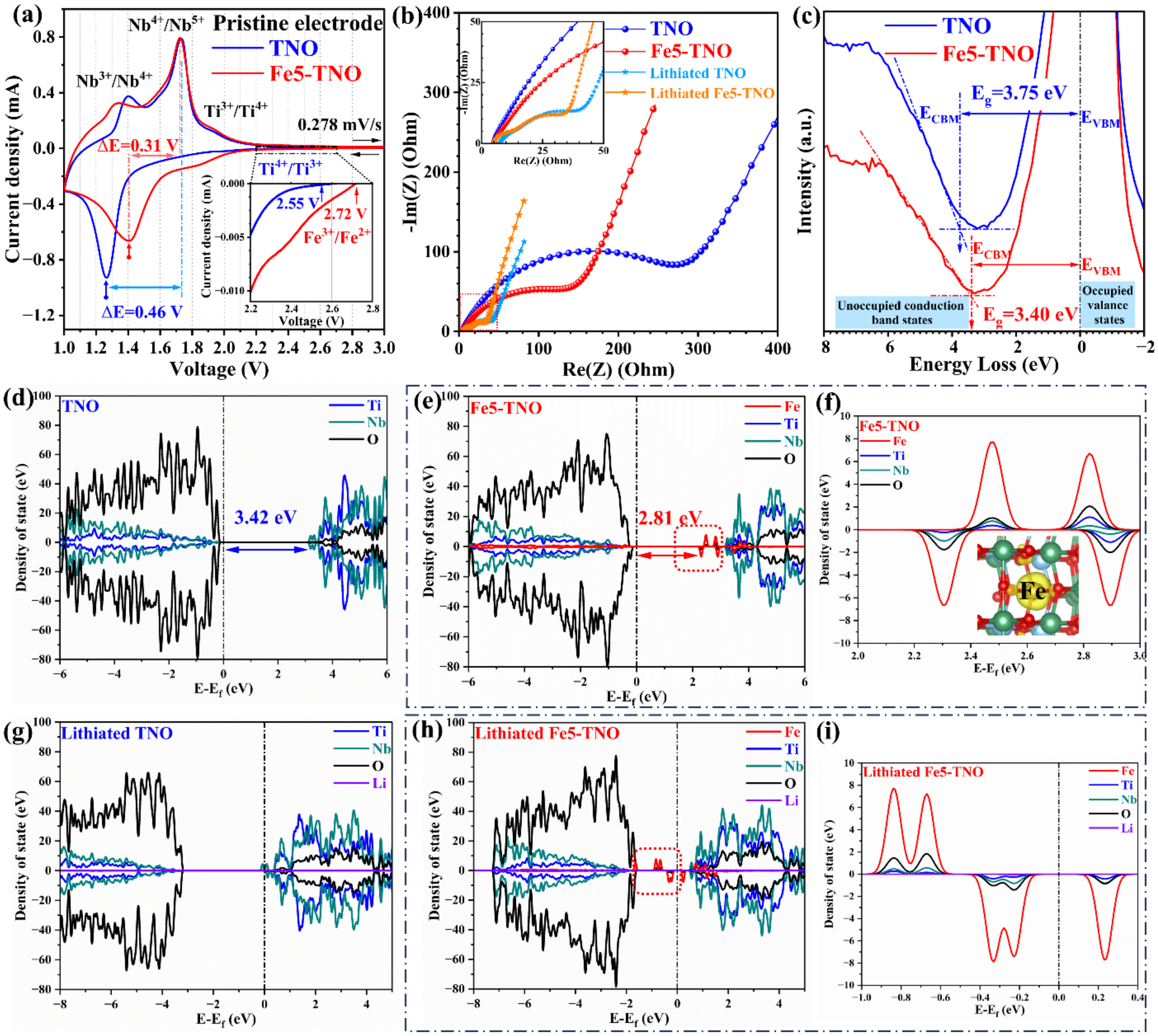

Figure 4.6 (a) CV of the pristine electrode of TNO and Fe5-TNO, (b) EIS of the pristine electrode and cycled electrode of TNO and Fe5-TNO. (c) Reflection electron energy loss spectroscopy (REELS) of TNO and Fe5-TNO electrodes. Density of states (DOS) of (d) TNO, (e, f) Fe5-TNO, (g) lithiated TNO, and (h, i) lithiated Fe5-TNO.

DFT calculations were performed to further investigate the changes in the electronic structure as a result of Fe^{3+} doping into TNO. To this end the projected density of states (PDOS) of pure TNO and Fe-doped TNO was calculated. For full details of the computational methods, see Section 2.4. The DOS of pure TNO as shown in **Figure 4.6(d)** depicts the E_g of ~ 3.42 eV characteristic of a wide gap semiconductor. In contrast, Fe^{3+} doping introduces empty energy levels in the energy gap which decreases the E_g to 2.81 eV (**Figure 4.6(e)**). This decrease in the E_g may lead to an increase in the electronic conductivity of the TNO anode. For an in-depth insight into the empty energy levels, the charge density plots were plotted, as shown in **Figure 4.6(f)**. These plots indicate the Fe-induced 3d orbitals localized below the conduction band as enlarged in **Figure 4.6(f)**. The presence of these unoccupied localized energy states below the conduction band further indicates the possibility of facilitating the redox reaction, where Fe^{3+} is likely to be reduced first, followed by Ti^{4+}/Nb^{5+} reduction.

To gain insights into electronic structural changes during the lithiation process (adding one Li atom per supercell), we also analyzed DOS plots of lithiated pure and Fe-TNO. The results indicate that lithiation shifts the conduction band towards the Fermi level. This is because the addition of the Li atom introduces 1 extra electron in the system which reduces 3d-orbitals of Ti^{4+} or 4d orbitals of Nb^{5+}. However, with Fe doping, this Li electron will likely first reduce Fe^{3+} dopant to Fe^{2+}. In addition, it was found that in both pure TNO (**Figure 4.6(h))** and Fe-doped TNO (**Figure 4.6(i)**), lithiation also narrows down the bandgap indicating a likely contribution to increased electronic conductivity since the charge state of the anode is unlikely to be ever fully delithiated [21].

4.3.6. Structural Stability and Long Cycling Performance

The long cycling performance under extremely fast charging-discharging (5 C) and the corresponding capacity fade mechanism were determined via galvanostatic cycling, electrochemical impedance spectroscopy (EIS), and cyclic voltammetry (CV). As shown in **Figure 4.7(a)**, Fe5-TNO offers a high initial capacity of 200 mAh/g and outstanding cycling stability at 5 C high rate, providing 93 % retention after 500 cycles and 85 % retention after 1000 cycles. By contrast, the TNO anode offers unstable cycling after 200 cycles with its capacity retention dropping to a dismal approximately 30 % after 1000 cycles.

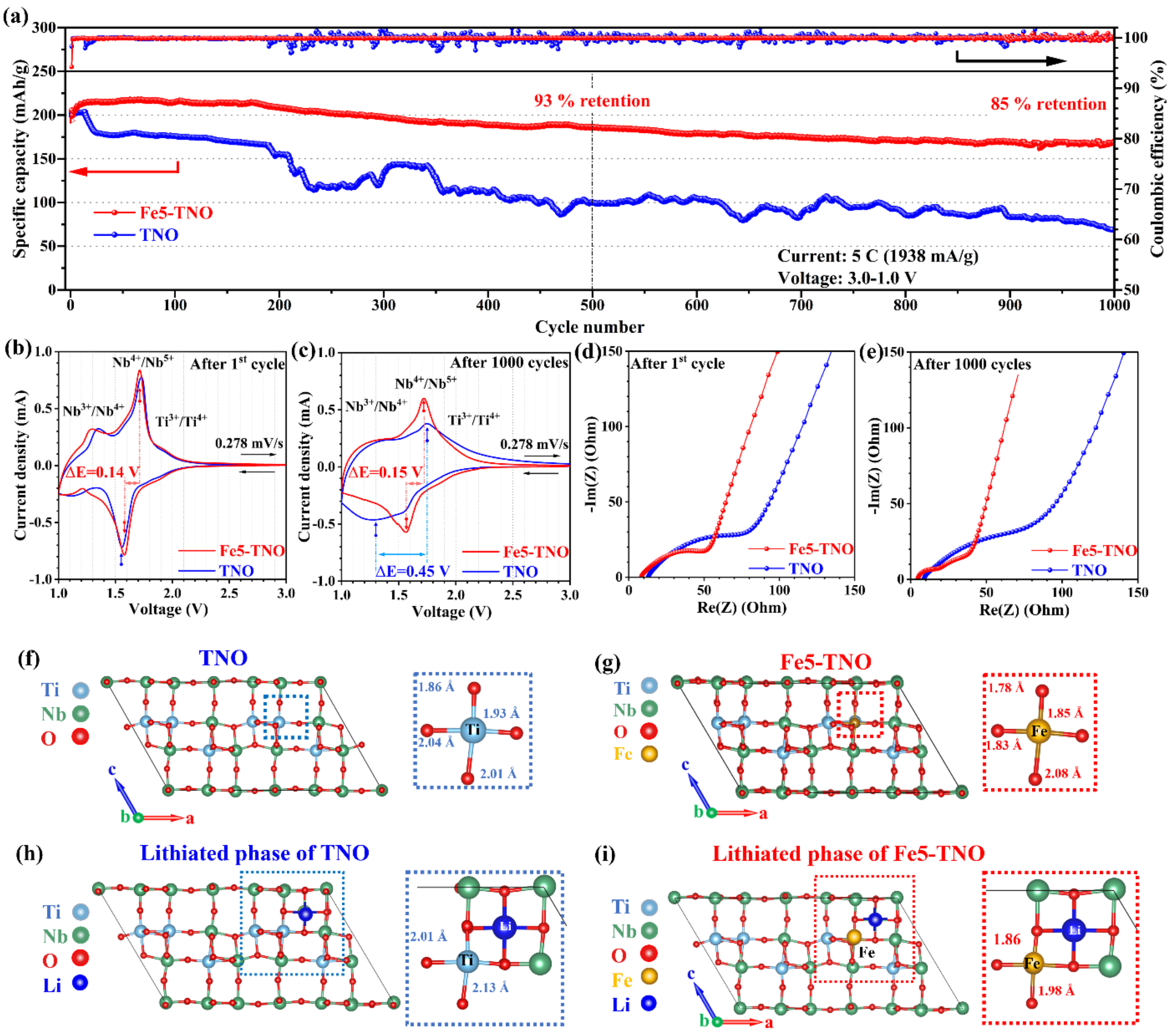

Figure 4.7 (a) Galvanostatic cycling of Fe5-TNO and TNO for 1000 cycles at 5 C. CV of TNO and Fe5-TNO electrodes: (b) after 1st galvanostatic cycle at 5 C and (c) after 1000 galvanostatic cycles at 5 C. EIS of TNO and Fe5-TNO electrodes: (d) after 1st galvanostatic cycle at 5 C and (e) after 1000 galvanostatic cycles at 5 C. Local distortion of (f) Ti-O bond lengths in pure TNO and (g) Fe-O bond lengths in Fe5-TNO. (h) Ti-O bond lengths in lithiated phase of pure TNO and (i) Fe-O bond lengths in lithiated phase of Fe TNO.

After the 1st galvanostatic cycle, both Fe5-TNO and TiNb$_2$O$_7$ electrodes manifest small overpotential (ΔE) of 0.14 V and 0.15 V, respectively, as shown in **Figure 4.7(b)**. After 1000 cycles (**Figure 4.7(c)**), the Fe5-TNO electrode maintains a small ΔE of 0.15 V, but the TiNb$_2$O$_7$ electrode exhibits a substantial polarization of 0.45 V. The corresponding EIS analysis of electrodes cycled after 1st cycle and 1000 cycles is presented in **Figure 4.7(d, e)**. After the 1st cycle (**Figure 4.7(d)**), the charge transfer resistance (R$_{CT}$) of Fe5-TNO and TiNb$_2$O$_7$ was determined to be ca. 30 ohm and ca. 35 ohm, respectively. After 1000 cycles (**Figure 4.7(e)**, Fe5-TNO registers a much-reduced impedance of 12 ohm and stable long cycling, while the TNO electrode has maintained an even increasing resistance of 40 ohm while suffering severe capacity fade (**Figure 4.7(a))**. It is noteworthy that the Nyquist pattern of Fe5-TNO shows two semicircles probably attributed to formation of a solid electrolyte interphase (SEI) layer during cycling, that may be contributing also to stabilized long cycling. Based on the analysis above, Fe substitutional doping proves effective in promoting long cycling performance by reducing the impedance and overpotential of the lithiation-delithiation reaction but also via local structural changes revealed by DFT analysis. Notably, as depicted in **Figure 4.7(f, g)**, before any lithiation, Fe doping reduces local bond lengths, i.e. Fe-O bonds are shorter than Ti-O bond lengths [21] and the same trend was observed in lithiated TNO and Fe-TNO structures (**Figure 4.7(h, i)**). However, a more detailed computational analysis (left for future work) is needed to fully verify the correspondence between local dopant-induced distortions and these improved properties.

4.4. Conclusion

In summary, we developed nanostructured Fe^{3+}-doped TNO monocrystalline materials ($Fe_xTi_{1-x}Nb_2O_{7-x/2}$) through a scalable water-based synthesis method. Furthermore, we have revealed the likely modification mechanism of iron substitution for stabilized long cycling electrochemical performance experimentally and theoretically. Fe^{3+} substitution of Ti^{4+} in TNO nanomaterials reduces the band gap from 3.75 eV of pure TNO to 3.40 eV of Fe5-TNO (5% Fe substitution), thereby increasing the conductivity of TNO materials and reducing the impedance of LIB electrodes. Moreover, Fe^{3+} dopants crystallographically extend the *ac*-plane and decrease the *b*-value, suggesting a widening diffusion channel and shortening pathway along the *b*-axis. Consequently, this Fe^{3+}-doped TNO demonstrates a higher Li diffusion coefficient as determined by GITT and a smaller Li diffusion energy barrier along the transport channel. As a result, Fe5-TNO provides remarkable extreme-fast-charging capability (220 mAh/g after 100 cycles under 10 C/1C situation) and superior cycling stability (85% capacity retention after 1000 cycles at 5 C). The findings of this work point the way towards further experimental and computational analyses by which high-capacity doped anodes may realize the long sought after fast-charging capabilities for next-generation LIBs. This includes more systematic future studies towards understanding how both the atomic and electronic structure contributions of dopants, across the periodic table, can be employed to improve charging rates.

4.5. References

[1] Y. Liu, Y. Zhu, Y. Cui, Challenges and opportunities towards fast-charging battery materials, Nat. Energy 4 (2019) 540-550. https://doi.org/https://doi.org/10.1038/s41560-019-0405-3.

[2] T. Gao, Y. Han, D. Fraggedakis, S. Das, T. Zhou, C.-N. Yeh, S. Xu, W.C. Chueh, J. Li, M.Z. Bazant, Interplay of lithium intercalation and plating on a single graphite particle, Joule 5 (2021) 393-414. https://doi.org/10.1016/j.joule.2020.12.020.

[3] J. Han, Y. Huang, J.B. Goodenough, New anode framework for rechargeable lithium batteries, Chem. Mater. 23 (2011) 2027-2029. https://doi.org/dx.doi.org/10.1021/cm200441h.

[4] H. Park, H.B. Wu, T. Song, X.W. Lou, U. Paik, Porosity-controlled $TiNb_2O_7$ microspheres with partial nitridation as a practical negative electrode for high-power lithium-ion batteries, Adv. Energy Mater. 5 (2015) 1401945. https://doi.org/10.1002/aenm.201401945.

[5] H. Wang, R. Qian, Y. Cheng, H.-H. Wu, X. Wu, K. Pan, Q. Zhang, Micro/nanostructured $TiNb_2O_7$-related electrode materials for high-performance electrochemical energy storage: recent advances and future prospects, J. Mater. Chem. A 8 (2020) 18425-18463. https://doi.org/10.1039/D0TA04209A.

[6] K.J. Griffith, I.D. Seymour, M.A. Hope, M.M. Butala, L.K. Lamontagne, M.B. Preefer, C.P. Koçer, G. Henkelman, A.J. Morris, M.J. Cliffe, S.E. Dutton, C.P. Grey, Ionic and electronic conduction in $TiNb_2O_7$, J. Am. Chem. Soc. 141 (2019) 16706-16725. https://doi.org/10.1021/jacs.9b06669.

[7] K.J. Griffith, Y. Harada, S. Egusa, R.M. Ribas, R.S. Monteiro, R.B. Von Dreele, A.K. Cheetham, R.J. Cava, C.P. Grey, J.B. Goodenough, Titanium niobium oxide: from discovery to application in fast-charging lithium-ion batteries, Chem. Mater. 33 (2021) 4-18. https://doi.org/10.1021/acs.chemmater.0c02955.

[8] C. Yang, D. Ma, J. Yang, M. Manawan, T. Zhao, Y. Feng, J. Li, Z. Liu, Y.-W. Zhang, R.B. Von Dreele, B.H. Toby, C.P.d.L. Albarrán, J.H. Pan, Crystallographic insight of reduced lattice volume expansion in mesoporous Cu^{2+}-doped $TiNb_2O_7$ microspheres during Li^+ insertion, Adv. Funct. Mater 33 (2023) 2212854. https://doi.org/https://doi.org/10.1002/adfm.202212854.

[9] L. Hu, L.J. Luo, L.F. Tang, C.F. Lin, R.J. Li, Y.J. Chen, $Ti_2Nb_{2x}O_{4+5x}$ anode materials for lithium-ion batteries: a comprehensive review, J. Mater. Chem. A 6 (2018) 9799-9815. https://doi.org/10.1039/c8ta00895g.

[10] J.L. Gao, X.Q. Cheng, S.F. Lou, Y.L. Ma, P.J. Zuo, C.Y. Du, Y.Z. Gao, G.P. Yin, Self-doping $Ti_{1-x}Nb_{2-x}O_7$ anode material for lithium-ion battery and its electrochemical performance, J. Alloy. Compd. 728 (2017) 534-540. https://doi.org/10.1016/j.jallcom.2017.09.045.

[11] S. Gong, Y. Wang, Q. Zhu, M. Li, Y. Wen, H. Wang, J. Qiu, B. Xu, High-rate lithium storage performance of $TiNb_2O_7$ anode due to single-crystal structure coupling with Cr^{3+}-doping, J. Power Sources 564 (2023) 232672. https://doi.org/https://doi.org/10.1016/j.jpowsour.2023.232672.

[12] K. Tian, Z. Wang, H. Di, H. Wang, Z. Zhang, S. Zhang, R. Wang, L. Zhang, C. Wang, L. Yin, Superimposed effect of La doping and structural engineering to achieve oxygen-deficient $TiNb_2O_7$ for ultrafast Li-ion storage, ACS Appl. Mater. Interfaces 14 (2022) 10478-10488. https://doi.org/10.1021/acsami.1c24909.

[13] M. Yu, Z.F. Cai, Q. Li, S. Wang, Y.Z. Ma, G.S. Song, W.D. Yang, C. Wen, Enhanced energy storage performance of Zr-doped $TiNb_2O_7$ nanospheres prepared by the hydrolytic method, ACS Sustain. Chem. Eng. 11 (2023) 5147-5154. https://doi.org/10.1021/acssuschemeng.2c07144.

[14] C. Lin, S. Yu, S. Wu, S. Lin, Z.-Z. Zhu, J. Li, L. Lu, $Ru_{0.01}Ti_{0.99}Nb_2O_7$ as an intercalation-type anode material with a large capacity and high rate performance for lithium-ion batteries, J. Mater. Chem. A 3 (2015) 8627-8635. https://doi.org/https://doi.org/10.1039/C5TA01073J.

[15] L.J. Zhao, S.T. Wang, Y.H. Dong, W. Quan, F. Han, Y.M. Huang, Y.T. Li, X.H. Liu, M. Li, Z.T. Zhang, J.Y. Zhang, Z.L. Tang, J. Li, Coarse-grained reduced $Mo_xTi_{1-x}Nb_2O_{7+y}$ anodes for high-rate lithium-ion batteries, Energy Storage Mater. 34 (2021) 574-581. https://doi.org/10.1016/j.ensm.2020.10.016.

[16] H. Song, Y.-T. Kim, A Mo-doped $TiNb_2O_7$ anode for lithium-ion batteries with high rate capability due to charge redistribution, Chem. Commun. 51 (2015) 9849-9852. https://doi.org/10.1039/C5CC02221E.

[17] C. Lei, X. Qin, S. Huang, T. Wei, Y. Zhang, Mo-doped $TiNb_2O_7$ microspheres as improved anode materials for lithium-ion batteries, ChemElectroChem 8 (2021) 3379-3383. https://doi.org/https://doi.org/10.1002/celc.202101056.

[18] Y.-S. Hsiao, C.-W. Chang-Jian, H. Chu Weng, H.-H. Chiang, C.-Z. Lu, W. Kong Pang, V.K. Peterson, X.-C. Jiang, P.-I. Wu, C.-P. Chen, J.-H. Huang, Doping with W^{6+} ions enhances the performance of $TiNb_2O_7$ as an anode material for lithium-ion batteries, Appl. Surf. Sci. 573 (2022) 151517. https://doi.org/https://doi.org/10.1016/j.apsusc.2021.151517.

[19] R.M. Tao, T.Y. Zhang, X.G. Sun, C.L. Do-Thanh, S. Dai, Ionothermally synthesized nanoporous $Ti_{0.95}W_{0.05}Nb_2O_7$: a novel anode material for high-performance lithium-ion batteries, Batteries & Supercaps 6 (2023) e202300101. https://doi.org/10.1002/batt.202300101.

[20] C. Yang, C. Lin, S. Lin, Y. Chen, J. Li, $Cu_{0.02}Ti_{0.94}Nb_{2.04}O_7$: An advanced anode material for lithium-ion batteries of electric vehicles, J. Power Sources 328 (2016) 336-344. https://doi.org/https://doi.org/10.1016/j.jpowsour.2016.08.027.

[21] J. Zheng, R. Xia, C.L. Sun, N. Yaqoob, Q.Y. Qiu, L.P. Zhong, Y.D. Li, P. Kaghazchi, K.N. Zhao, J.E. ten Elshof, M. Huijben, Fast and durable lithium storage enabled by tuning entropy in Wadsley-Roth phase titanium niobium oxides, Small 19 (2023) 2301967. https://doi.org/10.1002/smll.202301967.

[22] L. Zhang, H.B. Wu, X.W. Lou, Iron-oxide-based advanced anode materials for lithium-ion batteries, Adv. Energy Mater. 4 (2014) 1300958. https://doi.org/https://doi.org/10.1002/aenm.201300958.

[23] W. Wu, M. Liu, Y. Pei, W. Li, W. Lin, Q. Huang, M. Wang, H. Yang, L. Deng, L. Yao, Z. Zheng, Unprecedented superhigh-rate and ultrastable anode for high-power battery via cationic disordering, Adv. Energy Mater. 12 (2022) 2201130. https://doi.org/https://doi.org/10.1002/aenm.202201130.

[24] F. Yu, S. Wang, R. Yekani, A. La Monaca, G.P. Demopoulos, Single-crystal $TiNb_2O_7$ materials via sustainable synthesis for fast-charging lithium-ion battery anodes, J. Energy Storage 95 (2024) 112482. https://doi.org/https://doi.org/10.1016/j.est.2024.112482.

[25] L. Xiao, D. Wu, S. Han, Y. Huang, S. Li, M. He, F. Zhang, X. Feng, Self-assembled Fe_2O_3/graphene aerogel with high lithium storage performance, ACS Appl. Mater. Interfaces 5 (2013) 3764-3769. https://doi.org/10.1021/am400387t.

[26] G. Kresse, J. Furthmüller, Efficient iterative schemes for ab initio total-energy calculations using a plane-wave basis set, Phys. Rev. B 54 (1996) 11169-11186. https://doi.org/10.1103/PhysRevB.54.11169.

[27] G. Kresse, J. Furthmüller, Efficiency of ab-initio total energy calculations for metals and semiconductors using a plane-wave basis set, Computational Materials Science 6 (1996) 15-50. https://doi.org/https://doi.org/10.1016/0927-0256(96)00008-0.

[28] G. Kresse, J. Hafner, Ab initio molecular dynamics for liquid metals, Phys. Rev. B 47 (1993) 558-561. https://doi.org/10.1103/PhysRevB.47.558.

[29] P.E. Blöchl, Projector augmented-wave method, Phys. Rev. B 50 (1994) 17953-17979. https://doi.org/10.1103/PhysRevB.50.17953.

[30] G. Kresse, D. Joubert, From ultrasoft pseudopotentials to the projector augmented-wave method, Phys. Rev. B 59 (1999) 1758-1775. https://doi.org/10.1103/PhysRevB.59.1758.

[31] J. Heyd, G.E. Scuseria, M. Ernzerhof, Hybrid functionals based on a screened Coulomb potential, The Journal of Chemical Physics 118 (2003) 8207-8215. https://doi.org/10.1063/1.1564060.

[32] I.A. Vladimir, F. Aryasetiawan, A.I. Lichtenstein, First-principles calculations of the electronic structure and spectra of strongly correlated systems: the LDA+ U method, Journal of Physics: Condensed Matter 9 (1997) 767-808. https://doi.org/10.1088/0953-8984/9/4/002.

[33] A.I. Liechtenstein, V.I. Anisimov, J. Zaanen, Density-functional theory and strong interactions: Orbital ordering in Mott-Hubbard insulators, Phys. Rev. B 52 (1995) R5467-R5470. https://doi.org/10.1103/PhysRevB.52.R5467.

[34] A. Jain, S.P. Ong, G. Hautier, W. Chen, W.D. Richards, S. Dacek, S. Cholia, D. Gunter, D. Skinner, G. Ceder, K.A. Persson, Commentary: The Materials Project: A materials genome approach to accelerating materials innovation, APL Mater. 1 (2013) 011002. https://doi.org/10.1063/1.4812323.

[35] J. Paier, M. Marsman, K. Hummer, G. Kresse, I.C. Gerber, J.G. Ángyán, Screened hybrid density functionals applied to solids, The Journal of Chemical Physics 124 (2006) https://doi.org/10.1063/1.2187006.

[36] S. Yuan, K.H. Bevan, Engineering coexistence between free and trapped carriers via extrinsic polarons, Physical Review Materials 6 (2022) 114602. https://doi.org/10.1103/PhysRevMaterials.6.114602.

[37] Z. Wang, Ab initio modelling of adiabatic polaron dynamics in transition metal oxides, Materials Engineering, McGill University, Canada, 2017, p. 163.

[38] J. Heyd, G.E. Scuseria, Efficient hybrid density functional calculations in solids: Assessment of the Heyd–Scuseria–Ernzerhof screened Coulomb hybrid functional, The Journal of Chemical Physics 121 (2004) 1187-1192. https://doi.org/10.1063/1.1760074.

[39] K. Momma, F. Izumi, VESTA 3 for three-dimensional visualization of crystal, volumetric and morphology data, Journal of applied crystallography 44 (2011) 1272-1276. https://doi.org/https://doi.org/10.1107/S0021889811038970.

[40] X. Lu, Z. Jian, Z. Fang, L. Gu, Y.-S. Hu, W. Chen, Z. Wang, L. Chen, Atomic-scale investigation on lithium storage mechanism in $TiNb_2O_7$, Energy Environ. Sci. 4 (2011) 2638-2644. https://doi.org/https://doi.org/10.1039/C0EE00808G.

[41] S.F. Lou, X.Q. Cheng, Y. Zhao, A. Lushington, J.L. Gao, Q. Li, P.J. Zuo, B.Q. Wang, Y.Z. Gao, Y.L. Ma, C.Y. Du, G.P. Yin, X.L. Sun, Superior performance of ordered macroporous $TiNb_2O_7$ anodes for lithium ion batteries: Understanding from the structural and pseudocapacitive insights on achieving high rate capability, Nano Energy 34 (2017) 15-25. https://doi.org/10.1016/j.nanoen.2017.01.058.

[42] A. Tolosa, S. Fleischmann, I. Grobelsek, A. Quade, E. Lim, V. Presser, Binder-free hybrid titanium–niobium oxide/carbon nanofiber mats for lithium-ion battery electrodes, ChemSusChem 11 (2018) 159-170. https://doi.org/https://doi.org/10.1002/cssc.201701927.

[43] S. Lou, Y. Ma, X. Cheng, J. Gao, Y. Gao, P. Zuo, C. Du, G. Yin, Facile synthesis of nanostructured $TiNb_2O_7$ anode materials with superior performance for high-rate lithium ion batteries, Chem. Commun. 51 (2015) 17293-17296. https://doi.org/https://doi.org/10.1039/C5CC07052J.

[44] Y. Zeng, H.-C. Chiu, B. Ouyang, K. Zaghib, G.P. Demopoulos, Defect engineering of iron-rich orthosilicate cathode materials with enhanced lithium-ion intercalation capacity and kinetics, ACS Appl. Energy Mater. 3 (2020) 675-686. https://doi.org/10.1021/acsaem.9b01869.

[45] J.R. Dahn, J. Jiang, L.M. Moshurchak, M.D. Fleischauer, C. Buhrmester, L.J. Krause, High-rate overcharge protection of $LiFePO_4$-based Li-ion cells using the redox shuttle additive 2,5-Ditertbutyl-1,4-dimethoxybenzene, J. Electrochem. Soc. 152 (2005) A1283. https://doi.org/10.1149/1.1906025.

[46] K. Tang, X. Yu, J. Sun, H. Li, X. Huang, Kinetic analysis on $LiFePO_4$ thin films by CV, GITT, and EIS, Electrochim. Acta 56 (2011) 4869-4875. https://doi.org/https://doi.org/10.1016/j.electacta.2011.02.119.

[47] B. Meredig, A. Thompson, H.A. Hansen, C. Wolverton, A. van de Walle, Method for locating low-energy solutions within DFT+U, Phys. Rev. B 82 (2010) 195128. https://doi.org/10.1103/PhysRevB.82.195128.

[48] Z. Wang, C. Brock, A. Matt, K.H. Bevan, Implications of the DFT+U method on polaron properties in energy materials, Phys. Rev. B 96 (2017) 125150. https://doi.org/10.1103/PhysRevB.96.125150.

[49] Z. Wang, K.H. Bevan, Exploring the impact of semicore level electronic relaxation on polaron dynamics: An adiabatic ab initio study of $FePO_4$, Phys. Rev. B 93 (2016) 024303. https://doi.org/10.1103/PhysRevB.93.024303.

[50] S. Yuan, Z. Wang, M.L.F. Baron, K.H. Bevan, Ab initio insight into the formation of small polarons: A study across four metal peroxides, Phys. Rev. B 100 (2019) 205201. https://doi.org/10.1103/PhysRevB.100.205201.

[51] M. Uceda, H.-C. Chiu, J. Zhou, R. Gauvin, K. Zaghib, G.P. Demopoulos, Nanoscale assembling of graphene oxide with electrophoretic deposition leads to superior percolation network in Li-ion electrodes: $TiNb_2O_7$/rGO composite anodes, Nanoscale 12 (2020) 23092–23104. https://doi.org/https://doi.org/10.1039/D0NR06082H.

[52] R. Fong, N. Mubarak, S.-W. Park, G. Lazaris, Y. Liu, R. Malik, D.-H. Seo, J. Lee, Redox engineering of Fe-rich disordered rock-salt Li-ion cathode materials, Adv. Energy Mater. (2024) 2400402. https://doi.org/https://doi.org/10.1002/aenm.202400402.

[53] W. Wu, W. Lin, H.J. Chen, K.Y. Wei, Z.T. Li, H.T. Yang, M.X. Liu, H.C. Xiang, L.B. Deng, L. Yao, Iron oxide encapsulated titanium niobate nanotubes as a high-performance lithium-free anode for solid-state batteries, J. Mater. Chem. A 9 (2021) 4880-4889. https://doi.org/10.1039/d0ta11030b.

[54] M. Yang, S. Li, J. Huang, Three-dimensional cross-linked Nb_2O_5 polymorphs derived from cellulose substances: insights into the mechanisms of lithium storage, ACS Appl. Mater. Interfaces (2021) 39501-39512. https://doi.org/10.1021/acsami.1c11720.

[55] Z.J. Yao, X.H. Xia, S.Z. Zhang, C.A. Zhou, G.X. Pan, Q.Q. Xiong, Y.D. Wang, X.L. Wang, J.P. Tu, Oxygen defect boosted N-doped $Ti_2Nb_{10}O_{29}$ anchored on core-branch carbon skeleton

for both high-rate liquid & solid-state lithium ion batteries, Energy Storage Mater. 25 (2020) 555-562. https://doi.org/10.1016/j.ensm.2019.09.027.

[56] W.Q. Ye, H.X. Yu, X. Cheng, H.J. Zhu, R.T. Zheng, T.T. Liu, N.B. Long, M. Shui, J. Shu, Constructing hollow nanofibers to boost electrochemical performance: Insight into kinetics and the Li storage mechanism for $CrNb_{49}O_{124}$, ACS Appl. Energy Mater. 2 (2019) 2672-2679. https://doi.org/10.1021/acsaem.9b00010.

[57] Y.R. Denny, H.C. Shin, S. Seo, S.K. Oh, H.J. Kang, D. Tahir, S. Heo, J.G. Chung, J.C. Lee, S. Tougaard, Electronic and optical properties of hafnium indium zinc oxide thin film by XPS and REELS, Journal of Electron Spectroscopy and Related Phenomena 185 (2012) 18-22. https://doi.org/https://doi.org/10.1016/j.elspec.2011.12.004.

[58] D. Tahir, H.L. Kwon, H.C. Shin, S.K. Oh, H.J. Kang, S. Heo, J.G. Chung, J.C. Lee, S. Tougaard, Electronic and optical properties of Al_2O_3/SiO_2 thin films grown on Si substrate, Journal of Physics D: Applied Physics 43 (2010) 255301. https://doi.org/10.1088/0022-3727/43/25/255301.

5. Ultra-fast-charging and Long-cycling Titanium Niobate/Reduced Graphene Oxide Anode via Electrophoretic Interfacial Engineering

Bridge: **Chapter 4** reports an ultra-fast charging anode with long-term cycling stability enabled by Fe substitution in single-crystal TNO nanomaterials. The optimal Fe^{3+}-doped TNO monocrystalline material ($Fe_{0.05}Ti_{0.95}Nb_2O_{6.975}$) provides remarkable charge capacity of 238 mAh/g under 10 C (6 min charging time only) extreme fast-charging protocol (coupled with 1 C discharge), and high capacity of 200 mAh/g at 5 C and high cycling retention of 85 % after 1000 cycles. However, interphase issues such as the non-homogeneous electrode contacts and unstable electrode/electrolyte interphase, which affect electrochemical kinetics, electrode structural stability, and volume variations, cause significant performance loss during extended cycling under fast charging conditions. To address these challenges, this chapter addresses the third objective of thesis, i.e., to develop advanced electrode engineering by using electrophoretically depositing single-crystal $TiNb_2O_7$/graphene composite anode towards its practical application as ultrafast-charging lithium-ion battery anodes. Specifically, we have developed an advanced electrophoretic interfacial control technique to assemble carbon-coated Fe-doped TNO nanomaterial (C-FeTNO) and reduced graphene oxide (rGO) on a nanoscale, constructing a sandwich-like hybrid electrode that act as a binder-free, all-active-material electrode. Consequently, a high initial capacity of 212 mAh/g and excellent cycling retention of 70 % after 5000 cycles at 5 C were achieved. These insights pave the way towards the practical application of ultrafast-charging materials for next-generation LIBs.

This chapter is a reproduction of the manuscript that has been submitted to the ***Journal of Materials Chemistry A***, with following citation:

- **Fan Yu**, Yihan Wang, Nicolas Brodusch, Bobby Miglani, Jinhyuk Lee, Raynald Gauvin, George P. Demopoulos, Ultra-fast-charging and Long-cycling Titanium Niobate/Reduced Graphene Oxide Anode via Electrophoretic Interfacial Engineering.

Abstract

Titanium niobate ($TiNb_2O_7$, TNO) materials are emerging as high-performing anode candidates for fast charging Li-ion batteries. However, the non-homogeneous interphasial electrode microstructure, which directly affects electrochemical kinetics, electrode structural stability, and volume variation, result in significant performance loss upon extended cycling under fast charging. To address these issues, we have engineered a carbon-coated single-crystal Fe-doped

TNO (C-FeTNO)/reduced graphene oxide (rGO) anode with ultra-fast (10 C) and over 5,000 cycles capability. This is achieved via electrophoretic deposition (EPD) controlled at nanoscale with graphene oxide acting as binder and conductive component upon reducing annealing. The designed electrode exhibits dramatic reduction in charge transfer impedance from 183 ohm to 75 ohm and boosting of Li ion diffusion coefficient by one order of magnitude from 10^{-12} to 10^{-11} cm^2/s. Consequently, the EPD nanoengineered TNO/rGO hybrid anode demonstrates outstanding performance, namely capacities of 252, 246, 236, and 210 mAh/g at 0.5 C, 1 C, 2 C, and 5 C, respectively. But more remarkably, it is shown to have exceptional cycling stability of 70 % retention after 5000 cycles at 5 C. This remarkable electrochemical performance can be attributed to the EPD-enabled nanoscale interphasial contacting (between C-coated Fe-TNO and rGO) and the homogeneous microstructure endowing the electrode with a highly conducting stable charge percolation network.

5.1. Introduction

Electric vehicles (EVs) require ultrafast-charging lithium-ion batteries (LIBs) with high capacity and long cycle life[1-3]. For such applications, extreme fast charging (XFC) LIBs have been identified as those reaching 80% state of charge in less than 15 minutes (> 4 C fast charging) while maintaining high capacity retention after a decade of usage[1]. However, traditional anode materials, i.e., graphite with low working potential (ca., 0.1 V (*vs.* Li/Li^+)), are not suitable for such application as due to developed polarization under extremely fast changing, lithium plating is triggered leading to short circuiting, and battery failure[4]. Meanwhile, commercial $Li_4Ti_5O_{12}$ anode provides superior fast-charging capacity, safe working voltage, and long cycling characteristic, but it suffers from low theoretical capacity (only 175 mAh/g)[5]. Therefore, it is urgent to explore the next-generation fast-charging anode materials.

Titanium niobate ($TiNb_2O_7$, TNO) materials emerge as a promising candidate, offering fast ionic diffusion kinetics, high theoretical capacity, and safe working potential[6-8]. However, its application suffers from significant capacity fade after long cycling under fast-charging conditions due to poor electronic conductivity, crystal structure change, and unwanted insulating layer formation[6,8]. To address this issue, both the bulk material structure and the interphase need to be improved: the former can be modified by crystal control during nanomaterial synthesis, element doping, etc.[6,9,10]; and the latter can be improved by constructing conductive percolation networks via advanced electrode/interphase engineering[10-13]. While only few studies have explored this direction, the synergy between these strategies opens a promising path toward designing ultra-fast charging and long-cycling TNO anodes[6]. Towards this goal, rationally built three-dimensional fast-ionic/electronic networks consisting of cation-doped TNO single crystals and graphene are considered a potentially rewarding strategy in this context[14,15]. This novel electrode design approach leverages the multifunctionality of graphene, including excellent electronic conductivity, mechanical/thermal stability, Li-storage capability, and binding properties, which can enhance kinetics, suppress volume variation, and prevent electrolyte decomposition[9,16]. However, traditional electrode engineering and interphase control approaches encounter several obstacles in fabricating such 3D graphene/TNO electrodes with well-defined interphases. Conventional battery electrode manufacturing involves tape casting (or blade coating) a suspension made of organic solvent, carbon, binder, and active material, followed by drying in oxygen-exposed conditions. This process often leads to the oxidation of graphene, transforming the highly-conductive graphene material into a low-conductivity phase[17]. Additionally, nonhomogeneous coating processes lead to significant aggregation of nanomaterials and non-uniform electrode-electrolyte interphase formation, which causes severe polarization and subsequent battery degradation[13,14]. Also, non-active components including conductive carbon and binder limit the available capacity and volumetric electrode energy density[18]. Moreover, the use of toxic solvents like NMP (N-Methyl Pyrrolidone) raises safety and environmental concerns[13]. Thus, an alternative electrode engineering process that can achieve uniform electrode interphasial microstructure for high performance via environmentally friendly means becomes of great urgency.

Electrophoretic deposition (EPD) technology, as an advanced electrode engineering and interphase control technique, is known for its superior uniformity, low cost, equipment simplicity, and high scalability[19-21]. Recent studies have shown that the EPD approach outperforms the conventional tape casting method in constructing TNO/reduced graphene oxide (rGO) composite electrodes with high capacity and well-uniform interface[22,23]. For example, Uceda et al.[13] electrophoretically co-deposited micron-sized TNO particles and rGO to engineer binder-free all-active-materials LIB electrode with highly homogeneous percolation network but its cycling retention and rate performance were not satisfactory because the TNO material used obtained via solid-state calcination and milling it was coarse and full of defects. In addition, the precise control of electrode composition, and mass loading is still difficult to be realized. Therefore, developing high-performance TNO/rGO composite materials via EPD constitutes a yet unexplored but highly promising advanced electrode engineering avenue.

Herein, we describe the EPD-enabled design of carbon-coated Fe-doped single-crystal TNO nanomaterial/rGO advanced electrode structure with unparalleled ultra-fast charging and long-cycling performance. Thanks to the nanoscale assembling property of EPD the fabricated electrodes are characterized by excellent composition homogeneity boasting significantly reduced impedance and very high Li-ion diffusivity network. At the electrode level, this EPD anode offers remarkable rate performance, showing capacities of 252, 246, 236, and 210 mAh/g at 0.5 C, 1 C, 2 C, and 5 C, respectively, and demonstrates excellent cycling retention of 70% after 5000 cycles at 5 C.

5.2.Experimental Section

5.2.1. Synthesis of nanostructured Fe-doped TNO (FeTNO)

The single-crystal Fe-substituted TNO nanomaterial ($Fe_{0.05}Ti_{0.95}Nb_2O_{6.975}$, FeTNO) was synthesized using a universal and scalable approach featuring co-precipitation and high-temperature calcination (**Scheme S1(a)**), as described in previously[10,15]. Three feedstock aqueous colloidal solutions were prepared via temperature-controlled partial hydrolysis (under 10 ^oC) of ferric chloride hexahydrate ($FeCl_3·6H_2O$, 99%, Sigma-Aldrich, USA), titanium tetrachloride ($TiCl_4$, 99.0%, Sigma-Aldrich, USA), and niobium pentachloride ($NbCl_5$, 99%, Thermo Fisher Scientific, USA). By mixing these three feedstock solutions, the composite Fe-Ti-Nb-Cl solution was prepared containing 0.000125 mol/L Fe(III), 0.02375 mol/L Ti(IV), and 0.05 mol/L Nb(V). The latter solution was neutralized by dropwise adding ammonium hydroxide (99.9% NH_4OH, 29% NH_3 basis, Sigma-Aldrich, USA) inducing hydrolytic co-precipitation of a nanosized FeTNO intermediate. After washing and drying, the FeTNO precursor was crystallized at 900 ^oC for 4 hours in a continuous flow of oxygen gas with a heating ramping rate of 5 ^oC/min in a tube furnace oven (OTF-1200X-S50-2F Mini CVD tube furnace, MTI Corporation, USA).

5.2.2. Carbon coating of FeTNO (for C-FeTNO)

Carbon coating of FeTNO was conducted by the high-temperature decomposition of lactose carbon precursor (**Scheme S1(a)**), as reported in our previous research[13]. The 1 g FeTNO material was mixed with 5 mL lactose aqueous solution (22.4 g/L lactose), followed by drying at 120 ^oC in an oven. The carbon-coated FeTNO material (C-FeTNO) was obtained by annealing at 700 ^oC for 400 minutes in the tube furnace oven under pure argon atmosphere.

5.2.3. Electrophoretic deposition of C-FeTNO/rGO electrode

As shown in **Scheme S1(b)**, the electrode was engineered by electrophoretically co-depositing C-FeTNO and GO on Al foil immersed in an isopropanol suspension. After deposition, the EPD prepared electrode was subjected in thermal treatment in the presence of H_2 so GO is reduced and the C-FeTNO/rGO anode is constructed. The optimal parameters of the process have been investigated as discussed below.

5.2.3.1. Suspension preparation

The optimal EPD suspension contains 66.7 mL of pure isopropanol solvent, 184 mg of C-FeTNO, 16 mg of graphene oxide (GO, Sigma-Aldrich, powder, 15-20 sheets), and 66 ppm of lithium acetate (LiOAc, Sigma-Aldrich, 99 %) added as charging agent. This suspension make up corresponds to 3 g/L solid loading and mass ratio of 92/8 of C-FeTNO/GO between C-FeTNO and GO. In establishing the above suspension formulation different solvents were tested with and w/o prior C-coating or with or w/o charging additives. The different solvents tested are described in the **section C.2.** of the Supporting Information for Chapter 5 (in **Chapter 8. APPENDIXES**). The stability of suspensions was determined by settling tests (**Figure C.1**) and Zeta potential measurements. In the suspension stability tests, 15 mg solid particles (either GO or C-FeTNO) were added to 5 mL of different organic solvents, followed by sonication. These mixtures were then left to rest for 48 hours for visual inspection after 48 hours of resting.

5.2.3.2. EPD process for C-FeTNO/GO film

An EPD electrolytic cell with a 15 μm Al foil working electrode and a stainless steel counter electrode was set up with electrode spacing of 7.5 mm and a deposition area of 4 to 6 cm^2. Deposition occurred at the anode. EPD cell was operated at different constant voltages (50 V, 100 V, and 200 V) supplied by a SourceMeter (Keithley 2611A) instrument.

5.2.3.3. Reduction for C-FeTNO/rGO EPD electrode

The GO in C-FeTNO/GO films was reduced by annealing at 600 °C for 300 minutes in a 5 vol.% H_2/Ar gas mixture to obtain the target C-FeTNO/rGO electrode composition.

5.2.4. Conventional electrode via tape casting

The reduction of GO samples was processed with the same procedure (as shown in **2.3.3**) to obtain rGO. This rGO sample was applied to fabricate conventional electrodes.

In conventional electrode fabrication, a binder plus conductive carbon are used. Specifically, the active material, the conductive component (carbon black (CB)), and the polyvinylidene fluoride (PVDF) binder were mixed at a weight ratio of 8:1:1, and then added into N-Methyl-2-pyrrolidone (NMP) solvent. After milling, this slurry was cast on the Al foil using a doctor blade before drying overnight.

To investigate the effects of different components, three electrodes were fabricated by the tape casting approach. The conventional FeTNO/CB/PVDF electrode consisted of FeTNO material (active material), carbon black (conductive carbon), and PVDF binder, named the FeTNO electrode. To understand the carbon coating effect, C-FeTNO, carbon black, and PVDF binder were casted to fabricate the C-FeTNO/CB/PVDF electrode (namely, C-FeTNO electrode). Finally, the C-FeTNO/rGO/PVDF electrode was prepared by using C-FeTNO as active material, rGO as conductive agent, and PVDF as binder. The component ratio was 8:1:1 on wt. basis for all the formulations.

5.2.5. Material characterization

The elemental composition of Fe, Ti, and Nb in FeTNO samples and their concentrations in solutions were determined via inductively coupled plasma optical emission spectrometry (ICP-OES, Thermo scientific, iCAP 6700 Series). The crystal structures were determined by using a Bruker D8 Discovery X-ray diffractometer (VANTEC Detector Cu-Source) and analysed via TOPAS (Bruker) V5 software. Attenuated total reflection Fourier transform infrared (ATR-FTIR) spectroscopy was carried out using FTIR infrared spectrometer Vertex 70 from Bruker. Raman microscopy was performed using a Thermo Scientific DXR2 Raman microscope, equipped with DXR 532 nm wavelength laser. The morphology and elemental distribution of materials was determined using a Hitachi SU-8000 Cold Field-Emission scanning electron microscope (SEM) equipped with in-lens upper secondary electron detector and energy-dispersive X-ray spectroscopy (EDS) detector (XMax 80 mm^2 Oxford Instruments). Cross-sectional SEM image and EDS mapping for electrode film were performed with the Hitachi SU-9000 cold field-emission SEM/STEM instrument equipped with in-lens SE/BSE detectors with energy filtration (Upper and Top detectors) and Oxford Instrument windowless Extreme 100 mm^2 SDD detector. This setup is capable of achieving a resolution of 0.16 nm at 30 keV in BF mode and 0.4 nm in SE mode. Transmission electron microscopy (TEM), high-resolution transmission electron microscopy (HRTEM), scanning transmission electron microscopy (STEM), selected area electron diffraction (SAED), and Fast Fourier Transform (FFT) imaging were performed on Thermo Scientific Talos F200X G2 TEM/STEM instrument operated at 200 kV. Zeta potential, electrophoretic mobility, and suspension conductivity were measured using a Malvern Zetasizer Ultra (Malvern Instruments).

5.2.6. Electrochemical characterization

Both EPD electrodes and conventional electrodes were assembled in half-cell batteries for electrochemical testing. Each coin cell consists of the electrode sheet, a lithium metal, a separator film (PP/PE/PP, Celgard 2325), and 200 µL of 1M $LiPF_6$ in EC:DMC:DEC as electrolyte.

Battery charge-discharge cycling measurement and galvanostatic intermittent titration technique (GITT) analysis were carried out using a standard battery cycler (BT2043-10V-100 mA-40, Arbin) under different C rates (1 C= 387.6 mAh/g) and voltage range between 3.0 V and 1.0 V. Cyclic voltammetry (CV) and electrochemical impedance spectroscopy (EIS) measurements were performed using a BioLogic VSP electrochemical workstation and analyzed by EC-Lab software.

5.3. Results and Discussions

5.3.1. Advanced TNO/graphene Anode Design

This research introduces a novel design concept of advanced TNO/graphene composite electrode enabled by electrophoretic deposition. This novel electrode is made of single-crystal Fe-substitution TNO crystals ($Fe_{0.05}Ti_{0.95}Nb_2O_{6.975}$, optimal sample discussed in **Chapter 4**), following carbon coating and graphene oxide acting as binder and conductive component following reductive annealing with hydrogen.

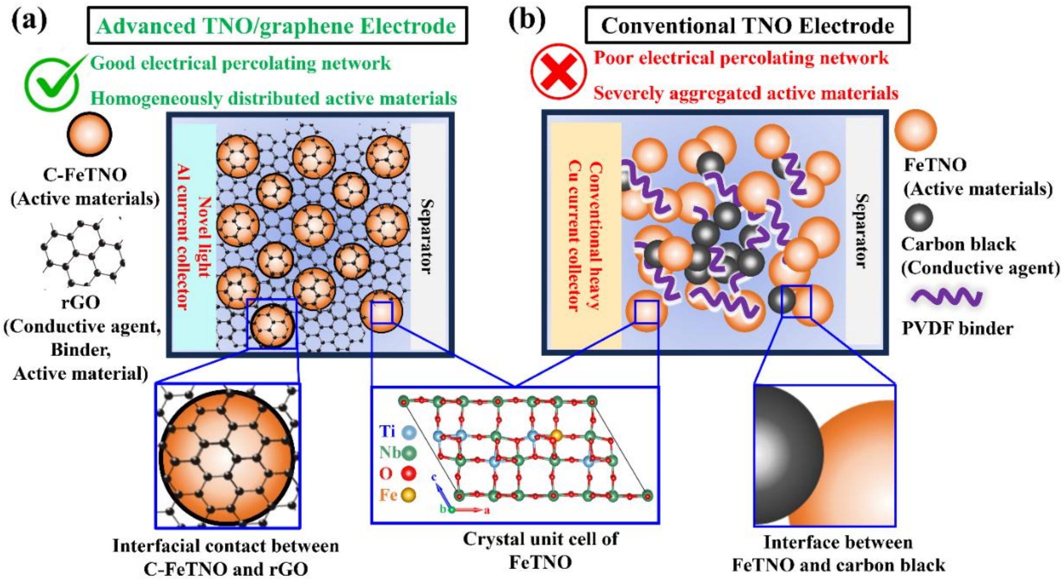

Figure 5.1 Schematic illustration of the design of advanced C-FeTNO/rGO electrode and its comparison to conventional electrode.

As shown in the graphical representation in **Figure 5.1(a)**, this advanced C-FeTNO/rGO EPD electrode consists of carbon-coated nanostructured Fe^{3+}-substitution TNO materials (C-FeTNO) and reduced graphene oxide (rGO), forming a binder-free all-active-material electrode. The advanced EPD electrode **(Figure 5.1(a))** is characterized by homogeneous distribution of the C-FeTNO nanomaterial component and the rGO multifunctional component. By contrast, the conventional LIB electrode (**Figure 5.1(b)**) featuring Fe-TNO active material, carbon black (conductive agent), and PVDF binder, assembled with assistance of organic solvent (e.g., N-Methyl-2-Pyrrolidone (NMP)) and deposited by doctor blading suffers from severe aggregation and poor electrical percolating network. In both cases Al is used as the electron collector substrate.

5.3.2. Electrode Engineering by EPD

To engineer the designed advanced electrode, we electrophoretically co-deposit GO and C-FeTNO from their suspension in isopropanol solvent employing LiOAc as charging additive. **Figure 5.2(a)** provides a schematic of the EPD cell.

5.3.2.1. Suspension Formulation

(1) Selection of Organic Solvents: Factors such as suspension stability, electrophoretic mobility, practical deposition rate, environmental friendliness, and potential health hazards need to be considered when selecting an optimal solvent. Given that C-FeTNO and GO are the main components, three benign organic solvents were short-listed as potential candidates, namely ethylene glycol, isopropanol, and ethanol , after suspension media screening (detailed in **C.2 section**). In stability testing, GO suspensions made with these solvents are highly stable (**Figure C.1(a)**), which arises from van der Waals interactions and hydrogen bonding between the oxygen-containing functional groups on GO and the organic molecules[24]. For C-FeTNO suspensions, the order of suspension stability (**Figure C.1(b)**) correlates strongly with solvent viscosity (**Table S2**): ethylene glycol (16.265 cP), isopropanol (2.044 cP), and ethanol (1.089 cP)[25-27]. Although ethylene glycol yielded the most stable suspension, it was observed the C-FeTNO particles to have limited electrophoretic mobility (-0.215 μm·cm/Vs, shown in **Table C.3**) resulting in poor deposit formation. In contrast, the suspensions based on isopropanol and ethanol found to exhibit good electrophoretic mobilities (-0.215 μm·cm/Vs and -0.480 μm·cm/Vs) and deposition rates. In particular, the isopropanol-based suspensions exhibited higher stability and more uniform deposition **(Figure C.3)** compared with ethanol-based suspensions. Therefore, isopropanol is deemed to be the optimal solvent for both C-FeTNO and GO.

(2) Zeta Potential Measurements: Mean Zeta potentials of isopropanol suspensions with C-FeTNO and GO (**Figure 2(b)**) were determined to be -43 mV and -53 mV, respectively, indicating the presence of negative charge carriers on the surface of C-FeTNO and GO solids. It is noteworthy that isopropanol-based suspension with C-FeTNO shows a higher absolute value of mean Zeta potential than ethanol-based suspension (with -35 mV) and ethylene glycol-based suspension (with -6 mV) as shown in **Figure C.2**, further confirming that isopropanol is the preferred solvent.

(3) Effect of charging agent: Lithium acetate (LiOAc) was added as a charging agent into the suspension to adjust the mean Zeta potential and stabilize the suspension, thereby improving the uniformity of the EPD coating film[28]. Different concentrations of LiOAc were tested: three suspensions with 0 ppm, 66 ppm, 660 ppm of LiOAc demonstrated Zeta potentials of -45 mV, -71 mV, and -95 mV, respectively (**Figure 2(b)**). The Zeta potential results are consistent with EPD deposition rates and deposition film qualities **(Figure C.3(d))**, making 66 ppm of LiOAc the optimal concentration. The observed negative value of Zeta potential caused by the addition of LiOAc can be attributed to the negative charge of acetate anions dominating the diffuse layer enwrapping the surface of C-FeTNO and GO.

5.3.2.2. Electrophoretic Deposition Parameters

EPD parameters including applied electric field and suspension composition are controlled to optimize the deposit quality in terms of rate of deposition and composition and mass loading. Given that the charging additive changed the zeta potential from positive to negative, the electrode deposit forms on the anode and not the cathode. In other words, during EPD, the applied electric field transports negatively charged particles to the anode.

(1) Applied electric field: During EPD, constant voltages of 50 V, 100 V, and 200 V were tested, all of which generate high-quality deposition film. A low voltage of 50 V was chosen to avoid the oxidation of Al foil substrate and safety concerns under high voltages, even though 100 V and 200 V were found to have higher deposition rates and efficiencies.

(2) Coating Composition Control: The composition ratio of C-FeTNO to GO in an EPD electrode can be adjusted by changing the suspension composition. This is shown in **Figure 5.2(d).** The composition was determined via TGA measurements. For subsequent electrode performance evaluation, the C-FeTNO/rGO electrode with composition 86.5 wt.% FeTNO, 1.4 wt.% carbon coating, and 12.1 wt,% rGO, or 87.9 wt.% C-FeTNO and 12.1 wt.% rGO was selected.

(3) Coating Mass Loading Control: EPD allows for precise control over the mass loading on a substrate. By increasing deposition time by 1 minute per stage, mass loading can be adjusted from 0.25 up to 3.0 mg/cm^2 within 6 min (**Figure 5.2(d)**).

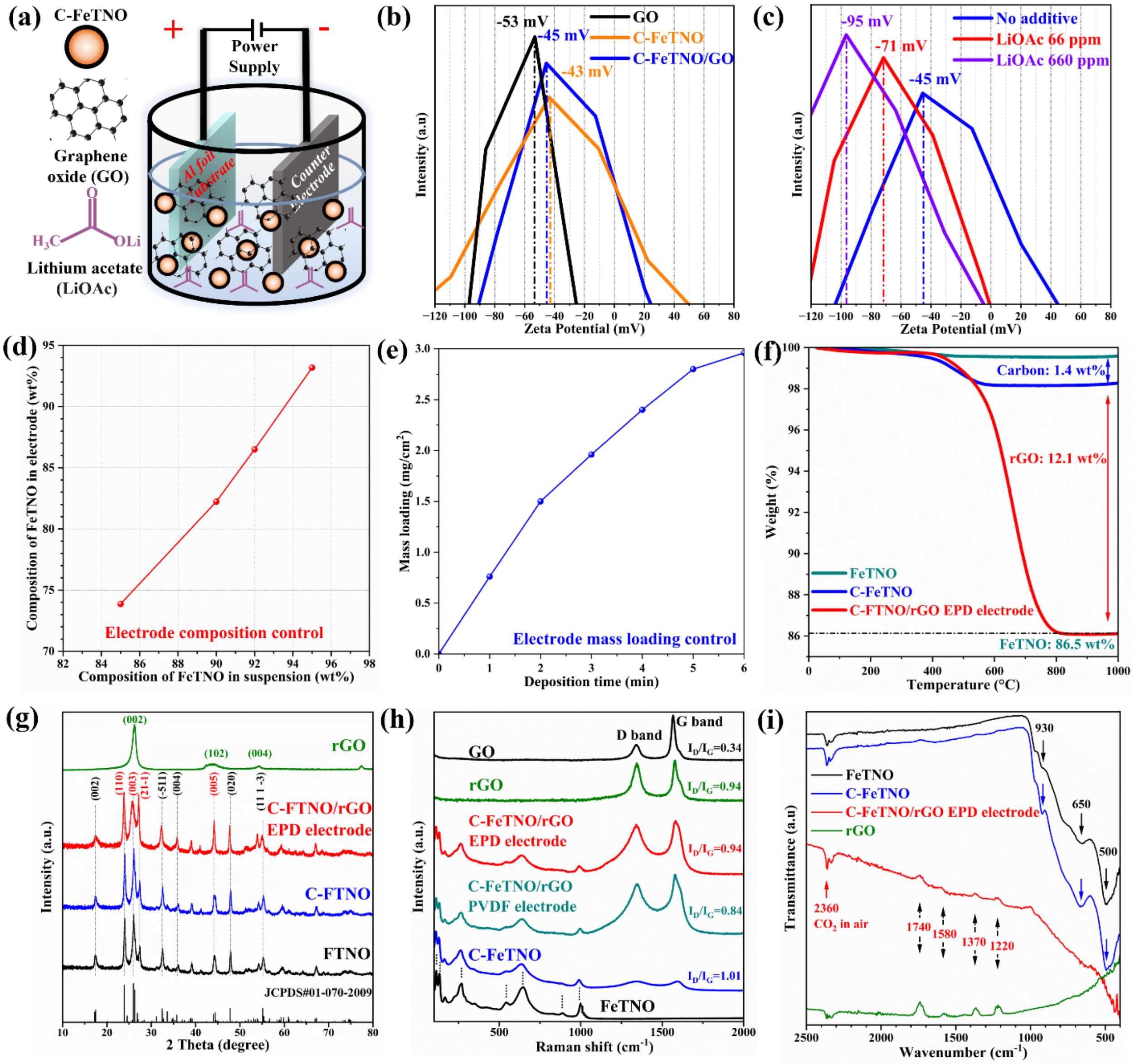

Figure 5.2 (a) Schematic illustration of EPD cell, (b) Zeta potential of C-FeTNO (2.76 g/L), GO (0.24 g/L), C-FeTNO (2.76 g/L)/GO (0.24 g/L) suspensions in isopropanol, (c) C-FeTNO/GO-isopropanol suspension with different concentrations of LiOAc additive (0 ppm, 66 ppm, and 660 ppm). (d) Composition of C-FeTNO/rGO EPD electrodes with varying suspension compositions. (e) Weight ratio of components determined by TGA. (f) Mass loading of electrode with increasing EPD deposition time. (g) XRD patterns, (h) Raman spectra, and (i) FT-IR spectra of FeTNO material, C-FeTNO material, C-FeTNO/rGO EPD electrode, and rGO material.

5.3.3. Physical Properties of Materials and Electrode

Crystallographic properties of FeTNO, C-FeTNO, C-FeTNO/rGO EPD electrode, and rGO were investigated by XRD analysis (**Figure 5.2(g)**). The phase patterns of FeTNO material, C-FeTNO material, and C-FeTNO/rGO EPD electrode can be indexed to the $TiNb_2O_7$ phase with a monoclinic C2/m space group (PDF#01-070-2009). Two predominant diffraction peaks of these three samples are positioned at 23.91^o and 25.99^o corresponding to (110) and (003) lattice planes. The peak intensity ratio of (110)/(003) for the C-FeTNO/rGO EPD electrode differs from that of FeTNO and C-FeTNO materials, which can be attributed to the influence of XRD peaks associated with the (002) plane of rGO[29].

Raman spectroscopy was carried out to determine spectral features of carbon (GO, rGO, and surface carbon) and FeTNO samples. As shown in **Figure 5.2(h)**, two prominent peaks, D band and G band, are positioned at ~1320-1350 cm^{-1} and ~1570-1605 cm^{-1}, which can be attributed to the vibrations of disordered carbon and ordered graphitic carbon, respectively[30,31]. The peak intensity ratio of the D band to G band (I_D/I_G) of the rGO sample (I_D/I_G=0.94) and the C-FeTNO/rGO EPD electrode (I_D/I_G=0.94) is higher than that of GO (I_D/I_G=0.33), suggesting that GO is successfully reduced to rGO[32,33]. The increase of D band signal is likely due to more local defects and disorders, formed due to the deoxygenation of GO[33]. By contrast, C-FeTNO/rGO PVDF electrode sample illustrates a lower I_D/I_G value (I_D/I_G=0.84), as some of the graphene layers in the rGO sample are re-oxidized by oxygen-containing groups during tape casting approach[17]. This comparative Raman analysis in **Figure 5.2(h)** suggests the EPD method is more effective than traditional tape casting (PVDF method) at preventing the oxidation of graphene. Meanwhile, the peaks of D band and G band that emerge in C-FeTNO sample (I_D/I_G=1.01) can be ascribed to the surface carbon coated on the FeTNO particles[11,34]. For the C-FeTNO and C-FeTNO/rGO EPD electrode, the peaks observed at <1200 cm^{-1} align closely with those of $TiNb_2O_7$ samples reported previously[35-37]. Specifically, the two peaks at 988 cm^{-1} and 880 cm^{-1} originate from the vibrations of the edge and corner-shared NbO_6 octahedra, respectively[35,36]. The peaks at 635 cm^{-1} and 540 cm^{-1} are indicative of the vibrations of the edge- and corner-shared TiO_6 octahedra, respectively. Additionally, the peaks at 263 cm^{-1} and 163 cm^{-1} are associated with vibrations of complex models that include the antisymmetric and symmetric bending vibrations of O-Nb-O and O-Ti-O[38].

FT-IR spectra (**Figure 5.2(i)**) were obtained to further confirm the bonding environment of the C-TNO/rGO composite anode. The bands at approximate 500 cm^{-1} and 930 cm^{-1} arise from the stretching vibrations of the Nb-O-Nb bridging bonds and Nb-O bonds, respectively[39]. The absorption peak at 650 cm^{-1} is attributed to the stretching vibration of Ti-O-Ti bonds[40]. The peak at 2360 cm^{-1} is associated with CO_2 in air[12]. Additionally, the FT-IR spectra revealed the nature of the functional groups in GO and C-FeTNO/rGO EPD electrodes. The absorption peaks at 1740 cm^{-1}, 1580 cm^{-1}, 1370 cm^{-1}, and 1220 cm^{-1} are attributed to C=O stretching, C=C stretching, C–O–H bending, and C–O stretching, respectively[41]. The peak signals corresponding to these functional groups were decreased in inensity, which likely suggests the successful reduction of GO to rGO[41]. Overall, both Raman and FT-IR spectra consistently confirm that GO is successfully converted to rGO by the H_2-reductive annealing process, while the properties of FeTNO and C-FeTNO remain unchanged.

5.3.4. Morphological structure of C-FeTNO material and C-FeTNO/rGO-EPD electrode

Figure 5.3 presents the morphological features of C-FeTNO material and C-FeTNO/rGO EPD electrode. The SEM image (**Figure 5.3(a)**), TEM image (**Figure 5.3(b)**), and HADDF image (**Figure 5.3(c)**) reveal C-FeTNO to be in the form of nanometric single crystals with size ranging from 20-100 nm. The single crystal structure of C-FeTNO is verified by the interlayer spacing of 1.04 nm correponding to (001) plane (d_{001}) of $TiNb_2O_7$, as shown in **Figure 5.3(d)**,. Additionally, the carbon layer coated on C-FeTNO has a thinkness of 1.34 nm. EDS mapping (**Figure 5.3(e)**) reveals that Fe, Ti, Nb, and O elements are homogeneously distributed within the bulk of C-FeTNO, while the C element is evenly distributed on the surface of FeTNO.

Furthermore, the microstructure of C-FeTNO/rGO EPD electrode (**Figure 5.3(f-j)**) has been investigated. As shown in **Figure 5.3(f-h)**, C-FeTNO particles are successfully assembled into a three-dimensional rGO composite structure. The corresponding SAED image (**Figure 5.3(i))** illustrates the periodic arrangements characteristic of C-FeTNO/rGO composite materials, aligning with the monocrystalline nature of FeTNO and the few-layer structure of rGO. Uniform distributions of C, Fe, Ti, Nb, and O elements is demonstrated by the EDS mapping (**Figure 5.3(j)**). The obtained C-FeTNO/rGO EPD electrode features nanostructured C-FeTNO homogeneously embedded between graphene sheets, which realizes the concept design demonstrated in **Figure 5.1**.

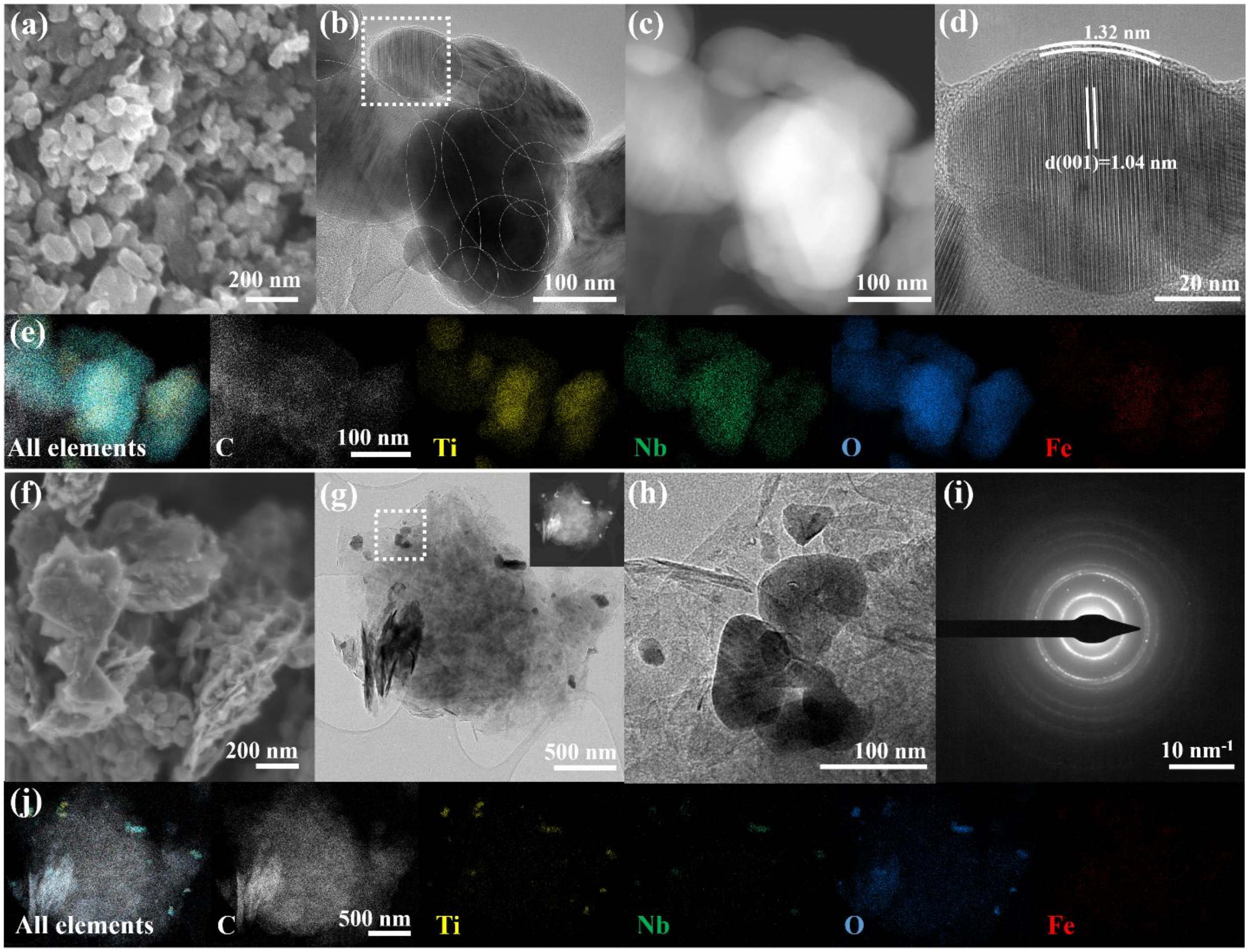

Figure 5.3 (a) SEM image, (b) TEM image, (c) HADDF image, (d) HRTEM image of selected area, and (e) EDX elemental mapping of C-FeTNO material. (f) SEM image, (g) TEM image with inserted HADDF image, (h) HRTEM image of selected area, (i) SAED pattern, (j) EDX elemental mapping of C-FeTNO/rGO EPD electrode.

5.3.5. Electrode Homogeneity and Microstructure

The electrode homogeneity and interfacial contact were investigated through cross-sectional SEM imaging (**Figure 5.4(a, c, e)**) and elemental mapping of C, Ti, Nb, and O (**Figure 5.4(b, d, f)**). **Figure 5.4(a, b)** reveals that C-FeTNO and rGO materials are homogeneously distributed within the C-FeTNO/rGO EPD electrode, suggesting the formation of a uniform three-dimensional percolation network, which is instrumental in constructing ultrafast electronic and ionic conduction pathways. These desirable characteristics of advanced electrodes can be attributed to the remarkable submicron/nanoscale self-assembly and deposition capability of EPD technique[19]. By contrast, the conventional tape casting method is limited by non-homogeneous deposition and aggregation of nanomaterials. For example, the C-FeTNO/rGO PVDF electrode (**Figure 5.4(c, d)**) and C-FeTNO/CB PVDF electrode (**Figure 5.4(e, f)**) demonstrate severe aggregation of C-FeTNO and conductive carbon (rGO and CB) materials, indicating non-uniform composition in bulk or interface of the electrode.

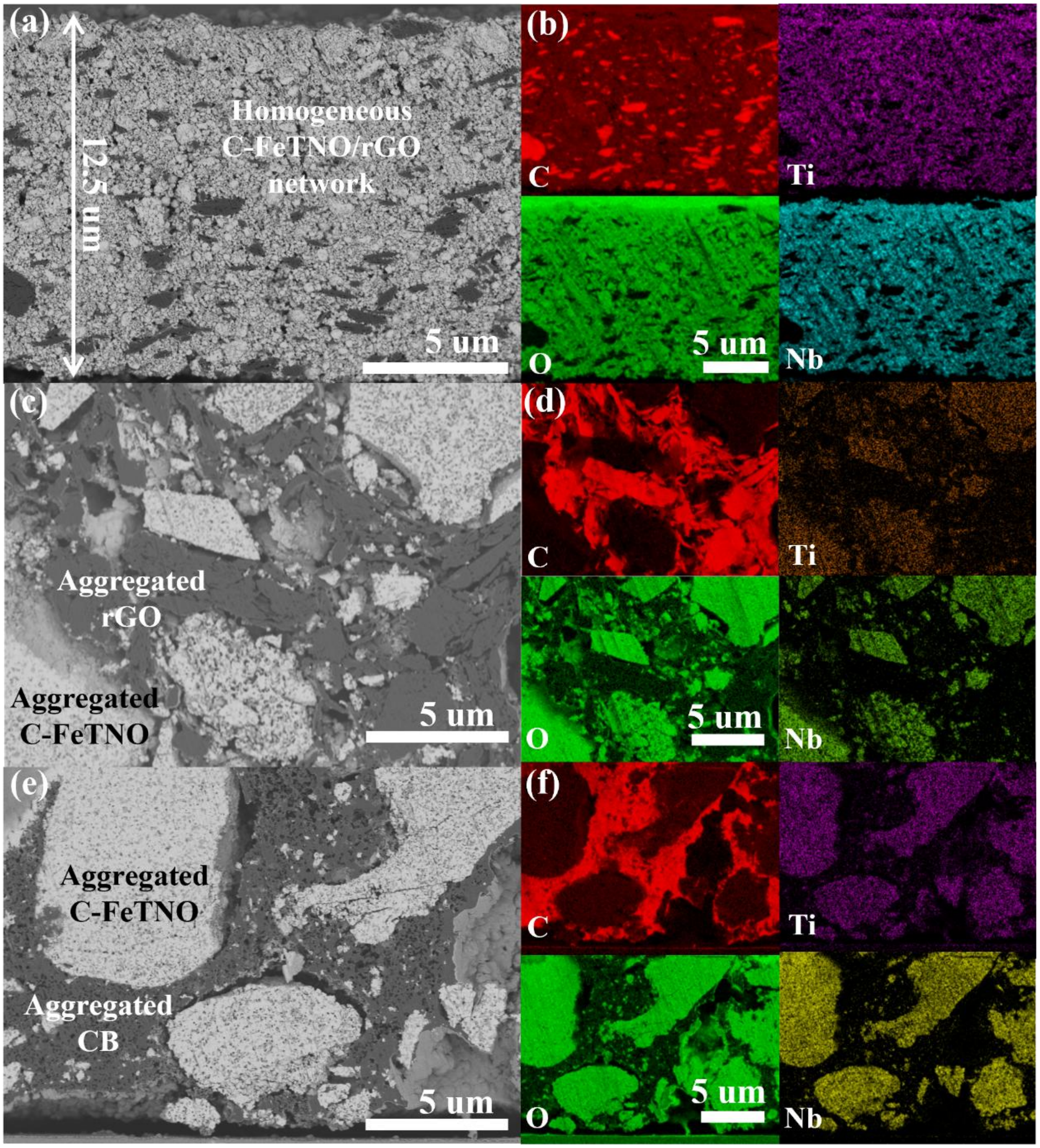

Figure 5.4 (a) Cross-sectional SEM image and (b) EDS mapping of C-FeTNO/rGO EPD electrode. (c) Cross-sectional SEM image and (d) EDS mapping of C-FeTNO/rGO PVDF electrode. (e) Cross-sectional SEM image and (f) EDS mapping of C-FeTNO electrode.

5.3.6. Electrochemical performance

The influence of advanced electrode microstructure on interface impedance (**Figure 5.5(a)**) and redox overpotential (**Figure 5.5(b)**) was investigated by EIS and CV measurements of the C-FeTNO/rGO EPD electrode, C-FeTNO/rGO PVDF electrode, C-FeTNO electrode, and FeTNO electrode, respectively. The EIS circuit model is shown in **Figure C.4**. As illustrated in **Figure 5.5(a)**, the charge transfer resistance (R_{CT}) of pristine electrode (without lithiation) for FeTNO electrode is measured to be 183 ohm. In contrast, the R_{CT} of C-FeTNO electrode is reduced to 132 ohm, suggesting the surface carbon coating improves the electronic conductivity of the electrode. Most notably, the C-FeTNO/rGO EPD electrode exhibits the lowest R_{CT} (only 75 ohm) among all electrodes tested, which can be attributed to highly-conductive rGO network and homogeneous electrode interphase enabled by the optimized EPD technique. Conversely, the C-FeTNO/rGO PVDF electrode has the highest R_{CT} of 241 ohm. This is likely because part of rGO materials in electrode has been oxidized back to GO, a low-conductivity phase, during the conventional electrode procedure, as revealed by the Raman spectra (**Figure 5.2(h)**). The significant difference in R_{CT} between C-FeTNO/rGO EPD electrode and C-FeTNO/rGO PVDF electrode highlights the superiority of EPD electrode fabrication method over conventional PVDF approach in constructing electrodes with high conductivity and superior interface contact for TNO/graphene composite electrodes. A similar trend is observed with CV data in **Figure 5.5(b)**; the graphene 3D electrode network enabled by the EPD technique promotes the depolarizing effect of TNO-based electrode during lithiation and delithiation. For example, the C-FeTNO/rGO EPD electrode, with cathodic potential of 1.60 V and anodic potential of 1.70 V (**Figure 5.5(b)**), has a smaller anodic and cathodic overpotential than C-FeTNO and FeTNO electrodes, respectively, compared with the equilibrium potential of 1.65 V for TNO-based electrode[6]. In addition, the Li-ion diffusion coefficient ($D_{Li^+, GITT}$) was calculated by GITT curves and **equation C.1**[42,43]. The $D_{Li^+, GITT}$ of the C-FeTNO/rGO EPD electrode is determined to be from 5.5×10^{-12} to 1.5×10^{-11} cm^2/s during charging (**Figure 5.5(d)**) and from 2.9×10^{-12} to 1.1×10^{-11} cm^2/s during discharging (**Figure 5.5(e)**). These results are an order of magnitude higher than those of the FeTNO electrode, which ranges from 3.7×10^{-13} to 9.8×10^{-13} cm^2/s during charging (**Figure 5.5(d)**) and from 6.1×10^{-13} to 1.1×10^{-12} cm^2/s during discharging (**Figure 5.5(e)**).

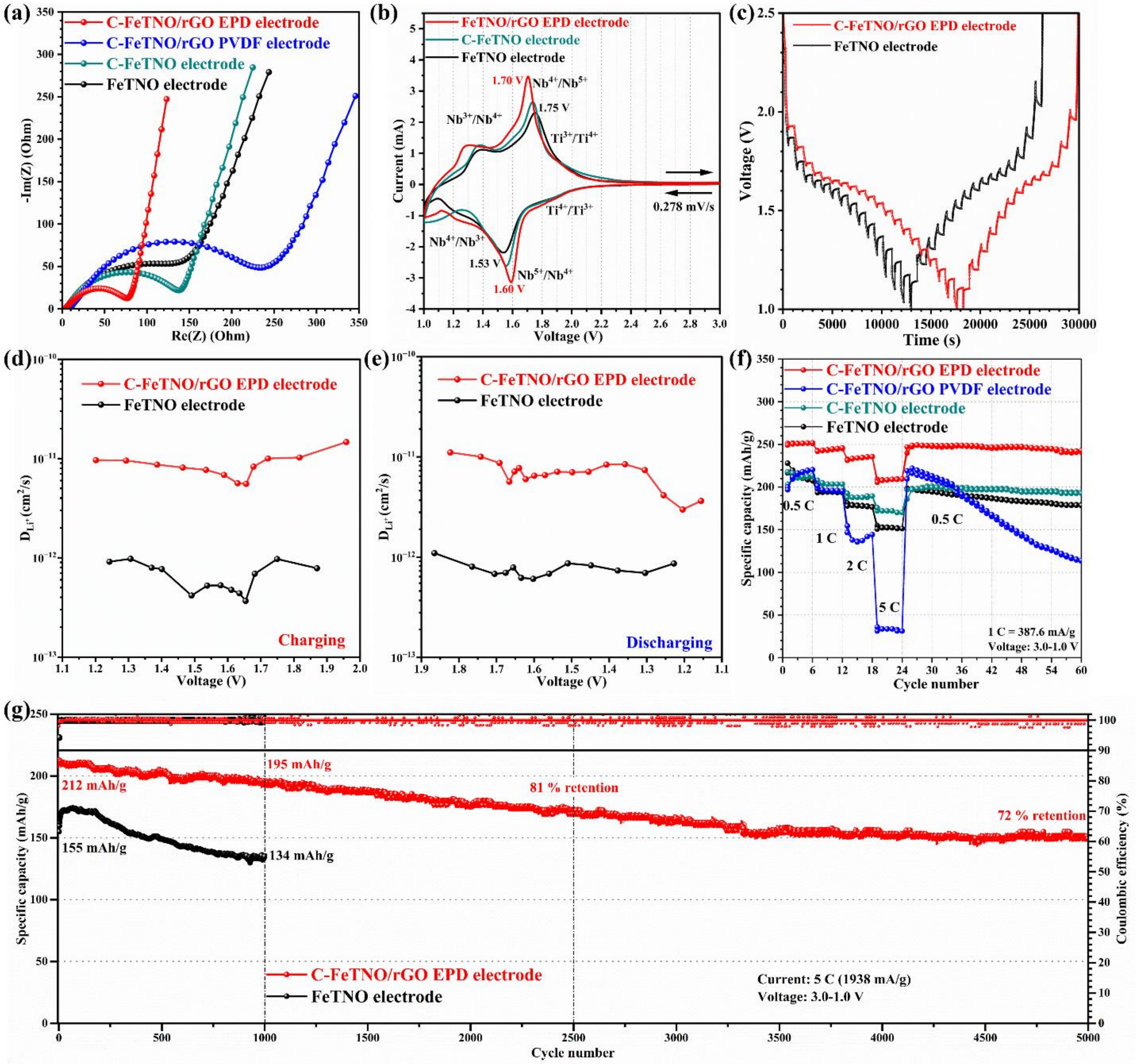

Figure 5.5 (a) EIS, (b) CV, (c) GITT and D_{Li^+} of the C-FeTNO/rGO EPD electrode and the FeTNO electrode during (d) charging and (e) discharging. (f) Rate performance of C-FeTNO/rGO EPD electrode, C-FeTNO/rGO PVDF electrode, C-FeTNO electrode, and FeTNO electrode, (g) Long cycling performance of the C-FeTNO/rGO EPD electrode and the FeTNO electrode.

The lithium storage performance of fabricated electrodes was tested under galvanostatic cycling in the voltage window from 3 V to 1 V. It is worth noting that all the capacity calculations are based on the mass of electrode, including both active materials, binder, and conductive agent. **Figure 5.5(f)** demonstrates rate performances of the C-FeTNO/rGO EPD electrode, C-FeTNO/rGO PVDF electrode, C-FeTNO electrode, and FeTNO electrode. The FeTNO electrode offers capacities of 228, 200, 180, and 156 mAh/g at 0.5 C, 1 C, 2 C, and 5 C, respectively. In contrast, the C-FeTNO electrode provides 218, 208, 192, and 176 mAh/g at same rates, illustrating improved rate performance due to the conductive carbon coating layer. Notably, the C-FeTNO/rGO EPD electrode displays the best rate performance, demonstrating 252, 246, 236, 210 mAh/g at 0.5 C, 1 C, 2 C, and 5 C, and shows superior recyclability (248 mAh/g) at 0.5 C after rate testing. In contrast, the C-FeTNO/rGO PVDF electrode (conventional electrode) illustrates poor rate performance of 220, 201, 140, 32 mAh/g at 0.5 C, 1 C, 2 C, and 5 C, respectively, demonstrating a severe capacity drop. This battery failure is likely due to severe aggregation of electrode materials (**Figure 5.4(c)**) and the oxidation of rGO in the C-FeTNO/rGO PVDF electrode, aligning with the findings in the EIS results (**Figure 5.5(a)**).

Accordingly, the optimal EPD electrode was selected to further investigate the battery cycling stability under the galvanostatic cycling at 5 C. The C-FeTNO/rGO EPD electrode (**Figure 5.5(g)**) provides high capacities of 212 mAh/g at 1st cycle and 195 mAh/g at 1000th cycle at 5 C and illustrates high retentions of 81% at 2500th cycle and 72 % after 5000 cycles, outperforming the FeTNO electrode (**Figure 5.5(g)**). This result is consistent with the observations in the EIS figure(**Figure 5.5(a)**), CV figure (**Figure 5.5(b)**), and $D_{Li^+, GITT}$ results (**Figure 5.5(d, e)**). The remarkable electrochemical performance of the advanced C-FeTNO/rGO EPD electrode demonstrates the advantage of advanced electrode engineering via EPD technique in constructing uniform interphase and functional electrode. It benefits from synergy strategies of carbon coating and graphene three-dimensional network, compared with conventional electrode engineering.

5.4.Conclusion

In summary, we developed an advanced EPD-based electrode engineering technique to fabricate Fe-doped single-crystal TNO nanomaterial (FeTNO)/reduced graphene oxide (rGO) composite materials for binder-free LIB electrodes. The novel EPD engineered anodes are characterized by homogeneous electrode microstructure and well-defined interfacial contact within the FeTNO/rGO 3D network, as evidenced by its morphological and composition analysis. Additionally, this advanced EPD approach effectively addresses the re-oxidation of rGO and its severe aggregation typically observed in conventional electrode fabrication. Consequently, C-FeTNO/rGO EPD electrode provides low impedance of 75 ohm compared with that of C-FeTNO/rGO PVDF electrode (241 ohm) and FeTNO electrode (183 ohm). The FeTNO/rGO EPD electrode provides remarkable capacity and rate capability: 252, 246, 236, 210 mAh/g at 0.5 C, 1 C, 2 C, and 5 C. Additionally, it offers an exceptional long-cycling performance with 81% retention (initial capacity of 212 mAh/g) at 2500th cycle and 72 % after 5000 cycles at 5 C, making it a strong ultrafast-charging and safe LIB anode. The remarkable battery performance can be attributed to advanced electrode engineering and interphase control endowed from the synergy of EPD's nanoscale assembly power, reduced graphene oxide network, carbon coating, and substitutional doping of TNO nanomaterials. These insights pave the way towards the practical application of ultrafast-charging materials for next-generation LIBs.

5.5. References

[1] Y. Liu, Y. Zhu, Y. Cui, Challenges and opportunities towards fast-charging battery materials, Nat. Energy 4 (2019) 540-550. https://doi.org/https://doi.org/10.1038/s41560-019-0405-3.

[2] W. Zhang, D.-H. Seo, T. Chen, L. Wu, M. Topsakal, Y. Zhu, D. Lu, G. Ceder, F. Wang, Kinetic pathways of ionic transport in fast-charging lithium titanate, Science 367 (2020) 1030-1034. https://doi.org/10.1126/science.aax3520.

[3] J.W. Choi, D. Aurbach, Promise and reality of post-lithium-ion batteries with high energy densities, Nat. Rev. Mater. 1 (2016) 16013. https://doi.org/10.1038/natrevmats.2016.13.

[4] X. Lu, L. Gu, Y.S. Hu, H.C. Chiu, H. Li, G.P. Demopoulos, L.Q. Chen, New insight into the atomic-scale bulk and surface structure evolution of $Li_4Ti_5O_{12}$ anode, J. Am. Chem. Soc. 137 (2015) 1581-1586. https://doi.org/10.1021/ja5115562.

[5] H.C. Chiu, X. Lu, J. Zhou, L. Gu, J. Reid, R. Gauvin, K. Zaghib, G.P. Demopoulos, Capacity fade mechanism of $Li_4Ti_5O_{12}$ nanosheet anode, Adv. Energy Mater. 7 (2017) 1601825. https://doi.org/10.1002/aenm.201601825.

[6] K.J. Griffith, Y. Harada, S. Egusa, R.M. Ribas, R.S. Monteiro, R.B. Von Dreele, A.K. Cheetham, R.J. Cava, C.P. Grey, J.B. Goodenough, Titanium niobium oxide: from discovery to application in fast-charging lithium-ion batteries, Chem. Mater. 33 (2021) 4-18. https://doi.org/10.1021/acs.chemmater.0c02955.

[7] Y. Yang, J. Zhao, Wadsley–Roth crystallographic shear structure niobium-based oxides: Promising anode materials for high-safety lithium-ion batteries, Adv. Sci. 8 (2021) 2004855. https://doi.org/https://doi.org/10.1002/advs.202004855.

[8] X. Wu, S. Lou, X. Cheng, C. Lin, J. Gao, Y. Ma, P. Zuo, C. Du, Y. Gao, G. Yin, Unravelling the interface layer formation and gas evolution/suppression on a $TiNb_2O_7$ anode for lithium-Ion batteries, ACS Appl. Mater. Interfaces 10 (2018) 27056-27062. https://doi.org/10.1021/acsami.8b08425.

[9] H. Wang, R. Qian, Y. Cheng, H.-H. Wu, X. Wu, K. Pan, Q. Zhang, Micro/nanostructured $TiNb_2O_7$-related electrode materials for high-performance electrochemical energy storage: recent advances and future prospects, J. Mater. Chem. A 8 (2020) 18425-18463. https://doi.org/10.1039/D0TA04209A.

[10] F. Yu, S. Wang, R. Yekani, A. La Monaca, G.P. Demopoulos, Single-crystal $TiNb_2O_7$ materials via sustainable synthesis for fast-charging lithium-ion battery anodes, J. Energy Storage 95 (2024) 112482. https://doi.org/https://doi.org/10.1016/j.est.2024.112482.

[11] C. Wang, Z. Guo, W. Shen, Q. Xu, H. Liu, Y. Wang, B-doped carbon coating improves the electrochemical performance of electrode materials for Li-ion batteries, Adv. Funct. Mater 24 (2014) 5511-5521. https://doi.org/https://doi.org/10.1002/adfm.201401006.

[12] W. Chung, J.H. Bang, Carbon-doped $TiNb_2O_7$ suppresses amorphization-induced capacity fading, ACS Appl. Mater. Interfaces 14 (2022) 19365-19375. https://doi.org/10.1021/acsami.2c00589.

[13] M. Uceda, H.-C. Chiu, J. Zhou, R. Gauvin, K. Zaghib, G.P. Demopoulos, Nanoscale assembling of graphene oxide with electrophoretic deposition leads to superior percolation network in Li-ion electrodes: $TiNb_2O_7$/rGO composite anodes, Nanoscale 12 (2020) 23092–23104. https://doi.org/https://doi.org/10.1039/D0NR06082H.

[14] R. Raccichini, A. Varzi, S. Passerini, B. Scrosati, The role of graphene for electrochemical energy storage, Nat. Mater. 14 (2015) 271-279. https://doi.org/10.1038/nmat4170.

[15] F. Yu, B. Miglani, S. Yuan, R. Yekani, K.H. Bevan, G.P. Demopoulos, Fe^{3+}-substitutional doping of nanostructured single-crystal $TiNb_2O_7$ for long-stable cycling of ultra-fast charging anodes, Nano Energy 133 (2025) 110494. https://doi.org/https://doi.org/10.1016/j.nanoen.2024.110494.

[16] J.Q. Zhou, H.Y. Dong, Y. Chen, Y.H. Ye, L. Xiao, B.H. Deng, J.P. Liu, Carbon-coated $TiNb_2O_7$ nanosheet arrays as self-supported high mass-loading anodes for flexible Li-ion batteries, Chem. Commun. 57 (2021) 1822-1825. https://doi.org/10.1039/d0cc08251a.

[17] C. Vallés, C. Drummond, H. Saadaoui, C.A. Furtado, M. He, O. Roubeau, L. Ortolani, M. Monthioux, A. Pénicaud, Solutions of negatively charged graphene sheets and ribbons, J. Am. Chem. Soc. 130 (2008) 15802-15804. https://doi.org/10.1021/ja808001a.

[18] N. Takami, K. Ise, Y. Harada, T. Iwasaki, T. Kishi, K. Hoshina, High-energy, fast-charging, long-life lithium-ion batteries using $TiNb_2O_7$ anodes for automotive applications, J. Power Sources 396 (2018) 429-436. https://doi.org/10.1016/j.jpowsour.2018.06.059.

[19] M. Diba, D.W.H. Fam, A.R. Boccaccini, M.S.P. Shaffer, Electrophoretic deposition of graphene-related materials: A review of the fundamentals, Prog. Mater. Sci. 82 (2016) 83-117. https://doi.org/10.1016/j.pmatsci.2016.03.002.

[20] L.H. Ye, K.C. Wen, Z.X. Zhang, F. Yang, Y.C. Liang, W.Q. Lv, Y.K. Lin, J.M. Gu, J.H. Dickerson, W.D. He, Highly efficient materials assembly via electrophoretic deposition for electrochemical energy conversion and storage devices, Adv. Energy Mater. 6 (2016) 1502018. https://doi.org/10.1002/aenm.201502018.

[21] S.J. Limmer, G.Z. Cao, Sol-gel electrophoretic deposition for the growth of oxide nanorods, Adv. Mater. 15 (2003) 427-431. https://doi.org/10.1002/adma.200390099.

[22] M.-J. Hwang, M.-G. Kim, S. Kim, Y.C. Kim, H.W. Seo, J.K. Cho, I.-K. Park, J. Suhr, H. Moon, J.C. Koo, H.R. Choi, K.J. Kim, Y. Tak, J.-D. Nam, Cathodic electrophoretic deposition (EPD) of phenylenediamine-modified graphene oxide (GO) for anti-corrosion protection of metal surfaces, Carbon 142 (2019) 68-77. https://doi.org/https://doi.org/10.1016/j.carbon.2018.10.017.

[23] Y.H. Lu, D.W. Zhang, L. Wang, M.W. Xu, J. Song, J.B. Goodenough, Electrochemical behavior of a graphite electrode prepared by anodic electrophoretic deposition, J. Electrochem. Soc. 159 (2012) A321-A324. https://doi.org/10.1149/2.078203jes.

[24] V.V. Neklyudov, N.R. Khafizov, I.A. Sedov, A.M. Dimiev, New insights into the solubility of graphene oxide in water and alcohols, Phys. Chem. Chem. Phys. 19 (2017) 17000-17008. https://doi.org/10.1039/C7CP02303K.

[25] H. Negishi, H. Yanagishita, H. Yokokawa, Electrophoretic deposition of solid oxide fuel cell material powders, Proceedings of the electrochemical society on electrophoretic deposition: fundamentals and applications 21 (2002)

[26] P. Amrollahi, J.S. Krasinski, R. Vaidyanathan, L. Tayebi, D. Vashaee, Electrophoretic deposition (EPD): fundamentals and applications from nano- to microscale structures, in: M. Aliofkhazraei, A.S.H. Makhlouf (Eds.), Handbook of Nanoelectrochemistry: Electrochemical Synthesis Methods, Properties, and Characterization Techniques, Springer International Publishing, Cham, 2016, pp. 561-591.

[27] Z. Mousavi, M. Pirdashti, A.A. Rostami, E.-N. Dragoi, Thermophysical properties analysis of poly (ethylene glycol) 600 + methanol, ethanol, 1-propanol, and 2-propanol binary liquid mixtures, International Journal of Thermophysics 41 (2020) 19. https://doi.org/10.1007/s10765-019-2600-7.

[28] R.J. Mou, S. Barua, A.K. Prasad, T.H. Epps, III, K.P.C. Yao, Electrophoretic Deposition as a Versatile Low-Cost Tool to Construct a Synthetic Polymeric Solid-Electrolyte Interphase on Silicon Anodes: A Model System Investigation, ACS Appl. Mater. Interfaces 16 (2024) 6908-6919. https://doi.org/10.1021/acsami.3c06721.

[29] Z.Y. Xia, S. Pezzini, E. Treossi, G. Giambastiani, F. Corticelli, V. Morandi, A. Zanelli, V. Bellani, V. Palermo, The exfoliation of graphene in liquids by electrochemical, chemical, and sonication-assisted techniques: A nanoscale study, Adv. Funct. Mater 23 (2013) 4684-4693. https://doi.org/10.1002/adfm.201203686.

[30] Y. Yang, J.Q. Li, D.Q. Chen, J.B. Zhao, A facile electrophoretic deposition route to the Fe_3O_4/CNTs/rGO composite electrode as a binder-free anode for lithium ion battery, ACS Appl. Mater. Interfaces 8 (2016) 26730-26739. https://doi.org/10.1021/acsami.6b07990.

[31] B. Lesiak, G. Trykowski, J. Tóth, S. Biniak, L. Kövér, N. Rangam, L. Stobinski, A. Malolepszy, Chemical and structural properties of reduced graphene oxide—dependence on the reducing agent, J. Mater. Sci. 56 (2021) 3738-3754. https://doi.org/10.1007/s10853-020-05461-1.

[32] K. Zhao, L. Zhang, R. Xia, Y. Dong, W. Xu, C. Niu, L. He, M. Yan, L. Qu, L. Mai, SnO_2 quantum dots@graphene oxide as a high-rate and long-life anode material for lithium-ion batteries, Small 12 (2016) 588-594. https://doi.org/https://doi.org/10.1002/smll.201502183.

[33] R. Sun, Q. Wei, Q. Li, W. Luo, Q. An, J. Sheng, D. Wang, W. Chen, L. Mai, Vanadium sulfide on reduced graphene oxide layer as a promising anode for sodium ion battery, ACS Appl. Mater. Interfaces 7 (2015) 20902-20908. https://doi.org/10.1021/acsami.5b06385.

[34] D. Liang, Y. Lu, N. Zhou, Z. Xu, 2022. Ultrathin carbon-coated porous $TiNb_2O_7$ nanosheets as anode materials for enhanced lithium storage. Nanomaterials. 12. https://doi.org/10.3390/nano12172943.

[35] N.G. Eror, U. Balachandran, Coordination of cations in $TiNb_2O_7$ by Raman spectroscopy, J. Solid State Chem. 45 (1982) 276-279. https://doi.org/https://doi.org/10.1016/0022-4596(82)90283-3.

[36] L. Perfler, V. Kahlenberg, C. Wikete, D. Schmidmair, M. Tribus, R. Kaindl, Nanoindentation, high-temperature behavior, and crystallographic/spectroscopic characterization of the high-refractive-index materials $TiTa_2O_7$ and $TiNb_2O_7$, Inorg. Chem. 54 (2015) 6836-6848. https://doi.org/10.1021/acs.inorgchem.5b00733.

[37] A.W. Bayeh, D.M. Kabtamu, Y.-C. Chang, G.-C. Chen, H.-Y. Chen, G.-Y. Lin, T.-R. Liu, T.H. Wondimu, K.-C. Wang, C.-H. Wang, Synergistic effects of a $TiNb_2O_7$–reduced graphene oxide nanocomposite electrocatalyst for high-performance all-vanadium redox flow batteries, J. Mater. Chem. A 6 (2018) 13908-13917. https://doi.org/10.1039/C8TA03408G.

[38] Y. Yang, J. Huang, Z. Cao, Z. Lv, D. Wu, Z. Wen, W. Meng, J. Zeng, C.C. Li, J. Zhao, Synchronous manipulation of ion and electron transfer in Wadsley–Roth phase Ti-Nb oxides

for fast-charging lithium-ion batteries, Adv. Sci. 9 (2022) 2104530. https://doi.org/https://doi.org/10.1002/advs.202104530.

[39] S.F. Lou, X.Q. Cheng, Y. Zhao, A. Lushington, J.L. Gao, Q. Li, P.J. Zuo, B.Q. Wang, Y.Z. Gao, Y.L. Ma, C.Y. Du, G.P. Yin, X.L. Sun, Superior performance of ordered macroporous $TiNb_2O_7$ anodes for lithium ion batteries: Understanding from the structural and pseudocapacitive insights on achieving high rate capability, Nano Energy 34 (2017) 15-25. https://doi.org/10.1016/j.nanoen.2017.01.058.

[40] W. Cai, G. Lu, J. He, Y. Lan, The adsorption feature and photocatalytic oxidation activity of $K_{1-2x}M_xTiNbO_5$ (M=Mn, Ni) for methyl mercaptan in methane, Ceram. Int. 38 (2012) 3167-3174. https://doi.org/https://doi.org/10.1016/j.ceramint.2011.12.020.

[41] L. Rout, A. Kumar, R.S. Dhaka, G.N. Reddy, S. Giri, P. Dash, Bimetallic Au-Cu alloy nanoparticles on reduced graphene oxide support: Synthesis, catalytic activity and investigation of synergistic effect by DFT analysis, Applied Catalysis A: General 538 (2017) 107-122. https://doi.org/https://doi.org/10.1016/j.apcata.2017.03.017.

[42] Y. Zeng, H.-C. Chiu, B. Ouyang, K. Zaghib, G.P. Demopoulos, Defect engineering of iron-rich orthosilicate cathode materials with enhanced lithium-ion intercalation capacity and kinetics, ACS Appl. Energy Mater. 3 (2020) 675-686. https://doi.org/10.1021/acsaem.9b01869.

[43] H. Park, H.B. Wu, T. Song, X.W. Lou, U. Paik, Porosity-controlled $TiNb_2O_7$ microspheres with partial nitridation as a practical negative electrode for high-power lithium-ion batteries, Adv. Energy Mater. 5 (2015) 1401945. https://doi.org/10.1002/aenm.201401945.

6. Global Discussion

As detailed in **Chapter 1** and **Chapter 2**, lithium-ion batteries (LIBs) are the technology behind the electrification of transportation.[1-3] As battery-powered vehicles grow as part of the transportation sector, they require new, more advanced lithium-ion batteries.[2,4] Some properties required for the new generation of LIBs are fast charging and long cycle life.[3,5] However, existing commercial anode materials can hardly meet these requirements.[6] For example, dominant and cost-effective commercial graphite anode materials with low working potential (ca., 0.1 V *vs.* Li/Li$^+$) suffer from Li dendrite formation and safety issues, primarily due to overpotential when operating under extremely fast charging.[1,7] Another commercialized anode material, spinel lithium titanate ($Li_4Ti_5O_{12}$) offers superior fast-charging capability, safe working potential (ca., 1.5 V *vs.* Li/Li$^+$), and excellent cycling stability.[6,8] However, $Li_4Ti_5O_{12}$ possesses a low theoretical capacity (175 mAh/g) that is only half that of the aforementioned commercial graphite anode (372 mAh/g), limiting its further application in EVs.[8,9] Next-generation fast-charging anode materials with a high capacity, high rate, safe operating potential, and long cycle life are thus needed to overcome these challenges.[10]

TNO provides good fast-charging properties, a safe operating voltage (ca. 1.6 V *vs.* Li/Li$^+$) at high rates, high theoretical gravimetric capacity (387 mAh/g), and high theoretical volumetric capacity (1682 mAh/cm^3).[11,12] From the perspective of availability, titanium (0.45 %) is an abundant element in the upper continental crust.[11] Additionally, niobium (10-26 ppm) is a relatively abundant element comparable to cobalt (10-18 ppm), nickel (19-60 ppm) and copper (14-32 ppm), ensuring that the supply can meet the growing demand for advanced batteries.[11] Therefore, the development of fast-charging titanium niobium oxide ($TiNb_2O_7$, TNO) anode may be viewed as key progress for the fast-charging market.

The past decades have witnessed the emergence of TNO anode materials.[11] In 2011, Prof. John B. Goodenough first introduced the $TiNb_2O_7$ anode material as a new framework for LIB anodes and matched it with a $LiNi_{0.5}Mn_{1.5}O_4$ cathode to determine the full cell performance.[13,14] After that, the Toshiba Company reported their research on TNO anodes in 2013, considering TNO to be a next-generation EV battery anode that promises high energy density and ultrafast recharging capability.[15-17] In 2017, Toshiba first launched the development of a commercial TNO and announced that their TNO anode achieves double volumetric capacity compared to graphite-based anode.[11,15-19] Impressively, this company commercially had developed the

$Li_4Ti_5O_{12}$ anode since 2008 and regarded TNO as a better alternative to produce a super-safe, durable, and fast-charging LIB anode.[9]

In this work, $TiNb_2O_7$ as a promising anode material for these applications, is investigated.[11] The first objective is synthesizing nanostructured single-crystal TNO material particles using a sustainable method for the practical application. Single-crystal electrode materials have been attracting a lot of attention in recent years as thanks to fewer grain boundaries they prove highly stable over longer cycling times. This is the case for example of single-crystal Ni-rich cathode materials.[20,21] As equally important with fast charging is the long-cycling of the battery, it is this reason that motivated the first part of the research described in **Chapter 3**. Current synthesis techniques including solid-state[22,23], and solvothermal methods[24,25], face obstacles of insufficient purity, complicated procedures, and scalability challenges[11,14,26]. The aqueous co-precipitation approach combined with calcination was selected in this work as a sustainable and scalable synthetic route given success with other nanostructured and single-crystalline electrode materials.[27,28] Aqueous co-precipitation methods avoid the use of problematic organic volatile and flammable solvents, or costly organic Ti/Nb precursor chemicals, hence its attractiveness for large-scale production[29-31]The design of such scalable synthesis approach for TNO materials is based on decades of crystallization research in our group.[32] This crystallization kinetics theory has been deeply investigated in hydrolysis reactions including the hydrolysis of titanium chloride ($TiCl_4$),[27,33-37] ferric chloride ($FeCl_3$),[38,39] and other metal chlorides[32]. For instance, the hydrolytic precipitation of titanium chloride ($TiCl_4$) can be applied for large-scale synthesis of titanium dioxide (TiO_2),[27,33-37] as shown in **equation 6.1**.

$$TiCl_4(aq)+2H_2O \rightarrow TiO_2(s)+4HCl(aq) \qquad \textbf{(equation 6.1)}$$

Nevertheless, this reaction is rather challenging to control when used for synthesizing TiO_2 particles at room temperature. As shown in **Figure 6.1**, our group has successfully advanced the hydrolytic precipitation method via controlling pH and temperature to develop nanosized TiO_2 of different crystal polymorphs.[27,33-37,40] For example, in 2009, Li et al.[33] developed a low-temperature partial hydrolysis process to prepare a homogeneous $TiCl_4$ aqueous solution. Using this stable $TiCl_4$ solution, Li[33] and Charbonneau et al.[34,35] explored pH-controlled co-precipitation via base chemicals (MgO or ammonia hydroxide) to obtain nanoscale TiO_2. Furthermore, Charbonneau et al.[35] also explored the high-temperature forced co-precipitation routes. Following these developments, Yasin et al.[36,37] investigated the large-scale fabrication of nanocrystalline TiO_2 in the continuous stirred-tank reactor (CSTR) equipment. Beyond TiO_2 synthesis, Chiu et al.[27] combined hydrolytic precipitation and high-temperature calcination to develop nanostructured LTO as a high-performance LIBs anode.

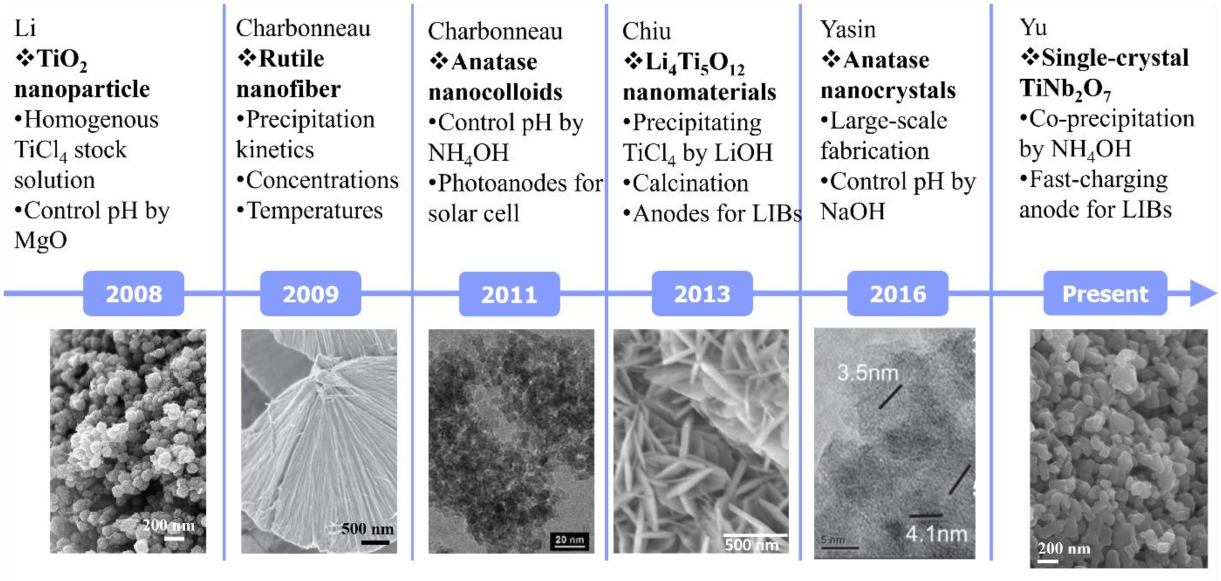

Figure 6.1 Application of hydrolytic precipitation and development of advanced materials in HydroMET.[27,33-37]

This success case of Ti-based materials inspired the new co-precipitation synthesis method of $TiNb_2O_7$ materials. For example, niobium chloride ($NbCl_5$) can also be employed for synthesizing niobium (V) pentoxide (Nb_2O_5),[41] as shown in **equation 6.2**.

$$2NbCl_5(aq)+5H_2O \rightarrow Nb_2O_5(s)+10HCl(aq) \qquad \textbf{(equation 6.2)}$$

$$2FeCl_3(aq)+3H_2O \rightarrow Fe_2O_3(s)+6HCl(aq) \qquad \textbf{(equation 6.3)}$$

Based on these in-depth understanding of hydrolytic co-precipitation of $TiCl_4$ and $NbCl_5$, we developed nanoscale titanium niobium hydroxide particles, which are crystallized to be monocrystalline TNO nanomaterials, as discussed in **Chapter 3**. Following the same idea, we introduced $FeCl_3$ hydrolysis reaction (**equation 6.3**) into this Ti-Nb-Cl aqueous system and realized the co-precipitation of Fe-Ti-Nb hydroxides. Eventually, we developed one universal substitutional Fe^{3+} doping strategy for $TiNb_2O_7$ materials[39] as shown in **Chapter 4**. From the viewpoint of scalability and sustainability, this aqueous approach can be adapted for continuous stirred-tank reactor (CSTR) equipment coupled with by-product and waste solution recycling procedures, which makes this materials fabrication process more practical.

In **Chapter 3**, we applied this hydrolytic co-precipitation fabrication approach to synthesize nanoscale titanium niobium hydroxide, enabling atom-level mixing of Ti, Nb, and O in the TNO amorphous precursor particles. These precursor nanoparticles were successfully crystallized into nano/submicron-structured monocrystalline $TiNb_2O_7$ materials during the calcination process. In comparison with polycrystalline or micron-sized materials, the single-crystal features and nanostructure of TNO can shorten Li ion diffusion pathways and stabilize the material crystal structure, thereby unlocking extremely fast charging capabilities and cycling durability[11,24,42]. This is evident from nanoscale LTO anode materials[27,28] and commercialized monocrystalline nickel manganese cobalt (NMC) cathode materials[43,44].

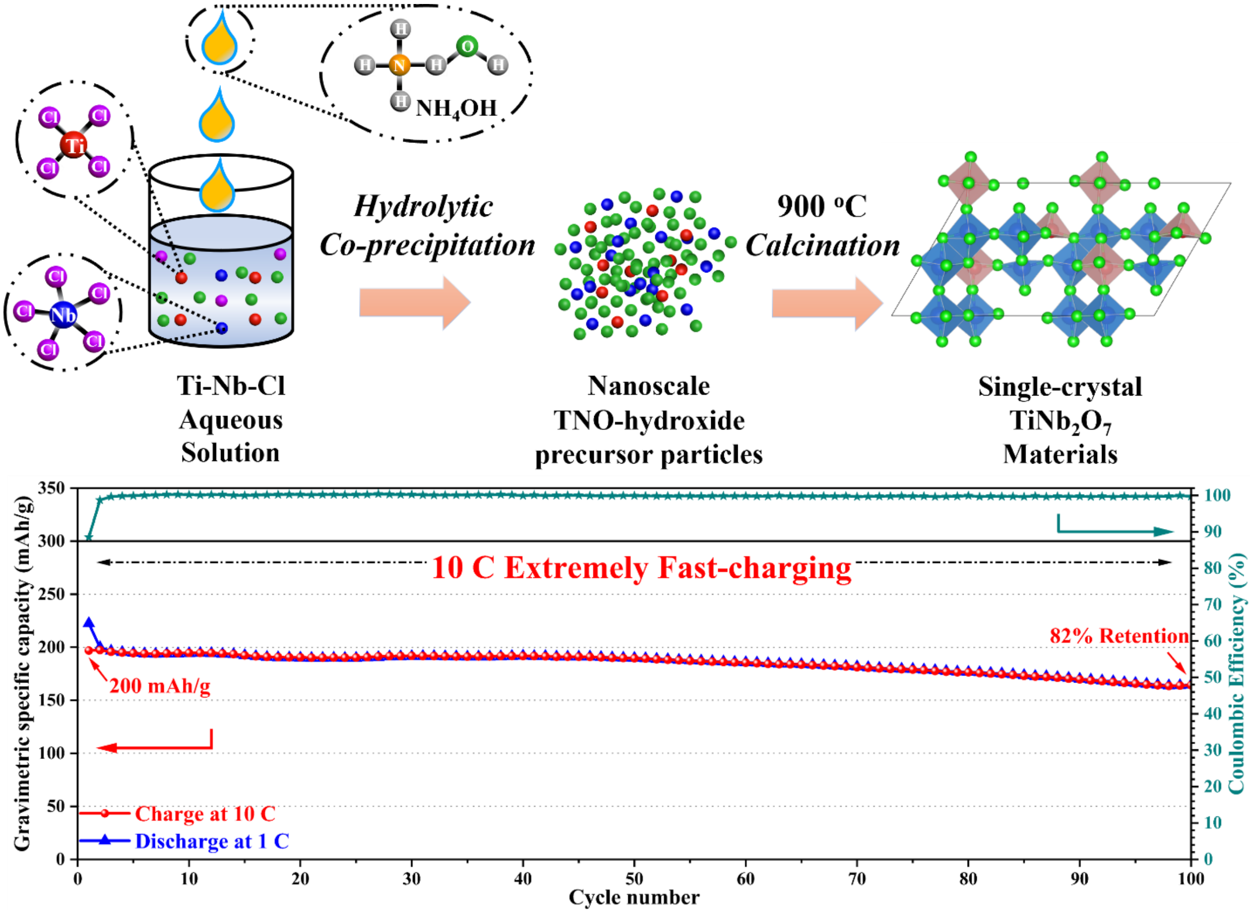

Figure 6.2 Sustainable aqueous hydrolytic co-precipitation synthesis of single-crystal $TiNb_2O_7$ and its fast-charging capability under 10 C fast-charging protocol. (Corresponding to **Chapter 3**)

As a result, the synthesized optimal single-crystal TNO anode delivers an initial capacity of 279 mAh/g and 219 mAh/g after 100 cycles capacities at 0.5 C respectively. The monocrystalline TNO provides many advantages as a fast-charging anode including an outstanding Li-storage capacity under 5 C high rate and 10 C extremely fast charging conditions (**Figure 6.2**). This remarkable rate capability can be attributed to a high Li diffusion coefficient of 1.37×10^{-13} cm^2/s of TNO and good conductivity of lithiated TNO after 1st cycle. It is noteworthy that the pristine TNO material, which has low conductivity, is transformed to a highly conductive lithiated TNO phase during the initial lithiation step, as determined systematically by GITT, CV, and EIS measurements. In addition, this TNO anode offers a high practical volumetric capacity of 351.7 mAh/cm^3 at 0.5 C, serving as a new reference for battery development targeting high volumetric capacity and high volumetric energy density.[11,16] Also, via a detailed analysis of nanostructure, crystallinity (XRD refinement), and porosity the formation mechanism of TNO single crystals was elucidated and the relationship between electrochemical performance and material properties was revealed.

Next, the challenge of achieving extended cycling stability under fast charging was addressed in **Chapter 4** via Fe^{3+} substitutional doping of TNO. Substitutional cation doping strategy is chosen in this research for further unlocking the extremely fast-charging capability of $TiNb_2O_7$ anode materials via crystal lattice expansion while stabilizing the structure to enable a longer cycle life[11,24,26,45], as demonstrated via a combination of experimental and computational probing work. Before, the present work on Fe^{3+} substitutional doping of TNO, a variety of either expensive, heavy, rare, or even environmentally harmful dopant elements, such as chromium (Cr^{3+}) [46], lanthanum (La^{3+}) [47], zirconium (Zr^{4+}) [29], ruthenium (Ru^{4+}) [48], Cerium (Ce^{4+}) [49], and Terbium (Tb^{5+}) [50], molybdenum (Mo^{5+} and Mo^{6+}) [51-53], vanadium (V^{5+}),[54] tungsten (W^{6+}) had been proposed[55,56]. By contrast, Fe that was studied in this work, is abundant, cost-efficient, and environmentally friendly element. In aqueous co-precipitation reactions during synthesis, Fe (in the form of $FeCl_3$) has similar chemical properties and thermodynamic behavior in comparation to $TiCl_4$ and $NbCl_5$. However, Fe^{3+} substitutional doping in $TiNb_2O_7$ crystals has not been investigated.

The present research aimed at investigating the in-depth mechanism underlying the enhanced electrochemical performance by substitutional doping. Previous studies applied larger-radius dopants compared to Ti^{4+} (*ca*. 0.61 Å) and Nb^{5+} (*ca*. 0.69 Å), such as Cu^{2+} [24,57], La^{3+} [47], Zr^{4+} [29]. It is commonly accepted that corresponding structural changes is the key to enlarge the Li^+ transport channels, thereby improving Li^+ diffusion kinetics.[24,57] However, more evidence from new aspects is needed to fully understand the cation substitutional doping mechanism. For example, the impact of structural distortions from quasi-equisized dopants on widening Li ion diffusion channels is unclear. Therefore, applying Fe^{3+} with a quasi-equisized ion radius (*ca*. 0.64 Å) [58] can provide valuable insights into this perspective of the mechanism study.

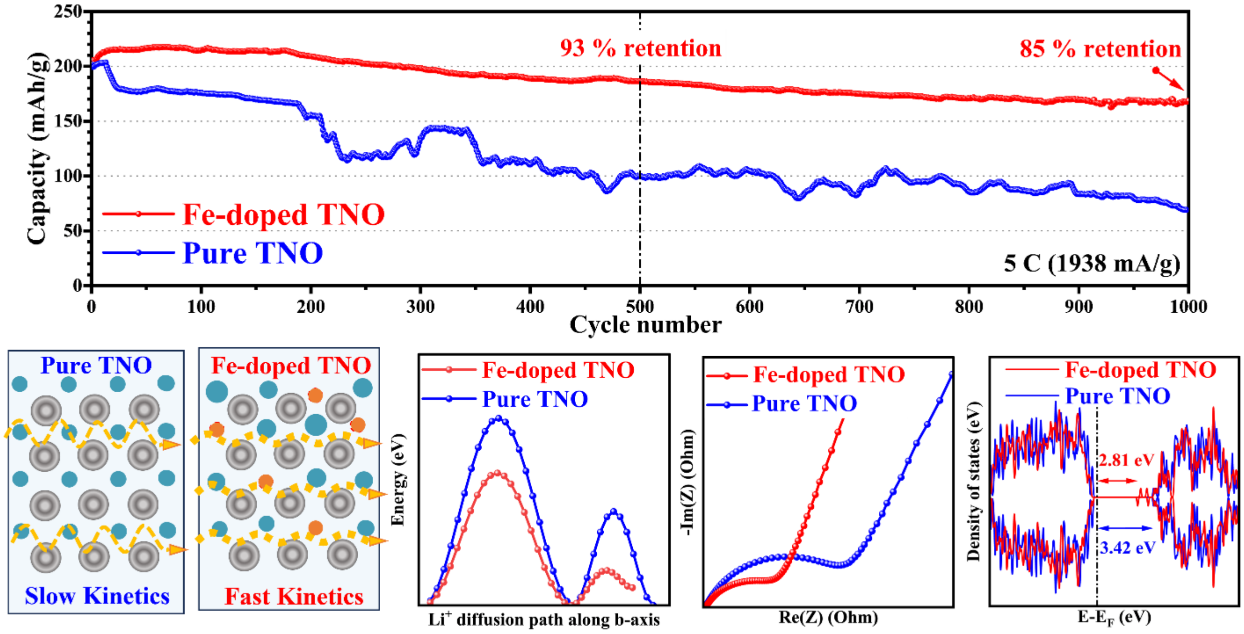

Figure 6.3 Cycling stability of TNO and Fe-doped TNO under 5 C high rate and underlying mechanism from the perspectives of decreased diffusion energy, decreased impedance, and narrowed band gap. (Corresponding to **Chapter 4**.)

Through synergetic experimental investigation and density functional theory (DFT) calculations, it was determined: (1) Fe dopants create a sub-band and lower the band gap, thus improving electronic conductivity. (2) Fe doping modulates the crystal structure and introduces disorder, according to the atomic-level TEM, XRD refinement, and strain in the DFT calculations. Typically, larger ions like Mo^{6+}[53], Cu^{2+}[57], and V^{5+}[54] have been used in the past to enlarge the lattice. Impressively, in this study, we found that equivalent-sized ions can also widen the Li ion diffusion channel along *b* axis in the crystal by introducing distortions. (3) The fast Li ion diffusion kinetics has been experimentally evaluated by GITT-determined Li ion diffusion coefficient and theoretically analyzed by DFT-calculated Li ion diffusion energy barrier. (4) Fe^{3+} doping enhances the overall capacity of the material due to the Fe^{3+}/Fe^{2+} redox couple, as revealed by CV and charge-discharge results. Based on this probing, the optimal 5% Fe^{3+}-doped TNO (Fe5-TNO) was shown to demonstrate remarkable extreme fast-charging capability (238 mAh/g under 10 C charge/1 C discharge), and outstanding cycling stability at 5 C high rate (85 % retention after 1000 cycles) as summarized in **Figure 6.3**. Finally, **Table 6.1** compares the present doping study to the best previous works exemplifying the significant advance made in knowledge and performance.

Table 6.1 Comparison of key doping studies on TNO materials.

Doping type	**Composition**	**Synthesis Methods**	**DFT Theoretical calculation**	**Advanced characterization**	**Rate performance**	**Ultra-Fast charging capability and cycling stability**	**Ref**
Fe^{3+} substitutional doping	$Fe_{0.05}Ti_{0.95}Nb_2O_{6.975}$	Scalable aqueous co-precipitation	Density of states (DOS), Li^+ diffusion energy barriers, Crystal structure evolution, Electronic structure	Atomic-level TEM, REELS, XRD refinement	285, 250, 225, and 195 mAh/g at 0.5, 1, 2, and 5 C respectively	200 mAh/g at 1st cycle and 170 mAh/g after 1000 cycles at 5 C. 238 mAh/g under 10 C charging (coupled with 1 C discharging)	This study
Cu^{2+} substitutional doping	$Cu_{0.02}Ti_{0.94}Nb_{2.04}O_7$	Solid-state synthesis	No	XRD refinement	274, 258, 238, 210 and 182 mAh/g at 0.5, 1, 2, 5 and 10 C	182 mAh/g at 1st cycle and 178 mAh/g 1000 cycles at 10 C	[57]
Mo^{6+} interstitial doping	$Mo_{0.03}$-$TiNb_2O_7$	Solvothermal method	No	No	264, 250, 239, 225, and 213 mAh/g at 0.5, 1, 2, 5, and 10 C	180 mAh/g at 1st cycle and 170 mAh/g after 500 cycles at 10 C	[53]
V^{5+} interstitial doping	$V_{0.030}$-$TiNb_2O_7$	Organic co-precipitation	Density of states (DOS), Li^+ diffusion energy barriers	XRD refinement	314.8, 291.3, 263.6, 244.6, 229.4 and 209.2 mAh/g at 0.5, 1, 2, 4, 6, and 8 C	210 mAh/g at 1st cycle and 163.5 mAh after 2000 cycles at 10 C	[54]
Nb^{5+} self-doping	$Ti_{0.98}Nb_{2.02}O_7$	Solid-state synthesis	Density of states (DOS)	XRD refinement	260, 250, 220, 215, 190, 170, 130, and 80 mAh/g at 0.1 C, 0.2 C, 0.5 C, 1 C, 2 C, 5 C, 10 C, and 20 C	150 mAh/g at 1st cycle and 112 mAh/g after 1000 cycle at 10 C	[45]

The final objective, dealt with in **Chapter 5**, is to optimize the fabrication method targeting extended cycling life at high rate. The goal is to address the significant capacity fade occurring upon long cycling under fast-charging conditions, that is due to low conductivity of TNO, non-uniform electrode/electrolyte interface, and structural evolution.[11,59] Having addressed the crystal design and bulk structure modification via doping, next the electrode interphasial microstructure was modified aiming at improving its conductive network.[60,61] Accordingly, we have carbon-coated the Fe-doped TNO single crystal material (C-FeTNO) and co-deposited with reduced graphene oxide (rGO) as C-FeTNO/rGO composite electrode via electrophoretic method followed by reductive annealing. This novel electrode design leverages the multifunctionality of graphene, including excellent theoretical electronic conductivity, mechanical/thermal stability, and binding property by combining it with the nanoscale assembly power of EPD.[62] By employing this strategy, a homogeneous 3D electrode structure was successfully build characterized by enhanced kinetics, suppressed volume variation, and electrolyte decomposition minimization.[63,64]

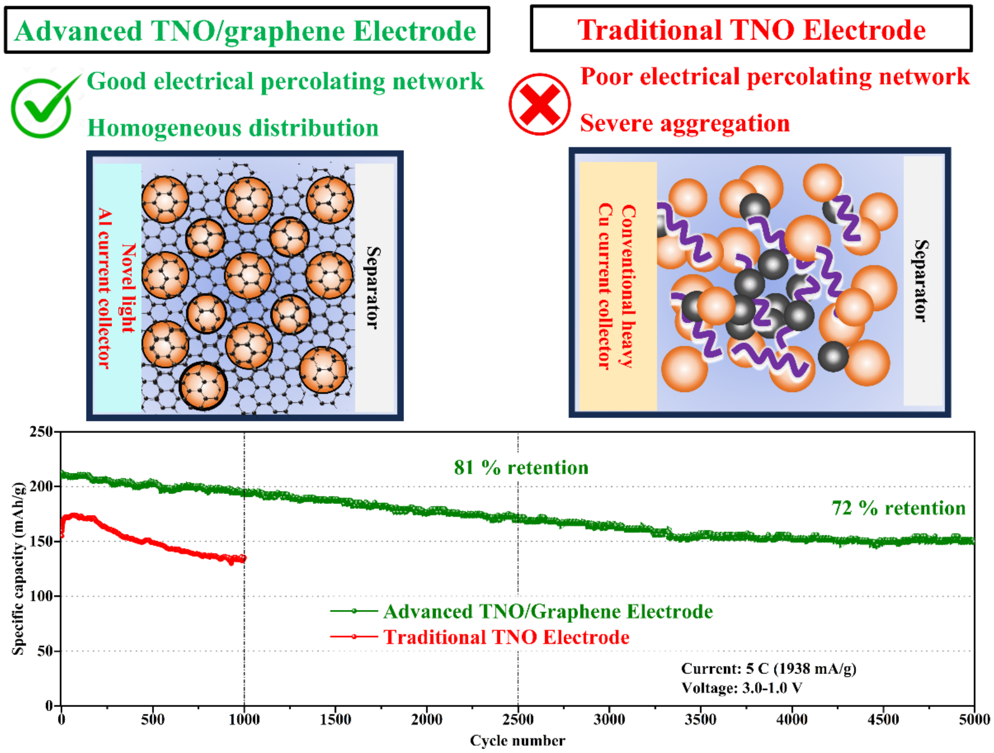

Figure 6.4 Comparison of microstructure and cycling stability of advanced TNO/graphene electrode vs. traditional TNO electrode under 5 C high rate. (Corresponding to **Chapter 5**)

Traditionally, electrode fabrication involves the use of acetylene black as conductive agent and polyvinylidene fluoride (PVDF) as a binder. The use of the latter, however, involves the toxic solvent N-Methyl-2-pyrrolidone (NMP), which draws health issues and environmental concern.[65] Conversely, the novel electrode structure based on electrophoretically deposited C-FeTNO and graphene oxide deploys rGO as both conductive component and binder, replacing PVDF and the toxic solvent NMP. EPD is conducted in this work in a widely available and used industrial solvent, iso-propanol, that it has sanitizing and disinfectant properties finding applications from electronics and coatings to medical devices offering a sustainable electrode fabrication method. The combined action of GO and EPD successfully prevents aggregation leading to advanced C-FeTNO/rGO electrodes with remarkable practical capacities, based on the total electrode mass rather than only active materials. It further enhanced rate performance with high capacities of 252, 246, 236, 210 mAh/g at 0.5 C, 1 C, 2 C, and 5 C, respectively. As a result, a high practical initial capacity of 212 mAh/g and remarkable cycling retention of 70 % after 5000 cycles at 5 C, was achieved making it a promising ultrafast-charging LIB anode.

Having successfully designed and tested in half-cells, the novel carbon-coated Fe-doped TNO single crystal active material co-deposited with reduced graphene oxide (rGO) as C-FeTNO/rGO composite electrode, next full cell testing with cathodes like LFP or NMC should be pursued. Finally, the application of the C-FeTNO/graphene anode in all-solid-state battery featuring a hybrid electrolyte[66] and a cathode deserves investigation as novel paradigm of safe and high-power battery.[67]

References

[1] M. Winter, B. Barnett, K. Xu, Before Li ion batteries, Chem. Rev. 118 (2018) 11433-11456. https://doi.org/10.1021/acs.chemrev.8b00422.

[2] M. Li, J. Lu, Z.W. Chen, K. Amine, 30 years of lithium-ion batteries, Adv. Mater. 30 (2018) 1800561. https://doi.org/10.1002/adma.201800561.

[3] C.-Y. Wang, T. Liu, X.-G. Yang, S. Ge, N.V. Stanley, E.S. Rountree, Y. Leng, B.D. McCarthy, Fast charging of energy-dense lithium-ion batteries, Nature 611 (2022) 485-490. https://doi.org/10.1038/s41586-022-05281-0.

[4] A. Manthiram, An outlook on lithium ion battery technology, ACS Cent. Sci. 3 (2017) 1063-1069. https://doi.org/10.1021/acscentsci.7b00288.

[5] Y. Liu, Y. Zhu, Y. Cui, Challenges and opportunities towards fast-charging battery materials, Nat. Energy 4 (2019) 540-550. https://doi.org/https://doi.org/10.1038/s41560-019-0405-3.

[6] S. Li, K. Wang, G. Zhang, S. Li, Y. Xu, X. Zhang, X. Zhang, S. Zheng, X. Sun, Y. Ma, Fast charging anode materials for lithium-ion batteries: Current status and perspectives, Adv. Funct. Mater (2022) 2200796. https://doi.org/https://doi.org/10.1002/adfm.202200796.

[7] T. Gao, Y. Han, D. Fraggedakis, S. Das, T. Zhou, C.-N. Yeh, S. Xu, W.C. Chueh, J. Li, M.Z. Bazant, Interplay of lithium intercalation and plating on a single graphite particle, Joule 5 (2021) 393-414. https://doi.org/10.1016/j.joule.2020.12.020.

[8] T. Yuan, Z. Tan, C. Ma, J. Yang, Z.-F. Ma, S. Zheng, Challenges of spinel $Li_4Ti_5O_{12}$ for lithium-ion battery industrial applications, Adv. Energy Mater. 7 (2017) 1601625. https://doi.org/https://doi.org/10.1002/aenm.201601625.

[9] H. Zhang, Y. Yang, H. Xu, L. Wang, X. Lu, X. He, $Li_4Ti_5O_{12}$ spinel anode: Fundamentals and advances in rechargeable batteries, InfoMat 4 (2022) e12228. https://doi.org/https://doi.org/10.1002/inf2.12228.

[10] M. Weiss, R. Ruess, J. Kasnatscheew, Y. Levartovsky, N.R. Levy, P. Minnmann, L. Stolz, T. Waldmann, M. Wohlfahrt-Mehrens, D. Aurbach, M. Winter, Y. Ein-Eli, J. Janek, Fast charging of lithium-ion batteries: A review of materials aspects, Adanced Energy Materials 11 (2021) 2101126. https://doi.org/https://doi.org/10.1002/aenm.202101126.

[11] K.J. Griffith, Y. Harada, S. Egusa, R.M. Ribas, R.S. Monteiro, R.B. Von Dreele, A.K. Cheetham, R.J. Cava, C.P. Grey, J.B. Goodenough, Titanium niobium oxide: from discovery to application in fast-charging lithium-ion batteries, Chem. Mater. 33 (2021) 4-18. https://doi.org/10.1021/acs.chemmater.0c02955.

[12] A.A. Voskanyan, M. Abramchuk, A. Navrotsky, Entropy stabilization of TiO_2-Nb_2O_5 Wadsley-Roth shear phases and their prospects for lithium ion battery anode materials, Chem. Mater. 32 (2020) 5301-5308. https://doi.org/https://dx.doi.org/10.1021/acs.chemmater.0c01553.

[13] J.-T. Han, J.B. Goodenough, 3-V full cell performance of anode framework $TiNb_2O_7$/spinel $LiNi_{0.5}Mn_{1.5}O_4$, Chem. Mater. 23 (2011) 3404-3407. https://doi.org/10.1021/cm201515g.

[14] J. Han, Y. Huang, J.B. Goodenough, New anode framework for rechargeable lithium batteries, Chem. Mater. 23 (2011) 2027-2029. https://doi.org/dx.doi.org/10.1021/cm200441h.

[15] N. Takami, H. Inagaki, Y. Tatebayashi, H. Saruwatari, K. Honda, S. Egusa, High-power and long-life lithium-ion batteries using lithium titanium oxide anode for automotive and stationary power applications, J. Power Sources 244 (2013) 469-475. https://doi.org/https://doi.org/10.1016/j.jpowsour.2012.11.055.

[16] N. Takami, K. Ise, Y. Harada, T. Iwasaki, T. Kishi, K. Hoshina, High-energy, fast-charging, long-life lithium-ion batteries using $TiNb_2O_7$ anodes for automotive applications, J. Power Sources 396 (2018) 429-436. https://doi.org/10.1016/j.jpowsour.2018.06.059.

[17] K. Ise, S. Morimoto, Y. Harada, N. Takami, Large lithium storage in highly crystalline $TiNb_2O_7$ nanoparticles synthesized by a hydrothermal method as anodes for lithium-ion batteries, Solid State Ion. 320 (2018) 7-15. https://doi.org/10.1016/j.ssi.2018.02.027.

[18] N. Takami, H. Inagaki, T. Kishi, Y. Harada, Y. Fujita, K. Hoshina, Electrochemical kinetics and safety of 2-volt class Li-ion battery system using lithium titanium oxide anode, J. Electrochem. Soc. 156 (2009) A128. https://doi.org/10.1149/1.3043441.

[19] N. Takami, A. Satoh, M. Hara, T. Ohsaki, Structural and kinetic characterization of lithium intercalation into carbon anodes for secondary lithium batteries, J. Electrochem. Soc. 142 (1995) 371-379. https://doi.org/10.1149/1.2044017.

[20] H. Li, J. Li, X. Ma, J.R. Dahn, Synthesis of single crystal $LiNi_{0.6}Mn_{0.2}Co_{0.2}O_2$ with enhanced electrochemical performance for lithium ion batteries, J. Electrochem. Soc. 165 (2018) A1038. https://doi.org/10.1149/2.0951805jes.

[21] J. Langdon, A. Manthiram, A perspective on single-crystal layered oxide cathodes for lithium-ion batteries, Energy Storage Mater. 37 (2021) 143-160. https://doi.org/https://doi.org/10.1016/j.ensm.2021.02.003.

[22] X. Lu, Z.L. Jian, Z. Fang, L. Gu, Y.S. Hu, W. Chen, Z.X. Wang, L.Q. Chen, Atomic-scale investigation on lithium storage mechanism in $TiNb_2O_7$, Energy Environ. Sci. 4 (2011) 2638-2644. https://doi.org/10.1039/c0ee00808g.

[23] K.J. Griffith, I.D. Seymour, M.A. Hope, M.M. Butala, L.K. Lamontagne, M.B. Preefer, C.P. Koçer, G. Henkelman, A.J. Morris, M.J. Cliffe, S.E. Dutton, C.P. Grey, Ionic and electronic conduction in $TiNb_2O_7$, J. Am. Chem. Soc. 141 (2019) 16706-16725. https://doi.org/10.1021/jacs.9b06669.

[24] C. Yang, D. Ma, J. Yang, M. Manawan, T. Zhao, Y. Feng, J. Li, Z. Liu, Y.-W. Zhang, R.B. Von Dreele, B.H. Toby, C.P.d.L. Albarrán, J.H. Pan, Crystallographic insight of reduced lattice volume expansion in mesoporous Cu^{2+}-doped $TiNb_2O_7$ microspheres during Li^+ insertion, Adv. Funct. Mater 33 (2023) 2212854. https://doi.org/https://doi.org/10.1002/adfm.202212854.

[25] D. Liang, Y. Lu, L. Hu, L. Wang, S. Liang, X. Liang, L. Liu, Z. Xu, C. Han, C. Liang, Mesoporous $TiNb_2O_7$ nanosheets anode with excellent rate capability and cycling performance in lithium ion half/full batteries, J. Power Sources 544 (2022) 231897. https://doi.org/https://doi.org/10.1016/j.jpowsour.2022.231897.

[26] L. Hu, L.J. Luo, L.F. Tang, C.F. Lin, R.J. Li, Y.J. Chen, $Ti_2Nb_{2x}O_{4+5x}$ anode materials for lithium-ion batteries: a comprehensive review, J. Mater. Chem. A 6 (2018) 9799-9815. https://doi.org/10.1039/c8ta00895g.

[27] H.C. Chiu, N. Brodusch, R. Gauvin, A. Guerfi, K. Zaghib, G.P. Demopoulos, Aqueous synthesized nanostructured $Li_4Ti_5O_{12}$ for high-performance lithium ion battery anodes, J. Electrochem. Soc. 160 (2013) A3041-A3047. https://doi.org/10.1149/2.008305jes.

[28] S. Ahmed, P.A. Nelson, K.G. Gallagher, N. Susarla, D.W. Dees, Cost and energy demand of producing nickel manganese cobalt cathode material for lithium ion batteries, J. Power Sources 342 (2017) 733-740. https://doi.org/https://doi.org/10.1016/j.jpowsour.2016.12.069.

[29] M. Yu, Z.F. Cai, Q. Li, S. Wang, Y.Z. Ma, G.S. Song, W.D. Yang, C. Wen, Enhanced energy storage performance of Zr-doped $TiNb_2O_7$ nanospheres prepared by the hydrolytic method, ACS Sustain. Chem. Eng. 11 (2023) 5147-5154. https://doi.org/10.1021/acssuschemeng.2c07144.

[30] C. Lin, L. Hu, C. Cheng, K. Sun, X. Guo, Q. Shao, J. Li, N. Wang, Z. Guo, Nano-$TiNb_2O_7$/carbon nanotubes composite anode for enhanced lithium-ion storage, Electrochim. Acta 260 (2018) 65-72. https://doi.org/https://doi.org/10.1016/j.electacta.2017.11.051.

[31] V. Paulraj, T. Saha, K. Vediappan, K. Kamala Bharathi, Synthesis and electrochemical properties of $TiNb_2O_7$ nanoparticles as an anode material for lithium ion batteries, Mater. Lett. 304 (2021) 130681. https://doi.org/https://doi.org/10.1016/j.matlet.2021.130681.

[32] G.P. Demopoulos, Aqueous precipitation and crystallization for the production of particulate solids with desired properties, Hydrometallurgy 96 (2009) 199-214. https://doi.org/https://doi.org/10.1016/j.hydromet.2008.10.004.

[33] Y. Li, G.P. Demopoulos, Precipitation of nanosized titanium dioxide from aqueous titanium(IV) chloride solutions by neutralization with MgO, Hydrometallurgy 90 (2008) 26-33. https://doi.org/https://doi.org/10.1016/j.hydromet.2007.09.008.

[34] C. Charbonneau, R. Gauvin, G.P. Demopoulos, Nucleation and growth of self-assembled nanofibre-structured rutile (TiO_2) particles via controlled forced hydrolysis of titanium tetrachloride solution, J. Cryst. Growth 312 (2009) 86-94. https://doi.org/https://doi.org/10.1016/j.jcrysgro.2009.09.033.

[35] C. Charbonneau, R. Gauvin, G.P. Demopoulos, Aqueous solution synthesis of crystalline anatase nanocolloids for the fabrication of DSC photoanodes, J. Electrochem. Soc. 158 (2011) H224. https://doi.org/10.1149/1.3529238.

[36] A. Yasin, F. Guo, M.J. Sussman, R. Gauvin, G.P. Demopoulos, Steady-state, scalable production of mesoporous Rutile and Brookite particles and their use in energy conversion and storage cells, ChemNanoMat 2 (2016) 980-988. https://doi.org/10.1002/cnma.201600185.

[37] A. Yasin, F. Guo, G.P. Demopoulos, Continuous-reactor, pH-controlled synthesis of multifunctional mesoporous nanocrystalline anatase aggregates, Chem. Eng. J. 287 (2016) 398-409. https://doi.org/https://doi.org/10.1016/j.cej.2015.11.045.

[38] Y. Jia, D. Zhang, R. Pan, L. Xu, G.P. Demopoulos, A novel two-step coprecipitation process using Fe(III) and Al(III) for the removal and immobilization of arsenate from acidic aqueous solution, Water Research 46 (2012) 500-508. https://doi.org/https://doi.org/10.1016/j.watres.2011.11.045.

[39] F. Yu, B. Miglani, S. Yuan, R. Yekani, K.H. Bevan, G.P. Demopoulos, Fe^{3+}-substitutional doping of nanostructured single-crystal $TiNb_2O_7$ for long-stable cycling of ultra-fast charging anodes, Nano Energy 133 (2025) 110494. https://doi.org/https://doi.org/10.1016/j.nanoen.2024.110494.

[40] K. Chalastara, F.Q. Guo, S. Elouatik, G.P. Demopoulos, Tunable composition aqueous-synthesized mixed-phase TiO_2 nanocrystals for photo-assisted water decontamination: comparison of anatase, brookite and rutile photocatalysts, Catalysts 10 (2020) 18. https://doi.org/10.3390/catal10040407.

[41] G. Meyer, J.F. Oosterom, W.J. van Oeveren, The system $NbCl_5$-Nb_2O_5, Recueil des Travaux Chimiques des Pays-Bas 80 (1961) 502-512. https://doi.org/https://doi.org/10.1002/recl.19610800505.

[42] W. Liu, J. Liu, M. Zhu, W. Wang, Y. Sun, Closely compacted $TiNb_2O_7$-C assembly for fast-charging battery anodes, ACS Appl. Energy Mater. 4 (2021) 12319-12325. https://doi.org/10.1021/acsaem.1c02144.

[43] W. Li, E.M. Erickson, A. Manthiram, High-nickel layered oxide cathodes for lithium-based automotive batteries, Nat. Energy 5 (2020) 26-34. https://doi.org/10.1038/s41560-019-0513-0.

[44] V. Pimenta, M. Sathiya, D. Batuk, A.M. Abakumov, D. Giaume, S. Cassaignon, D. Larcher, J.-M. Tarascon, Synthesis of Li-rich NMC: a comprehensive study, Chem. Mater. 29 (2017) 9923-9936. https://doi.org/10.1021/acs.chemmater.7b03230.

[45] J.L. Gao, X.Q. Cheng, S.F. Lou, Y.L. Ma, P.J. Zuo, C.Y. Du, Y.Z. Gao, G.P. Yin, Self-doping $Ti_{1-x}Nb_{2-x}O_7$ anode material for lithium-ion battery and its electrochemical performance, J. Alloy. Compd. 728 (2017) 534-540. https://doi.org/10.1016/j.jallcom.2017.09.045.

[46] S. Gong, Y. Wang, Q. Zhu, M. Li, Y. Wen, H. Wang, J. Qiu, B. Xu, High-rate lithium storage performance of $TiNb_2O_7$ anode due to single-crystal structure coupling with Cr^{3+}-doping, J. Power Sources 564 (2023) 232672. https://doi.org/https://doi.org/10.1016/j.jpowsour.2023.232672.

[47] K. Tian, Z. Wang, H. Di, H. Wang, Z. Zhang, S. Zhang, R. Wang, L. Zhang, C. Wang, L. Yin, Superimposed effect of La doping and structural engineering to achieve oxygen-deficient $TiNb_2O_7$ for ultrafast Li-ion storage, ACS Appl. Mater. Interfaces 14 (2022) 10478-10488. https://doi.org/10.1021/acsami.1c24909.

[48] C. Lin, S. Yu, S. Wu, S. Lin, Z.-Z. Zhu, J. Li, L. Lu, $Ru_{0.01}Ti_{0.99}Nb_2O_7$ as an intercalation-type anode material with a large capacity and high rate performance for lithium-ion batteries, J. Mater. Chem. A 3 (2015) 8627-8635. https://doi.org/https://doi.org/10.1039/C5TA01073J.

[49] A. Shi, Y. Zhang, S. Geng, X. Song, G. Yin, S. Lou, L. Tan, Highly oxidized state dopant induced Nb-O bond distortion of $TiNb_2O_7$ for extremely fast-charging batteries, Nano Energy (2024) 109349. https://doi.org/https://doi.org/10.1016/j.nanoen.2024.109349.

[50] Y. Zhang, C. Kang, W. Zhao, B. Sun, X. Xiao, H. Huo, Y. Ma, P. Zuo, S. Lou, G. Yin, Crystallographic engineering to reduce diffusion barrier for enhanced intercalation pseudocapacitance of $TiNb_2O_7$ in fast-charging batteries, Energy Storage Mater. 47 (2022) 178-186. https://doi.org/https://doi.org/10.1016/j.ensm.2022.01.061.

[51] L.J. Zhao, S.T. Wang, Y.H. Dong, W. Quan, F. Han, Y.M. Huang, Y.T. Li, X.H. Liu, M. Li, Z.T. Zhang, J.Y. Zhang, Z.L. Tang, J. Li, Coarse-grained reduced $Mo_xTi_{1-x}Nb_2O_{7+y}$ anodes for high-rate lithium-ion batteries, Energy Storage Mater. 34 (2021) 574-581. https://doi.org/10.1016/j.ensm.2020.10.016.

[52] H. Song, Y.-T. Kim, A Mo-doped $TiNb_2O_7$ anode for lithium-ion batteries with high rate capability due to charge redistribution, Chem. Commun. 51 (2015) 9849-9852. https://doi.org/10.1039/C5CC02221E.

[53] C. Lei, X. Qin, S. Huang, T. Wei, Y. Zhang, Mo-doped $TiNb_2O_7$ microspheres as improved anode materials for lithium-ion batteries, ChemElectroChem 8 (2021) 3379-3383. https://doi.org/https://doi.org/10.1002/celc.202101056.

[54] K. Liu, J.-a. Wang, J. Yang, D. Zhao, P. Chen, J. Man, X. Yu, Z. Wen, J. Sun, Interstitial and substitutional V^{5+}-doped $TiNb_2O_7$ microspheres: A novel doping way to achieve high-

performance electrodes, Chem. Eng. J. 407 (2021) 127190. https://doi.org/https://doi.org/10.1016/j.cej.2020.127190.

[55] Y.-S. Hsiao, C.-W. Chang-Jian, H. Chu Weng, H.-H. Chiang, C.-Z. Lu, W. Kong Pang, V.K. Peterson, X.-C. Jiang, P.-I. Wu, C.-P. Chen, J.-H. Huang, Doping with W^{6+} ions enhances the performance of $TiNb_2O_7$ as an anode material for lithium-ion batteries, Appl. Surf. Sci. 573 (2022) 151517. https://doi.org/https://doi.org/10.1016/j.apsusc.2021.151517.

[56] R.M. Tao, T.Y. Zhang, X.G. Sun, C.L. Do-Thanh, S. Dai, Ionothermally synthesized nanoporous $Ti_{0.95}W_{0.05}Nb_2O_7$: a novel anode material for high-performance lithium-ion batteries, Batteries & Supercaps 6 (2023) e202300101. https://doi.org/10.1002/batt.202300101.

[57] C. Yang, C. Lin, S. Lin, Y. Chen, J. Li, $Cu_{0.02}Ti_{0.94}Nb_{2.04}O_7$: An advanced anode material for lithium-ion batteries of electric vehicles, J. Power Sources 328 (2016) 336-344. https://doi.org/https://doi.org/10.1016/j.jpowsour.2016.08.027.

[58] J. Zheng, R. Xia, C.L. Sun, N. Yaqoob, Q.Y. Qiu, L.P. Zhong, Y.D. Li, P. Kaghazchi, K.N. Zhao, J.E. ten Elshof, M. Huijben, Fast and durable lithium storage enabled by tuning entropy in Wadsley-Roth phase titanium niobium oxides, Small 19 (2023) 2301967. https://doi.org/10.1002/smll.202301967.

[59] X. Wu, S. Lou, X. Cheng, C. Lin, J. Gao, Y. Ma, P. Zuo, C. Du, Y. Gao, G. Yin, Unravelling the interface layer formation and gas evolution/suppression on a $TiNb_2O_7$ anode for lithium-Ion batteries, ACS Appl. Mater. Interfaces 10 (2018) 27056-27062. https://doi.org/10.1021/acsami.8b08425.

[60] C. Wang, Z. Guo, W. Shen, Q. Xu, H. Liu, Y. Wang, B-doped carbon coating improves the electrochemical performance of electrode materials for Li-ion batteries, Adv. Funct. Mater 24 (2014) 5511-5521. https://doi.org/https://doi.org/10.1002/adfm.201401006.

[61] M. Uceda, H.-C. Chiu, J. Zhou, R. Gauvin, K. Zaghib, G.P. Demopoulos, Nanoscale assembling of graphene oxide with electrophoretic deposition leads to superior percolation network in Li-ion electrodes: $TiNb_2O_7$/rGO composite anodes, Nanoscale 12 (2020) 23092–23104. https://doi.org/https://doi.org/10.1039/D0NR06082H.

[62] L. Ye, K. Wen, Z. Zhang, F. Yang, Y. Liang, W. Lv, Y. Lin, J. Gu, J.H. Dickerson, W. He, Highly efficient materials assembly via electrophoretic deposition for electrochemical energy conversion and storage devices, Adv. Energy Mater. 6 (2016) 1502018. https://doi.org/https://doi.org/10.1002/aenm.201502018.

[63] J.Q. Zhou, H.Y. Dong, Y. Chen, Y.H. Ye, L. Xiao, B.H. Deng, J.P. Liu, Carbon-coated $TiNb_2O_7$ nanosheet arrays as self-supported high mass-loading anodes for flexible Li-ion batteries, Chem. Commun. 57 (2021) 1822-1825. https://doi.org/10.1039/d0cc08251a.

[64] H. Wang, R. Qian, Y. Cheng, H.-H. Wu, X. Wu, K. Pan, Q. Zhang, Micro/nanostructured $TiNb_2O_7$-related electrode materials for high-performance electrochemical energy storage: recent advances and future prospects, J. Mater. Chem. A 8 (2020) 18425-18463. https://doi.org/10.1039/D0TA04209A.

[65] M. Léger, A. La Monaca, N. Basu, G.P. Demopoulos, Alternatives assessment of polyvinylidene fluoride-compatible solvents for N-methyl pyrrolidone substitution in lithium-ion battery cathodes, Next Sustainability 5 (2025) 100084. https://doi.org/https://doi.org/10.1016/j.nxsust.2024.100084.

[66] S. Wang, G.P. Demopoulos, High-conductive polymer-in-porous garnet solid electrolyte structure for all-solid-state lithium batteries enabled by molecular engineering, Energy

Storage Mater. 71 (2024) 103604. https://doi.org/https://doi.org/10.1016/j.ensm.2024.103604.

[67] F. Yu, G.P. Demopoulos, Ultra-fast charging with over 5000 cycles $TiNb_2O_7$ anodes for lithium-ion batteries and all-solid-state batteries, ECS Meeting Abstracts (2025)

7. Synopsis

7.1. Conclusions

The overall goal of this thesis was to advance the development of titanium niobium oxide ($TiNb_2O_7$, TNO) as an ultrafast charging anode via a concerted approach involving nanocrystal control, crystal structure alteration via doping, and electrode engineering. Towards this goal, we developed a scalable synthesis method for single-crystal TNO materials, investigated substitutional Fe^{3+} doping via combined experimental and computational probing and advanced the electrophoretic engineering of highly conductive and long-cycling stable Fe-dope TNO/rGO anodes.

The major conclusions drawn from this work are summarized below:

Single-crystal TNO anode materials with sub-micron size were synthesized through controlled hydrolytic co-precipitation and optimized high-temperature calcination. Co-precipitation by neutralization of a solution made with abundant chloride salts with NH_4OH is producing 10-nm precursor particles of mixed metal hydroxides. These nanoscale and homogeneous in composition precursor particles are conducive to single crystal formation upon calcination at the appropriate temperature and time, 900 °C for 4 hours.

The as-synthesized single-crystal TNO exhibited a high gravimetric capacity of 279 mAh/g and high volumetric capacity of 351.7 mAh/cm^3 (after calendering at 3000 atm) at 0.5 C. Furthermore, it is characterized by a high diffusion coefficient of up to 1.37×10^{-13} cm^2/s, and a remarkable fast charging capability of 200 mAh/g under 10 C fast charging (coupled with 1 C discharging). However, its cycling lifespan required improvement as its initial capacity of 223 mAh/g will fade down to 81.4 % after 200 cycles.

To improve the cycling stability of the new TNO single-crystal anode material, in-situ substitution of Fe and compositional control was realized to develop nanostructured Fe^{3+}-doped TNO monocrystalline material ($Fe_{0.05}Ti_{0.95}Nb_2O_{6.975}$). The obtained $Fe_{0.05}Ti_{0.95}Nb_2O_{6.975}$ provides remarkable fast-charging capability (220 mAh/g after 100 cycles under 10 C/1C charging/discharging protocol) and enlarged cycling stability (85% capacity retention after 1000 cycles at 5 C). The mechanism by which iron substitution helped stabilize battery cycling was revealed by both experimental and computational studies. Fe^{3+} substitution of Ti^{4+} in TNO nanomaterials (5% Fe substitution) reduces the band gap from 3.75 eV of pure TNO to 3.40 eV of Fe5-TNO, thereby increasing the conductivity of TNO and reducing the impedance of LIB electrodes. Crystallographically, Fe^{3+} dopants extend the *ac*-plane and decrease the *b*-value, suggesting a widening diffusion channel and shortening pathway along the *b*-axis. Consequently, this Fe^{3+}-doped TNO demonstrates a higher Li diffusion coefficient (determined by GITT) and a smaller Li-ion diffusion activation energy (calculated by DFT).

Finally, an advanced electrophoretic deposition (EPD) method was developed to fabricate carbon-coated $Fe_{0.05}Ti_{0.95}Nb_2O_{6.975}$/reduced graphene oxide (rGO) composites for binder-free all-active-material fast charging anodes. The innovative technique ensures homogeneous interphasing of TNO nanocrystals and graphene oxide that is free of aggregation and which upon reductive annealing creates a highly conductive 3D percolation network. The newly engineered C-FeTNO/rGO electrode provides a low impedance of 75 ohm, it offers a high practical initial capacity of 212 mAh/g and remarkable cycling retention of 81% after 2500 cycles extended to 70 % retention after 5000 cycles at 5 C, making it highly suitable for ultrafast-charging applications.

7.2.Original Contributions to Knowledge

The original contributions to scientific knowledge achieved by the research studies described in this thesis, are listed below:

- For the first time, single-crystal $TiNb_2O_7$ materials are successfully synthesized by a novel sustainable production featuring hydrolytic co-precipitation and calcination.
- First time investigation into Fe^{3+} substitutional doping in $TiNb_2O_7$ nanomaterials, which promotes ultra-fast charging and long-cycling capability has been reported. The Fe^{3+} substitutional mechanism was investigated through state-of-the-art theoretical modeling and nanostructure characterization to reveal crystal structure and redox reaction evolution, ionic diffusion, and electronic conductivity
- The design of ultra-fast charging and long-cycling carbon-coated Fe^{3+}-doped $TiNb_2O_7$/ reduced graphene oxide by electrophoretic deposition enabling homogeneous-interphase binder-free all-active-material electrode microstructure is also considered novel.

7.3.Future Research Direction

Future research is recommended to enhance the work as following:

During finishing the work for **Chapter 3** and **Chapter 4**, we determined that our synthesis method is scalable for material fabrication and effective for Fe substitutional doping. However, further research into kilogram-level materials synthesis and additional cationic doping work is necessary to advance it towards industrial application. To be more specific, we need to further increase the concentration of aqueous solution, improve the production yield, and design a protocol for continuous stirred tank reactor. From an environmental aspect, we need to recycle the by-products, including spent ammonium chloride solution.

Secondly, in **Chapter 4**, the doping modification mechanism was investigated by using advanced characterization and theoretical DFT calculations. Further investigation with ultraviolet photoelectron spectroscopy (UPS) is recommended to determine valence band, work function, ionization energy, etc. Applying also post-mortem analysis by XRD, TEM, XPS could shed more light into the redox and structural modification effects induced by Fe doping helping further improve the long-term cycling stability.

Thirdly, in **Chapter 5**, novel electrode/interphase engineering was applied. In the future, in-situ observation, including in-situ XRD and in-situ SEM, can be explored to further understand the electrode interphase formation. Moreover, state-of-the-art theoretical calculations such as machine learning, DFT, and molecule-dynamics calculation should be tried for an in-depth understanding of the electrode system.

Beyond the above, it is recommended to explore the application of the new TNO/rGO composite anode in full cell configuration by properly pairing it with optimal cathode and electrolyte, and upsizing it from coin cell to pouch cell. The practical energy density and power density of full cell batteries needs to be determined.

Additionally, the application of TNO/rGO in solid-state batteries in combination with polymer or hybrid (ceramic-polymer) electrolytes as safer alternative to Li metal anodes is another challenging and meaningful research topic.

8. APPENDIXES: Supplementary Information

A. Supplementary Information for Chapter 3: Single-crystal $TiNb_2O_7$ Materials via Sustainable Synthesis for Fast-charging Lithium-ion Battery Anodes

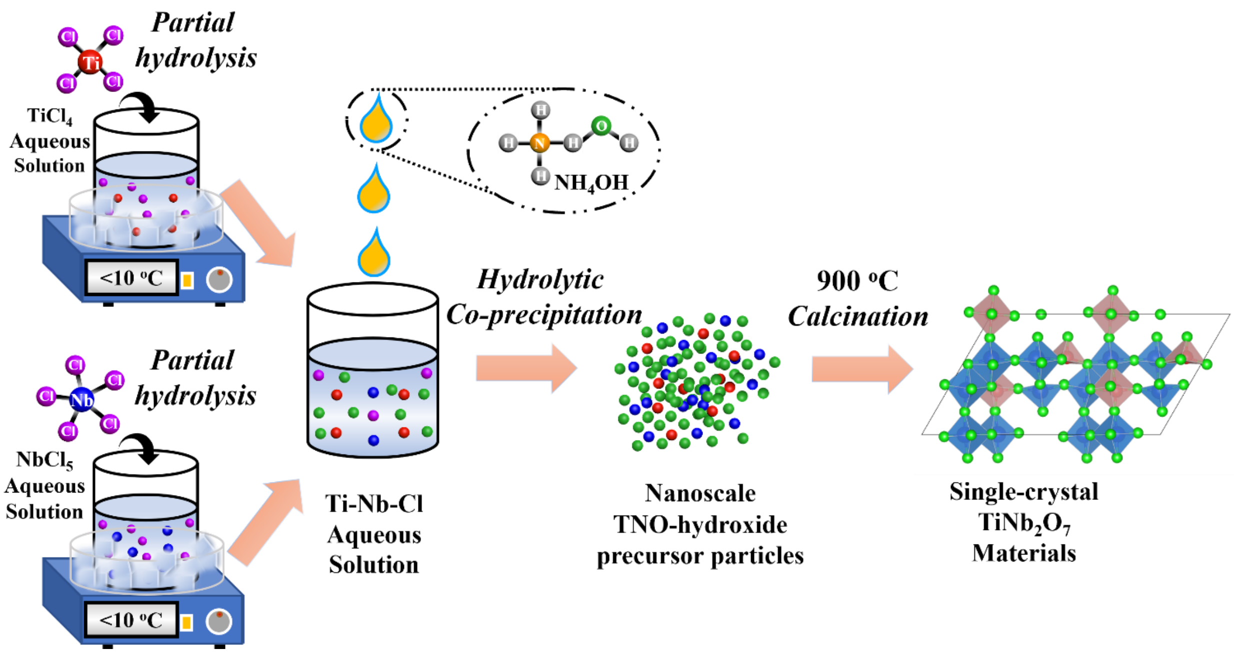

Scheme A.1 Schematic diagram of experimental procedure.

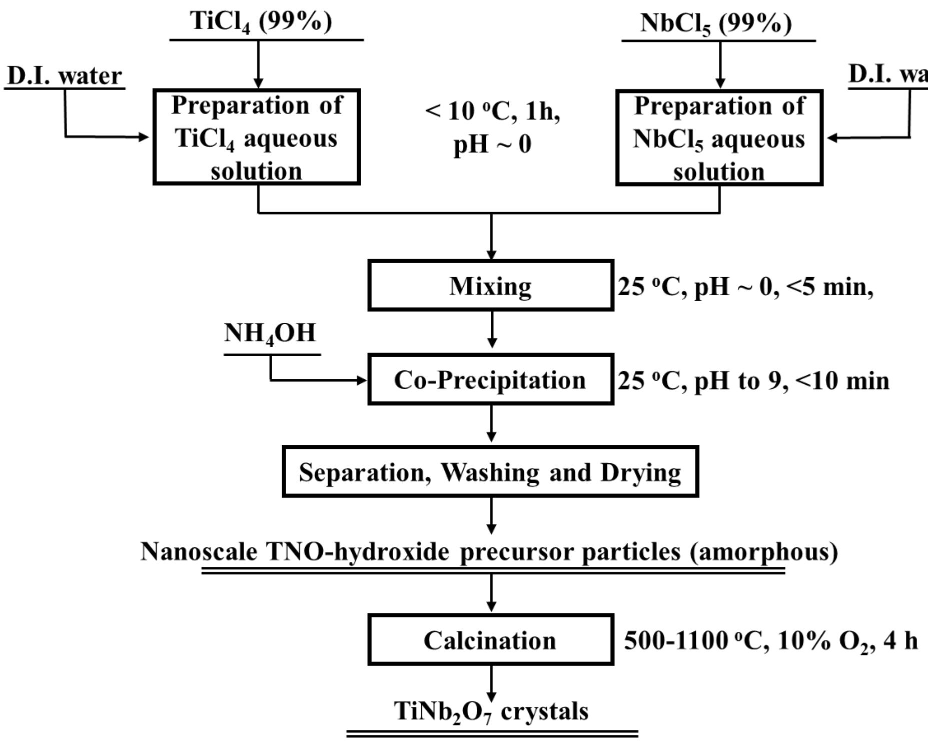

Scheme A.2 Flow chart of the experimental procedure with details.

The following reactions are proposed to account for the synthesis of the hydroxide intermediate precipitate:

(1) Partial Hydrolytic Reaction of $TiCl_4$:

$TiCl_4\,(aq) + xH_2O \rightarrow Ti\text{-}(OH)_x\text{-}Cl_{4-x}\,(aq) + xHCl(aq)$ **(equation A.1)**

(2) Partial Hydrolytic Reaction of $NbCl_5$:

$NbCl_5\,(s) + yH_2O \rightarrow Nb\text{-}(OH)_y\text{-}Cl_{5-y}\,(aq) + yHCl(aq)$ **(equation A.2)**

(3) Co-precipitation Reaction:

$NH_4OH(aq) + HCl(aq) \rightarrow NH_4Cl(aq) + H_2O(l)$ **(equation A.3)**

$Ti\text{-}(OH)_x\text{-}Cl_{4-x}\,(aq) + (4-x)NH_4OH \rightarrow Ti(OH)_4\,(s) + (4-x)\,NH_4Cl$ **(equation A.4)**

$2Nb\text{-}(OH)_y\text{-}Cl_{5-y}\,(aq) + (10-2y)\,NH_4OH \rightarrow 2Nb(OH)_5\,(s) + (10-2y)\,NH_4Cl$ **(equation A.5)**

$Ti(OH)_4 + 2Nb(OH)_5 \rightarrow TiNb_2(OH)_{14}$ **(equation A.6)**

$TiNb_2(OH)_{14} \rightarrow TiO_2{*}Nb_2O_5{*}nH_2O + (7-n)H_2O$ **(equation A.7)**

(4) Calcination:

$TiO_2{*}Nb_2O_5{*}nH_2O$ (amorphous) $\rightarrow TiNb_2O_7$ (crystalline) **(equation A.8)**

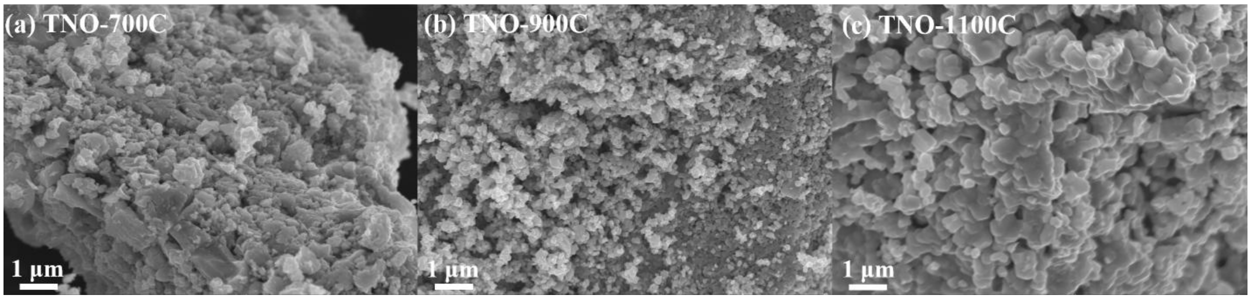

Figure A.1 Low-magnification SEM images of (a) TNO-700C, (b) TNO-900C, and (c) TNO-1100C samples.

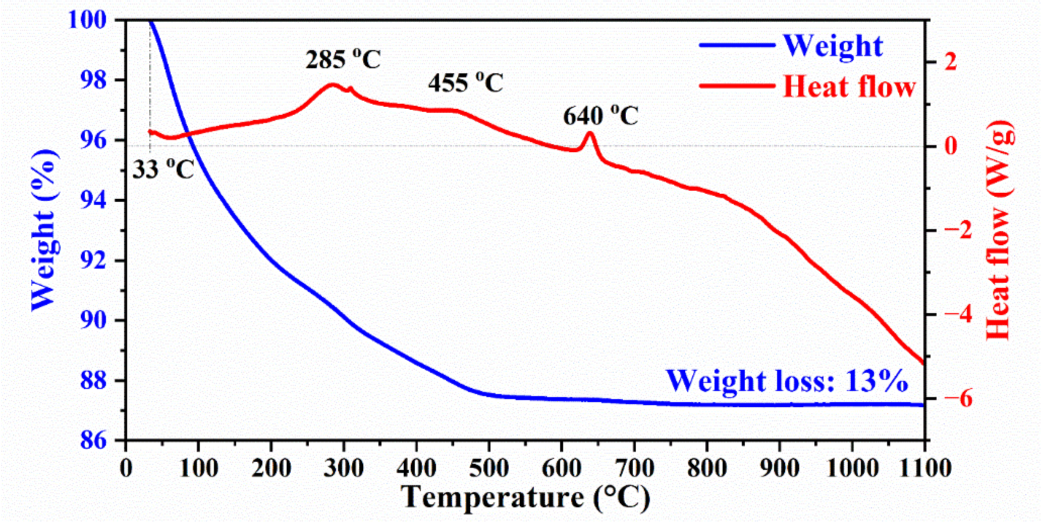

Figure A.2 TGA and DSC curve of the TNO-Precursor

The degree of crystallinity was determined using **equation A.9**.

$$\text{Crystallinity}=\frac{\text{Area of cystallinine peaks}}{\text{Area of cystalline peaks + Area of amorphous peaks}}\times 100\% \qquad (\textbf{equation A.9})$$

The average crystalline grain sizes of TNO-700C, TNO-900C, and TNO-1100C samples were determined to be around 50 nm, 100 nm, and 500 nm, respectively, as calculated by the Scherrer equation (Equation A.10))[1].

Scherrer equation can be represented as follows:

$$D_{hkl}=\frac{K\lambda}{B_{hkl}\cos\theta} \qquad (\textbf{equation A.10})$$

where D_{hkl} is the crystallite size in the direction perpendicular to the lattice planes, hkl are the Miller indices of the lattice planes, K is the shape factor constant (0.8-1.2), λ is the wavelength of the X-rays (λ=1.54056 Å), B_{hkl} is the full-width at half-maximum (FWHM), θ is the diffraction angle.

Table A.1 Crystallographic data obtained by LeBail Refinement of TNO-900C and TNO-1100C.

	Crystal system	Space group	a (Å)	b (Å)	c (Å)	α (deg)	β (deg)	γ (deg)	V (Å^3)	Density (g/cm^3)
TNO-900C	Monoclinic	C2/m	11.876	3.799	20.358	90	120.199	90	793.776	4.355
TNO-1100C	Monoclinic	C2/m	11.894	3.797	20.377	90°	120.199	90	795.379	4.346

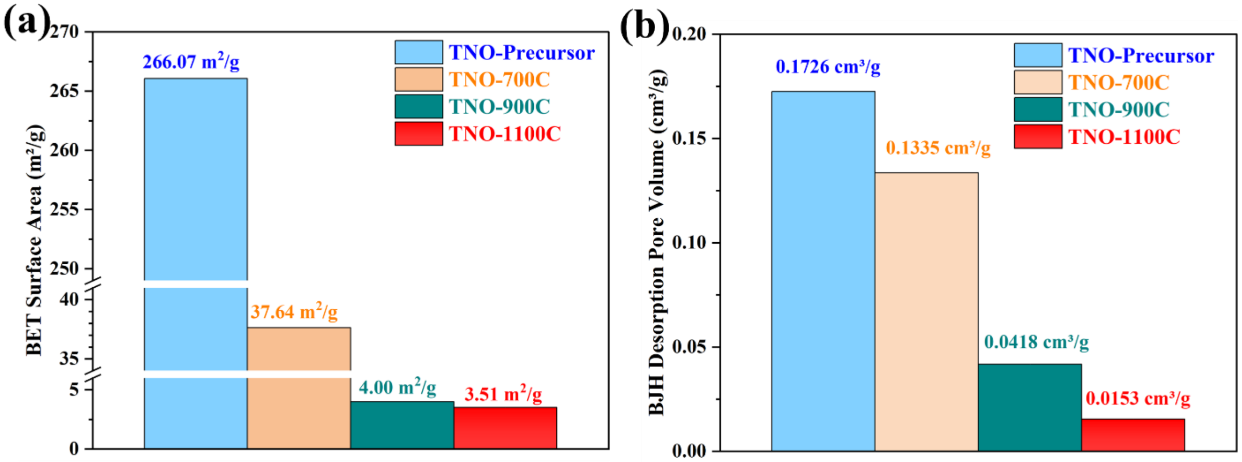

Figure A.3 (a) BET specific surface area and (b) BJH desorption pore volume of TNO-Precursor, TNO-700C, TNO-900C, and TNO-1100C samples.

Furthermore, the equivalent particle size of samples in **Table A.2** can be determined using the BET method, as shown in equation A.11 below[2].

$$d_{BET}=\frac{6000}{(S_{BET}*\rho)} \qquad \textbf{(equation A.11)}$$

Where d_{BET} is the equivalent particle size in nm, S_{BET} represents the BET specific surface areas in m^2/g, ρ is the density of the particles in g/cm^3. Using the true densities calculated for TNO-900C and TNO-1100C (**Figure A.1**), the BET particle size is calculated to be 100 nm and 393 nm, respectively, using **equation A.11**. We assume the true density of TNO-Precursor and TNO-700C is to be 4.3 g/cm^3 because the theoretical value can not be determined (due to lack of crystallinity), which results in particle sizes of 5 nm and 37 nm, respectively.

Table A.2 Characteristic properties of TNO samples

Samples	Crystallinity (%)	Particle size of primary particle(nm)		BET surface area (m^2/g)	Porous structure of secondary particle	Pore size (nm)
		DLS	TEM			
TNO-Precursor	0	-	5-10	266.07	Mesoporous	3
TNO-700C	58.6	150-450	50-300	37.64	Mesoporous	10
TNO-900C	71.5	180-520	50-300	4	Macroporous	55
TNO-1100C	81.7	360-820	200-500	3.51	nonporous	-

Note: Presented particle size of primary particles was determined by DLS and TEM

Electrochemical testing data:

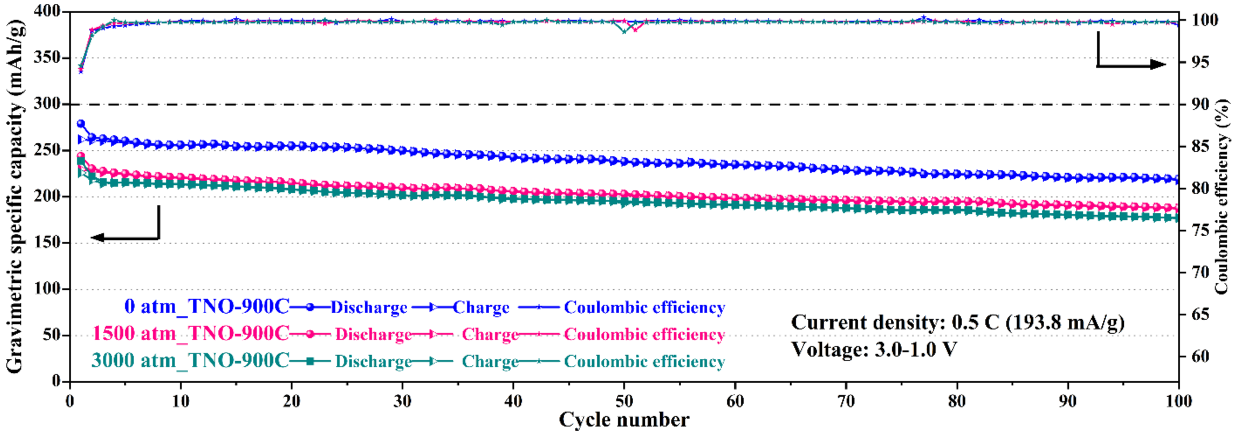

Figure A.4 The gravimetric capacity of TNO-900C materials calendered under different pressures (0 atm, 1500 atm, 3000 atm).

Table A.3 Basic physical and electrochemical properties of TNO-900C electrodes with an area of 0.785 cm^2, pressed under different calendaring pressures.

Calendaring Pressure		**0 atm**	**1500 atm**	**3000 atm**
Electrode physical properties	Mass of composite electrode (mg)	2.92	3.08	3.47
	Electrode mass loading (mg/cm^2)	3.72	3.92	4.42
	TNO active materials mass loading (mg/cm^2)	2.98	3.14	3.54
	Electrode thickness (um)	54	27	24
	Electrode volume (cm^3)	0.00424	0.00212	0.00188
	Electrode density (g/cm^3)	0.69	1.45	1.84
Electrode electrochemical properties	Initial discharge gravimetric capacity (mAh/g)	279	243.9	238.8
	Initial discharge volumetric capacity (mAh/cm^3)	153.6	283.3	351.7
	1st cycle coulombic efficiency	94%	94%	95%
	Cycling retention after 100 cycles	79%	77%	74%

Note: The term “Electrode” refers to the electrode composite consisting of TNO active material (80 wt.%), binder, and carbon black.[3]

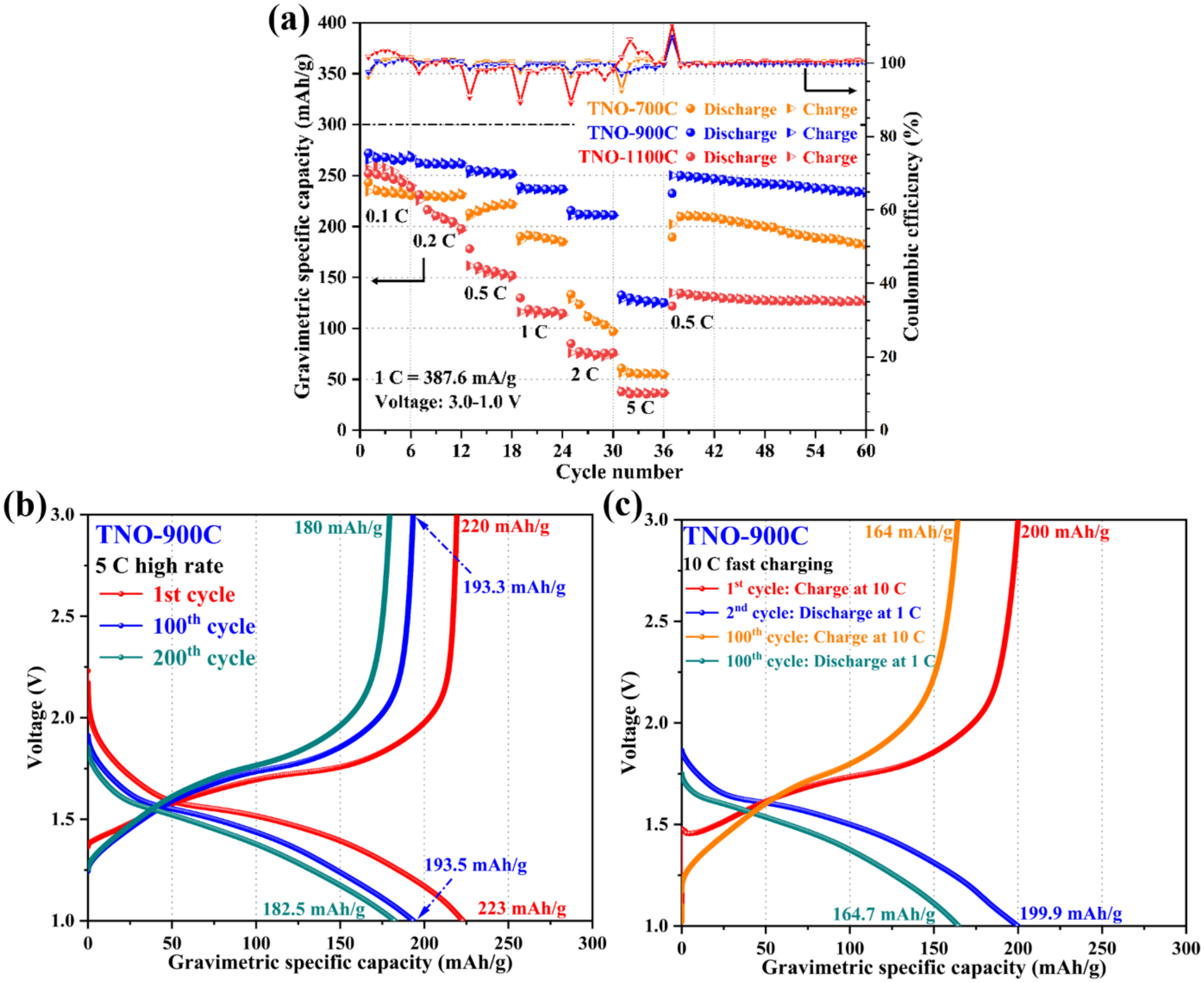

Figure A.5 (a) Rate performance and corresponding coulombic efficiency of TNO-700C, TNO-900C, and TNO-1100C. (b) Capacity-voltage profiles of TNO-900C measured at 5 C rate (5 C discharge and 5 C charge). (c) Capacity-voltage profiles of TNO-900C operated under 10 fast charging situation (10 C fast charging coupled with 1 C discharging).

Table A.4 summarizes the data from key papers in literature that were used to build comparative **Figure 3.5(d)**. As indicated in **Table A.4**, the TNO mass loading in most of the studies mentioned was in the order 1-2 mg/cm^2 compared with 3.2 mg/cm^2 mass loading for the present study. Lyu, et al.,[4] determined the rate performance of TNO with different mass loading from 2.3, 4.3, and 6.7 mg/cm^2 to decrease with increasing mass loading; see **Figure A.6** on which our data is superimposed. As it can be seen, our TNO-900C material (at 3.2 mg/cm^2 mass loading) shows competitive performance, nearly as high as Lyu's sample at 2.3 mg/cm^2 sample despite the higher amount used.

Table A.4 Capacity comparison at 5 C of $TiNb_2O_7$ anode materials synthesized via different methods.

Anode Materials	Synthesis Methods	Discharge Capacity at 5 C	References	
Single crystal $TiNb_2O_7$ Particles	**Hydrolytic co-precipitation synthesis method** **(New sustainable route: green, aqueous, additive-free)** Chemicals: $TiCl_4$, $NbCl_5$, DI water, ammonia hydroxide Step 1. Partial hydrolysis: Add $TiCl_4$ and $NbCl_5$ into DI water (<10 °C), respectively; followed by mixing. Step 2. Co-precipitation: Add NH_4OH into Ti-Nb-Cl solution to pH=9 Step 3. Calcination: 900 °C for 4 h in air	223 mAh/g at 1st cycle, 200 mAh/g after 100 cycles, 181.5 mAh/g after 200 cycles. (Mass loading: 3.2±0.3 mg/cm^2)	**This research, TNO-900C sample**	
$TiNb_2O_7$ nanospheres	**Hydrolytic co-precipitation synthesis method** **(flammable organic-solvent, expensive additive supported route)** Chemicals: $NbCl_5$, titanium isopropoxide (TPT), oxalic acid dihydrate, urea, Solution: ethanol and water Step 1. Hydrolysis Step 2. Calcination: 800 °C for 6 h in air	170 mAh/g at 1st cycle, 160 mAh/g at 100th cycle, 150 mAh/g at 200th cycle (Mass loading: 1.6-2.2 mg/cm^2)	*Yu et al.*, ACS Sustain. Chem. Eng. 11(13) (2023) 5147-5154.	[5]
$TiNb_2O_7$ microparticles	**Solid-state synthesis method** Chemicals: TiO_2 and Nb_2O_5 Step 1. Ball milling: 6 h Step 2. Calcination: 1200 °C for 4 h in air	150 mAh/g at 1st cycle, 125 mAh/g at 100th cycle, 120 mAh/g at 200th cycle (Mass loading: 1 mg/cm^2)	*Cui et al.*, ACS Appl. Mater. Interfaces 15(37) (2023) 43745-43755.	[6]
$TiNb_2O_7$ Micron-sized particles	**Solid-state synthesis method** Chemicals: TiO_2 and Nb_2O_5 Step 1. Ball milling: 3 h Step 2. Calcination: 1100 °C for 8 h	180 mAh/g at 1st cycle, 145 mAh/g at 100th cycle, 137 mAh/g at 200th cycle (Mass loading: 1-1.5 mg/cm^2)	Bian et al., Journal of Materials Science-Materials In Electronics 34(26) (2023) 1826.	[7]
Porous $TiNb_2O_7$ microspheres	**Solvothermal synthesis method** Chemicals: $Ti(OC_4H_9)_4$, $Nb(OC_2H_5)_5$, DETA Solution: isopropyl alcohol (IPA) Step 1. Solvothermal: 200 °C for 12 h. Step 2. Calcination: 700 °C for 5 h in air	215 mAh/g at 1st cycle, 200 mAh/g at 100th cycle, 200 mAh/g at 200th cycle (Mass loading: 1 mg/cm^2)	Park et al., *Adv. Energy Mater.* 5(8) (2015) 1401945	[8]
$TiNb_2O_7$ /Nb_2O_5/TiO_2 composite microsphere	**Solvothermal synthesis method** Chemicals: tetrabutyl titanate, $NbCl_5$ Solution: ethanol Step 1. Solvothermal: 170 °C for 20h. Step 2. Calcination: 800 °C for 6 h in air	185.3 mAh/g at 1st cycle, 180 mAh/g at 100th cycle, 170 mAh/g at 200th cycle (Mass loading: N/A)	Wang et al., *J. Power Sources* **2017,** 367, 106-115.	[9]
$TiNb_2O_7$ microspheres	**Solvothermal synthesis method** **(Microwave-assisted)** Chemicals: $Ti(OC_3H_7)_4$, $NbCl_5$ Solution: ethanol Step 1. Microwave-assisted solvothermal: 200 °C/ 30 min Step 2. Calcination: 800 °C for 8 h in air	220 mAh/g at 1st cycle, 209 mAh/g at 100th cycle (Mass loading: N/A)	Gupta et al, Journal of the American Ceramic Society 106(7) (2023) 4192-4201.	[10]

*Note that the rate of 1 C was set as 387.6 mA/g based on the theoretical capacity of $TiNb_2O_7$ (387.6 mAh/g), consistent with the cited papers.

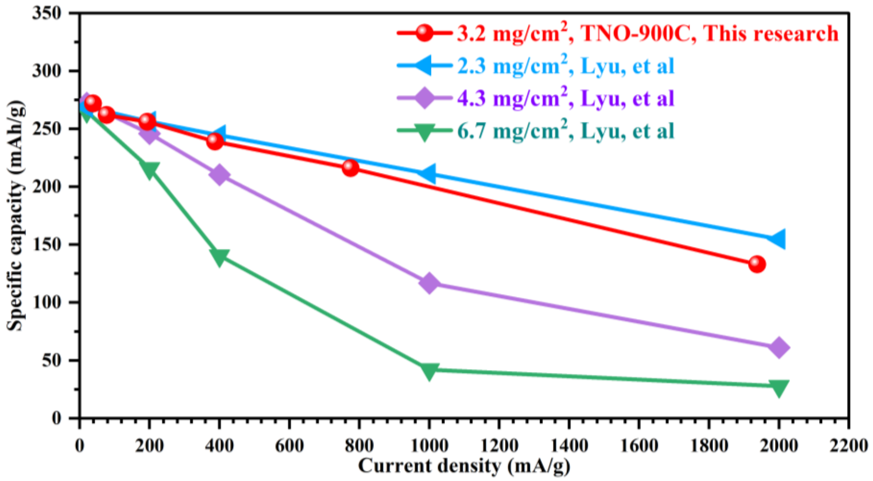

Figure A.6 Rate performance of TNO half-cells with various active material mass loadings: comparison of our data to those of Lyu et al.[4]

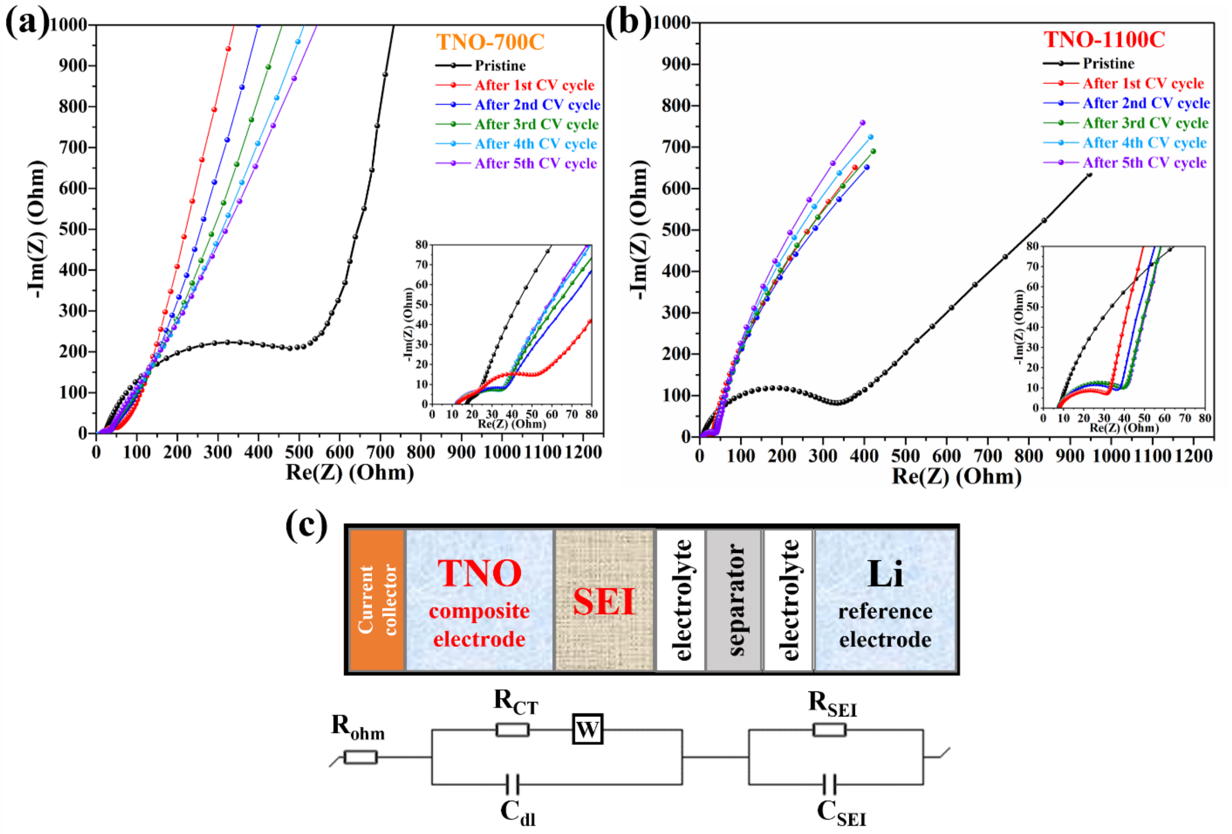

Figure A.7 EIS results before and after each CV cycle of (a) TNO-700C and (b) TNO-1100C, (c) equivalent circuit model of EIS for half-cell battery.

Figure A.7(c) illustrates the individual LIB half-cell components: TNO composite electrode represents $TiNb_2O_7$/Carbon black/PVDF composite electrode, Li metal serves as reference electrode, and the solid-electrolyte interphase (SEI) is formed between electrode and electrolyte after lithiation/delithiation process. In the EIS equivalent circuit model, R_{ohm} is the Ohmic resistance corresponding to electrolyte (dominated) and current collector; and R_{CT} and C_{dl} the Faradaic charge transfer resistance and relative double-layer capacitance in the bulk of composite electrode, related to the semicircle at medium frequencies; R_{SEI} and C_{SEI} are resistance and capacitance of the SEI layer, corresponding to the semicircle at high frequency; W is the Warburg impedance indicated by a straight line at low frequency, which reflects a combination of the diffusional effects of lithium ion on the interface between the active materials particles and electrolyte[11,12].

Li ion diffusion coefficient ($D_{\text{Li}^+,\ \text{EIS}}$) can be determined by using **equation A.12** and **equation A.13**[13,14].

$$\text{Re}(Z)=R_{\text{ohm}}+R_{\text{CT}}+\sigma_W\omega^{-0.5} \qquad \textbf{(equation A.12)}$$

$$D_{\text{Li}^+,\ \text{EIS}}=\frac{R^2T^2}{2n^4F^4\sigma_W{}^2A^2C^2} \qquad \textbf{(equation A.13)}$$

where σ_W, R, T, n, F, A, and C correspond to Warburg coefficient, gas constant, absolute temperature, number of electron transfer per molecule, Faraday constant, surface area of the electrode, and Li ion concentration, respectively.

Table A.5 Calculated Li^+ diffusion coefficient ($D_{\text{Li}^+,\text{CV}}$) of pristine TNO based on cyclic voltammetry

No.	**Synthesis method**	**Anode Materials**	**D_{Li^+} during Lithiation (cm^2/s)**	**D_{Li^+} during Delithiation (cm^2/s)**	**Ref.**	
1	Sol-gel method	Mesoporous $TiNb_2O_7$	1.09×10^{-16}	1.52×10^{-16}	*Qian et al, J. Colloid Interface Sci.* **2022,** 608, 1782-1791.	[15]
2	Template method	Mesoporous $TiNb_2O_7$	1.17×10^{-16}	1.29×10^{-16}	*Qian et al., Electrochim. Acta* 2021, 379, 138179.	[16]
3	Solvothermal method	Hollow $TiNb_2O_7$ nanospheres	3.08×10^{-14}	3.28×10^{-14}	*Qian et al, ACS Sustain. Chem. Eng.* **2022,** 10, (1), 61-70.	[17]
5	Hydrolytic co-precipitation	TNO-700C	6.68×10^{-16}	8.20×10^{-16}	This research	
6		TNO-900C	1.12×10^{-13}	1.08×10^{-13}		
7		TNO-1100C	8.33×10^{-14}	7.03×10^{-14}		

The quantitative contribution of pseudocapacitance for three samples was investigated with **equation A.14** [14,18] as a function of the sweep rate (reproduced below):

$$i(\text{V})=\text{k}_1 v+\text{k}_2 v^{\frac{1}{2}} \qquad (\textbf{equation A.14})$$

where $i(V)$ is total current at specific voltage (V), v is voltage sweep speed, k_1 and k_2 are adjustable parameters, $k_1 v$ denotes surface-controlled capacitive storage and $k_2 v^{1/2}$ corresponds to diffusion-controlled intercalation storage process.

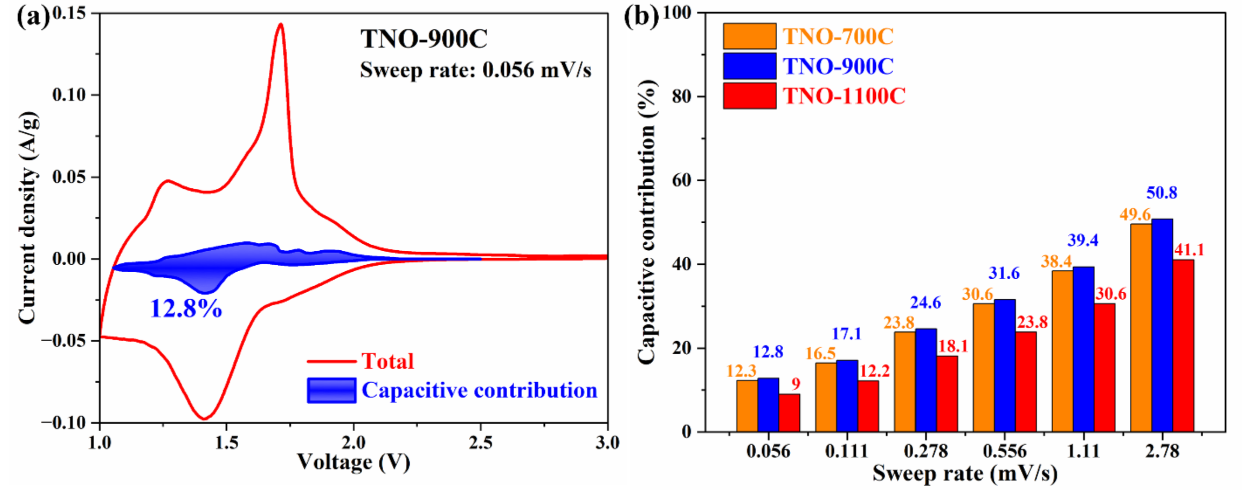

Figure A.8 (a) CV behavior of TNO-900C at 0.056 mV/s and (b) Capacitive contributions of TNO-700C, TNO-900C, and TNO-1100C at different sweep rates.

B. Supplementary Information for Chapter 4: Fe^{3+}-substitutional Doping of Nanostructured Single-crystal $TiNb_2O_7$ for Long-stable Cycling of Ultra-Fast Charging Anodes

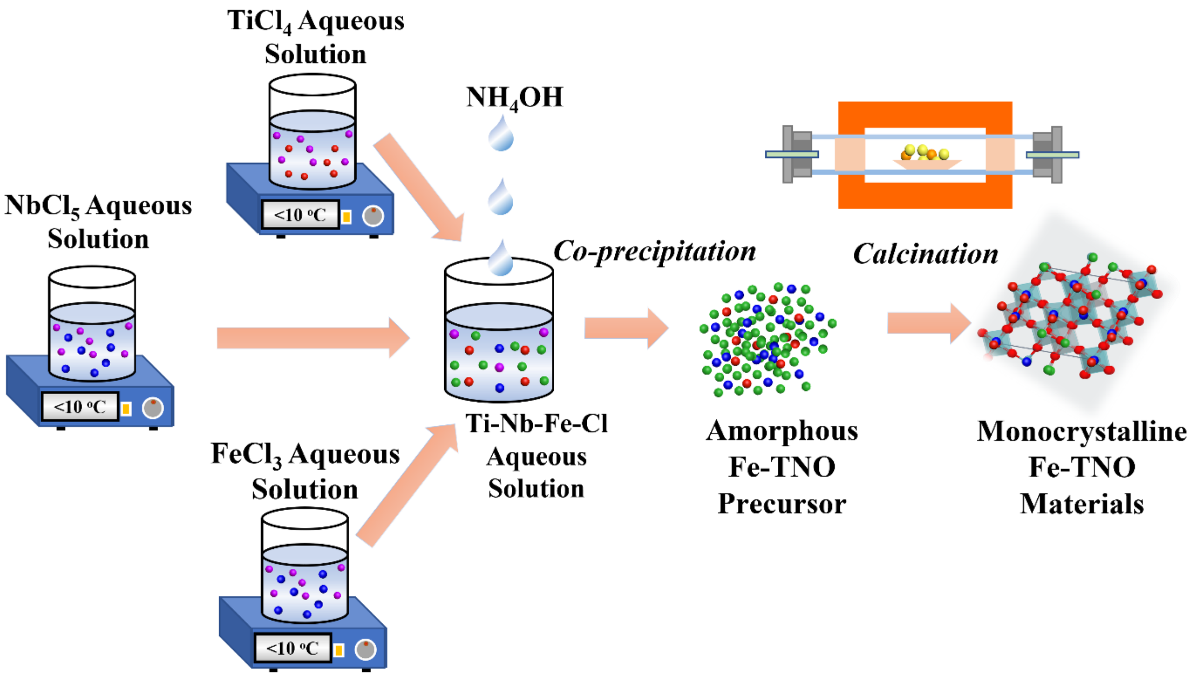

Scheme B.1. Synthesis flowchart of in-situ Fe^{3+} substitutional doped titanium niobate ($Fe_xTi_{1-x}Nb_2O_{7-x/2}$, x=0.01, 0.05, 0.10) materials via scalable homogeneous aqueous co-precipitation and calcination

Table B.1 Elemental composition analysis via ICP-OES

Composition analysis via ICP								
Sample name	**TNO**		**Fe1-TNO**		**Fe5-TNO**		**Fe10-TNO**	
Theoretical composition	$TiNb_2O_7$		$Fe_{0.01}Ti_{0.99}Nb_2O_{6.995}$		$Fe_{0.05}Ti_{0.95}Nb_2O_{6.975}$		$Fe_{0.1}Ti_{0.9}Nb_2O_{6.95}$	
	theoretical	**ICP result**	theoretical	**ICP result**	theoretical	**ICP result**	theoretical	**ICP result**
Fe	**0**	**0**	**0.01**	**0.01**	**0.05**	**0.05**	**0.1**	**0.1**
Ti	**1**	**1.02**	**0.99**	**0.99**	**0.95**	**0.95**	**0.9**	**0.91**
Nb	**2**	**2**	**2**	**2**	**2**	**2**	**2**	**2**
Fe/Ti	**0**	**0**	**0.01**	**0.01**	**0.064**	**0.064**	**0.11**	**0.11**
Fe/Nb	**0**	**0**	**0.005**	**0.005**	**0.03**	**0.03**	**0.05**	**0.05**

Table B.2 Elemental composition analysis and oxidation states of TNO and Fe5-TNO via X-ray photoelectron spectroscopy (XPS)

Sample name		**TNO**		**Fe5-TNO**	
Theoretical composition		$TiNb_2O_7$		$Fe_{0.05}Ti_{0.95}Nb_2O_{6.975}$	
Elemental composition %	Oxidation state	theoretical	**XPS**	theoretical	**XPS**
Fe	+3	**0**	**0**	**0.5**	0.54
Ti	+4	**10**	**10.28**	**9.5**	9.47
Nb	+5	**20**	**20.51**	**20**	20.30
O	-2	**70**	**69.21**	**69.75**	69.69
Fe/Ti		**0**	**0**	**0.064**	**0.064**
Fe/Nb		**0**	**0**	**0.03**	**0.03**

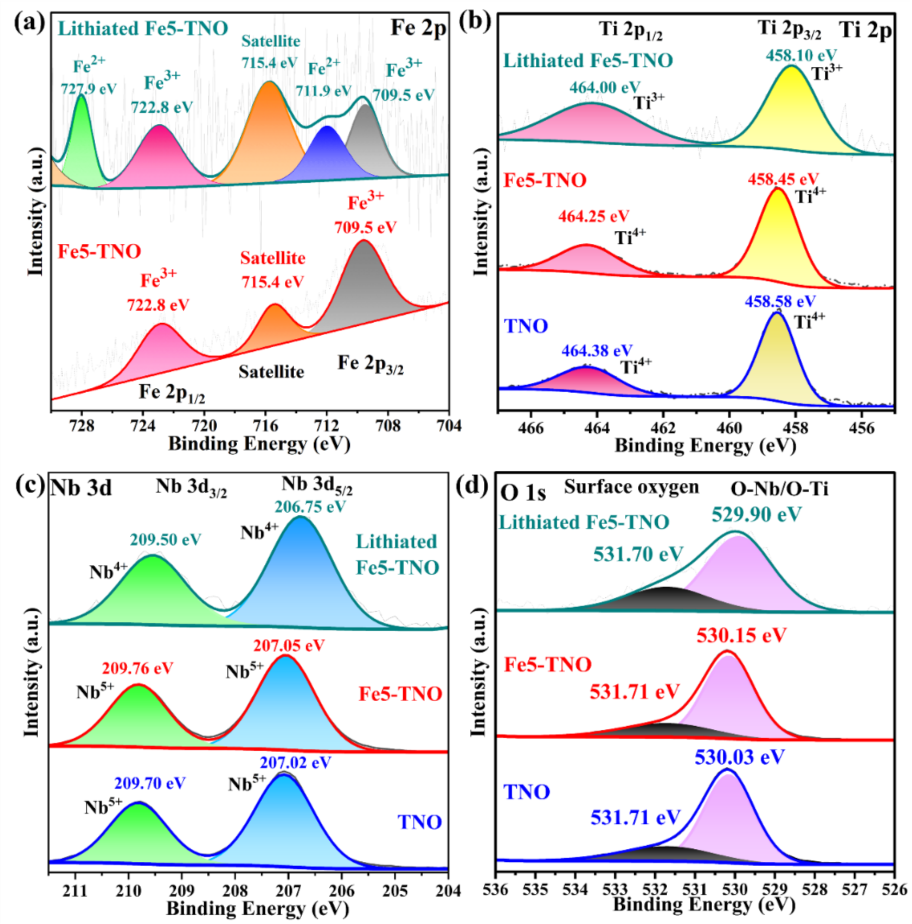

Figure B.1 High-resolution XPS spectra of (f) Fe 2p, (g) Ti 2p, (h) Nb 3d, and (i) O 1s for TNO, Fe5-TNO, and lithiated Fe5-TNO (discharged to 1 V)

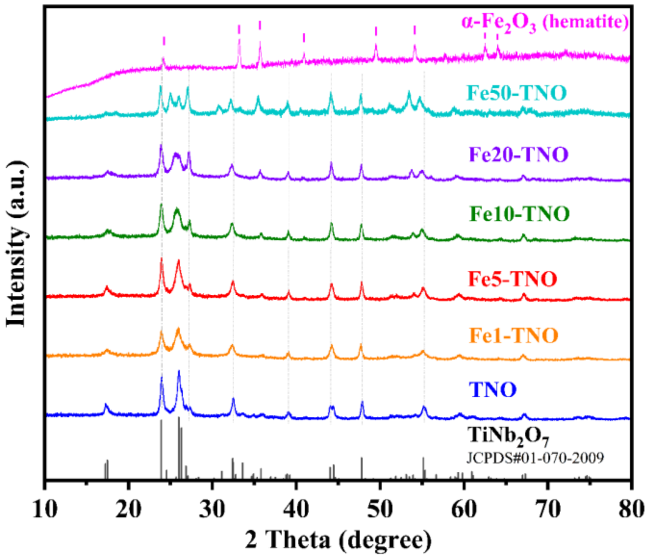

Figure B.2 XRD patterns of nanostructured Fe^{3+}-doped TNO materials (Fe$_x$Ti$_{1-x}$Nb$_2$O$_{7-x/2}$, x=0.01, 0.05, 0.10, 0.20, 0.50), TNO material, and hematite sample

Table B.3 Crystal parameters of TNO and Fe5-TNO via Le Bail refinement and DFT calculation

Crystal parameters by XRD refinement

	Crystal system	Space group	*a* (Å)	*b* (Å)	*c* (Å)	*β* (°)	*α, γ* (°)	V (Å^3)
TNO	Monoclinic	C2/m	**20.358**	**3.799**	**11.876**	120.199	90	**793.776**
Fe5-TNO	Monoclinic	C2/m	**20.539**	**3.754**	**11.892**	**120.386**	90	**790.968**
Difference			**+0.89 %**	**-1.18%**	**+0.13%**	**+0.16 %**		**-0.35%**

Crystal parameters by DFT calculation

	Crystal system	Space group	a (Å)	b (Å)	c (Å)	β (°)	α, γ (°)	V (Å^3)
TNO	Monoclinic	C2/m	**20.410**	**3.892**	**11.883**	119.588	90	**820.876**
Fe5-TNO	Monoclinic	C2/m	**20.682**	**3.836**	**11.981**	**120.639**	90	**816.387**
Difference			**+1.33 %**	**-1.44 %**	**+0.82 %**	**+0.88 %**		**-0.55 %**

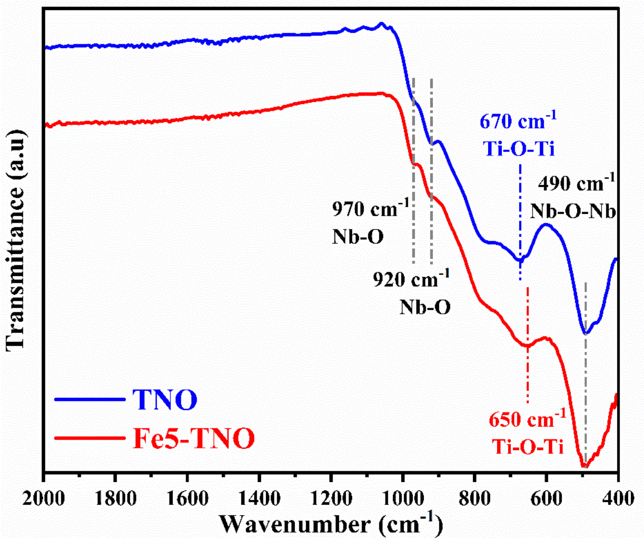

Figure B.3 FT-IR spectra of TNO and Fe5-TNO single-crystal materials

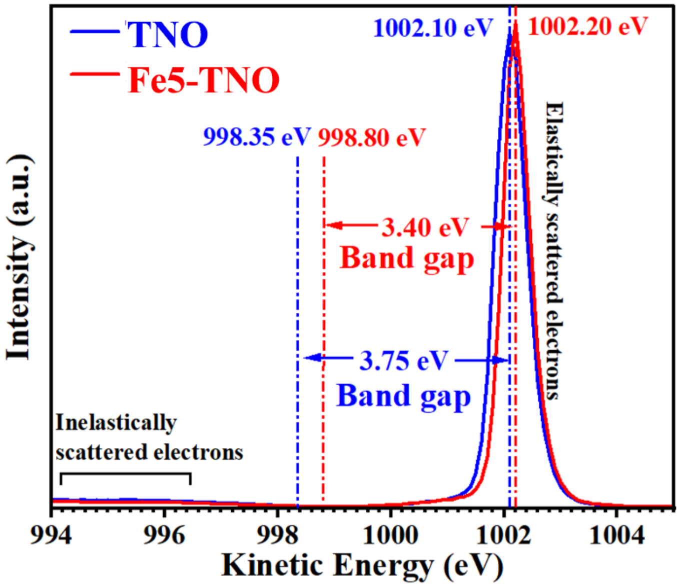

Figure B.4 Original REELS spectra of $TiNb_2O_7$ and Fe5-TNO based on applied kinetics energy and responded count intensity.

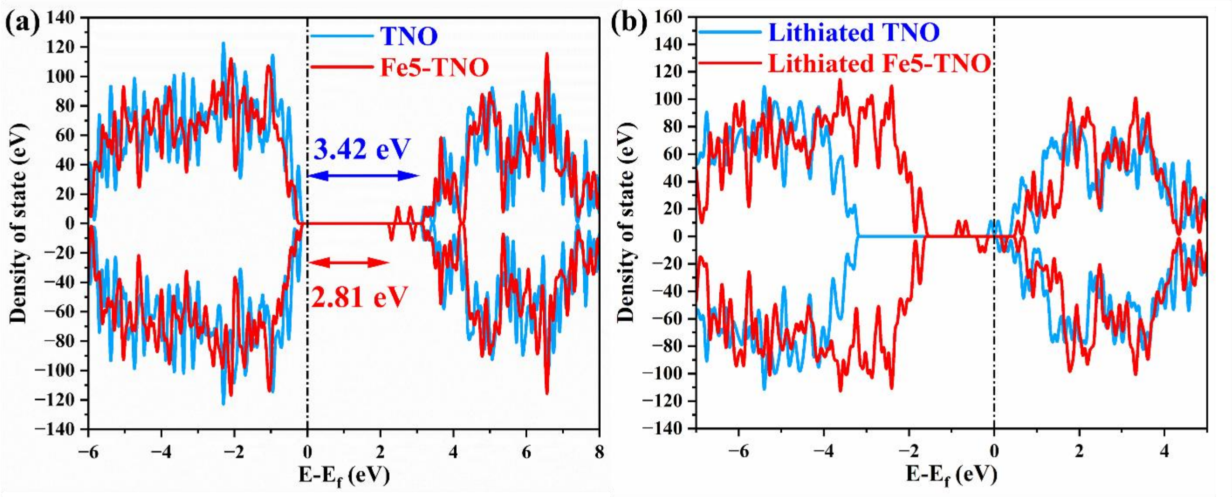

Figure B.5 The calculated DOS of TNO and Fe5-TNO

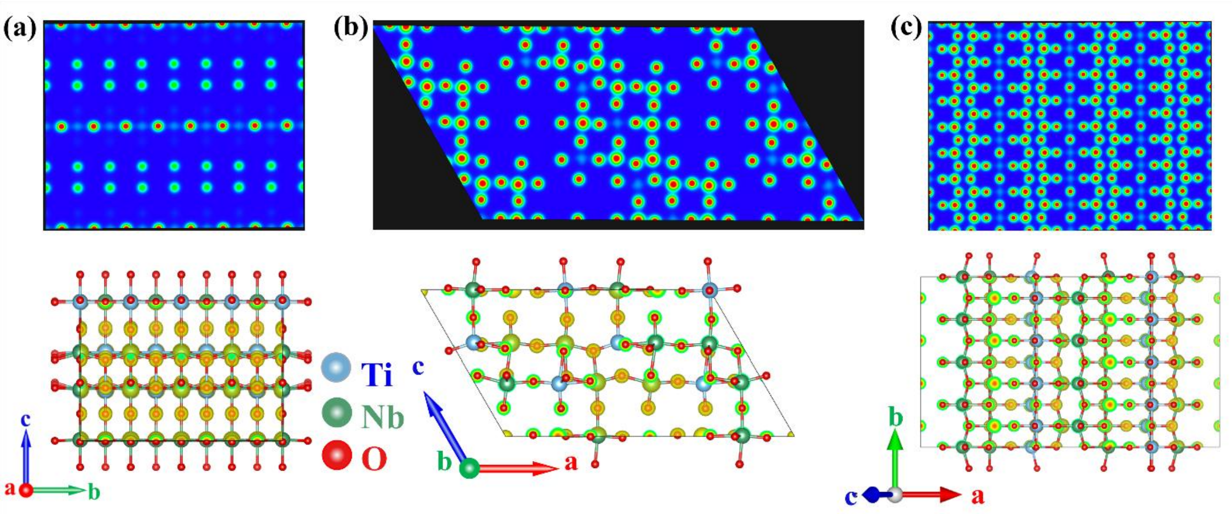

Figure B.6 The simulated charge density of $TiNb_2O_7$ crystal at (a) [100] zone axis, (b) [010] zone axis, (c) [001] zone axis

The formation energies in **Figure 4.3(e)** of the main manuscript are calculated to find the most favorable substitutional site for Fe^{3+} in $TiNb_2O_7$. The formation energy of four structures with different doping sites (Ti1, Ti2, Ti3, Ti4) was estimated after geometry optimization. The formation energy per unit cell, where the supercell contains 18 units of $TiNb_2O_7$, was calculated using following equations:

$$\Delta E_f = (E_{Ti_{18}Nb_{36}O_{126}} - 18E_{Ti} - 36E_{Nb} - 126E_O)/18 \qquad \textbf{(equation B.1)}$$

$$\Delta E_{f,\,(Ti \to Fe)} = (E_{Ti_{17}Nb_{36}O_{126}} - 17E_{Ti} - 36E_{Nb} - 126E_O - E_{Fe})/18 \qquad \textbf{(equation B.2)}$$

Where, $E_{Ti_{18}Nb_{36}O_{126}}$ is the total energy of supercell, and E_{Ti}, E_{Nb}, E_{O}, E_{Fe} are total energies of Ti, Nb, O and Fe atoms respectively. $\Delta E_{f,\,(Ti\rightarrow Fe)}$ corresponds to the formation energy when one Ti is substituted by Fe atom.

Li-ion chemical diffusion coefficient can be determined by **equation B.3**[8,19], using the data collected with the galvanostatic intermittent titration technique (GITT) data. This equation is derived from Fick's law assuming the following conditions: the electrode material is homogeneous, the molar volume change of the host material is not significant, the current is very low with a short duration time, and the cell voltage varies linearly with the square root of the duration time.[20,21]

$$D_{Li^+,\,GITT}=\frac{4}{\pi\tau}\left(\frac{m_B V_M}{M_B A}\right)^2\left(\frac{\Delta E_s}{\Delta E_t}\right)^2 \qquad \left(\tau \ll L^2/D_{Li^+}\right) \qquad \textbf{(equation B.3)}$$

Where τ (s) is the duration time of the constant current pulse (300 s), m_B (g) is the mass of active materials, M_B (g/mol) is the molar mass of active materials (345.68 g/mol), V_M (cm^3/mol) is the molar volume of the active materials, A (cm^2) is the contact area between the electrode and the electrolyte; ΔE_s is the steady-state voltage change stemming from the current pulse during different rest steps, and ΔE_t is the voltage change during the galvanostatic discharge-charge time (from τ_0 to τ_{0+t}) eliminating the iR drop. L represents diffusion length.

Additionally, Li-ion chemical diffusion coefficient can also be determined using CV data at varying sweep rates and Randle-Sevcik equation (**equation B.4**)[22,23]:

$$I_p=2.69\times10^5 n^{3/2} S C D^{1/2}_{Li^+,\ CV} v^{1/2} \qquad \textbf{(equation B.4)}$$

where n is the number of electrons involved in the redox reaction (n=1 in this case), S (cm^2) is the surface area of the electrode, and C (mol/cm^3) is the concentration of Li ions in the $TiNb_2O_7$ anode.

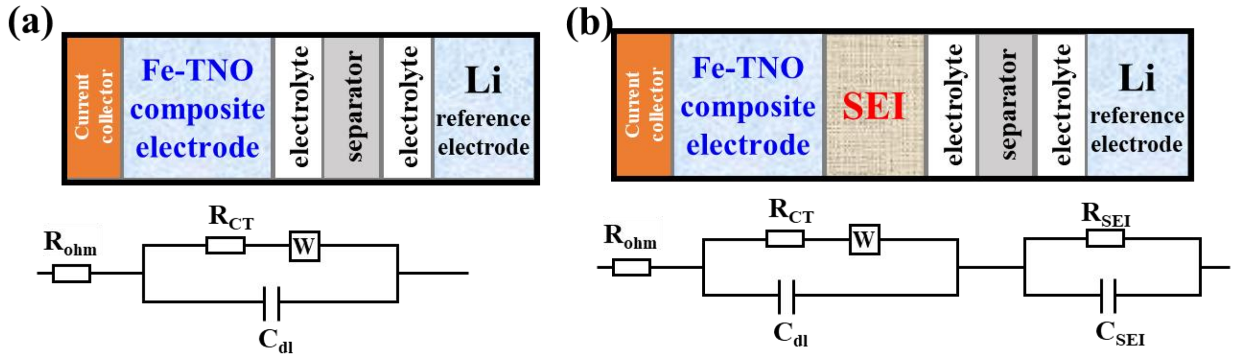

Figure B.7 Model of the LIB half-cell consisted of Fe-TNO composite anode and EIS equivalent circuit model (a) without SEI and (b) with SEI

Figure B.7(a) illustrates the individual LIB half-cell components: Fe-TNO composite electrode represents Fe-doped TNO/Carbon black/PVDF composite active electrode, Li metal serves as reference electrode. In the EIS equivalent circuit model, R_{ohm} is the Ohmic resistance corresponding to electrolyte (dominated) and current collector; and R_{CT} and C_{dl} the faradic charge transfer resistance and relative double-layer capacitance in the bulk of composite electrode, related to the single semicircle at high frequencies, W is the Warburg impedance indicated by a straight line at low frequency, which reflects a combination of the diffusional effects of lithium ion on the interface between the active materials particles and electrolyte[11,12]. As shown in **Figure B.7(b)**, the solid-electrolyte interphase (SEI) is formed between electrode and electrolyte after lithiation/delithiation process. Correspondingly, R_{SEI} and C_{SEI} are resistance and capacitance of the SEI layer, corresponding to the semicircle at high frequency.

Table B.4 Calculated results of EIS data for TNO and Fe5-TNO electrode cycled at 5 C.

	R_{ohmic} (ohm)	R_{CT} (ohm)	R_{SEI} (ohm)	C_{dl} (F)	C_{SEI} (F)	W (ohm·$s^{-1/2}$)
After 1st galvanostatic cycle at 5 C						
TNO	13.2 ±0.2	35 ±2	5 ±1	$3.9\ e^{-6}$	$1.65\ e^{-6}$	562.6
Fe5-TNO	8.2 ±0.2	30 ±2	3 ±1	$4.7\ e^{-6}$	$1.55\ e^{-6}$	322.5
After 1000 galvanostatic cycles at 5 C						
TNO	8.8 ±0.2	40 ±2	5 ±1	$5.2\ e^{-6}$	$1.45\ e^{-6}$	458.9
Fe5-TNO	4.5 ±0.2	12 ±2	3 ±1	$1.0\ e^{-6}$	$1.2\ e^{-4}$	412.4

Note: Simulation method method: Randomize + Simplex, Simulation software: Zfit-Bio-Logic

C. Supplementary Information for Chapter 5: Ultra-fast-charging and Long-cycling Titanium Niobate/Reduced Graphene Oxide Anode via Electrophoretic Interfacial Engineering

C.1. Experimental procedure

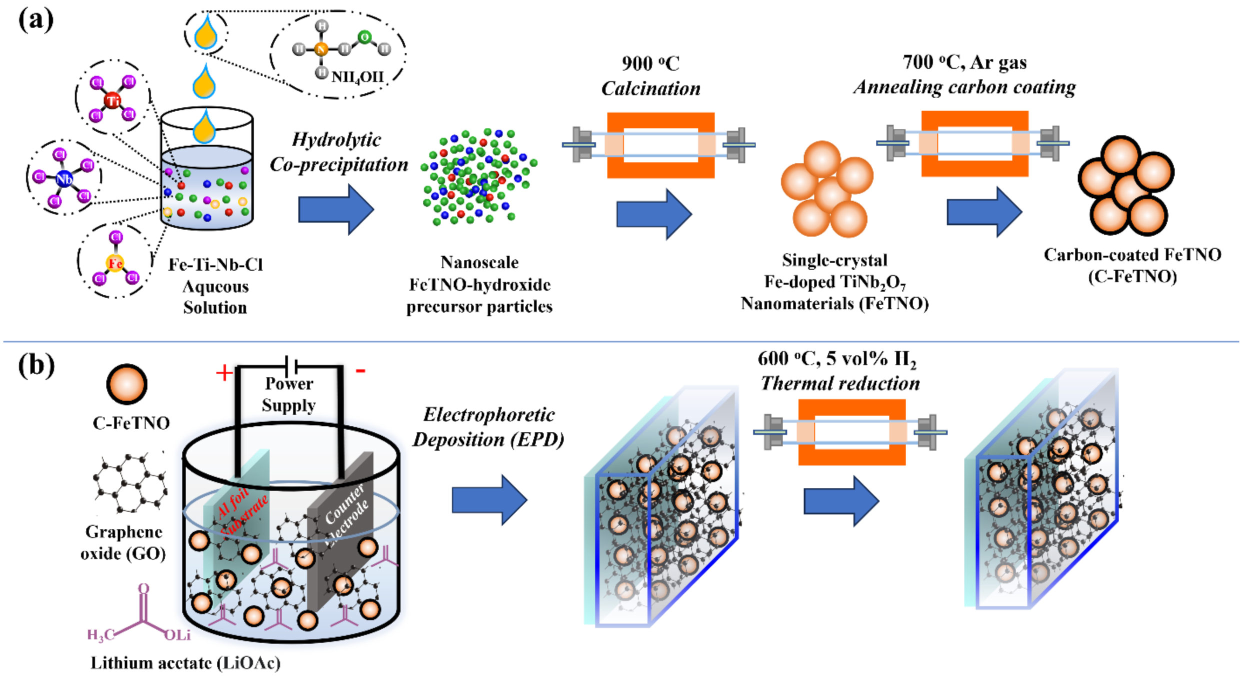

Scheme C.1 (a) Synthesis flowchart of carbon-coated single-crystal Fe-doped $TiNb_2O_7$ nanomaterials (C-FeTNO). (b) Experimental flowchart of advanced electrode engineering via electrophoretic deposition (EPD).

Table C.1 Elemental composition analysis of FeTNO via ICP-OES

Sample name	Molecular formula	Elemental composition %	Fe	Ti	Nb	O
FeTNO	$Fe_{0.05}Ti_{0.95}Nb_2O_{6.975}$	theoretical	0.5	9.5	20	69.75
		experimental	0.52	9.46	20.13	69.85

C.2. EPD experiments

Several solvents, including ethylene glycol, isopropanol, ethanol, water, acetonitrile, and acetone, were tested for their ability to form stable suspensions with FeTNO, C-FeTNO, and GO.

These solvents were widely applied for previous EPD research[24,25], as listed in **Table C.2**. Suspensions with a solid loading of 3 g/L were sonicated for at least 30 minutes prior to settling tests (**Figure C.1**) and measurements via Zetasizer instrument (**Figure 2(b, c)** and **Figure C.2**).

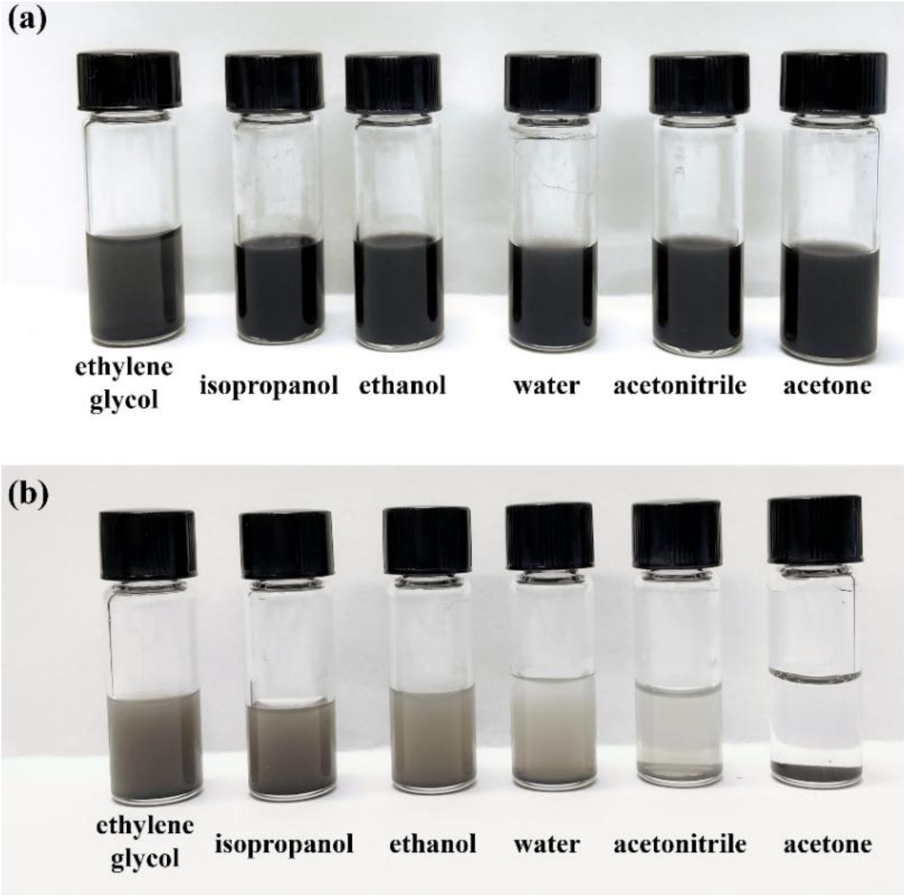

Figure C.1 Settling tests of suspensions containing (a) graphene oxide (GO) and (b) C-FeTNO materials in different solvents. Note: Photos were taken after 48 hours of settling.

It was observed that GO formed stable suspensions in all solvents tested (**Figure C.1(a)**). On the other hand, FeTNO suspensions were not stable resulting in particle settling. By contrast, stable suspensions were possible with the carbon-coated FeTNO (C-FeTNO) material. The stabilities of C-FeTNO suspensions proved to be dependent on the type of solvent, as illustrated in **Figure C.1(b)**. Significant sedimentation of C-FeTNO was observed in acetone, acetonitrile, and DI water. Conversely, C-FeTNO particles settled at much slower rate in isopropanol, ethylene glycol, and ethanol. Overall, the stability of these C-FeTNO suspensions is correlated with the viscosity of the solvents, as detailed in **Table C.2**.

Table C.2 Physical properties of some solvents used in EPD

Solvents	**Viscosity** (cP = mPa·s =10^{-3} N·s/m^2)	**Relative dielectric constant**	**Ref.**
ethylene glycol	16.265	37.7	[24-26]
isopropanol	2.044	19.92	[24,25,27]
ethanol	1.089	24.55	[24,25,27]
water	0.890	78.2	[25,26]
acetonitrile	0.369	36.64	[28,29]
acetone	0.309	20.7	[24,25]

Based on the stability observed during the settling test, ethylene glycol, isopropanol, and ethanol have been selected as candidates for further analysis. Suspensions of C-FeTNO in these solvents, each at 3 g/L concentration, are prepared to determine the zeta potential, suspension conductivity, electrophoretic mobility (**Table C.3)** and to conduct electrophoretic deposition (EPD) experiments (**Figure C.3**).

Table C.3 Properties of C-FeTNO suspensions with different solvents

Materials	**Solvent**	**Conc. (g/L)**	**Zeta potential (mV)**	**Suspension conductivity (µS/cm)**	**Electrophoretic Mobility (µm·cm/Vs)**
C-FeTNO	**isopropanol**	3	-43	0.339	-0.215
C-FeTNO	**ethanol**	3	-35	1.26	-0.480
C-FeTNO	**ethylene glycol**	3	-6	0.546	-0.029

Although ethylene glycol produced the most stable C-FeTNO suspension with the least sedimentation, it demonstrates a low electrophoretic mobility of -0.029 µm·cm/V·s and a low absolute value of zeta potential (-6 mV), as illustrated in **Table C.3**. Consequently, neither C-FeTNO or GO would deposit with strong adhesion onto the Al foil working electrode during the EPD process, potentially due to low electrophoretic mobilities of charged particles in viscous media. Conversely, both C-FeTNO and GO in isopropanol suspensions and ethanol suspensions can be deposited on the Al substrate. These findings are consistent with high electrophoretic mobilities of C-FeTNO isopropanol suspension (-0.215 µm·cm/Vs) and C-FeTNO ethanol suspension (-0.480 µm·cm/Vs). Notably, isopropanol suspension assembles a more uniform EPD film than ethanol suspension, which can be contributed the higher quality of suspension as indicated by the higher absolute value of zeta potential (-43 mV *vs.* -35 mV) (**Figure C.2**). Therefore, the isopropanol was selected as the optimal solvent.

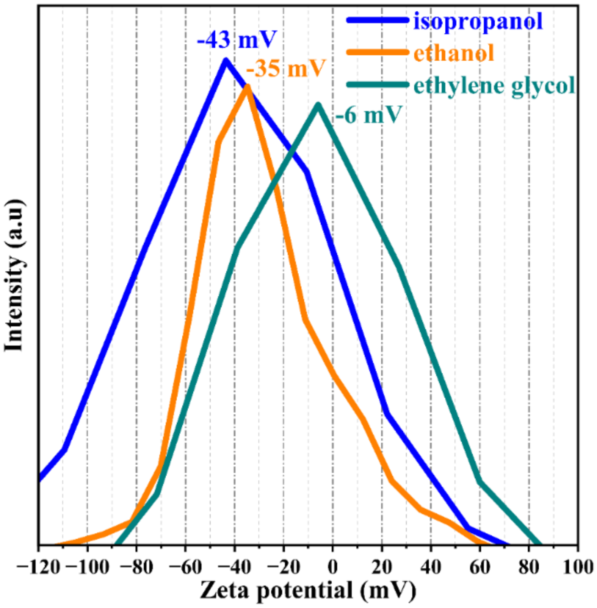

Figure C.2 Zeta potential of C-FeTNO suspensions (3 g/L) in different solvents

Furthermore, isopropanol suspensions containing C-FeTNO materials (3 g/L), GO materials (3 g/L), and a mixture of C-FeTNO (2.76 g/L) and GO (0.24 g/L) materials were prepared for depositing the EPD films. As illustrated in **Figure C.3**, C-FeTNO EPD film (**Figure C.3(a)**) exhibits a low deposition rate and low uniformity, whereas GO EPD film (**Figure C.3(b)**) shows a high deposition loading and uniform deposition. To improve the deposition rate of C-FeTNO, GO was added to create a suspension with a mixture of C-FeTNO (2.76 g/L) and GO (0.24 g/L). After adding GO, the absolute value of Zeta potential, conductivity, and electrophoretic mobility of suspension increased compared with C-FeTNO as indicated in **Table C.4**. Finally, the C-FeTNO/GO film produced via EPD shows a higher deposition loading (**Figure C.3(c)**). However, the film uniformity needs to be further improved.

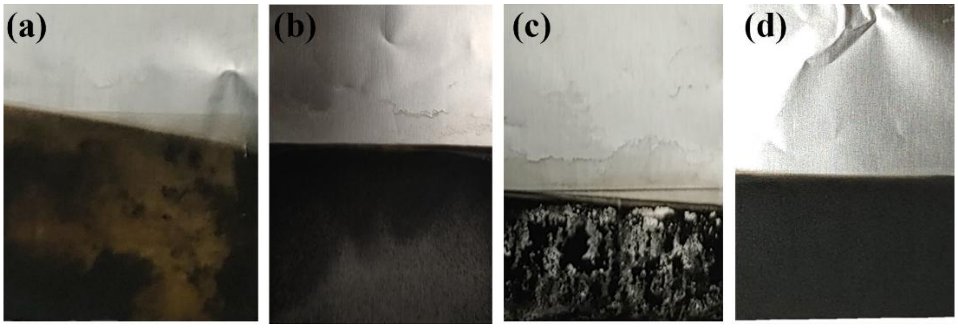

Figure C.3 EPD film substrates prepared from (a) C-FeTNO suspension (3 g/L), (b) GO suspension (3 g/L), (c) C-FeTNO (2.76 g/L)/GO (0.24 g/L) suspension, and (d) C-FeTNO (2.76 g/L)/GO (0.24 g/L) suspension with 66 ppm LiOAc.

Table C.4 Properties of isopropanol suspensions with different materials

Materials	**Solvent**	**Conc. (g/L)**	**Zeta potential (mV)**	**Suspension conductivity (µS/cm)**	**Electrophoretic mobility (µm·cm/Vs)**
C-FeTNO	isopropanol	2.76	-37	0.339	-0.215
GO	isopropanol	0.24	-60	0.351	-0.262
C-FeTNO +GO	isopropanol	3	-42	0.447	-0.225

To improve the quality of deposition films, various concentrations (66 ppm and 660 ppm) of LiOAc additives are applied in C-FeTNO (2.76 g/L)/GO (0.24 g/L) isopropanol suspension. The addition of LiOAc charging agent directly improved the suspension conductivity, absolute value of zeta potential, and electrophoretic mobilities, with these values increasing as the concentration increased (**Table C.5**). As a result, the stabilized C-FeTNO/GO suspension with 66 ppm LiOAc yields a more uniform deposition film (**Figure C.3(d)**). Concentration of 660 ppm was not selected due to the potential risk of adding more impurity in EPD film. More in-depth analysis about the effect of charging agent are discussed in the **Section 3.2.1 (3)** of the main manuscript.

Table C.5 Properties of C-FeTNO/GO-isopropanol suspensions with different concentrations of LiOAc additives

Additive	**Solvent**	**Conc. (g/L)**	**Zeta potential (mV)**	**Suspension conductivity (µS/cm)**	**Electrophoretic mobility (µm·cm/Vs)**
0 ppm LiOAc	isopropanol	3	-42	0.447	-0.225
66 ppm LiOAc	isopropanol	3	-70	3.06	-0.354
660 ppm LiOAc	isopropanol	3	-93	5.65	-0.477

C.3. Li-ion diffusion coefficient determined by GITT

Li-ion diffusion coefficient can be determined by **equation (C.1)** by collecting the GITT data at varying sweep rates.[8,19]

$$D_{Li^+,\,GITT}=\frac{4}{\pi\tau}\left(\frac{m_B V_M}{M_B A}\right)^2\left(\frac{\Delta E_s}{\Delta E_t}\right)^2 \qquad \left(\tau \ll L^2/D_{Li^+}\right) \qquad \textbf{(equation C.1)}$$

Where τ (s) is the duration time of the constant current pulse (300 s), m_B (g) is the mass of active material, M_B (g/mol) is the molar mass of active material, V_M (cm^3/mol) is the molar volume of the active material, A (cm^2) is the contact area between the electrode and the electrolyte; ΔE_s is the steady-state voltage change stemming from the current pulse during different rest steps, and ΔE_t is the voltage change during the galvanostatic discharge-charge time (from τ_0 to τ_{0+t}) eliminating the IR drop.

C.4. EIS Impedance Testing

Figure C.4 illustrates the individual LIB half-cell components: Fe-TNO composite electrode and Li metal as reference electrode. In the EIS equivalent circuit model, R_{ohm} is the Ohmic resistance corresponding to electrolyte (dominated) and current collector; and R_{CT} and C_{dl} the faradaic charge transfer resistance and relative double-layer capacitance in the bulk of composite electrode, related to the single semicircle at high frequencies, W is the Warburg impedance indicated by a straight line at low frequency, which reflects a combination of the diffusional effects of lithium ion on the interface between the active materials particles and electrolyte.[11,12]

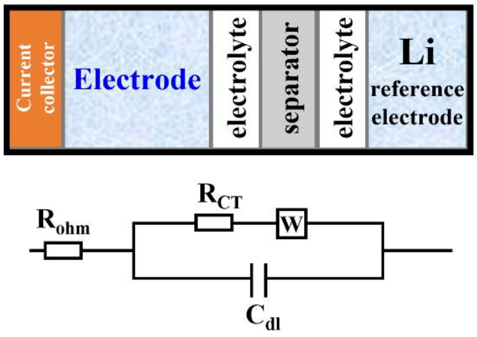

Figure C.4 Model of the LIB half-cell and EIS equivalent circuit model.

Reference:

[1] U. Holzwarth, N. Gibson, The Scherrer equation versus the 'Debye-Scherrer equation', Nat. Nanotechnol. 6 (2011) 534-534. https://doi.org/10.1038/nnano.2011.145.

[2] Y. Li, G.P. Demopoulos, Precipitation of nanosized titanium dioxide from aqueous titanium(IV) chloride solutions by neutralization with MgO, Hydrometallurgy 90 (2008) 26-33. https://doi.org/https://doi.org/10.1016/j.hydromet.2007.09.008.

[3] N. Takami, K. Ise, Y. Harada, T. Iwasaki, T. Kishi, K. Hoshina, High-energy, fast-charging, long-life lithium-ion batteries using $TiNb_2O_7$ anodes for automotive applications, J. Power Sources 396 (2018) 429-436. https://doi.org/10.1016/j.jpowsour.2018.06.059.

[4] H. Lyu, J. Li, T. Wang, B.P. Thapaliya, S. Men, C.J. Jafta, R. Tao, X.-G. Sun, S. Dai, Carbon coated porous titanium niobium oxides as anode materials of lithium ion batteries for extreme fast charge applications, ACS Appl. Energy Mater. 3 (2020) 5657-5665.

[5] M. Yu, Z.F. Cai, Q. Li, S. Wang, Y.Z. Ma, G.S. Song, W.D. Yang, C. Wen, Enhanced energy storage performance of Zr-doped $TiNb_2O_7$ nanospheres prepared by the hydrolytic method, ACS Sustain. Chem. Eng. 11 (2023) 5147-5154. https://doi.org/10.1021/acssuschemeng.2c07144.

[6] P. Cui, P. Zhang, X. Chen, X. Chen, T. Wan, Y. Zhou, M. Su, Y. Liu, H. Xu, D. Chu, Oxygen defect and Cl^--doped modulated $TiNb_2O_7$ compound with high rate performance in lithium-ion batteries, ACS Appl. Mater. Interfaces 15 (2023) 43745-43755. https://doi.org/10.1021/acsami.3c08524.

[7] H.W. Bian, J.J. Gu, Z.C. Song, H.X. Gong, Z.X. Zhang, W.T. Mao, K.Y. Bao, An effective strategy to achieve high-power electrode by tin doping: $Sn_xTiNb_2O_7$ as a promising anode material with a large capacity and high-rate performance for lithium-ion batteries, Journal of Materials Science-Materials In Electronics 34 (2023) 1826. https://doi.org/10.1007/s10854-023-11183-2.

[8] H. Park, H.B. Wu, T. Song, X.W. Lou, U. Paik, Porosity-controlled $TiNb_2O_7$ microspheres with partial nitridation as a practical negative electrode for high-power lithium-ion batteries, Adv. Energy Mater. 5 (2015) 1401945. https://doi.org/10.1002/aenm.201401945.

[9] G.Q. Wang, Z.S. Wen, L.L. Du, Y.E. Yang, S. Li, J.C. Sun, S.J. Ji, Hierarchical Ti-Nb oxide microspheres with synergic multiphase structure as ultra-long-life anode materials for lithium-ion batteries, J. Power Sources 367 (2017) 106-115. https://doi.org/10.1016/j.jpowsour.2017.09.061.

[10] K.K. Gupta, K.-C. Li, S. Balaji, P.S. Kumar, C.-H. Lu, Microwave-assisted synthesis and electrochemical characterization of $TiNb_2O_7$ microspheres as anode materials for lithium-ion batteries, Journal of the American Ceramic Society 106 (2023) 4192-4201. https://doi.org/https://doi.org/10.1111/jace.19000.

[11] U. Westerhoff, K. Kurbach, F. Lienesch, M. Kurrat, Analysis of lithium-ion battery models based on electrochemical impedance spectroscopy, Energy Technol. 4 (2016) 1620-1630. https://doi.org/https://doi.org/10.1002/ente.201600154.

[12] S.S. Zhang, K. Xu, T.R. Jow, Electrochemical impedance study on the low temperature of Li-ion batteries, Electrochim. Acta 49 (2004) 1057-1061. https://doi.org/https://doi.org/10.1016/j.electacta.2003.10.016.

[13] A.C. Lazanas, M.I. Prodromidis, Electrochemical impedance spectroscopy—A tutorial, ACS Measurement Science Au 3 (2023) 162-193. https://doi.org/10.1021/acsmeasuresciau.2c00070.

[14] Y. Zhang, C. Kang, W. Zhao, B. Sun, X. Xiao, H. Huo, Y. Ma, P. Zuo, S. Lou, G. Yin, Crystallographic engineering to reduce diffusion barrier for enhanced intercalation pseudocapacitance of $TiNb_2O_7$ in fast-charging batteries, Energy Storage Mater. 47 (2022) 178-186. https://doi.org/https://doi.org/10.1016/j.ensm.2022.01.061.

[15] R. Qian, M. Yao, F. Xiao, T. Yao, H. Lu, Y. Liu, J.-W. Shi, Y. Cheng, H. Wang, Polyvinylpyrrolidone regulated synthesis of mesoporous titanium niobium oxide as high-performance anode for lithium-ion batteries, J. Colloid Interface Sci. 608 (2022) 1782-1791. https://doi.org/https://doi.org/10.1016/j.jcis.2021.10.073.

[16] R. Qian, C. Yang, D. Ma, K. Li, T. Feng, J. Feng, J.H. Pan, Robust lithium storage of block copolymer-templated mesoporous $TiNb_2O_7$ and $TiNb_2O_7$@C anodes evaluated in half-cell and full-battery configurations, Electrochim. Acta 379 (2021) 138179. https://doi.org/https://doi.org/10.1016/j.electacta.2021.138179.

[17] R. Qian, H. Lu, T. Yao, F. Xiao, J. Shi, Y. Cheng, H. Wang, Hollow $TiNb_2O_7$ nanospheres with a carbon coating as high-efficiency anode materials for lithium-ion batteries, ACS Sustain. Chem. Eng. 10 (2022) 61-70. https://doi.org/10.1021/acssuschemeng.1c04712.

[18] C. Choi, D.S. Ashby, D.M. Butts, R.H. DeBlock, Q. Wei, J. Lau, B. Dunn, Achieving high energy density and high power density with pseudocapacitive materials, Nat. Rev. Mater. 5 (2020) 5-19. https://doi.org/10.1038/s41578-019-0142-z.

[19] Y. Zeng, H.-C. Chiu, B. Ouyang, K. Zaghib, G.P. Demopoulos, Defect engineering of iron-rich orthosilicate cathode materials with enhanced lithium-ion intercalation capacity and kinetics, ACS Appl. Energy Mater. 3 (2020) 675-686. https://doi.org/10.1021/acsaem.9b01869.

[20] J. Kim, S. Park, S. Hwang, W.-S. Yoon, Principles and Applications of Galvanostatic Intermittent Titration Technique for Lithium-ion Batteries, Journal of Electrochemical Science and Technology 13 (2022) 19-31. https://doi.org/10.33961/jecst.2021.00836.

[21] T. Schied, A. Nickol, C. Heubner, M. Schneider, A. Michaelis, M. Bobeth, G. Cuniberti, Determining the diffusion coefficient of lithium insertion cathodes from GITT measurements: Theoretical analysis for low temperatures, ChemPhysChem 22 (2021) 885-893. https://doi.org/https://doi.org/10.1002/cphc.202001025.

[22] J.R. Dahn, J. Jiang, L.M. Moshurchak, M.D. Fleischauer, C. Buhrmester, L.J. Krause, High-rate overcharge protection of $LiFePO_4$-based Li-ion cells using the redox shuttle additive 2,5-Ditertbutyl-1,4-dimethoxybenzene, J. Electrochem. Soc. 152 (2005) A1283. https://doi.org/10.1149/1.1906025.

[23] K. Tang, X. Yu, J. Sun, H. Li, X. Huang, Kinetic analysis on $LiFePO_4$ thin films by CV, GITT, and EIS, Electrochim. Acta 56 (2011) 4869-4875. https://doi.org/https://doi.org/10.1016/j.electacta.2011.02.119.

[24] H. Negishi, H. Yanagishita, H. Yokokawa, Electrophoretic deposition of solid oxide fuel cell material powders, Proceedings of the electrochemical society on electrophoretic deposition: fundamentals and applications 21 (2002)

[25] P. Amrollahi, J.S. Krasinski, R. Vaidyanathan, L. Tayebi, D. Vashaee, Electrophoretic deposition (EPD): fundamentals and applications from nano- to microscale structures, in: M. Aliofkhazraei, A.S.H. Makhlouf (Eds.), Handbook of Nanoelectrochemistry: Electrochemical Synthesis Methods, Properties, and Characterization Techniques, Springer International Publishing, Cham, 2016, pp. 561-591.

[26] W. Hayduk, V.K. Malik, Density, viscosity, and carbon dioxide solubility and diffusivity in aqueous ethylene glycol solutions, Journal of Chemical & Engineering Data 16 (1971) 143-146. https://doi.org/10.1021/je60049a005.

[27] Z. Mousavi, M. Pirdashti, A.A. Rostami, E.-N. Dragoi, Thermophysical properties analysis of poly (ethylene glycol) 600 + methanol, ethanol, 1-propanol, and 2-propanol binary liquid mixtures, International Journal of Thermophysics 41 (2020) 19. https://doi.org/10.1007/s10765-019-2600-7.

[28] M. Inagaki, H. Konno, O. Tanaike, Carbon materials for electrochemical capacitors, J. Power Sources 195 (2010) 7880-7903. https://doi.org/https://doi.org/10.1016/j.jpowsour.2010.06.036.

[29] R.J. Sengwa, P. Dhatarwal, S. Choudhary, Static permittivities, viscosities, refractive indices and electrical conductivities of the binary mixtures of acetonitrile with poly(ethylene glycol)-200 at temperatures 288.15–318.15 K, Journal of Molecular Liquids 271 (2018) 128-135. https://doi.org/https://doi.org/10.1016/j.molliq.2018.08.137.

D. Equipment and Methods

D.1 Electrochemical Characterization

Conventional electrode fabrication for lithium-ion batteries

Coin cells were assembled for electrochemical testing. TNO active material (80 wt.%), acetylene black (10 wt.%), and poly(vinylidene difluoride) (PVDF) binder (10 wt.%) were manually milled with N-Methyl-2-pyrrolidone (NMP) solvent in a mortar and blade-coated on copper foil (99.99% Cu, 25 μm thick, MTI Corporation), followed by drying in an 80 °C vacuum oven overnight, punching, and calendering. The mass loading of TNO active material was maintained at 3 ± 0.5 mg/cm^2.

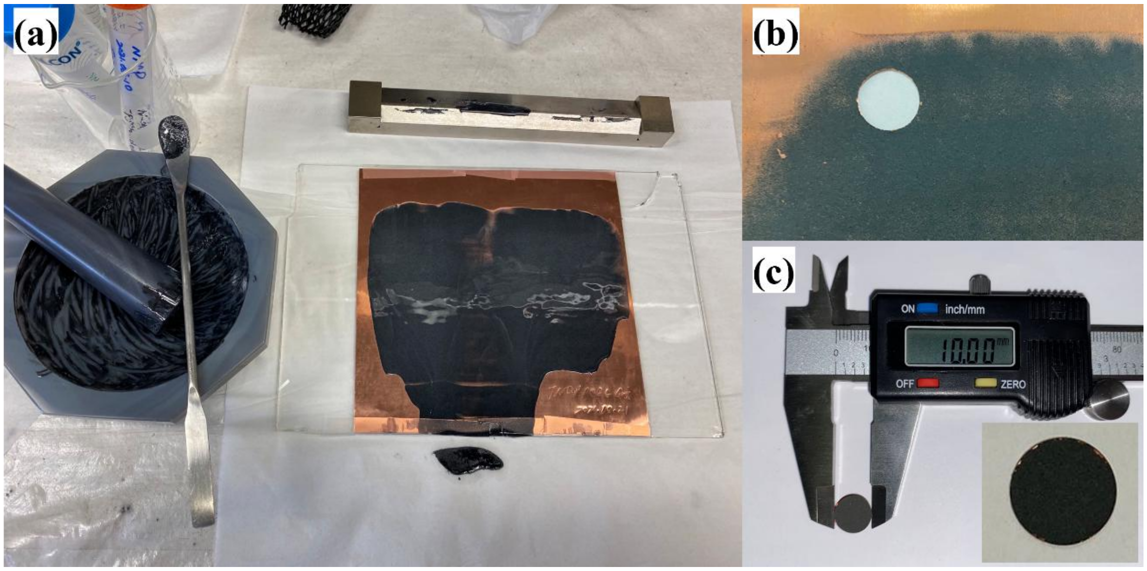

Figure D.1 Conventional electrode fabrication method via slurry cast blade coating.

Advanced electrode fabrication method via electrophoretic deposition

An EPD electrolytic cell (**Figure D.2(b)**). with a 15 um Al foil working electrode and a stainless steel counter electrode was set up to have electrode spacing of 7.5 mm and a deposition area of 4 to 6 cm^2. The anodic deposition was operated under different constant voltages (50 V, 100 V, and 200 V) which were controlled by a SourceMeter (Keithley 2611A) instrument (**Figure D.2(a)**).

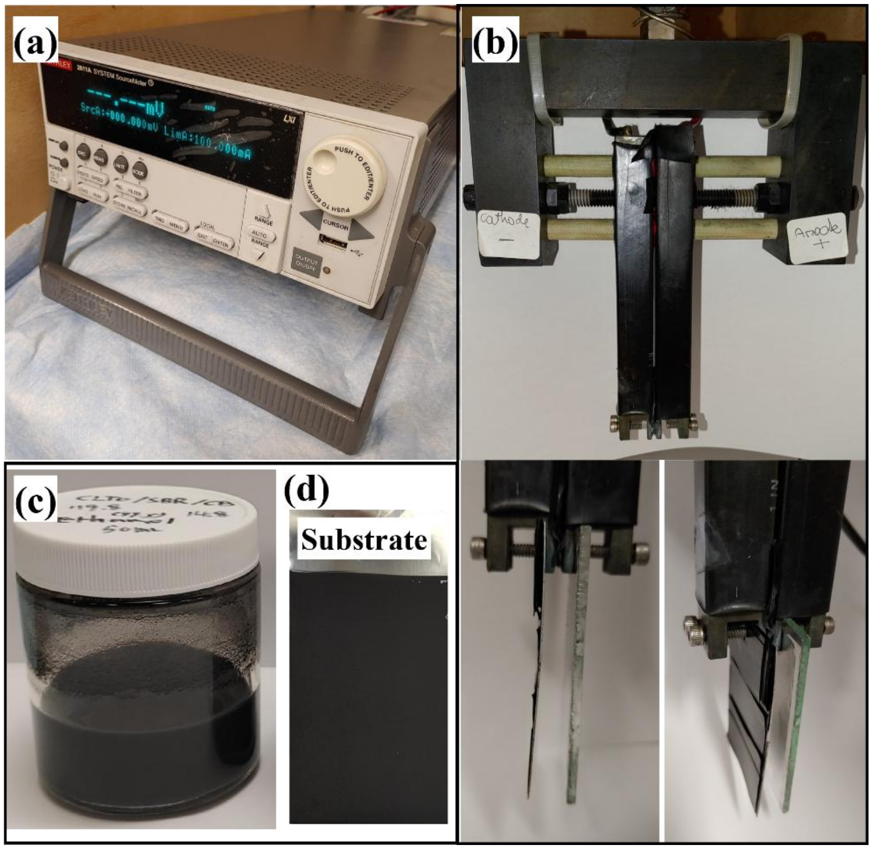

Figure D.2 (a) Keithley 2611A SourceMeter used for voltage and current control during EPD process. (b) Electrode rack setup with two electrodes: a working electrode for deposition (thin copper/aluminum foil substrate attached to glass) and a counter electrode (thick aluminum electrode). (c) EPD suspension container, (d) Substrate deposited with TNO/GO composite material.

Battery assembly

In an argon-filled MBraun glovebox (**Figure D.3(a)**), the coin cells (2032) or Swagelok-type batteries (**Figure D.3(b)**) were assembled with a TNO working electrode, lithium metal reference electrode, polypropylene-polyethylene-polypropylene (PP/PE/PP) film separator (Celgard 2300), and 200 µL 1M $LiPF_6$ electrolyte (in EC:DMC:DEC at 2:2:1).

Figure D.3 The Argon-filled glovebox utilized for battery assembling and material preparation.

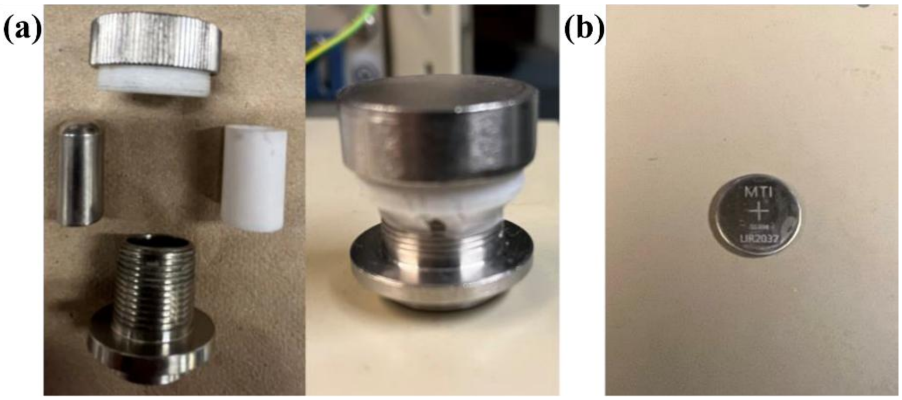

Figure D.4 (a) The Swagelok-type battery and (b) the coin-type battery utilized for lithium ion batteries assembling.

D.2 Electrochemical Performance Testing

Galvanostatic charging/discharging cycling testing was performed using a standard 8 channel battery analyzer (BST8 WA, MTI Corp) (**Figure D.5(a)**) at varying rate (1 C=387.6 mA/g). Galvanostatic intermittent titration technique (GITT) experiments were performed using an Arbin standard battery cycler (BT2043-10V-100mA-40, Arbin) (**Figure D.5(b)**).

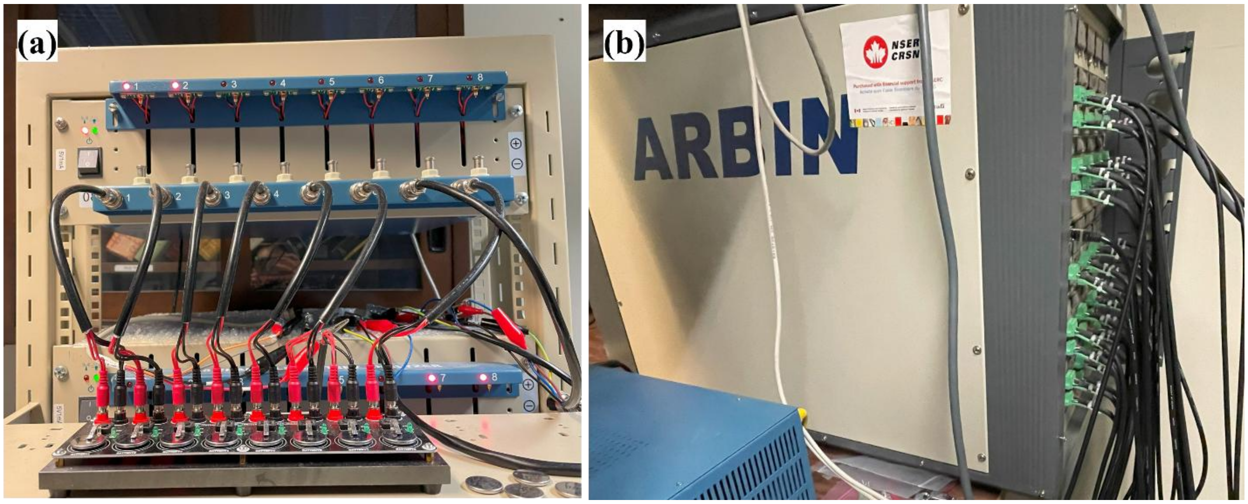

Figure D.5 (a) The MTI battery tester (BST8-WA, MTI corporation) employed for battery galvanostatic cycling tests and (b) Arbin standard battery cycler for galvanostatic intermittent titration technique (GITT).

Bio-Logic VSP potentiostat/galvanostat system (**Figure D.6**) operated via EC-Lab software is used to perform cyclic voltammetry (CV) and electrochemical impedance spectroscopy (EIS) testing. The voltammograms were collected at sweep rates of 0.056 mV/s, 0.111 mV/s, 0.278 mV/s, 0.556 mV/s, 1.110 mV/s, and 2.780 mV/s, respectively, operating between 3.0 V and 1.0 V (vs. Li/Li$^+$). Electrochemical Impedance Spectroscopy (EIS) measurements were carried out under potentiostatic mode at 3 V operated in the frequency range of 1 MHz to 0.01 Hz under room temperature. The impedance values are calculated by fitting the Nyquist plot with the equivalent electric circuit by the Z-fit method using EC-Lab software.

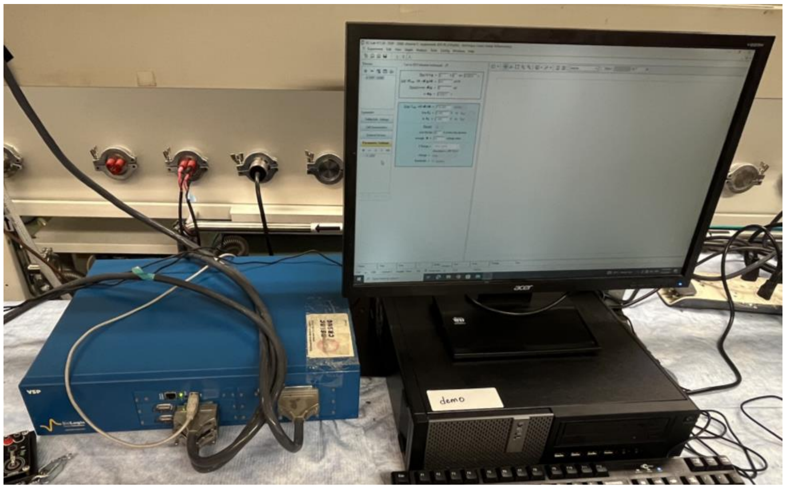

Figure D.6 The electrochemical workstation (Bio-Logic) used for EIS and CV measurements.

D.3 Material Characterization

X-ray diffraction (XRD)

Throughout this thesis, the crystal structures of materials were characterized by X-ray diffraction (XRD) using a Bruker D8 Discovery X-ray diffractometer (VANTEC Detector Cu-Source) (**Figure D.7**). Scan parameters ranged from 10° to 80° in 2θ with a scan rate of 1 °/min (70 minutes per sample) for normal XRD testing, or a scan rate of 0.05 °/min (about 24 hours per sample) for refinement analysis. LeBail Refinement was performed with TOPAS (Bruker) V5 software.

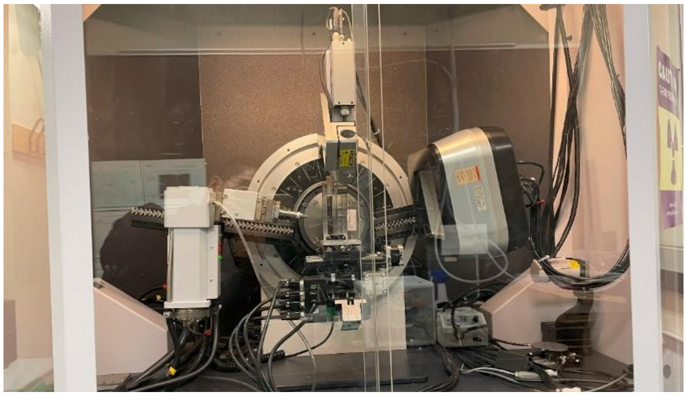

Figure D.7 Bruker D8 Discovery X-ray diffractometer (VANTEC Detector Cu-Source) utilized for XRD testing.

Scanning electron microscopy (SEM)

Throughout this thesis, crystal morphology structures and elemental distribution were recorded by scanning electron microscopy (SEM) using a Hitachi SU-8000 Cold Field-Emission Microscopy (**Figure D.8**) equipped with in-lens upper secondary electron detector and energy-dispersive X-ray spectroscopy (EDS) detector (80 mm^2 X-Max SDD EDS detector, Oxford Instrument). The Hitachi SU-8000 cold field FE-SEM has a resolution of 0.5 nm at 30 keV and 2 nm at 0.2 keV. The maximum probe current is 30 nA and this allows to perform quantitative x-ray microanalysis at low voltage and in the STEM mode. SEM images are acquired under using 8mm of working distance with 30 kV acceleration voltage and emission current of 40 μA.

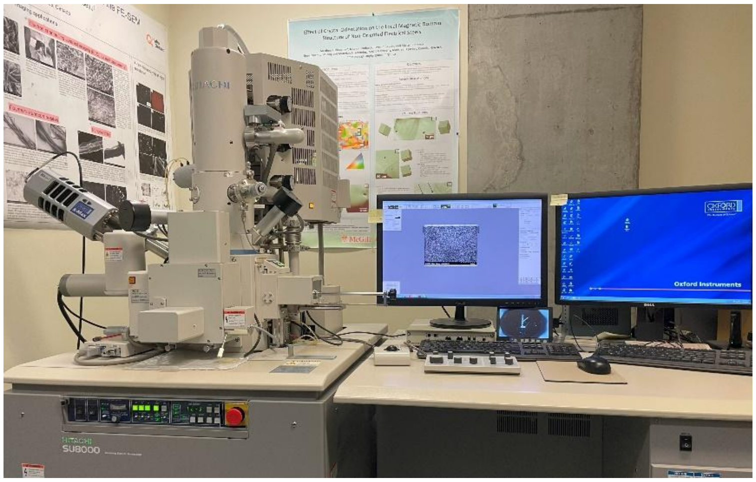

Figure D.8 The Hitachi SU-8000 microscope for obtaining SEM and EDX images.

In Chapter 5, the morphological characteristics of materials and cross-section of electrodes have been determined by the Hitachi SU-9000 cold field-emission SEM/STEM (**Figure D.9**). This instrument has a high resolution of 0.16 nm at 30 keV in BF mode and 0.4 nm in SE mode and is equipped with Oxford Instrument windowless Extreme 100 mm^2 SDD and energy dispersive spectroscopy (EDS). SEM images are acquired under using 0.2 mm of working distance with 1.2 kV acceleration voltage and emission current of 20 μA.

Figure D.9 The Hitachi SU-9000 cold field-emission SEM/STEM.

Transmission electron microscopy (TEM)

Throughout this thesis, transmission electron microscopy (TEM), high-resolution transmission electron microscopy (HRTEM), scanning transmission electron microscopy (STEM), and selected area electron diffraction (SAED) were carried out on Thermo Scientific Talos F200X G2 TEM/STEM instrument operated at 200 kV (**Figure D.10**). The STEM high-angle annular dark-field (HAADF) images were acquired at a beam convergence angle of 10.5 mrad and the detector collection angle of 58-200 mrad. The energy-dispersive X-ray spectroscopy (EDS) mapping was applied to reveal the elemental composition of Ti (K*a* 4.5 keV), Nb (L*a* 2.17 keV), and O (K*a* 0.52 keV).

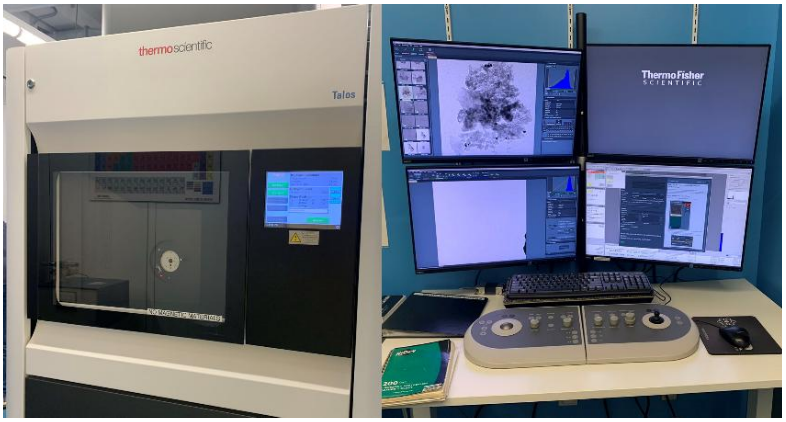

Figure D.10 Thermo Scientific Talos F200X G2 TEM/STEM used for morphological characterization.

Inductively coupled plasma optical emission spectrometry (ICP-OES)

Inductively coupled plasma optical emission spectrometry (ICP-OES) was applied to determine the Ti concentration and Nb concentration in precursor aqueous chloride solutions, and the composition of TNO-Precursor, and TNO crystal particles after digestion. All solid samples were digested in an acid solution (1 wt.% HF and 1 wt.% HCl) before being analyzed on a Thermo Scientific iCAP 6000 Series ICP spectrometer (**Figure D.11**). Ti standard solution (1.002 g/L, NIST Traceable) and Nb standard solution (1.003 g/L, NIST Traceable) were used to prepare reference solutions with concentrations of 50 ppm, 5 ppm, 0.5 ppm.

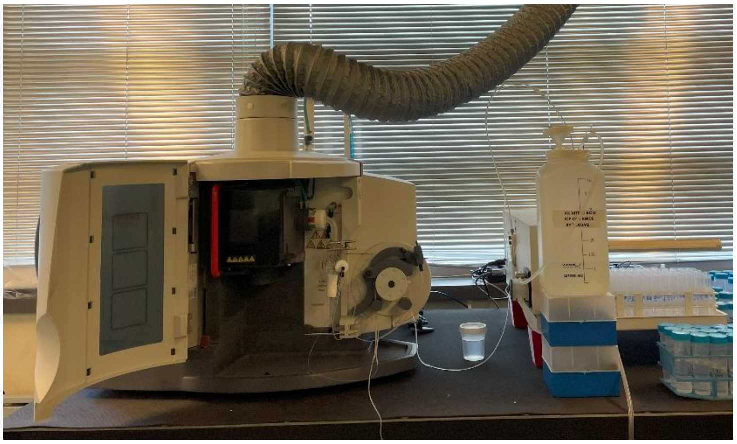

Figure D.11 Thermo Scientific iCAP 6000 Series ICP spectrometer used for ICP-OES testing.

X-ray photoelectron spectroscopy (XPS)

Thermo Scientific Nexsa G2 surface analysis system (**Figure D.12**) is employed for X-ray photoelectron spectroscopy (XPS). XPS is utilized to determine the elemental composition (C, Ti, Nb, Fe, O) and oxidation states. The survey spectrum and high-resolution spectra at the edges of Ti 2p, Nb 3d, and O 1s were identified. XPS data were analyzed with Thermo Advantage software and normalized/calibrated referenced to adventitious C1s peak at 284.80 eV.

Figure D.12 Thermo Scientific Nexsa G2 surface analysis system for XPS and REELS testing.

Raman microscopy

Raman microscopy was performed using a Thermo Scientific DXR2 Raman microscope, equipped with DXR 532 nm wavelength laser. (**Figure D.13**).

Figure D.13 Thermo Scientific DXR2 Raman microscope.

Fourier transform infrared (FTIR) spectroscopy

Attenuated total reflection Fourier transform infrared (ATR-FTIR) spectroscopy was carried out using FTIR infrared spectrometer Vertex 70 from Bruker (**Figure D.14**).

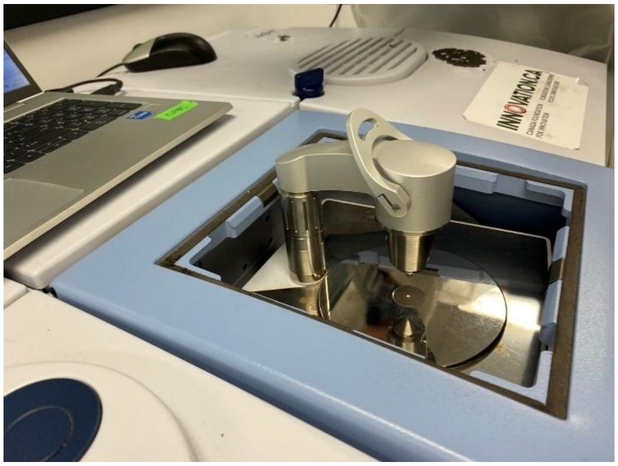

Figure D.14 FTIR infrared spectrometer Vertex 70 from Bruker.

Brunauer-Emmett-Teller (BET) and Barrett-Joyner-Halenda (BJH)

In Chapter 3, the N_2 adsorption/desorption analysis was performed with a Micromeritics TriStar 3000 apparatus (**Figure D.15**) to determine the Brunauer-Emmett-Teller (BET) specific surface area and Barrett-Joyner-Halenda (BJH) pore distribution.

Figure D.15 The Brunauer-Emmett-Teller (BET) Micromeritics TriStar 3000 instrument.

Thermogravimetric analysis (TGA)

In Chapter 3 and Chapter 5, thermogravimetric analysis (TGA) and differential scanning calorimetry (DSC) were conducted by using Discovery 5500 from TA instruments (**Figure D.16**).

In Chapter 3, the crystallization mechanism of precursors has been investigated by using both TGA and DSC. In Chapter 5, the mass compositions of carbon and TNO in electrode are determined by TGA. The analysis was conducted with a ramp rate of 10 ºC/min from 25 ºC to 1000 oC under an air atmosphere.

Figure D.16 The thermogravimetric analysis (TGA) Discovery 5500 from TA Instruments.